A COVID-19 vaccine faces a crisis of confidence pp. 1289 & 1294

Mutations and deletions in coronavirus variants p. 1306

Ambient growth of perovskites p. 1359

Science

$15
26 MARCH 2021
sciencemag.org

AAAS

DEADLY CASCADE

Cyanobacterial toxin responsible for decades of mysterious bald eagle deaths pp. 1298 & 1335

horizon™
INSPIRED CELL SOLUTIONS

Outsourcing solutions to support you in uncertain times

RNAi and CRISPR specialists

Expand lab capacity, maintain velocity

Cell line engineering service

- Experience and expertise with an affordable solution
- Knockouts, knock-ins and unique projects (iPSCs)

Assay development and screening services

- Functional genomic screens
- 2D & 3D cell panel screens
- Immune cell-based assays
- Fit-for-purpose assay development

Custom RNA synthesis service

- For unlimited experimental workflows
- Choose from a wide variety of chemical modifications

Explore

horizondiscovery.com

Lectures that could change your company's future

As technologies such as 5G and artificial intelligence (AI) mature, they bring about enormous changes to almost all industries. The "Systems Architect Growth Plan," an online lecture series codesigned by *Science* and Intel, aims at enhancing the skills of cloud career professionals, specifically in systems, infrastructure, emerging technologies, and solutions as well as helping companies to accelerate their digital transformation by presenting real-world, problem-solving best practices. Five top engineers and team leaders from five pioneering companies–namely Amazon Web Services (AWS), Baidu, Ping An Technology, Alibaba Cloud, and SF–participated in these recently recorded lectures.

The lecture series is clearly needed, as many architects and developers have questions on how to build a more efficient big data platform to better realize their business values. In the first lecture, Xiaolong Yao, assistant chief data officer (CDO) of SF, a leading Chinese logistics company, shares the company's practice of constructing a plan for efficient collection, storage, extraction, transformation, loading, and analysis of its huge data reservoir, and eventually building a system that is flexible and scalable.

Yao explains that his company's system deploys edge computing in several scenarios; edge computing is a paradigm in which the computing process is carried out close to the user device rather than at the computing center. "At the edge, we have [the capability for] more real-time reasoning, real-time calculation, and analysis; in the cloud, [computing] is more like data management, such as postevent analysis and algorithm training," says Yao.

The top priority for the financial industry in achieving its transformation is to construct a big data system that elevates efficiency, improves customer experience, and leads to income growth. In the second lecture, Zhi Weng, CDO at Ping An Technology, a cloud-service supplier under the leading Chinese insurance company Ping An Insurance Group, introduces four technological areas of big data platform construction for financial businesses: risk-based decision making, anti-fraud, AI technology, and blockchain applications, the latter involving a decentralized digital ledger that records information in a way that is difficult to change or hack.

While the first two lectures introduce solutions for contemporary issues, the third, delivered by Zhenyu Hou, deputy director of Baidu, a Chinese multinational technology company specializing in Internet-related services and products as well as artificial intelligence, is for entrepreneurs who want to embrace the future. As the demand for technological innovation and economic structural reform grows, and as the pandemic continues, big data centers will become an important part of China's strategic plan to revive the economy. In his lecture, Hou envisions what a future big data center will look like, the challenges it will face as data accumulate, and the software and hardware solutions to these challenges. "We can see that data center software and hardware has come to a [management] crossroads, and it is time for a serious overhaul," he says.

The fourth lecture covers cloud-native technologies, such as containers, service meshes, and immutable infrastructure. In August 2020, web service and cloud-computing company AWS introduced its cloud-native database Amazon Aurora, which became the fastest-growing cloud service in its history. In this lecture, Lianghong Fei, chief developer evangelist of AWS, examines the advantages that cloud-native technologies bring to enterprises as well as how to ensure the stability and safety of such technologies. "In the era of cloud computing, cloud native is the best choice for architects and developers," says Fei. "It can facilitate our work, no matter what scenario [we find ourselves in]."

Wei Lin, AI researcher at Alibaba Cloud, a Chinese multinational cloud-computing company and subsidiary of Alibaba Group, is responsible for its machine learning PAI (Platform of Artificial Intelligence). In the fifth lecture, Lin addresses AI applications, sharing how to best construct deep-learning models for searching, advertising, and user recommendations. Lin also discusses data labeling and management for specific targets in natural-language, audio, and image-processing models.

At the end of each lecture, a top systems architect from Intel speaks with the lecturer to further explore technological issues. For example, after the first lecture, Congchao Cheng, principal engineer at Intel and director of the China Cloud Innovation Center, interviews Yao about how to manage big data and how the company has made progress in meeting the increasing demand for high bandwidth and its Ethernet adapter. In addition to Cheng, the moderators include Jinquan Dai, Intel's fellow and chief architect, big data AI; Wenxin Wu, Intel's principal engineer and CTO of China Industry Solutions; Zhiming Li, Intel's principal engineer and platform architect; and Lei Xia, Intel's principal engineer and China's chief AI architect.

Learn more about the lectures at https://time.geekbang.org/course/intro/100058901.

IMAGE: COURTESY OF INTEL

NOMIS & Science
YOUNG EXPLORER AWARD

Research at the intersection of the social and life sciences

Unconventional. Interdisciplinary. Bold.

The newly launched **NOMIS & *Science* Young Explorer Award** recognizes bold, early-career researchers with an M.D., Ph.D., or M.D./Ph.D. who ask fundamental questions at the intersection of the social and life sciences. It is awarded to scientists who conduct research with an enthusiasm that catalyzes cross-disciplinary collaboration and who take risks to creatively address relevant and exciting questions.

Award winners will receive a cash prize of up to $15,000, and their essay submissions will be published in *Science*. They will also be invited to share their ideas with leading scientists in their respective fields at an award ceremony and to present their research to the NOMIS Board of Directors for potential future funding.

Apply by May 15, 2021
at www.sciencemag.org/nomis

Science
AAAS

NOMIS
FOUNDATION
Creating the Spark

CONTENTS

26 MARCH 2021 • VOLUME 371
ISSUE 6536

1302

Queens of the Texas leafcutter ant (*Atta texana*) dwarf their workers and have a much longer life span.

PHOTO: ALEX WILD

NEWS

IN BRIEF

IN DEPTH

FEATURES

INSIGHTS

PERSPECTIVES

POLICY FORUM

BOOKS *ET AL.*

WHERE IS CANCER RESEARCH HEADED NEXT?

Research behind cancer treatments are not just about the development of a cure but about the person in need of the cure.

Dr. Wayne Newhauser, the LSU Department of Physics & Astronomy's Dr. Charles M. Smith Chair in Medical Physics, along with LSU alumnus Will Donahue are the first to fully detail blood flow through any single organ or tissue by using computational modeling.

"No one had modeled with a computational model blood flow through an entire human organ. What people *have* done is model blood flow in complete detail in one cubic millimeter of an organ, and they've modeled blood flow throughout the entire body but with absolutely no detail of the finer vessels," said Newhauser.

Setting out to prove this was computationally possible—with the assistance of LSU's Center for Computation and Technology—, the researchers designed and implemented a two-step computational algorithm to calculate the blood flow rates using principles of steady-state fluid dynamics, an accurate approximation for the microvascular and venous structures in the human body.

They were able to demonstrate that it is computationally feasible to calculate the blood flow rate through 17 billion vessels in 6.5 hours using 256 compute nodes.

This newly developed computational modeling may change our methods of cancer treatments and drug delivery by allowing physicians to target the specific jeopardized areas, while also limiting serious collateral damage to patients post-cure.

Join LSU's community of fearless explorers.
lsu.edu/science

LSU | College of Science

YOUR QUESTION NEXT.

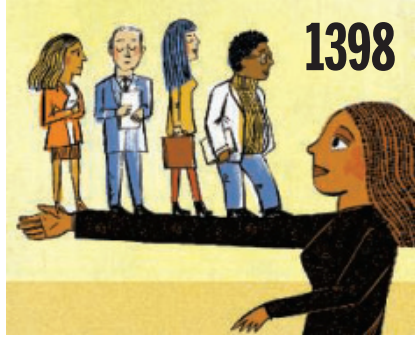

ON THE COVER

A bald eagle (*Haliaeetus leucocephalus*) clutches a shad as it flies over the White River in Arkansas. Bald eagles and other wildlife can succumb to vacuolar myelinopathy, a neurological disease. A cyanobacterium that grows on invasive aquatic plants produces the disease-causing neurotoxin, affecting wildlife in a bottom-up trophic cascade through the food chain. Toxin biosynthesis relies on bromide, so monitoring and management of the plant host, bromide levels, and neurotoxin are critical for protecting wildlife and human health. See pages 1298 and 1335.
Photo: Mike Martin

SCIENCE (ISSN 0036-8075) is published weekly on Friday, except last week in December, by the American Association for the Advancement of Science, 1200 New York Avenue, NW, Washington, DC 20005. Periodicals mail postage (publication No. 484460) paid at Washington, DC, and additional mailing offices. The title SCIENCE is a registered trademark of the AAAS. Domestic individual membership, including subscription (12 months): $165 ($74 allocated to subscription). Domestic institutional subscription (51 issues): $2148; Foreign postage extra: Air assist delivery: $98. First class, airmail, student, and emeritus rates on request. Canadian rates with GST available upon request, GST #125488122. Publications Mail Agreement Number 1069624. **Printed in the U.S.A.**
Change of address: Allow 4 weeks, giving old and new addresses and 8-digit account number. **Postmaster:** Send change of address to AAAS, P.O. Box 96178, Washington, DC 20090–6178. **Single-copy sales:** $15 each plus shipping and handling available from backissues.sciencemag.org; bulk rate on request. **Authorization to reproduce** material for internal or personal use under circumstances not falling within the fair use provisions of the Copyright Act can be obtained through the Copyright Clearance Center (CCC), www.copyright.com. The identification code for *Science* is 0036-8075. *Science* is indexed in the *Reader's Guide to Periodical Literature* and in several specialized indexes.

ILLUSTRATION: ROBERT NEUBECKER

Science AAAS

Editor-in-Chief Holden Thorp, hthorp@aaas.org

Executive Editor Monica M. Bradford

Editors, Research Valda Vinson, Jake S. Yeston **Editor, Insights** Lisa D. Chong

DEPUTY EDITORS Julia Fahrenkamp-Uppenbrink (UK), Stella M. Hurtley (UK), Phillip D. Szuromi, Sacha Vignieri **SR. EDITORIAL FELLOW** Andrew M. Sugden (UK) **SR. EDITORS** Gemma Alderton (UK), Caroline Ash (UK), Brent Grocholski, Pamela J. Hines, Di Jiang, Marc S. Lavine (Canada), Yevgeniya Nusinovich, Ian S. Osborne (UK), Beverly A. Purnell, L. Bryan Ray, H. Jesse Smith, Keith T. Smith (UK), Jelena Stajic, Peter Stern (UK), Valerie B. Thompson, Brad Wible, Laura M. Zahn **ASSOCIATE EDITORS** Michael A. Funk, Priscilla N. Kelly, Tage S. Rai, Seth Thomas Scanlon (UK), Yury V. Suleymanov **LETTERS EDITOR** Jennifer Sills **LEAD CONTENT PRODUCTION EDITORS** Harry Jach, Lauren Kmec **CONTENT PRODUCTION EDITORS** Amelia Beyna, Jeffrey E. Cook, Chris Filiatreau, Julia Katris, Nida Masiulis, Suzanne M. White **SR. EDITORIAL COORDINATORS** Carolyn Kyle, Beverly Shields **EDITORIAL COORDINATORS** Aneera Dobbins, Joi S. Granger, Jeffrey Hearn, Lisa Johnson, Maryrose Madrid, Ope Martins, Shannon McMahon, Jerry Richardson, Hilary Stewart (UK), Alana Warnke, Alice Whaley (UK), Anita Wynn **PUBLICATIONS ASSISTANTS** Jeremy Dow, Alexander Kief, Ronmel Navas, Brian White **EXECUTIVE ASSISTANT** Jessica Slater **ASI DIRECTOR, OPERATIONS** Janet Clements (UK) **ASI SR. OFFICE ADMINISTRATOR** Jessica Waldock (UK)

News Editor Tim Appenzeller

NEWS MANAGING EDITOR John Travis **INTERNATIONAL EDITOR** Martin Enserink **DEPUTY NEWS EDITORS** Elizabeth Culotta, Lila Guterman, David Grimm, Eric Hand (Europe), David Malakoff **SR. CORRESPONDENTS** Daniel Clery (UK), Jon Cohen, Jeffrey Mervis, Elizabeth Pennisi **ASSOCIATE EDITORS** Jeffrey Brainard, Catherine Matacic **NEWS REPORTERS** Adrian Cho, Jennifer Couzin-Frankel, Jocelyn Kaiser, Kelly Servick, Robert F. Service, Erik Stokstad, Paul Voosen, Meredith Wadman **INTERNS** Lucy Hicks, Cathleen O'Grady **CONTRIBUTING CORRESPONDENTS** Warren Cornwall, Andrew Curry (Berlin), Ann Gibbons, Sam Kean, Eli Kintisch, Kai Kupferschmidt (Berlin), Andrew Lawler, Mitch Leslie, Eliot Marshall, Virginia Morell, Dennis Normile (Shanghai), Elisabeth Pain (Careers), Charles Piller, Michael Price, Tania Rabesandratana (Barcelona), Joshua Sokol, Emily Underwood, Gretchen Vogel (Berlin), Lizzie Wade (Mexico City) **CAREERS** Donisha Adams, Rachel Bernstein (Editor), Katie Langin (Associate Editor) **COPY EDITORS** Julia Cole (Senior Copy Editor), Cyra Master (Copy Chief) **ADMINISTRATIVE SUPPORT** Meagan Weiland

Creative Director Beth Rakouskas

DESIGN MANAGING EDITOR Marcy Atarod **GRAPHICS MANAGING EDITOR** Alberto Cuadra **PHOTOGRAPHY MANAGING EDITOR** William Douthitt **WEB CONTENT STRATEGY MANAGER** Kara Estelle-Powers **DESIGN EDITOR** Chrystal Smith **DESIGNER** Christina Aycock **GRAPHICS EDITOR** Nirja Desai **INTERACTIVE GRAPHICS EDITOR** Kelly Franklin **SENIOR SCIENTIFIC ILLUSTRATORS** Valerie Altounian, Chris Bickel **SCIENTIFIC ILLUSTRATOR** Alice Kitterman **SENIOR GRAPHICS SPECIALISTS** Holly Bishop, Nathalie Cary **SENIOR PHOTO EDITOR** Emily Petersen **PHOTO EDITOR** Kaitlyn Dolan **WEB DESIGNER** Jennie Pajerowski

Chief Executive Officer and Executive Publisher Sudip Parikh

Publisher, Science Family of Journals Bill Moran

DIRECTOR, BUSINESS SYSTEMS AND FINANCIAL ANALYSIS Randy Yi **DIRECTOR, BUSINESS OPERATIONS & ANALYSIS** Eric Knott **DIRECTOR OF ANALYTICS** Enrique Gonzales **MANAGER, BUSINESS OPERATIONS** Jessica Tierney **SENIOR BUSINESS ANALYST** Cory Lipman, Meron Kebede **FINANCIAL ANALYST** Alexander Lee **ADVERTISING SYSTEM ADMINISTRATOR** Tina Burks **SENIOR SALES COORDINATOR** Shirley Young **DIGITAL/PRINT STRATEGY MANAGER** Jason Hillman **QUALITY TECHNICAL MANAGER** Marcus Spiegler **ASSISTANT MANAGER DIGITAL/PRINT** Rebecca Doshi **SENIOR CONTENT SPECIALISTS** Steve Forrester, Jacob Hedrick, Antoinette Hodal, Lori Murphy **PRODUCTION SPECIALIST** Kristin Wowk **DIGITAL PRODUCTION MANAGER** Lisa Stanford **CONTENT SPECIALIST** Kimberley Oster **ADVERTISING PRODUCTION OPERATIONS MANAGER** Deborah Tompkins **DESIGNER, CUSTOM PUBLISHING** Jeremy Huntsinger **SR. TRAFFIC ASSOCIATE** Christine Hall **SPECIAL PROJECTS ASSOCIATE** Sarah Dhere

ASSOCIATE DIRECTOR, BUSINESS DEVELOPMENT Justin Sawyers **GLOBAL MARKETING MANAGER** Allison Pritchard **DIGITAL MARKETING MANAGER** Aimee Aponte **JOURNALS MARKETING MANAGER** Shawana Arnold **MARKETING ASSOCIATES** Tori Velasquez, Mike Romano, Ashley Hylton **DIGITAL MARKETING SPECIALIST** Asleigh Rojanavongse **SENIOR DESIGNER** Kim Huynh

DIRECTOR AND SENIOR EDITOR, CUSTOM PUBLISHING Sean Sanders **ASSISTANT EDITOR, CUSTOM PUBLISHING** Jackie Oberst

DIRECTOR, PRODUCT & PUBLISHING DEVELOPMENT Chris Reid **DIRECTOR, BUSINESS STRATEGY AND PORTFOLIO MANAGEMENT** Sarah Whalen **ASSOCIATE DIRECTOR, PRODUCT MANAGMENT** Kris Bishop **PRODUCT DEVELOPMENT MANAGER** Scott Chernoff **PUBLISHING TECHNOLOGY MANAGER** Michael Di Natale **SR. PRODUCT ASSOCIATE** Robert Koepke **SPJ ASSOCIATE** Samantha Bruno Fuller

DIRECTOR, INSTITUTIONAL LICENSING Iquo Edim **ASSOCIATE DIRECTOR, RESEARCH & DEVELOPMENT** Elisabeth Leonard **MARKETING MANAGER** Kess Knight **SENIOR INSTITUTIONAL LICENSING MANAGER** Ryan Rexroth **INSTITUTIONAL LICENSING MANAGER** Marco Castellan **MANAGER, AGENT RELATIONS & CUSTOMER SUCCESS** Judy Lillibridge **SENIOR OPERATIONS ANALYST** Lana Guz **FULFILLMENT COORDINATOR** Melody Stringer **SALES COORDINATOR** Josh Haverlock

DIRECTOR, GLOBAL SALES Tracy Holmes **US EAST COAST AND MID WEST SALES** Stephanie O'Connor **US WEST COAST SALES** Lynne Stickrod **US SALES MANAGER, SCIENCE CAREERS** Claudia Paulsen-Young **US SALES REP, SCIENCE CAREERS** Tracy Anderson **ASSOCIATE DIRECTOR, ROW** Roger Goncalves **SALES REP, ROW** Sarah Lelarge **SALES ADMIN ASSISTANT, ROW** Bryony Cousins **DIRECTOR OF GLOBAL COLLABORATION AND ACADEMIC PUBLISHING RELATIONS, ASIA** Xiaoying Chu **ASSOCIATE DIRECTOR, INTERNATIONAL COLLABORATION** Grace Yao **SALES MANAGER** Danny Zhao **MARKETING MANAGER** Kilo Lan **ASCA CORPORATION, JAPAN** Kaoru Sasaki (Tokyo), Miyuki Tani (Osaka) **COLLABORATION/ CUSTOM PUBLICATIONS/JAPAN** Adarsh Sandhu

DIRECTOR, COPYRIGHT, LICENSING AND SPECIAL PROJECTS Emilie David **RIGHTS AND LICENSING COORDINATOR** Jessica Adams **RIGHTS AND PERMISSIONS ASSOCIATE** Elizabeth Sandler **CONTRACTS AND LICENSING ASSOCIATE** Lili Catlett

---

MAIN HEADQUARTERS
Science/AAAS
1200 New York Ave. NW
Washington, DC 20005

SCIENCE INTERNATIONAL
Clarendon House
Clarendon Road
Cambridge, CB2 8FH, UK

SCIENCE CHINA
Room 1004, Culture Square
No. 59 Zhongguancun St.
Haidian District, Beijing, 100872

SCIENCE JAPAN
ASCA Corporation
Sibaura TY Bldg. 4F, 1-14-5
Shibaura Minato-ku
Tokyo, 108-0073 Japan

EDITORIAL
science_editors@aaas.org

NEWS
science_news@aaas.org

INFORMATION FOR AUTHORS
sciencemag.org/authors/science-information-authors

REPRINTS AND PERMISSIONS
sciencemag.org/help/reprints-and-permissions

MEDIA CONTACTS
scipak@aaas.org

MULTIMEDIA CONTACTS
SciencePodcast@aaas.org
ScienceVideo@aaas.org

INSTITUTIONAL SALES AND SITE LICENSES
sciencemag.org/librarian

PRODUCT ADVERTISING & CUSTOM PUBLISHING
advertising.sciencemag.org/products-services
science_advertising@aaas.org

CLASSIFIED ADVERTISING
advertising.sciencemag.org/science-careers
advertise@sciencecareers.org

JOB POSTING CUSTOMER SERVICE
employers.sciencecareers.org
support@sciencecareers.org

MEMBERSHIP AND INDIVIDUAL SUBSCRIPTIONS
sciencemag.org/subscriptions

MEMBER BENEFITS
aaas.org/membercentral

EDITORIAL

Volatility of vaccine confidence

Last week, the European Medicines Agency declared the AstraZeneca COVID-19 vaccine safe and effective, after several European Union member states had suspended its use because of blood clot concerns. Will the public trust this message? This week's news could help—a U.S. phase 3 clinical trial of the vaccine shows promising efficacy in preventing symptomatic COVID-19. But sentiments toward vaccines are volatile and reflect external events—such as recent concern about AstraZeneca's efficacy data—as well as internal emotions.

Various polls on vaccine willingness made early predictions of low vaccine uptake owing to vaccine hesitancy. But with the ups and downs of virus surges, and more information—and misinformation—around the vaccines, confidence levels also had ups and downs. Vaccine willingness started to climb with news of an effective Pfizer vaccine, a second wave of infection, the emergence of new variants, and more lockdowns. Now, a reported safety risk and consequent anxieties have sent sentiments plummeting in some countries.

> **"But sentiments toward vaccines... reflect external events...as well as internal emotions."**

Author and physician Danielle Ofri called this undulation of sentiment "emotional epidemiology" as she reflected on the seeming eagerness, then hesitation or refusal, to receive the H1N1 influenza virus vaccine during the 2009 pandemic. COVID-19 is affecting the world at a much larger scale than H1N1; thus, vaccine hesitancy could pose a major threat to controlling the pandemic.

Scientists, politicians, and public health officials may not always recognize that vaccine hesitancy is not the same as being "anti-vaccine." The vaccine hesitant are often mischaracterized as "anti-science" or simply "anti-vaxx." But being hesitant or undecided in the face of a possible safety risk is not being anti-vaccine. A failure to understand the distinction can feed both fires.

What distinguishes the vaccine hesitant from anti-vaxxers? *The Anti-Vaxx Playbook*, recently published by the Center for Countering Digital Hate, underlined three key messages used by organized anti-vaccine groups: COVID-19 is not dangerous, the vaccine is dangerous, and vaccine advocates cannot be trusted. This builds upon a long history of "anti-vaccine tropes" identified by medical anthropologist Anna Kata, including questioning the safety and efficacy of vaccines, promoting alternative cures, claiming that vaccination infringes on individuals' civil liberties, promoting conspiracy theories, and asserting that vaccines are immoral. Anti-vaccination advocates typically represent well-organized entities with explicit agendas, ranging from financial interests (such as selling alternative cures) to ideological or political commitments (such as opposing specific legislation). These organizations also frequently shift their goalposts, claiming that vaccines cause any number of maladies while supporting opposing political platforms. Unfortunately, these themes are widespread on social media—nearly 150 anti-vaxx organizations have over 10 million followers online.

The vaccine hesitant are a highly diverse group. Modalities of hesitancy range from delays over receiving a vaccine because of anxiety around safety concerns, to fears due to historic individual or community experiences, to questions about COVID-19 vaccines. Those who refuse vaccines are not necessarily "anti-vaxx," although vaccine-hesitant individuals may consume content from anti-vaxx organizations as they search for evidence to confirm or dispel their concerns. The vaccine hesitant are therefore vulnerable to manipulation by anti-vaccine activists. They also risk being judged or labeled "anti-vaxx" by the very people—health care professionals—who are best positioned to encourage healthy behaviors.

How can vaccine hesitancy be addressed? Communication about vaccines must be delivered in an empathic manner to avoid stigmatizing those who question inoculation. This requires leveraging established relationships to address concerns of the vaccine hesitant. Examples include the Engaging in Medical Education with Sensitivity initiative during the 2019 measles outbreaks, in which Orthodox Jewish nurses empowered parents in that community to reach their own conclusions about vaccines while listening to their concerns and helping them contextualize information. Also, the University of Maryland's Health Advocates In-Reach and Research network of Black barbershops and salons trains personnel as health educators to encourage customers to pursue healthy behaviors.

In addition to the official regulatory endorsements of the safety of COVID-19 vaccines, it is locally trusted voices who will help build confidence in them. The world needs all the safe and effective vaccines that exist to end the pandemic. But it needs people who believe in them too.

–Heidi J. Larson and David A. Broniatowski

Heidi J. Larson is director of The Vaccine Confidence Project and a professor of Anthropology, Risk and Decision Science at the London School of Hygiene & Tropical Medicine, London, UK, and a clinical professor of Health Metrics Sciences at the University of Washington, Seattle, WA, USA. heidi.larson@lshtm.ac.uk

David A. Broniatowski is an associate professor of Engineering Management and Systems Engineering and associate director of the Institute for Data, Democracy, and Politics at The George Washington University, Washington, DC, USA. broniatowski@gwu.edu

10.1126/science.abi6488

50% The increase in atmospheric carbon dioxide since preindustrial times. The gas, which contributes to global warming, crossed that threshold for the first time when its concentration reached 417 parts per million this month (U.K. Met Office).

IN BRIEF

Edited by **Jeffrey Brainard**

NASA's likely new director backed the Space Launch System, which had a successful engine test last week at the Stennis Space Center in Mississippi.

LEADERSHIP

Biden picks former astronaut and senator to head NASA

President Joe Biden last week nominated former Senator Bill Nelson (D–FL) to lead NASA, a job that would require him to balance returning humans to the Moon with sending robots to observe Earth, Mars, and beyond. Nelson, who flew as a civilian on the space shuttle in 1986, was a lead Senate sponsor of NASA's new Moon rocket, the Space Launch System, which last week had the first successful test of its engines. Some advocates have called for replacing the delayed project, which has spent $20 billion so far, with privately operated rockets; but Nelson's nomination appears likely to cement the program. He has little track record of engagement with the agency's science programs, which have enjoyed rising budgets in recent years, especially for planetary science. But many members of Congress support an ambitious project to recover rock samples drilled by the Perseverance rover on Mars. Nelson is also seen as a backer of climate research, and earth scientists hope he will help reverse a long-term drop in NASA's spending on that discipline.

Virus variant earns CDC warning

COVID-19 | The U.S. Centers for Disease Control and Prevention (CDC) last week named as a "variant of concern" a spreading strain of the pandemic coronavirus identified in California in January. The variant, which comes in two slightly different forms called B.1.427 and B.1.429, becomes the fourth given that designation by CDC. A variant of concern may evade immunity, drugs, and diagnostic tests; make people sicker; and be more transmissible than the original virus. A recent preprint study indicated that the new variant flagged by CDC resists antibodies generated by vaccines and natural infection. In the past 30 days, the variant has accounted for some 61% of the samples sequenced in California and 65% of sequences in Nevada. Also last week, the U.S. Food and Drug Administration updated its emergency use authorization for the monoclonal antibody bamlanivimab to indicate that when used alone, it is unlikely to be effective against the new variant.

PHOTO: NASA/ROBERT MARKOWITZ

Pandemic curtails TB treatments

INFECTIOUS DISEASES | In countries that bear a heavy burden of tuberculosis (TB), diagnosis and treatment for the disease declined markedly in 2020 because health care facilities closed or diverted resources to COVID-19, a nonprofit group said last week. The Stop TB Partnership collected data from nine countries, seven of them in Asia, that account for 60% of the global TB burden. It found that TB diagnosis and treatment fell on average by 23%; at least 1 million fewer new cases were treated, the lowest level since 2008. In 2019, TB was the world's leading infectious killer, with 1.4 million deaths, more than 95% of them in developing countries. The Stop TB Partnership predicts that in 2020, TB remained the leading infectious killer in these countries even though COVID-19 surpassed it globally. The group urges health systems to simultaneously test for and tackle COVID-19 and TB, both infectious respiratory diseases.

EPA restores climate web page

CLIMATE CHANGE | It's back! The U.S. Environmental Protection Agency (EPA) last week relaunched a web page focused on climate change that former President Donald Trump's administration dismantled 4 years ago. The agency says it plans to add new, updated information in coming months about climate science and its actions to curb global warming. In 2017, then-EPA Administrator Scott Pruitt erased the page, which had existed for some 20 years, along with many other mentions of climate science on the agency's website.

Snail threatens African rice

AGRICULTURE | The golden apple snail (*Pomacea canaliculata*), an invasive pest that costs rice farmers in Asia more than $1 billion a year, has been documented in continental Africa for the first time. Farmers in Kenya's Mwea irrigation area, a 10,000-hectare region that produces more than 70% of the country's rice, noticed the 2-centimeter snails, which were later confirmed by DNA tests, researchers report this week in *CABI Agriculture and Bioscience*. The snails are eating 90% of seedlings, the farmers say. The snail species is native to the Americas. To help prevent its spread in Africa, researchers say Kenya should consider restricting movement of farm machinery and host plants from the infected area.

Eggs of the golden apple snail, a rice pest, on a stalk.

PHOTOS: (LEFT TO RIGHT) CABI; DIEGO J. SANTANA

The Gonzaga's leaf frog (*Pithecopus gonzagai*) was discovered in 2020 in northeastern Brazil.

BIODIVERSITY

A global treasure map for finding undiscovered species

Ecologists involved in mapping life on Earth have taken the next step: predicting where to find the 85% of the planet's species waiting to be discovered. Worried that conservation efforts usually ignore these hidden species, Mario Moura, an ecologist at the Federal University of Paraíba in Brazil, created an interactive map showing biodiversity hot spots with the richest potential for hosting unknown, land-dwelling species of mammals, birds, reptiles, and amphibians. He and ecologist Walter Jetz of Yale University built it using data about known vertebrates' size, habitat, and nine other attributes that influence the likelihood of discovery at a particular location. For example, large mammals living near people are much more likely to be found than tiny frogs in a remote jungle. The map predicts that Brazil has more mystery species, 10% of all, than any other country. Colombia, Indonesia, and Madagascar account for 5% each, Moura and Jetz reported this week in *Nature Ecology & Evolution*.

NIH's translation head moves on

BIOMEDICINE | The founding director of the U.S. National Institutes of Health's (NIH's) center focusing on the translation of basic science into treatments is stepping down. Neurologist and geneticist Christopher Austin, who led the National Center for Advancing Translational Sciences (NCATS), will become a partner at the venture capital firm Flagship Pioneering. NIH Director Francis Collins persuaded Congress to create NCATS in 2011, despite skepticism from industry. Under Austin, the center's efforts included screening small molecules for drug candidates, developing treatments for rare diseases, and streamlining clinical trials at academic health centers. Some observers say NCATS never had the budget to realize its ambitions (*Science*, 27 September 2019, p. 1363). But the government's role in drug development may soon grow, with President Joe Biden expected to reveal details for a health agency modeled after the applications-oriented Defense Advanced Research Projects Agency.

Drug for Huntington disease fails

DRUG DEVELOPMENT | A late-stage drug trial that had buoyed the hopes of families afflicted by Huntington disease, a devastating, incurable neurological illness, was stopped on 22 March by the manufacturer, Roche. A data monitoring committee had recommended the move after weighing benefits and risks of the drug, tominersen (formerly called IONIS-HTTRx and RG6042). The company said no new safety issues had emerged during the trial, but provided no additional details. Tominersen is an antisense oligonucleotide, a snippet of genetic code designed to interfere with production of a protein—in this case,

IN FOCUS The stems, air bladders, and blades of giant kelp (*Macrocystis pyrifera*), the world's largest seaweed, form a golden still life. With fronds reaching more than 30 meters, the species thrives in cold, clear water, forming dense forests that host diverse ecosystems. This prize-winning image is part of an outdoor exhibit about algae at the University of Nottingham that can be seen at http://scim.ag/3f6MoRU.

PHOTO: ERASMO EMACAYA

the mutant protein called huntingtin that causes the inherited disease. The drug was developed by Ionis Pharmaceuticals, which licensed it to Roche in 2017, shortly after an early human trial showed it caused dose-dependent reductions in huntingtin (*Science,* 24 August 2018, p. 742). The sudden cessation stunned trial leaders, who had finished enrolling nearly 800 people in April 2020 and expected results in 2022.

Gorillas adopt young orphans

ANIMAL BEHAVIOR | Adult mountain gorillas, including male silverbacks, often adopt motherless or orphaned young members of their social groups—a behavior previously thought to be rare in mammals other than humans—a study reports. Chimpanzees and other social mammals that lose their mothers face a greater risk of dying, and gorillas often kill orphans from different social groups. But thanks to the in-group communal care, gorillas who were motherless or orphaned survived as well as youngsters whose mothers were still around. This week in *eLife*, scientists describe the analysis, which used a remarkable 53 years of data on mountain gorillas collected at the Dian Fossey Gorilla Fund's Karisoke Research Center in Rwanda, in one of the longest field studies. Scientists found that 59 motherless or orphaned gorillas also suffered no long-term decline in social rank or ability to reproduce. Older sisters and peers of orphans joined males, including dominant silverbacks, in frequent child care. Some motherless males who spent lots of time with the silverback in their social group did well: They grew up to become its dominant ape.

Lubchenco goes to White House

CLIMATE SCIENCE | The Biden administration last week appointed Jane Lubchenco, who headed the National Oceanic and Atmospheric Administration under former President Barack Obama, to serve as its top climate scientist in the White House Office of Science and Technology Policy. A marine ecologist and advocate for the ocean, Lubchenco will work as deputy director for climate and the environment, coordinating climate science across federal agencies and the U.S. Global Change Research Program. Lubchenco's focus will be to spur research and action on climate mitigation that can also benefit the U.S. economy.

Europe disagrees on misconduct

SCIENCE POLICY | In Sweden, a national code uses 44,000 words to define research misconduct and discuss scientific values. Next door, Norway's equivalent is a brisk 900 words. An analysis of scientific integrity policies in 32 European nations has found wide differences not only in length, but in standards and definitions of research misconduct. The nonbinding European Code of Conduct for Research Integrity, issued by the European Federation of Academies of Sciences and Humanities in 2017, was intended to promote consistency; it also allows countries to add language to fit their circumstances. But only two of 32 countries examined—Bulgaria and Luxembourg—have adopted the code wholesale, according to a study last month in *Bioethics*. And there's just one principle that all countries have agreed on: that fabrication, falsification, and plagiarism of data and findings constitute research misconduct. Research ethicists say the differences threaten to create confusion and disputes for multinational scientific collaborations as they decide which country's rules apply.

Microbial spores hitch rides

MICROBIOLOGY | Soil bacteria called *Streptomyces* are guardian angels of the microbial world: They produce antibiotics that humans depend on and protect plants from harmful microbes. But because they lack self-propulsion, researchers have long puzzled over how they find the plants they defend. Now, scientists have discovered that the microbe's dormant spores typically hitch rides on the whiplike flagella of other, mobile soil microbes heading for plant roots, researchers reported last week in *The ISME Journal: Multidisciplinary Journal of Microbial Ecology*. A few other species of bacteria and a fungus are known to catch rides on other microbes. But the observed piggybacking on microbes by spores—previously known to latch on to insects and other small animals for travel—is a first, says co-author Alise Muok of Leiden University. With this mystery solved, researchers may one day modify the hitchhiking to improve plant protection, she adds.

SCIENCEMAG.ORG/NEWS
Read more news from *Science* online.

eppendorf & Science

PRIZE FOR NEUROBIOLOGY

2020 Winner
Christopher Zimmerman, Ph.D.
Princeton Neuroscience Institute
For research on thirst and drinking behavior

Application Deadline
June 15, 2021

Now It's Your Turn!

Eppendorf & Science Prize for Neurobiology
The annual Eppendorf & Science Prize for Neurobiology is an international prize which honors young scientists for their outstanding contributions to neurobiological research based on methods of molecular and cell biology. The winner and finalists are selected by a committee of independent scientists, chaired by *Science*'s Senior Editor, Dr. Peter Stern. If you are 35 years of age or younger and doing great research, now is the time to apply for this prize.

As the Grand Prize Winner, you could be next to receive
> Prize money of US$25,000
> Publication of your work in *Science*
> Full support to attend the Prize Ceremony held in conjunction with the Annual Meeting of the Society for Neuroscience in the USA
> 10-year AAAS membership and online subscription to *Science*
> Complimentary products worth US$1,000 from Eppendorf
> An invitation to visit Eppendorf in Hamburg, Germany

It's easy to apply! Write a 1,000-word essay and tell the world about your work. Learn more at:

eppendorf.com/prize

eppendorf Science AAAS

IN DEPTH

A physician prepares a dose of AstraZeneca's COVID-19 vaccine in Bologna, Italy, on 19 March.

PHOTO: MICHELE LAPINI/GETTY IMAGES

COVID-19

New problems erode confidence in AstraZeneca's vaccine

Rare clotting disorders interrupt vaccination in Europe as U.S. expert panel rebukes company over efficacy data

By **Gretchen Vogel** *and* **Kai Kupferschmidt**

In the global battle against COVID-19, the vaccine made by British-Swedish firm AstraZeneca has been a source of great hope. It's easy to store—requiring only refrigeration, not a deep freeze—and the firm has partnered with several other manufacturers as part of its pledge to make the vaccine, developed by researchers at the University of Oxford, available to countries around the world at low cost.

But the vaccine's journey has been anything but smooth. The company's early efficacy claims were confusing and, in some cases, disappointing. And over the past 2 weeks, the waters got particularly choppy. More than 20 European countries suspended use of the shots after more than a dozen recently vaccinated people developed unusual clotting disorders. Immunizations resumed in most countries after the European Medicines Agency (EMA) investigated the matter.

Then, the company announced the long-awaited results of a large trial in the Americas that seemed to end lingering doubts about the vaccine's efficacy—only to be rebuffed by the Data and Safety Monitoring Board (DSMB) overseeing the study, which, in a highly unusual clash, suggested the company had presented "outdated information" on efficacy. "It appears that [AstraZeneca] may have been using the most favorable data, and the DSMB wanted to make sure they corrected that," says Anthony Fauci, director of the U.S. National Institutes of Allergy and Infectious Diseases (NIAID), which appointed the DSMB and made the discord public in a 23 March statement. (The DSMB saw no safety concerns, however.)

The company promised to publish more up-to-date data by 25 March. But the drama left public health experts reeling and raised fears that trust in the vaccine would erode further. "From everything I know, the AZ vaccine is a good vaccine that I would be comfortable having my family get," Ashish Jha, dean of the Brown University School of Public Health, tweeted. "From everything I know, AZ's incompetence at communicating trial results, working with regulatory agencies, etc. is stunning."

The very rare hematological disorders seen in European recipients are perhaps the most worrisome development for the vaccine, but many scientists are still unsure what to make of them. Germany, Italy, Austria, Norway, and Denmark have all reported cases of people who developed widespread blood clots, low platelet counts, and internal bleeding; at least seven have died. "It's a very special picture" of symptoms, says Steinar Madsen, medical director of the Norwegian Medicines Agency. "Our leading hematologist said he had never seen anything quite like it."

The problems appear to be more common among vaccinees than would be expected by chance. Germany's regulatory agency, the Paul Ehrlich Institute, recommended pausing vaccinations after receiving seven reports of what it called cerebral venous thrombosis, a rare type of stroke leading to massive, life-threatening bleeding in the brain, occurring in a 2-week window after vaccination; only one such case would have been expected among the 1.6 million vaccinees in that time period.

On 18 March, EMA said its experts could not rule out a connection to the vaccine and decided to add a warning to the product information. But it stressed that the vaccine's benefits outweighed the risks and urged European countries to start administering the shots again. As *Science* went to press, most countries had done so, but five Nordic nations had not. (France decided to restrict its use to people 55 and over, because the suspected side effects appeared mostly in younger people.) Initial polls showed the public's confidence in the vaccine had been significantly dented, a worrying sign in countries that are facing rapidly increasing infections and sluggish vaccination campaigns.

A somewhat similar blood disorder, called immune thrombocytopenia (ITP), has been seen in at least 40 people in the United States who received the Pfizer or Moderna vaccines against COVID-19, but the U.S. Food and Drug Administration said that syndrome did not appear to be more common in vaccinated people.

Madsen says the European cases are distinct from ITP, which does not result in widespread blood clots.

Just how AstraZeneca's vaccine could cause the problems seen in Europe is unclear. "The combination of thromboses and low platelet counts immediately raises the possibility of an immune reaction," says Sabine Eichinger, a hematologist at the Medical University of Vienna who treated a 49-year-old intensive care nurse who died 11 days after receiving the vaccine. The timing of symptom onset—between 4 and 16 days following vaccination—was another clue that renegade antibodies might be playing a role, says hematologist Andreas Greinacher at the University of Greifswald in Germany.

Greinacher, Eichinger, and other scientists have found that blood samples from at least six patients tested positive for antibodies that react to platelet factor 4, a key molecule involved in clotting and inflammation. The finding led the researchers to conclude that the process resembles an autoimmune disorder called heparin-induced thrombocytopenia (HIT)—a rare side effect of the blood thinner heparin that leads to plummeting platelet counts and clotting. Something about the AstraZeneca vaccine seems to trigger a similar syndrome, the researchers say, which they dubbed vaccine-induced prothrombotic immune thrombocytopenia (VIPIT). A research group in Norway has come to a similar conclusion.

HIT can be treated with high doses of intravenous immunoglobulins and nonheparin blood thinners; the same approach works for VIPIT, says Greinacher, noting that a doctor whom the group advised successfully treated at least one case. He stresses that the AstraZeneca vaccine should remain in use, even if the rare syndrome occurs, "We know what to do: how to diagnose it, and how to treat it," he says.

Greinacher and his colleagues announced their findings in a 19 March press release—and have alerted AstraZeneca—but they have not published their data, leading other experts to reserve judgment. And some of the cases do not fit the VIPIT description. For instance, one vaccinee in Germany has been diagnosed with atypical hemolytic uremic syndrome, another disease that can show up as widespread blood clotting and low platelet counts but that's caused by damage to the endothelial lining of blood vessels. The VIPIT hypothesis "may explain a few of the cases. I don't think this explains all of them," says Robert Brodsky, a hematologist at Johns Hopkins University.

In a statement, AstraZeneca emphasized that blood clots in general are no more common among people who have received its vaccine. But the statement did not address the unusual set of symptoms seen in Europe, or Greinacher's hypothesis.

The data from the new phase 3 trial, in 32,000 people in the United States, Chile, and Peru, seemed to offer some good news for the vaccine. According to a 22 March press release from the company, the trial showed it had 79% efficacy at preventing symptomatic COVID-19. After the earlier, mixed results, the clear-cut finding excited public health experts and raised hopes that the vaccine might soon be used in the United States, where AstraZeneca has not yet filed a request for emergency use authorization.

But less than 24 hours later, NIAID issued a statement saying AstraZeneca might have provided "an incomplete view of the efficacy data." The company says the press release was based on data gathered until 17 February, when a prespecified cutoff point was reached. But the DSMB was "very concerned" that later data were excluded," Fauci says. The company said it would update its results "within 48 hours," but a letter from the DSMB to the company reportedly said that when later trial data were included, the efficacy fell to between 69% and 74%.

Science's COVID-19 reporting is supported by the Heising-Simons Foundation.

A delay in the vaccine's authorization in the United States is unlikely to slow that country's immunization campaign; the U.S. expects to have enough doses of three other vaccines for its entire population by the end of May. That is not the case in Europe, where the AstraZeneca vaccine was envisioned as a key weapon in the pandemic arsenal.

The European Union has ordered 400 million doses, which have arrived much more slowly than foreseen. Even as the safety questions developed, the European Commission charged that AstraZeneca has favored the United Kingdom over the European Union in deliveries and threatened to block doses made on the continent from being exported to the U.K. The pause in immunizations, and the dropping confidence, may cause further delays just as cases across the continent are soaring. It is not yet clear, experts say, what impact the setbacks might have on global use of AstraZeneca's vaccine, a cornerstone of the World Health Organization's plan to help low-income countries beat the pandemic.

The speed of immunizations in the next 4 weeks will be crucial for how many people eventually get sick and die in Europe's third wave, says Dirk Brockmann, a disease modeler at the Robert Koch Institute. "We actually need to speed up vaccinations—a lot," he says. ■

GEOPHYSICS

Remains of Moon-forming impact may lie deep in Earth

Mysterious rocks at mantle's base tied to violent "Theia" strike 4.5 billion years ago

By **Paul Voosen**

Scientists have long agreed that the Moon formed when a protoplanet, called Theia, struck Earth in its infancy some 4.5 billion years ago. Now, a team of scientists has a provocative new proposal: Theia's remains can be found in two continent-size layers of rock buried deep in Earth's mantle.

For decades, seismologists have puzzled over these two blobs, which sit below West Africa and the Pacific Ocean and straddle the core like a pair of headphones. Up to 1000 kilometers tall and several times that wide, "they are the largest thing in the Earth's mantle," says Qian Yuan, a Ph.D. student in seismology at Arizona State University (ASU), Tempe. Seismic waves from earthquakes abruptly slow down when they pass through the layers, which suggests they are denser and chemically different from the surrounding mantle rock.

The large low-shear velocity provinces (LLSVPs), as seismologists call them, might simply have crystallized out of the depths of Earth's primordial magma ocean. Or they might be dense puddles of primitive mantle rock that survived the trauma of the Moon-forming impact. But based on new isotopic evidence and modeling, Yuan believes the LLSVPs are the guts of the alien impactor itself. "This crazy idea is at least possible," says Yuan, who presented the hypothesis last week at the Lunar and Planetary Science Conference.

The idea has rattled around lab corridors and conference halls for years. But Edward Garnero, a seismologist at ASU Tempe who was not involved in the work, says it's the first time anyone has marshaled multiple lines of evidence and mounted a serious case for it. "I think it's completely viable until someone tells me it's not."

Evidence from Iceland and Samoa sug-

Theia, perhaps as big as the proto-Earth, would have delivered its densest rocks inside the planet.

gests the LLSVPs have existed since the time of the Moon-forming impact, says Sujoy Mukhopadhyay, a geochemist at the University of California (UC), Davis, who considers Yuan's idea plausible but is open to other explanations. Seismic imaging has traced plumes of magma that feed volcanoes on both islands all the way down to the LLSVPs. Over the past decade, Mukhopadhyay and others have discovered that lavas on the islands contain an isotopic record of radioactive elements that formed only during the first 100 million years of Earth history.

Moreover, a new picture of the Moon-forming impactor suggests it could have delivered a cargo of dense rock deep inside Earth. The impact theory was developed in the 1970s to explain why the Moon is dry and doesn't have much of an iron core: In a cataclysmic impact, volatiles like water would have vaporized and escaped, while a ring of less dense rocks thrown up in the collision would have eventually coalesced into the Moon. The theory invoked an impactor the size of Mars or—in recent variants—much smaller. But recent work from Yuan's coauthor, ASU Tempe astrophysicist Steven Desch, suggests Theia was nearly as big as Earth.

> **"This crazy idea is at least possible."**
>
> **Qian Yuan**, Arizona State University, Tempe

In studies of Apollo Moon rocks, Desch and his colleagues measured the ratios of hydrogen to deuterium, a heavier hydrogen isotope. Light hydrogen was far more abundant in some of the Moon samples than in Earth rocks, they found. To capture and hold onto so much light hydrogen, Theia must have been massive, they proposed in a 2019 study in *Geochemistry*. It must also have been quite dry, as any water, which is naturally enriched in heavy hydrogen during its formation in interstellar space, would have raised the overall deuterium levels. Such a dry, large protoplanet would have separated into layers with an iron-depleted core and an iron-rich mantle, Desch says, some 2% to 3.5% denser than present-day Earth.

Even before Yuan learned of Desch's density estimates, he was modeling Theia's fate. His model suggests that after the collision, Theia's core would have quickly merged with Earth's. He also probed the fate of Theia's mantle, varying Theia's size and density to see what conditions would have allowed the material to persist, rather than mixing in, and sink to the mantle's base. The simulations consistently showed that mantle rocks 1.5% to 3.5% denser than Earth's would survive and end up as piles near the core. The result lined up perfectly with Desch's deuterium evidence. "It's this sweet spot for the density," Desch says.

A massive Theia would also explain the scale of the LLSVPs, which together contain six times more mass than the Moon. If they are extraterrestrial, Yuan says, only an impactor as large as Theia could have delivered them.

There are many caveats, however, including the fuzzy evidence for the LLSVPs themselves. Their pilelike structure could simply be an illusion created by models of the interior that rely on low frequency seismic waves, which blur small differences, Barbara Romanowicz, a seismologist at UC Berkeley, and Anne Davaille, a geophysicist at Paris-Saclay University, suggested in a study in *Tectonics* last year. Rather than reaching up 1000 kilometers, the piles may rise only a few hundred kilometers before breaking off into branched plumes. "There may be holes in them," Romanowicz says. "They may be a bundle of tubes."

Smaller or less monolithic LLSVPs would also be consistent with a forthcoming analysis that finds the LLSVPs are densest at the bottom, says Harriet Lau, a geophysicist at UC Berkeley. The analysis relies on two ways of imaging the deep Earth: using GPS stations to measure the way the Moon's tidal pull stretches Earth, and seismometers to sense how Earth's natural vibrations pass through the deep mantle. "Perhaps the real story behind the density is the distribution depth," she says.

Less massive LLSVPs could complicate the idea that Theia was nearly the size of a proto-Earth, says Jennifer Jenkins, a seismologist at Durham University. Yuan's picture, she adds, "is not inconsistent with what we know, but I'm not entirely convinced."

Desch says the team could test its idea by looking for geochemical similarities between the island lavas and rocks from the Moon's mantle. None of the Apollo samples capture the unaltered mantle, which is one reason scientists want samples from the Moon's largest impact crater, on its south pole, where such rocks may be exhumed. NASA and China are both planning robotic missions to the south pole this decade, and it is a leading candidate site for NASA's return of astronauts to the Moon.

If Theia's remnants do lie deep in Earth's mantle, they may not be alone. Seismologists are increasingly seeing small, ultradense pockets of material in the deep mantle, only a few hundred kilometers across, often near the edges of the LLSVPs. Maybe they are the sunken remnants of iron-rich cores from other miniature planets that hit early Earth, Jenkins says. Theia, in fact, might be just one grave in a planetary cemetery. ■

IMAGE: TOBIAS ROETSCH/*ALL ABOUT SPACE* MAGAZINE/GETTY IMAGES

VETERINARY SCIENCE

Deadly viral outbreak ravages European horses

Researchers are studying why a common herpesvirus suddenly took a serious toll

By **Christa Lesté-Lasserre**

Late last month, an international horse jumping competition in Spain that usually offers a sunny getaway for elite riders took a grim turn. A disease outbreak sickened scores of horses, leaving many so weak they couldn't stand and others exhibiting unusually aggressive behavior. At least 17 animals have since died; others have had abortions or needed surgery to repair organ damage.

The equestrian world is bracing for worse to come. Before researchers were able to identify the outbreak's cause—a known pathogen named equine herpesvirus type 1 (EHV-1)—some 600 of the 750 horses participating in the event were already heading home, threatening to spread what officials already call the most serious EHV-1 outbreak in Europe in decades. In a bid to contain the damage, the International Federation for Equestrian Sports (FEI), which oversees international equestrian competitions, has canceled all European events—including its World Cup—through at least mid-April. Horse owners, meanwhile, are frantically trying to vaccinate and isolate their horses.

For scientists, the outbreak has raised a host of questions. They are examining why EHV-1, a familiar virus that typically produces milder symptoms, appears to have hit these animals, particularly mares, unusually hard. Some are wondering whether drugs or the vaccine against EHV-1 itself may have played a role. "Our top priority must be to deal with the immediate impact of this terrible virus," says Göran Åkerström, veterinary director of FEI. But, "It is also crucial that we … expand our epidemiological data." A special FEI working group to study the outbreak had its first meeting on 18 March.

Researchers say conditions at the monthlong competition, held in Valencia, Spain, were ripe for an outbreak of EHV-1, which is primarily spread by exhaled droplets. The horses were housed in tightly packed stalls, and "All it takes is for one horse carrying a latent virus to have some sort of stress, and his virus gets activated and starts shedding," says equine disease specialist Lutz Goehring of Ludwig Maximilian University of Munich.

Sick animals soon overwhelmed an equine hospital at the nearby CEU Cardenal Herrera University, says Ana Velloso Álvarez, a veterinarian there. Exhausted medics were treating up to 20 animals simultaneously, with many horses hoisted in slings, literally hanging between life and death. "I think I understand more what it's been like for [COVID-19] doctors," Álvarez says.

A horse suffering from neurological symptoms caused by EHV-1 is treated in Valencia, Spain.

PHOTO: ANA VELLOSO/VETERINARY TEACHING HOSPITAL CARENDAL HERRERA

Studies have found that nearly all horses have been exposed to at least one of EHV-1's five major strains, and animals can carry inactive virus for years. Active infections usually cause fever and mild respiratory disease, sometimes abortion. One especially worrying variant, known as type 1, can cause serious neurological damage, rendering horses wobbly or unable to stand. Occasionally, it kills them.

Most outbreaks affect just a handful of horses before a farm is quarantined and disinfected. And less than 15% of infected animals typically exhibit neurological symptoms. But in Valencia up to 40% of sick horses have shown signs of neurological damage, Álvarez says. And, in an unusual twist for EHV-1, each horse had its own cocktail of problems. Some had intestinal blood clots and needed surgery. Others had swollen legs, walked like they were drunk, or exhibited unusual behavior. "This is completely different from what we're used to [with EHV-1]," Álvarez says.

Genetic sequencing suggests the outbreak wasn't caused by a new strain of EHV-1. That has researchers looking at other factors that might have worsened outcomes. One is travel. Some horses spent up to 3 days journeying to the event, and such long trips can be "a huge stressor," says Barbara Padalino, an equine scientist at the University of Bologna. Recent studies by her team have shown that after just a 12-hour trip, a horse's immune defenses against EHV-1 drop, increasing the chance of infection.

Other scientists are examining the role of sex. About 80% of the most severe Valencia cases involved mares, Álvarez says. Some researchers wonder whether medications used to stop the mares' reproductive cycles—a treatment some riders think makes a horse easier to handle—might have contributed to illness. One popular drug, altrenogest, is based on progesterone, which has been shown to weaken immune function, notes Christine Aurich, an equine gynecologist at the Graf Lehndorff Institute in Germany.

Researchers are also scrutinizing the EHV-1 vaccine, which has a spotty record of preventing disease and requires booster shots every 6 months. Many of the sick horses had been vaccinated, Åkerström says—but past studies have hinted that horses may be at higher risk of neurological symptoms in the weeks after vaccination. FEI's working group is gathering vaccination records, as well as infection and symptom data, in hopes of clarifying such issues—and developing better ways to treat and prevent future outbreaks. ■

Christa Lesté-Lasserre is a journalist in Paris.

Eagles may get exposed to a neurotoxin through their prey.

PHOTO: MIKE MARTIN

WILDLIFE ECOLOGY

Mysterious eagle killer identified

A new species of cyanobacteria that lives on invasive waterweed produces an unusual neurotoxin

By **Erik Stokstad**

More than 25 years ago, biologists in Arkansas began to report dozens of bald eagles paralyzed, convulsing, or dead. Their brains were pocked with lesions never seen before in eagles. The disease was soon found in other birds across the southeastern United States. Eventually, researchers linked the deaths to a new species of cyanobacteria growing on an invasive aquatic weed that is spreading across the country. The problem persists, with the disease detected regularly in a few birds, yet the culprit's chemical weapon has remained unknown.

On page 1335, a team identifies a novel neurotoxin produced by the cyanobacteria and shows that it harms not just birds, but fish and invertebrates, too. "This research is a very, very impressive piece of scientific detective work," says microbiologist Susanna Wood of the Cawthron Institute. An unusual feature of the toxic molecule is the presence of bromine, which is scarce in lakes and rarely found in cyanobacteria. One possible explanation: the cyanobacteria produce the toxin from a bromide-containing herbicide that lake managers use to control the weed.

The discovery highlights the threat of toxic cyanobacteria that grow in sediment and on plants, Wood says, where routine water quality monitoring might miss them. The finding also equips researchers to survey lakes, wildlife, and other cyanobacteria for the new toxin. "It will be very useful," says Judy Westrick, a chemist who studies cyanobacterial toxins at Wayne State University and was not involved in the new research. "I started jumping because I got so excited."

Wildlife biologists with U.S. Geological Survey and local institutions first detected the eagles' brain disease, now called vacuolar myelinopathy, at DeGray Lake in Arkansas in late 1994. They soon learned that coots and owls at the lake were dying with similar brain lesions. The researchers ruled out industrial pollutants and infectious disease, and they couldn't find any algal toxins in the water. Then funding ran out, and the scientists turned to other projects.

But Susan Wilde, an aquatic ecologist at the University of Georgia, Athens, persisted, with intermittent funding. "I just had a lot of colleagues and graduate students that were self-propelled to work on this." Birds were dying at lakes and reservoirs throughout the southeast, and at every lake her team visited, they found *Hydrilla verticillata*, a tough and fast-growing invasive plant. In 2001, Wilde noticed dark spots on the underside of the leaves. Back in the lab, she put a sample under a microscope and shone light that makes cyanobacteria glow red. The whole leaf lit up. "I was running around the hallways," Wilde recalls. "It was kind of a eureka moment." The cyanobacterium was a new species, which Wilde named *Aetokthonos hydrillicola* in 2014. She suspected it was producing a neurotoxin.

To confirm that hunch, Wilde and colleagues fed hydrilla to mallards in the lab. Only those that ate leaves harboring the cyanobacteria developed brain lesions. Next, a group led by Timo Niedermeyer, a natural products chemist at Martin Luther University Halle-Wittenberg, figured out how to culture the cyanobacterium and initially found that the lab-grown strain did not cause lesions in chickens. "Huge disappointment," he recalls. But when they added bromide salts to the culture medium, the cyanobacteria began to produce the neurotoxin. In further tests, Wilde and colleagues found that the toxin also kills fish, insects, and worms. "This is a really potent neurotoxin, even at fairly low levels," she says. Wilde suspects mammals are also vulnerable; her colleagues hope to test the compound on mice.

Niedermeyer's lab discovered the neurotoxin was fat-soluble, which is unusual for cyanobacterial toxins and suggests it can accumulate in tissues. Fish and birds are exposed when they eat hydrilla coated with the new species of cyanobacteria, and then the toxin may move through the food web as eagles and owls consume afflicted prey. "If verified, bioaccumulation has important consequences to the whole ecosystem and human health" if people consume toxin-contaminated fish or waterfowl, says Kaarina Sivonen, a microbiologist at the University of Helsinki.

The cyanobacterium appears to get the bromide it needs to make the toxin from hydrilla, which can concentrate bromide from lake sediment in its leaves. Bromides are rare in freshwater, but they could be eroding from rocks, or they might originate from coal-fired power plants. Other sources could include brominated flame retardants, fracking fluids, and road salt. Wilde suspects one local source might be an herbicide, diquat dibromide, that is used to kill hydrilla.

Wilde points to recent success managing the weed without chemicals, by stocking lakes with fish that eat hydrilla. Although grass carp are not desirable for fishing, using sterile carp would ensure the population would die out once its work was done. The Army Corps of Engineers has already released the fish into a reservoir on the border of Georgia and South Carolina, where they removed the hydrilla. Since then, no more sick eagles have been found.

Saving the birds from the neurotoxin will be a long fight, however, because both hydrilla and the cyanobacteria are exceptionally hardy. The invasive plant is likely to continue to be spread by boats, researchers say, and perhaps also migrating birds. "We should expect the cyanobacterium to follow," says George Bullerjahn, a microbiologist at Bowling Green State University, "and the threat of toxicity to become a broader issue." ■

ARCHAEOLOGY

Great Lakes people among first coppersmiths

New dates show Native Americans worked pure ore nearly 10,000 years ago

By **David Malakoff**

About 8500 years ago, hunter-gatherers living beside Eagle Lake in Wisconsin hammered out a conical, 10-centimeter-long projectile point made of pure copper. The finely crafted point, used to hunt big game, highlights a New World technological triumph—and a puzzle. A new study of that artifact and other traces of prehistoric mining concludes that what is known as the Old Copper Culture emerged, then mysteriously faded, far earlier than once thought.

The dates show that early Native Americans were among the first people in the world to mine metal and fashion it into tools. They also suggest a regional climate shift might help explain why, after thousands of years, the pioneering metallurgists abruptly stopped making most copper tools and largely returned to stone and bone implements.

Earth's largest and purest copper deposits are found around North America's Great Lakes. At some point, Native Americans learned to harvest the ore and heat, hammer, and grind it into tools. They left behind thousands of mines and countless copper artifacts, including lethal projectile points, hefty knives and axes, and petite fish hooks and awls. Today, it's not uncommon to meet residents of the region "who have buckets of copper artifacts [that they've found] tucked away in their basements," says David Pompeani, a geologist at Kansas State University, Manhattan, who studies ancient mining.

When researchers began to date the artifacts and mines, they saw a perplexing pattern: The dates suggested the people of the Old Copper Culture began to produce metal tools about 6000 years ago and then, for reasons that weren't clear, mostly abandoned copper implements about 3000 years ago. After that, early Native Americans used copper mostly for smaller, less utilitarian items associated with adornment, such as beads and bracelets. "The history is just so peculiar," Pompeani says. In many other ancient cultures that learned how to make metal tools, the technology persisted, he says.

About 10 years ago, Pompeani began doctoral research that cast doubt on the Old Copper timeline. He extracted sediment cores from lakes adjacent to prehistoric mines on Michigan's Keweenaw Peninsula and Isle Royale and measured trace metals in the cores, including lead and titanium, that had been released by processing the ore. The analyses showed copper mining began about 9500 years ago in some areas—some 3500 years earlier than once thought. It also ended earlier, about 5400 years ago, Pompeani reported in *The Holocene* in 2015.

Now, a team led by Pompeani presents new evidence for the revised timeline. The researchers used modern methods to reanalyze 53 radiocarbon dates—including eight newly collected dates—associated with the Old Copper Culture. Some came from wood or cordage still attached to spearpoints; others came from charcoal, wood, or bone found at mines and human burials. The oldest reliably dated artifact turned out to be the 8500-year-old projectile point found in Wisconsin.

This month in *Radiocarbon*, the team reports that the most reliable dates, combined with the sediment data, indicate the Old Copper Culture emerged at least 9500 years ago and peaked between 7000 and 5000 years ago. That makes it at least as old, and perhaps older, than copper-working cultures documented in the Middle East, where archaeologists have documented a copper pendant believed to be 8700 years old.

The older window for Old Copper's peak doesn't surprise archaeologist Michelle Bebber of Kent State University who has studied the culture. The dates confirm "that hunter-gatherers [were] highly innovative," she says, and willing to "regularly experiment with novel materials."

But why did the ancient copper experiment abruptly end? Bebber's work replicating Old Copper–style arrowheads, knives, and awls suggests they weren't necessarily superior to the alternatives, especially after factoring in the time and effort required to produce metal implements. In controlled laboratory tests, such as shooting arrows into clay blocks that simulate meat, she found that stone and bone implements were mostly just as effective as copper. That might be because Great Lakes copper is unusually pure, which makes it soft, unlike harder natural copper alloys found elsewhere in the world, she says. Only copper awls proved superior to bone hole punchers.

Pompeani has identified another potential contributor to Old Copper's fade about 5000 years ago. Sediment cores, tree ring data, and other evidence suggest a sustained dry period struck the region around that time, he says. That could have fueled social and ecological disruptions that made it hard to devote time and resources to making copper tools. Over time, copper may have become something of a luxury item, used to signal social status.

Copper awls, however, bucked this trend: They required relatively little ore to make, Bebber notes, and the people of the Great Lakes continued to use them for thousands of years. ■

Archaeologists made these spears, replicas of those crafted by people of the Old Copper Culture.

PHOTO: MICHELLE BEBBER/KENT STATE UNIVERSITY EXPERIMENTAL ARCHAEOLOGY LAB

ENERGY

Carbon capture marches toward practical use

New CO_2-grabbing materials and policies could cut emissions from fossil fuel plants

By **Robert F. Service**

Windmills and solar panels are proliferating fast, but not fast enough to stave off the worst of climate change. Doing so, U.N. climate experts say, will also require capturing carbon dioxide (CO_2) from the tens of thousands of fossil fuel power plants and industrial smokestacks likely to keep belching for years to come. Today's most popular approach for capturing CO_2 is too expensive for widespread use. But researchers are now developing a new generation of chemical CO_2 traps, including one shown this month to reduce the cost by nearly 20%. When existing U.S. tax credits are added to the mix, carbon capture is nearing commercial viability, says Joan Brennecke, a carbon capture expert at the University of Texas, Austin.

Today's technology uses CO_2-grabbing chemicals called amines, dissolved in water. The problem is that once the amines capture CO_2, the greenhouse gas must be stripped off and stored so the amines can be reused. Releasing the CO_2 requires boiling the water and later recondensing the water vapor, which requires a vast amount of energy and increases the cost. Enter new "water lean" capture materials, including one described in the latest report. "This is a beautiful, very complete study," Brennecke says.

For decades, researchers have worked to find ways to capture carbon from industrial emissions and either use it to make chemicals or store it underground. Last year, companies captured some 40 million tons of CO_2 emissions, and the additional 30 carbon capture facilities planned worldwide could up that figure to 140 million tons—still minuscule compared with current annual global emissions of some 35 billion tons. For carbon capture efforts to be scaled up by orders of magnitude, the U.S. Department of Energy projects that by 2035, the cost needs to fall from roughly $58 per ton with state-of-the-art water-based amines to $30 per ton.

Typically, water that contains amines is sprayed into the top of an exhaust tower. As the droplets fall through the gas, they sop up CO_2. At the bottom of the tower, the CO_2-rich liquid gets pumped into a separate vessel and heated to boil off the water. Then, applied pressure causes water vapor to condense, leaving a pure stream of CO_2 to be captured and stored. The condensed water is added back to the amines and piped to the tower for another round of CO_2 capture.

In 2009, David Heldebrant, a chemist at the Pacific Northwest National Laboratory (PNNL), sought a new approach: "The goal was to get away from the water," he says. Over the next decade, he and his team created a collection of liquid organic solvents, eventually settling on one containing CO_2-grabbing amine groups with no need for water or dissolved capture agents. Organic solvents can release CO_2 when heated but, unlike water, need not be boiled and recondensed, potentially saving energy.

It wasn't an instant success. Heldebrant's team found that when the solvent captured CO_2, carbon-rich solids precipitated out, making the liquid viscous and difficult to pump. A collaboration with a team led by Robert Perry, a chemist at GE Global Research, revealed that when the amines bound CO_2, hydrogen atoms on solvent molecules became attracted to neighboring molecules, tying them together. So, the researchers tweaked the structure of the solvent, creating a molecule called 2-EEMPA. When the new solvent bound CO_2, the hydrogen bonds were more likely to form within individual 2-EEMPA molecules, rather than between neighbors, they reported in November 2020 in *Energy & Environmental Science*.

Now, in the March issue of *International Journal of Greenhouse Gas Control*, the PNNL team, together with researchers at the Electric Power Research Institute and the engineering giant Fluor, have published a detailed analysis showing that a full-scale coal-fired power plant using 2-EEMPA would require 17% less energy than today's state of the art carbon-capture systems. That would drop the cost of CO_2 capture to $47 per ton, not including the cost of transporting and pumping the CO_2 underground. "It's a very promising solvent," says Marty Lail, a carbon capture chemist at RTI International. Next year, the PNNL team plans to test 2-EEMPA at a small 0.5 megawatt coal-fired carbon capture testbed in Alabama.

Other researchers have made progress with their own solvents. In 2014, Brennecke and colleagues developed an ionic liquid-based CO_2 absorbent that has been projected to capture carbon at about the same cost as 2-EEMPA. And Lail and his colleagues have devised their own low-cost, proprietary water-lean solvent, which they will begin testing at a power plant in Norway early next year. Organic capture solvents "have a real future," he says.

They could also get a boost from policymakers. The United States already offers companies a tax credit of $50 for each ton of CO_2 they capture and store underground. And last week, a bipartisan group in Congress introduced a bill that would provide $4.9 billion for carbon capture projects. Both environmentalists and fossil fuel backers support the legislation, a rare alignment in today's divided political landscape. ■

A cheaper cleanup

Organic solvents promise to capture carbon dioxide (CO_2) from fossil fuel-burning power plants more cheaply than the water-based capture systems of today. All CO_2 capture agents must be purified so they can be reused, but unlike water-based agents, organic solvents don't need to be boiled to release the CO_2.

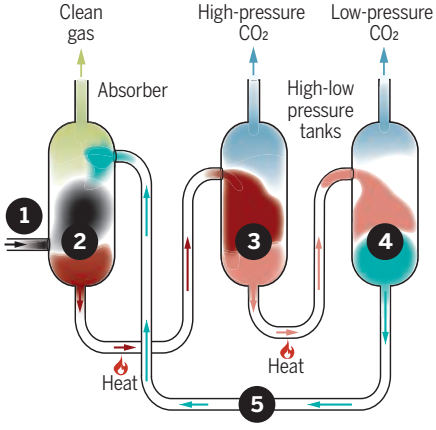

1 CO_2-rich flue gas (●) from the power plant enters an absorber vessel.

2 Organic solvent absorbs CO_2 (●) and releases clean exhaust to the atmosphere (●).

3 Solvent rich in CO_2 is heated and piped to a high-pressure tank, where CO_2 (●) is released and piped away for storage.

4 Solvent with less CO_2 (●) is heated and piped to a low-pressure tank to remove the remaining CO_2.

5 Cleaned solvent (●) is returned to the absorber for reuse.

GRAPHIC: MICHAEL PERKINS/PACIFIC NORTHWEST NATIONAL LABORATORY. ADAPTED BY N. DESAI/*SCIENCE*

PHOTO: PIETER VAN DOKKUM

With wide fields of view, Dragonfly's telephoto lenses have spotted sprawling, faint galaxies that lack stars.

ASTRONOMY

Lens array captures dim objects missed by giant telescopes

Upgraded Dragonfly will study how dark matter shapes diffuse galaxies and faint tendrils of gas

By **Govert Schilling**

Improving on a Dutch invention, Galileo Galilei in 1609 used glass lenses to build the first telescope capable of studying the night sky. But soon after Isaac Newton constructed the first reflecting telescope later that century, mirrors took over: Astronomy today is dominated by telescopes with giant mirrors up to 10 meters wide.

Galileo's approach has made a comeback with Dragonfly, a telescope in New Mexico built from two fly-eye arrays of 24 Canon telephoto lenses. This month, the Dragonfly team announced it would add 120 more of the lenses in a $3.65 million upgrade, which will make it the largest lens-based telescope in the world in terms of light-gathering power. With a field of view far greater than that of an equivalent reflecting telescope, Dragonfly promises to capture the dim glow of vast, tenuous gas clouds that hold clues to the universe's unseen dark matter. "Dragonfly is going to provide a completely new view of the universe," says team member Deborah Lokhorst of the University of Toronto (UT).

Large telescope mirrors excel at gathering photons from the distant universe and zooming in on particular objects with sharp resolution. But they tend to have small fields of view, and scattered starlight from internal reflections can swamp the faint signals from extended structures like diffuse nebulae.

A decade ago, astronomers Roberto Abraham of UT and Pieter van Dokkum of Yale University realized that an array of dozens of commercial telephoto lenses could gather as much light as a 1-meter telescope while maintaining the lenses' wide fields of view. Moreover, Canon had just produced a 14-centimeter-wide lens with a special coating to reduce scattered light. By pointing all 48 lenses at the same part of the sky and stacking their exposures, Abraham, van Dokkum, and their colleagues could find dim objects that were hiding in plain sight. "Dragonfly is a very interesting project," says Joop Schaye, a Leiden Observatory astronomer. "The low–surface-brightness universe has long been neglected."

So far, Dragonfly's main claim to fame has been the discovery of numerous ultradiffuse galaxies (UDGs), some of them as large as the Milky Way, but with hardly any stars. In 2016, the team discovered one that is spinning far faster than it should, given how few stars there are to hold the galaxy together by gravity. That suggested that fully 98% of its mass must be in the form of dark matter, the mysterious stuff that, on average, constitutes some 85% of all gravitating mass in the universe.

In 2018, the Dragonfly team discovered the fast-spinning galaxy's opposite: a galaxy rotating so slowly that it must contain hardly any dark matter at all. "UDGs are very interesting galaxies," says Reynier Peletier, an astronomer at the University of Groningen who is looking for similar objects with the much larger European VLT Survey Telescope in Chile. "One way or the other, they may hold the key to the mystery of dark matter." Indeed, van Dokkum says, the contrasting galaxies discovered by Dragonfly are already posing problems for theories that try to explain away dark matter by modifying the laws of gravity.

The new lenses to be added in the next 18 months should allow the Dragonfly team to go after a new target: faint clouds of gas surrounding galaxies. These clouds are the dense ends of gaseous filaments that connect far-flung galaxies in a cosmic web, which is thought to have coalesced around regions rich in dark matter. Filters on the new lenses will transmit only the feeble red light of glowing hydrogen or the green glow of ionized oxygen to make these wisps of hot, tenuous gas stand out more clearly.

The expansion of the universe stretches light from cosmic objects to longer wavelengths, depending on their distance. To let this "redshifted" light pass through, Dragonfly's filters can be tilted to various degrees. Increasing the light's path length through the glass also increases the filters' transmission wavelength—a trick that will extend the reach of the instrument to gas clouds some 100 million light-years away.

The observations will help the team learn how gas flows into galaxies to form new stars, and how stellar explosions blow the gas back into space. They will also help guide efforts to model the properties of the dark matter–laden cosmic web and how galaxies took shape within it.

To map the much fainter filaments of the cosmic web that lie farther from the galaxies, Abraham dreams of expanding Dragonfly to a 2000-lens array, giving it the same light-gathering power as a 6-meter telescope. "It's not crazy," he says. "Dragonfly could well be the first example of a completely new class of optical telescope." ■

Govert Schilling is an astronomy journalist in Amersfoort, the Netherlands.

LONG LIVE THE QUEEN

PHOTO: ALEX WILD

In insect societies, a queen can live for years, whereas workers expire in months. What can hives and anthills reveal about aging? *By* **Yao-Hua Law**

A small room in the University of Regensburg is home to more than 50 boxes of black, strikingly slender ants. Native to Central America, the clonal ant *Platythyrea punctata* has evolved a trait rare among ants: It can produce daughters from unfertilized eggs. A *P. punctata* colony can consist entirely of clones, produced by one or two dominant females. That uniformity underscores a mystery.

"What is really fascinating is that they are the same" genetically, says evolutionary biologist Abel Bernadou, pointing to the 30 or so ants in a box, "but depending on their jobs, they will have totally different life spans." Members of the colony's working caste, which nurse the brood, hunt for food, and defend the nest, die within 7 months, even when well-fed and protected in the lab. But ants in the reproductive caste, whose sole job is to lay eggs, can live 10 to 16 months.

To Bernadou, the questions raised by those disparities are irresistible. What causes some ants to live twice as long as nest mates that have exactly the same ge-

At almost 2 centimeters, the queen of the Texas leafcutter ant (*Atta texana*) is far bigger than her workers. She also has a longer life span.

PHOTOS: ALEX WILD

nome? And how can reproduction, a taxing effort that speeds up aging in most animals, make these ants live longer instead?

Bernadou and his myrmecologist colleagues at Regensburg are part of a small cadre of researchers who have turned to social insects—ants, bees, and termites—to help unravel the mysteries of aging. It's a developing field that rarely features in conferences on aging biology, where the spotlight is on mice, *Drosophila* fruit flies, and the minuscule nematode *Caenorhabditis elegans*—three species researchers have probed and tweaked for well over half a century to learn what controls their life spans.

Many who study those species have yet to be convinced that social insects have something important to contribute. "They think it's fun and worthwhile to know the diversity of aging," says biologist Gro Amdam, who studies aging in bees at the Norwegian University of Life Sciences and Arizona State University, Tempe. "But they don't think we will make major discoveries in social insects that are relevant to their work."

But Amdam and other social insect researchers—who this month published a big batch of findings in a thematic issue on aging and sociality in the *Philosophical Transactions of the Royal Society B*—say they promise new ways to understand aging. One reason is that many social insects live far longer than the more popular model organisms. Honey bee queens live up to 5 years, and termite and ant queens more than 20. *Drosophila*, by contrast, has a life span of 13 weeks at most, and *C. elegans* a mere 18 days. "If you want to know how to die quickly, then work on *Drosophila*," quips evolutionary biologist Laurent Keller, who studies aging in ants at the University of Lausanne.

In the western honey bee (*Apis mellifera*), queens (middle) live longer than workers (top) and drones (bottom).

Even more intriguing is the fact that aging in social insects is plastic, changing with social context. Few social insects are as homogenous as clonal ants, but in most, queens and workers have very similar genomes, because all colony members are offspring of one or several queens. Yet whereas queens seem to stay youthful through their long lives, workers age quickly and die fast. And within a colony, a worker's job determines its life span, even though by and large all workers are siblings. Scientists can rush, slow, or even reverse aging in ants and bees simply by having them mate or changing their tasks.

Revealing the molecular mechanisms behind these strange phenomena may ultimately shed more light on aging in general, including in humans, says molecular biologist Roberto Bonasio at the University of Pennsylvania, who studies epigenetics in mammals, flies, and ants: "That's the idea."

AGING, OR SENESCENCE, is a progressive loss of function and performance with time. It saps the individual's capacity to withstand stress, fight diseases, heal wounds, or learn new skills. But must we age? Why did organisms not evolve to maintain their youth-like vigor until they're about to die?

Rather counterintuitively, scientists argue aging is the outcome of natural selection, which favors genes that help an organism survive to reproductive age. Once the individual has produced offspring, selection for survival weakens, which opens the door for injurious genetic effects to accumulate. Aging sets in.

The strong selection to survive until reproduction may favor so-called pleiotropic genes, which are helpful in early life but harmful later on. An example is the *clk1* gene in *C. elegans*, which is known to boost the nematode's metabolism. The gene promotes early reproduction and gives individuals a fitness edge over competitors, but shortens their life span by 40%, in part because it speeds the buildup of harmful metabolic byproducts.

Scientists have suggested organisms living in more precarious environments—for instance ones thick with predators or competitors—experience higher selection for survival and reproduction early in life, at the cost of faster aging later on. This so-called "extrinsic mortality hypothesis" is often used to explain why animals that fly, live underground, or are venomous—and as a result face fewer threats—also seem to live longer and presumably age less rapidly. Think of bats, which live far longer than other mammals of similar size.

Back in the 1990s, Keller realized social insects offered "an interesting way" to test the extrinsic mortality hypothesis, he says. Safely ensconced in their nests and guarded by a legion of workers, ant queens are assumed to face a much lower risk of predation and disease, and thus of dying, than insects living a solitary life.

Keller and his Lausanne colleague Michel Genoud collected life span records of queens in 61 species of ants, termites, and the honey bee, and compared these with adults of 81 solitary insect species. On average, queens live 5 to 11 years, whereas solitary insects live only months, they reported in a 1997 paper. Everything was as the hypothesis predicted—and the paper kick-started aging research in social insects.

THE FIELD FACES plenty of challenges. Insect queens and kings are rare, which limits studies' sample sizes. And keeping colonies of social insects alive can be laborious. At Regensburg, evolutionary biologist Jan

Oettler and graduate student Luisa Jaimes maintain 200 *Cardiocondyla obscurior* ant colonies that they need to feed and clean several times weekly over the 6 months or more that their queens live. By contrast, to grow hundreds of *Drosophila* maggots into adults, you only need a bottle, premade fly food, and 10 days. "One nasty reviewer asked why, since we can't get the numbers, do we still use *Cardiocondyla*"—a tiny tropical ant—"instead of *Drosophila*," says myrmecologist Jürgen Heinze, who has been studying the ants for 30 years at Regensburg. "They can't see the benefits."

Lagging experimental techniques are a problem as well. In mice, scientists can document physiological aging in urine and blood samples; in *Drosophila* and *C. elegans*, they can insert molecular tags into cells that show gene expression in real time. Such molecular clocks don't exist yet for ants and termites. That's a problem because aging isn't always a linear process: Queen ants often churn out eggs for months or years without visible aging, only to drop dead abruptly. Without reliable and nonlethal ways to trace aging or physiological changes at the molecular level, comparisons between "old" and "young" individuals are questionable. "If you have a 10-day-old worker, to what do you compare it? A 10-day-old queen? Or a queen that has lived the same proportion of its average life span?" Keller asks. "This is difficult."

Gene editing would be a "game changer" for these studies, Oettler says, enabling scientists to disable specific genes and watch for effects on aging. But it has barely started to be used in social insects. Scientists only created the first genetically modified honey bees in 2014, and two species of transgenic ants in 2017. Amdam would love to see transgenic technology developed for free-flying honey bees, allowing real-world experiments on aging. But beekeepers staunchly oppose genetic modification, which they worry could affect their colo-

For some insects, living socially means living long

The average maximum life span for solitary insects is much less than for reproductive individuals—queens, kings, and some workers—among social insects.

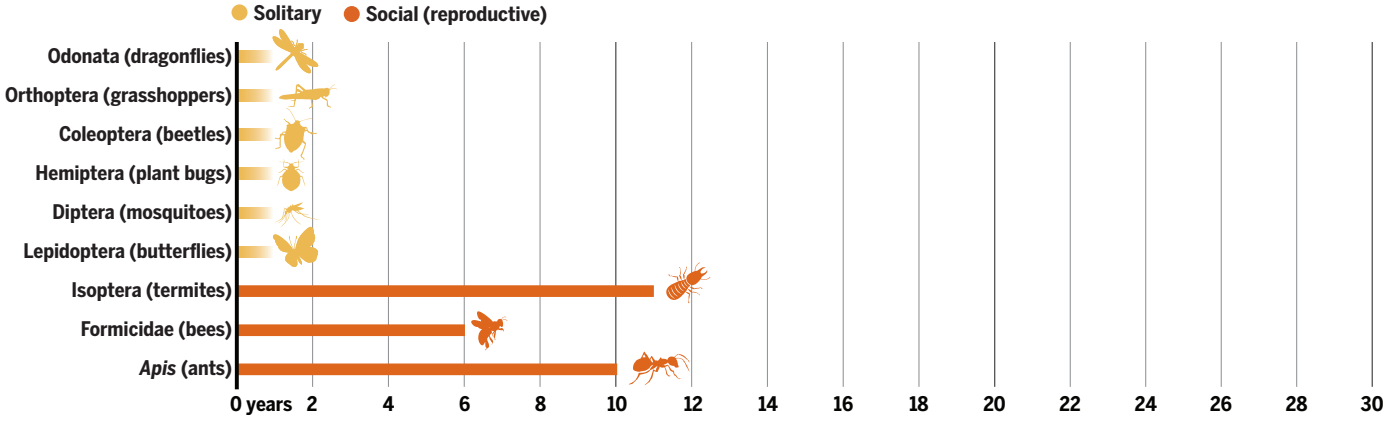

A fountain of youth—for the happy few

Within social insect species, the life span of reproductive individuals far exceeds that of those that do not produce offspring.

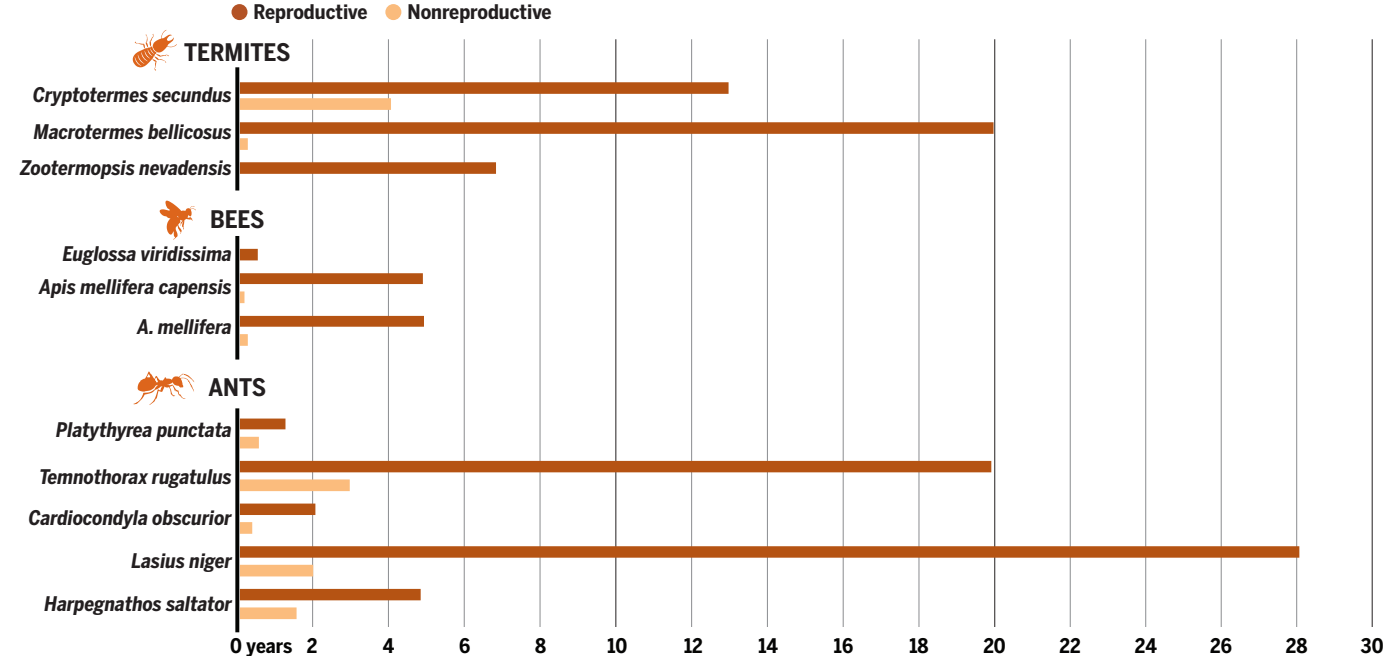

CREDITS: (GRAPHIC) N. DESAI/*SCIENCE*; (DATA) L. KELLER AND M. GENOUD, *NATURE*, **389**, 958 (1997); KORB *ET AL.*, *PHIL. TRANS. R. SOC. B*, 376 (2021); KRAMER *ET AL.*, *EXPERIMENTAL GERONTOLOGY*, **85**, 18, (2016); OETTLER *ET AL.*, *CURRENT OPINION IN INSECT SCIENCE*, **16**, 58, (2016); THORNE *ET AL.*, *JOURNAL OF ANIMAL ECOLOGY*, **71**, 1030, (2002); PEETERS *ET AL.*, *INSECTES SOC.*, **47**, 325 (2000)

nies, and regulators are wary. "The moment you say 'free-flying transgenic bee,' it's no-no," Amdam says.

One way to speed progress, Bonasio says, is to "consolidate our efforts on one or two species so that more [molecular] tools are available to everybody." But Heinze says researchers should embrace the bewildering variety of life histories and aging patterns seen in social insects. "There is no standard ant," he says; for understanding the diverse causes and effects of aging, "plurality is best."

DESPITE THE CHALLENGES, scientists are starting to link aging patterns in social insects to the underlying molecules. One oddity they're probing is the link between reproduction and longevity.

In most animals, high fecundity almost universally comes with a quick burnout; red deer, for example, age faster if they reproduce early. But social insect queens buck the trend: Reproduction stretches their life span rather than snipping it. For example, a 2005 study by Heinze's team found that *C. obscurior* queens that mated had life spans 44% longer than virgin queens (26 weeks versus 18). And that's despite these mated queens' hectic lifestyles: They laid up to five times more eggs, and at faster rates, than queens that did not mate or were mated with sterile males.

Other scientists have discovered that procreation also extends the life spans of queens of other ant species, honey bee queens, and termite queens and kings. In species where a limited number of workers in a colony can also reproduce, such as the *P. punctata* ants that Bernadou studies, those that reproduce live longer, too.

In termites, reproduction may blunt the impact of transposons, bits of DNA that jump through the genome, disrupting genes and, at least in humans and *C. elegans*, promoting aging. Judith Korb, who studies aging in termites at the Albert Ludwig University of Freiburg, compared transposon activity in two termite species. In the species with sterile workers, older workers have higher transposon activity; in the species where older workers can reproduce, they show better defense against damage from transposons.

Social insects' brains appear to benefit from sex as well. When *Harpegnathos saltator* ants, also known as Indian jumping ants, lay eggs, their brain develops 40% more of a type of protective cell called ensheathing glia, Lihong Sheng, a postdoc in Bonasio's lab, reported in August 2020. A decline of these cell types is associated with aging in flies and cognition loss in mice. "If we know what the ants themselves use to control the number of [ensheathing glia] in the brains," Bonasio says, it could point to similar mechanisms in flies, mice, and "maybe in humans." (Bonasio is now studying the phenomenon in *Drosophila* flies; the ants "showed us the way but once I know what the pathway is, I prefer to do the experiment in *Drosophila* … because it is easier," he says.)

Workers of the Japanese termite (*Reticulitermes speratus*) can't repair oxidative damage as well as queens (not shown) and live shorter lives.

PHOTO: YOSEI MINAGOSHI/MINDEN PICTURES

A worker's job can also slow or speed up its aging. Honey bee workers, for instance, start out as nurse bees that stay in the hive and tend to the brood and the queen. About 3 weeks into their lives, they become foragers that fly out to collect food. Various studies show that nurse bees do not age, but foragers do so rapidly, declining in flight performance, immunity, and learning.

Amazingly, that process can be reversed. When a hive needs more nurse bees, foragers can switch back to their former roles. When Amdam removed nurse bees from hives, foragers were forced to revert to their former roles—and they also recovered their youthful traits. Such reverted nurse bees produce more cells that "mop up pathogens," Amdam says. They also regain high levels of vitellogenin, "a multipurpose, Swiss knife sort of protein" that regulates a bee's changing roles across its lifetime and declines as the insects age. She has found that reverted nurse bees learn faster than foragers of the same age and that their brains have more proteins associated with cellular stress resilience and repair.

These job switches in bees don't only mean a new line of work; they also bring a different set of interactions with other members of the colony. Amdam thinks a bee's social life plays an important role in its longevity. Social contact is also known to affect human physiological and mental health, and loneliness has been identified as a risk factor for cognitive decline—a provocative similarity. Although scientists have yet to determine how sociality can affect insects' life span at the molecular level, "it certainly has people's attention," Amdam says.

SEVERAL PAPERS in this month's theme issue of the *Philosophical Transactions* delve deeper into the molecular control of aging in social insects. One compared gene-expression patterns between young and old individuals of six species of ants, bees, and termites, for example. The study measured the activity of two biochemical pathways, both ubiquitous in animals, that detect nutrients and regulate cell development. Scientists had previously found strong links between these pathways and life spans in flies and other solitary insects—but not in social insects.

In the new study, however, they scrutinized parts and products of the same pathways that had been largely neglected in aging research, and found genes and proteins—including vitellogenin—that strongly associate with aging in social insects. These results reinforce the need to cast a wide net and study aging in many species, says Korb, lead author of the new paper.

Thomas Flatt, who studies the genetics of aging in *Drosophila* at the University of Fribourg, is one of the researchers who has been won over by the promise of social insects. Flatt has been working with Korb, Heinze, and other researchers in a €6.2 million project funded by the German Research Foundation to study the unusual relationship between fecundity and aging in social insects. The genomic revolution will eventually help the field take flight, Flatt predicts, and give scientists a much better understanding of how aging works across the animal kingdom. "My dream is that we will discover stuff in ants that … is universally important," he says—things "we don't even know existed in *Drosophila*." ■

Yao-Hua Law is a science journalist in Kuala Lumpur, Malaysia.

Mutations (red) in the spike protein (green) of SARS-CoV-2 variants that affect host receptor (light gray) or antibody (dark gray) binding could impair immunity.

ILLUSTRATION: V. ALTOUNIAN/*SCIENCE*

VIEWPOINT: COVID-19

The emerging plasticity of SARS-CoV-2

The evolution of SARS-CoV-2 poses challenges for vaccines and immunotherapies

By **Kevin D. McCormick, Jana L. Jacobs, John W. Mellors**

Viruses evolve as a result of mutation (misincorporations, insertions or deletions, and recombination) and natural selection for favorable traits such as more efficient viral replication, transmission, and evasion of host defenses. Newly selected traits may be linked in unpredictable ways and raise concern that virus spread and evolution could result in greater virulence (disease severity). The limited diversity of severe acute respiratory syndrome coronavirus 2 (SARS-CoV-2) reported during 2020, ascribed to the 3′-5′ exonuclease proofreading function of nonstructural protein 14 (nsp14), led to the view that vaccines based on a single sequence of the viral spike (S) protein, which mediates host cell entry, would likely generate immune protection to all circulating variants (*1*). However, variants of SARS-CoV-2 with mutations in S have emerged around the world, posing potential challenges for vaccination and antibody-based therapies. The continued spread of SARS-CoV-2 creates the opportunity for accumulation of additional consequential mutations in S and throughout the viral genome.

Although SARS-CoV-2 shares high sequence homology with SARS-CoV, which caused the 2002–2004 SARS outbreak, the coronavirus family is diverse in both sequence and in host receptor preference. For example, SARS-CoV-2 and a "common cold" human coronavirus, HCoV-NL63, both recognize angiotensin-converting enzyme 2 (ACE2) as the host cell receptor, but SARS-CoV-2 and HCoV-NL63 belong to different coronavirus genera and have major sequence and structural differences in the receptor-binding domain (RBD) of S, sharing <30% sequence homology (*2*). This diversity in S indicates that coronaviruses have broad potential to tolerate changes in both sequence and structure without substantial loss of function. This may partially explain why coronaviruses can undergo zoonotic transmission and suggests that the full evolutionary potential of SARS-CoV-2 has yet to be revealed.

The S protein comprises two subunits: S1, which contains the RBD, and S2, which mediates virus–host cell fusion. Antibody-neutralizing epitopes are scattered throughout S but are mostly concentrated within the RBD. Despite the potential for plasticity, after nearly a year of spread (from December 2019) to >100 million people, there was limited evidence for evolution of SARS-CoV-2 S. The only notable evolutionary event was the D614G (Asp^{614}→Gly) substitution in S1, which increases ACE2 affinity, leading to higher infectivity and transmissibility. Viral sequences deposited in public databases were mostly obtained from the upper respiratory tract during acute infection, before major immune responses have occurred. Such sequences might not capture the effect of within-host immune selection on viral diversification.

Extensive intrahost evolution of SARS-CoV-2 has been reported in at least five individuals with protracted infection because of immune impairment from therapy for hematologic malignancies or autoimmunity (*3*–*7*). They had active SARS-CoV-2 infection for an average of 115 days before clearing the infection or succumbing to COVID-19. Each patient also had at least one convalescent plasma (CP) treatment (intravenous transfusion of blood plasma from a donor who has recovered from COVID-19) and/or monoclonal antibody therapy. Some of these individuals were shedding high titers of SARS-

Division of Infectious Diseases, University of Pittsburgh School of Medicine, University of Pittsburgh, Pittsburgh, PA, USA. Email: jwm1@pitt.edu

CoV-2 at the time of discharge from hospital or before death, indicating the potential for transmission. SARS-CoV-2 variants from two of these patients had up to fivefold reduction in neutralization sensitivity to CP (*3, 7*). Although these are case studies in immunocompromised individuals, they raise concern because the deletions of amino acids 69 to 70 (Δ69–70), Δ141–144, or Δ242–248 in S1 were observed in four out of the five infections (*3*, *5*–*7*); the N501T (Asn^{501}→Thr) or N501Y (Asn^{501}→Tyr) mutations were seen in two out of the five (*5*, *6*); and the E484K (Glu^{484}→Lys) and Q493K (Gln^{493}→Lys) mutations in the RBD of one infection also arose in antibody-resistant viruses after in vitro selection.

These reports preceded the detection of three major circulating variants—B.1.1.7, B.1.351, and P.1—which all contain at least eight single, nonsynonymous nucleotide changes, including E484K, N501Y, and/or K417N (Lys^{417}→Asn) in the ACE2 interface of the RBD (shown in the illustration). There are also various deletions in the amino (N)-terminal domain (NTD) of S1 in B.1.1.7 and B.1.351 (see the figure). Although most of the mutations in these variants were observed in a minor fraction of SARS-CoV-2 sequences during the first year of the pandemic, including K417N, E484K, and N501Y, there is no evidence to suggest that these variants were created through sequential addition of each substitution during interhost transmission.

Because only a few SARS-CoV-2 mutations were in circulation during most of 2020, it is likely that the three major variants are the result of selective pressures and adaptation of the virus during prolonged individual infections and subsequent transmission. All the case reports of individuals with extensive intrahost SARS-CoV-2 evolution indicated that they had been treated with suboptimal neutralizing antibodies (that is, the CP treatment did not neutralize the entire virus population). Whether or not antibody therapy played a role, it is likely that the same variants or variants containing new mutations will continue to emerge in different geographic locations as the result of intrahost selection and subsequent transmission. Indeed, other variants have been reported with multiple mutations in S1, including the lineages B.1.526 (detected in New York) and B.1.429 (which originated in California) containing a substitution in the RBD that is distinct from other variants; and B.1.525 and A.23.1 that are thought to have originated in Nigeria and Uganda, respectively (*8*) (see the figure).

The individual phenotypic effects of the mutations in S1 are incompletely understood, but some initial clues are emerging. Substitution at position Asn^{501} with Thr or Phe increases affinity for ACE2 binding (*9*), and Tyr^{501} increases infectivity and virulence in a mouse model (*10*). Some circulating variants may have reduced sensitivity to neutralizing antibodies that bind to the RBD directly (attributed to triple substitutions of key amino acids in the RBD at the ACE2-binding interface: Lys^{417}, Glu^{484}, and Asn^{501}) or to the NTD (conformational changes in the NTD are required for ACE2 attachment). More studies to correlate viral genotype and phenotype are needed.

It is possible that mutations that reduce neutralizing antibody binding, such as E484K, may require compensatory mutations that restore infectivity, such as N501Y. There appears to be convergent association of mutations such as the triple RBD mutation (Lys^{417}, Glu^{484}, and Asn^{501}) that evolved in two distinct lineages (B.1.351 and P.1). Moreover, E484K was also recently detected with N501Y in the B.1.1.7 lineage (*11*). Δ69–70 in S1 doubled the infectivity of SARS-CoV-2 pseudovirus, implying that the deletion may have been required to compensate for a mutation, D796H (Asp^{796}→His), that reduced antibody neutralization sensitivity at a cost to viral fitness (*7*). The role of compensatory mutations is also supported by the emerging B.1.525 lineage that has both E484K (reduction in antibody sensitivity) and Δ69-70 (compensatory increase in infectivity).

It is not yet known whether the complex mutational patterns observed in SARS-CoV-2 variants are linked on the same viral genome or represent mixtures of different variants within the same patient. Studies evaluating the linkage of these mutations in individual SARS-CoV-2 genomes using single-genome amplification and sequencing, as has been used to characterize genetic diversity of HIV-1 and other viruses, are needed to accurately assess the infectivity and phenotype of individual variants. A case report of intrahost SARS-CoV-2 evolution showed that SARS-CoV-2 can evolve multiple distinct lineages within the same individual (*6*).

Several studies suggest that the major circulating variants have reduced neutralizing sensitivity to CP and plasma from recently vaccinated individuals. For example, CP from individuals who were infected with the B.1 lineage (D614G-containing SARS-CoV-2) had varying reductions in neutralizing activity against live virus isolates of the B.1.351 lineage. Additionally, vaccine-elicited antibodies have reduced neutralization of pseudovirus containing the triple mutation in S1 (K417N, E484K, and N501Y) of the P.1 and B.1.351 variants (*12*). Pseudovirus bearing the deletions and mutations found in the B.1.1.7 lineage also showed reduced neutralization sensitivity, but titers of antibody were sufficient for complete neutralization of B.1.1.7 in sera from 40 individuals vaccinated with BNT162b2 (Pfizer/BioNTech) (*13*). Continued phenotypic assessments of emerging, rapidly spreading variants, including those with nonsynonymous mutations in S1 (NTD and RBD) and S2, to neutralization by CP and postvaccination sera should be a high priority to monitor possible effects on vaccine efficacy.

Phase 3 trials of SARS-CoV-2 vaccines derived from a single S sequence have shown them to be highly effective in preventing infection with the initial SARS-CoV-2 variants, including those with the D614G mutation (*14, 15*). More recent data suggest that certain vaccines are less protective against the B.1.351 variant, although additional studies are needed. Studies showing reduced antibody sensitivities against new variants do not inherently prove that a vaccine is less effective. In addition to effector B cells

Mutations and deletions in the spike protein

Currently, B.1.1.7, B.1.351, and P.1 are the major circulating variants of severe acute respiratory syndrome coronavirus 2 (SARS-CoV-2); others are emerging. The spike S1 subunit contains an amino (N)-terminal domain (NTD) and receptor-binding domain (RBD), which mediate host receptor recognition and contain epitopes for antibody binding. Deletions and substitutions in S1 can affect transmissibility (Tr), vaccine efficacy (Ef), and virulence (Vi). Additional mutations that define the variants can be tracked at (*8*). SP, signal peptide.

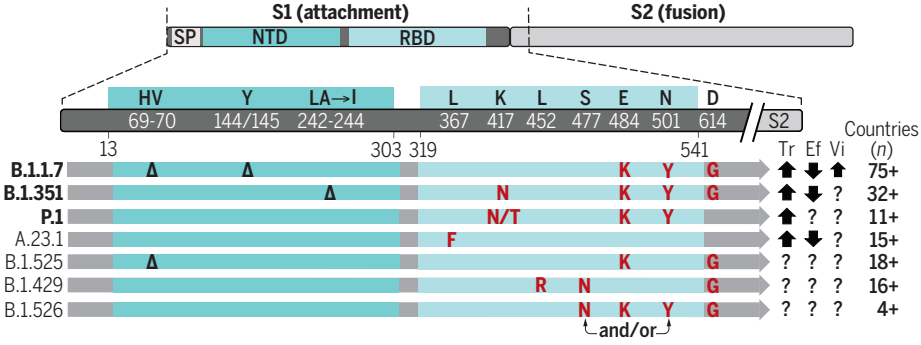

A, Ala; D, Asp; E, Glu; F, Phe; G, Gly; H, His; I, Ile; K, Lys; L, Leu; N, Asn; R, Arg; S, Ser; T, Thr; V, Val; Y, Tyr.

GRAPHIC: N. CARY/*SCIENCE*

(which produce neutralizing antibodies), there are numerous additional vaccine-induced responses of the innate and adaptive immune systems that may protect against infection and further viral immune escape. Conversely, there are uncharacterized mutations outside of S that could facilitate SARS-CoV-2 immune evasion.

The growing evidence for the emergence of immune escape mutations in protracted SARS-CoV-2 infection and for multiple, rapidly spreading variants should raise broad concern and action. Reducing the spread of SARS-CoV-2 is most likely to prevent further selection of immune escape variants. This will require a coordinated and comprehensive global vaccination and prevention strategy. Partial roll-out and incomplete immunization of individuals leading to suboptimal titers of neutralizing antibody could promote selection of escape variants that negatively affect vaccine efficacy. Increased genotypic and phenotypic testing capacities are essential worldwide to detect and characterize circulating SARS-CoV-2 variants that may emerge from selection by natural or vaccine-mediated immune responses. Infections that occur among vaccinated individuals should be aggressively evaluated for the mechanisms of breakthrough. The explosive, global spread of SARS-CoV-2 and the devastation it has wreaked is a stark warning of the potential for new variants to further complicate pandemic control. Vaccine manufacturers are now testing potential booster vaccines against circulating SARS-CoV-2 variants, and more broadly active monoclonal antibodies are in development for therapy. Such proactive approaches are likely to be needed to ensure pandemic control and elimination. ■

REFERENCES AND NOTES

1. B. Dearlove *et al.*, *Proc. Natl. Acad. Sci. U.S.A.* **117**, 23652 (2020).
2. N. M. A. Okba *et al.*, *Emerg. Infect. Dis.* **26**, 1478 (2020).
3. V. A. Avanzato *et al.*, *Cell* **183**, 1901 (2020).
4. J. H. Baang *et al.*, *J. Infect. Dis.* **223**, 23 (2021).
5. B. Choi *et al.*, *N. Engl. J. Med.* **383**, 2291 (2020).
6. M. K. Hensley *et al.*, *Clin. Infect. Dis.* 10.1093/cid/ciab072 (2021).
7. S. A. Kemp *et al.*, *Nature* (2021). 10.1038/s41586-021-03291-y
8. A. H. O'Toole *et al.*, International Lineage Report. 2021, PANGO lineages, https://cov-lineages.org/
9. T. N. Starr *et al.*, *Cell* **182**, 1295 (2020).
10. H. Gu *et al.*, *Science* **369**, 1603 (2020).
11. Public Health England, Investigation of novel SARS-CoV-2 variant: Variant of Concern 202012/01 Technical Briefing 5 (2021); https://bit.ly/3c2iJ9k.
12. Z. Wang *et al.*, *Nature* 10.1038/s41586-021-03324-6 (2021).
13. A. Muik *et al.*, *Science* 371, eabg6105 (2021).
14. F. P. Polack *et al.*, *N. Engl. J. Med.* **383**, 2603 (2020).
15. L. R. Baden *et al.*, *N. Engl. J. Med.* **384**, 403 (2021).

ACKNOWLEDGMENTS

We thank L. Pollini for assistance. J.W.M. is a consultant to Gilead Sciences and holds shares or share options in Co-Crystal Pharma, Inc., Abound Bio, Inc., and Infectious Disease Connect.

10.1126/science.abg4493

IMMUNOLOGY

Unusual T cell receptor in opossum

The structure of a marsupial T cell receptor illustrates the emerging trend of noncanonical antigen binding

By **Michael F. Criscitiello**

B and T lymphocytes of the vertebrate adaptive immune system have structurally, genetically, and evolutionarily related receptors for antigen recognition that initiate immune responses with notable specificity and memory. In general, the antigen binding sites of these receptors are evolutionarily conserved, yet a few very different immunoglobulin (Ig) structures have been characterized from shark, camelids, and cow B cells. On page 1383 of this issue, Morrissey *et al.* (*1*) reveal the structure of an opossum T cell receptor (TCR) that also eschews the vertebrate norm. This marsupial TCR is the latest in an emerging trend of smaller, projecting structural domains that are used for antigen recognition by the adaptive immune systems of some species, and it might have therapeutic potential.

From sharks to man, vertebrates have two varieties of T lymphocytes for orchestration of immune responses through cytokine secretion and direct killing of infected or cancerous cells. T cells of αβ and γδ lineages differentiate in the thymus where they rearrange genetic loci encoding either an αβ or a γδ heterodimeric TCR for antigen recognition. More than a decade ago, a fifth TCR chain in the older nonplacental mammals (including platypus, echidna, and marsupials), called TCRμ, was discovered (*2*). Although most similar to TCRδ, TCRμ is encoded at a distinct locus and was predicted to have two variable domains at its membrane-distal amino terminus. Little is known of the T cells that express TCRμ.

Morrissey *et al.* greatly extend our understanding of TCRμ and the cells that express it. Although the TCRμ chain was found not to be expressed in the peripheral blood mononuclear cells in opossums, nearly as many γμ T cells were found in the spleen as αβ-expressing T cells. In addition to confirming TCRγ as the heterodimeric partner of the TCRμ chain, single-cell RNA sequencing analysis showed that most of the γμ T cells use the CD8αα$^+$ homodimer, although some expressed neither the CD4 nor the CD8 TCR coreceptor. The more common CD8αβ$^+$ heterodimer is used by cytotoxic T lymphocytes. CD8αα$^+$ function is largely unknown, although in humans it can be an inhibitory coreceptor on natural killer cells (*3*). Functional studies will have to determine if TCRγμ signaling is inhibitory or more regulatory in nature.

Reaching for antigen

TCRγδ is part of a growing trend of T and B cell antigen receptors with reach. Most vertebrate antigen receptors bind antigen with six CDRs, three contributed by V domains of each partner chain (heavy and light chains, TCRα and β, or TCRγ and δ). TCRμ is the latest to break from this canon.

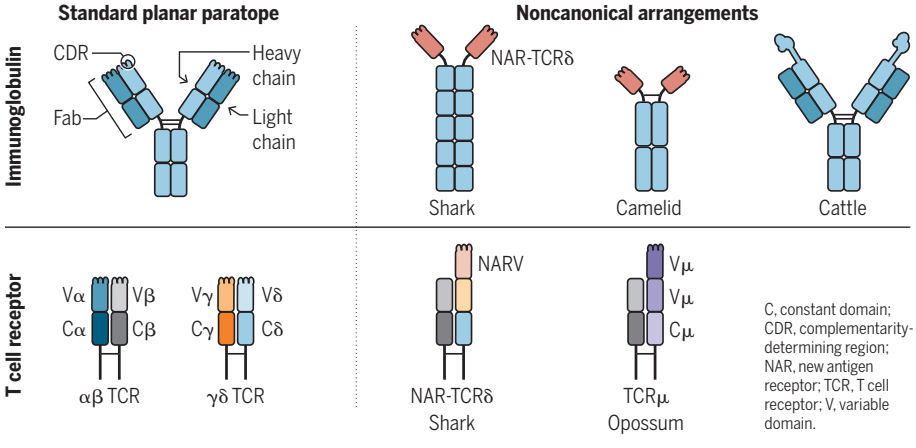

C, constant domain; CDR, complementarity-determining region; NAR, new antigen receptor; TCR, T cell receptor; V, variable domain.

GRAPHIC: C. BICKEL/*SCIENCE*

The usual structure of the TCR is similar to one antigen binding arm (Fab) of Ig (including secreted antibodies) produced by B cells. The TCR and Fab of Ig are a heterodimer of two chains, each comprising a constant domain and a variable domain, which is diversified by somatic gene rearrangement. Three hypervariable loops from each variable domain interact with antigen differently in each lymphocyte, providing a repertoire of antigen recognition for the host's immune defense. The three hypervariable loops of each variable domain are called complementarity-determining regions (CDRs). CDR1 and CDR2 are encoded within a variable (V) gene segment; CDR3 is the product of the DNA junctions produced by the rearrangement of V, diversity (D), and joining (J) gene segments in lymphocyte development. Notably, the TCRγ variable gene rearrangements that paired with marsupial TCRμ showed restricted diversity compared with those pairing with TCRδ, often relying on microhomology in the ends of Vγ2 and Jγ3. This supports the idea that TCRγ variable domains may play a supportive role for the TCRμ chain rather than contribute to antigen recognition. CDR3 of the protruding membrane-distal TCRμ domain was longer and more diversified, which is suggestive of a role in antigen recognition.

The TCRγμ crystal structures reported by Morrissey *et al.* show a projecting μ variable domain with a relatively long and diverse CDR3, which is more similar to Ig variable domains in amino acid sequence and structure than to the variable domains of TCRs. Because the TCRγ chain does not provide a variable domain partner for the TCRμ membrane-distal variable domain, the authors rightly compare TCRμ to the Igs that do not use light chains: camelid single-domain antibodies (VHH) (*4*) and immunoglobulin new antigen receptor (IgNAR) from cartilaginous fish (*5*). These Igs have a lone variable domain jutting out without three adjacent CDRs provided by an Ig light chain (see the figure). The structures (*6*) of these single–variable domain paratopes (antigen binding sites) are being developed as immunotherapeutics, including for COVID-19 (*7*). These single-domain binders nearly have the specificity of traditional monoclonal antibodies but are less bulky so they can access sites and bind recessed epitopes. This may also be the case for marsupial TCRμ.

Another lymphocyte antigen receptor that appears to break the two–variable domain and six-CDR paradigm occurs in sharks. NAR-TCR comprises two variable domains and a TCRδ constant domain (*8*), possibly to yield a structure convergent upon that of marsupial TCRμ (*9*). Additionally, a textbook-defying antigen receptor was discovered in cattle, which contains a subset of ultralong Ig heavy chain CDR3 "cattlebodies" (*10*). Hyperactivation of AID (activation-induced cytidine deaminase) for somatic hypermutation diversifies CDR3 (*11*), which has produced broadly neutralizing cattlebodies to HIV when cows were immunized with gp120 (*12*).

The study of Morrissey *et al.* is a reminder of how conserved B and T cell antigen receptor immunogenetics are and how the interrelationships of antibodies and TCR are not only obvious in ancestral shark immunity but also in mammals. The antigen binding variable domain of the TCRμ paratope is similar to various single-domain Ig structures that have evolved in other species; whether they bind antigen similarly remains unknown. This perpetuates an emerging theme of Ig heavy chain variable domains being used on TCRδ in most vertebrate taxa, along with somatic hypermutation of TCR loci, demonstrating general plasticity between Ig and TCR immunogenetic components and diversification mechanisms (*13*). It is doubtful that these instances are as phylogenetically rare as they seem now. "Reaching," smaller, protruding paratopes will continue to be engineered into human antibodies, and perhaps one day the TCR as well.

Studies of thymic development of γμ T cells, identification of the antigens or ligands bound, and assays of cellular effector function will be needed to understand if this third TCR heterodimer also defines a third lineage of T cells. However, it is now clear that many taxa of diverse vertebrates have innovated the lymphocyte antigen receptor away from the relatively planar, six-CDR paratope to somatically diversify a smaller, more probing antigen binding surface. Human malaria patients can also make similar single-domain antibody paratopes (*14*). Perhaps these TCRs with reach will also be suited for immunotherapeutics. ■

REFERENCES AND NOTES

1. K. A. Morrissey *et al.*, *Science* **371**, 1383 (2021).
2. Z. E. Parra *et al.*, *Proc. Natl. Acad. Sci. U.S.A.* **104**, 9776 (2007).
3. J. Geng, M. Raghavan, *Proc. Natl. Acad. Sci. U.S.A.* **116**, 17951 (2019).
4. C. Hamers-Casterman *et al.*, *Nature* **363**, 446 (1993).
5. A. S. Greenberg *et al.*, *Nature* **374**, 168 (1995).
6. R. L. Stanfield *et al.*, *Science* **305**, 1770 (2004).
7. D. Wrapp *et al.*, *Cell* **181**, 1436 (2020).
8. M. F. Criscitiello *et al.*, *Proc. Natl. Acad. Sci. U.S.A.* **103**, 5036 (2006).
9. R. D. Miller, *Semin. Immunol.* **22**, 3 (2010).
10. F. Wang *et al.*, *Cell* **153**, 1379 (2013).
11. T. C. Deiss *et al.*, *Cell. Mol. Immunol.* **16**, 53 (2019).
12. D. Sok *et al.*, *Nature* **548**, 108 (2017).
13. J. A. Ott *et al.*, *Immunogenetics* **73**, 17 (2021).
14. J. Tan *et al.*, *Nature* **529**, 105 (2016).

ACKNOWLEDGMENTS

The author appreciates discussions with S. Bonissone, M. Flajnik, and V. Smider while writing this Perspective and the support of National Science Foundation award IOS 1656870.

10.1123/science.abg7639

Department of Veterinary Pathobiology, Texas A&M University, College Station, TX, USA. Email: mcriscitiello@cvm.tamu.edu

IMMUNOLOGY

Catching the wave

Uncoupling metabolism from cytoskeletal regulation leads to T cell dysfunction

By **Sophie Hambleton**

A central paradox in many inborn errors of immunity is the conjunction of autoimmune and autoinflammatory pathology with susceptibility to infection. On page 1333 of this issue, Liu *et al.* (*1*) explore the molecular mechanisms of immune dysfunction in mice whose T cells lack expression of the cytoskeletal regulatory protein WAVE2 (Wiskott-Aldrich syndrome protein family member 2). Without WAVE2, T cells do not move around normally, interact closely with antigen-presenting cells, nor generate protective immune responses (*1*–*3*). Nonetheless, they are adept at infiltrating nonlymphoid tissues and exhibit dysregulated proliferation and pro-inflammatory effector function, associated with excessive activity of mechanistic target of rapamycin (mTOR). Treatment of WAVE2-deficient mice with an mTOR inhibitor restored T cell quiescence and immune homeostasis. The description of WAVE2 as a negative regulator of mTOR, the master regulator of lymphocyte metabolism, draws attention to an underexplored, and eminently druggable, candidate mechanism for inflammatory complications of immunocytoskeletal disorders.

To do their job effectively, T cells need to move to the correct location, sense antigen by forming an immunological synapse (IS), and respond appropriately. This requires dynamic reorganization of the actin cytoskeleton at the IS to support the receipt of an array of cell-associated and soluble signals, as well as the polarized delivery of effector responses such as cytotoxicity molecules and cytokines (*4*) (see the figure).

Downstream of T cell receptor (TCR) signaling, WAVE2 is activated by the cell membrane–associated small guanosine triphosphatase RAC1 and nucleates actin branching by actin-related protein 2 (ARP2)–ARP3 (*2*). Assembly of the branched actin network

Primary Immunodeficiency Group, Newcastle University Translational and Clinical Research Institute, and Great North Children's Hospital, Newcastle upon Tyne, UK. Email: sophie.hambleton@newcastle.ac.uk

at the periphery of the IS drives both local spreading (lamellipodia formation) and retrograde flow toward the center of the IS (*4*). Mutations within the cytoskeletal machinery are associated with impaired T cell activation and function in a range of primary immunodeficiency disorders, often producing inflammatory complications as well as susceptibility to infections and lymphoma (*5*). However, WAVE2 deficiency has not been described in humans and its deletion in mice causes embryonic lethality.

Recently, several groups described a human disorder caused by deficiency of a related cytoskeletal regulator, hematopoietic protein 1 (HEM1) (*6*–*8*). Affected children manifest a mixture of infection and prominent immune dysregulation in the form of autoimmunity, lymphoproliferation, and in one-third of patients, the potentially fatal inflammatory syndrome hemophagocytic lymphohistiocytosis. Because HEM1 and WAVE2 are mutually stabilizing within a multiprotein WAVE-regulatory complex (WRC), deficiency of either protein leads to reduced expression of both (*1*, *2*, *6*, *7*). Together, HEM1-deficient humans and mice with WAVE2-deficient T cells offer a powerful opportunity to characterize immune dysregulation in the absence of the WRC.

Like WAVE2-deficient mouse T cells, human HEM1-deficient T and B lymphocytes exhibit impaired formation of IS and lamellipodia (*6*, *7*). WRC-deficient T cells of both species also showed hyperproliferation, cytokine hypersecretion, and excessive degranulation upon stimulation (*1*, *6*). Liu *et al.* discovered that naïve WAVE2-deficient T cells showed markedly excessive activation of mTOR both at baseline and upon stimulation. mTOR is a dynamically regulated master coordinator of the metabolic reprogramming that supports T cell activation, exit from quiescence, and differentiation (*9*–*11*). Pathological activation of mTOR in the human immune system, caused by gain-of-function mutations in the upstream regulator phosphoinositide-3-kinase-δ, leads to immunodeficiency with prominent lymphoproliferative features and has been called a TOR-opathy (*12*, *13*). Conversely, pharmacologic inhibitors of mTOR restrain T cell proliferation and skew cell fate away from effector function in favor of a quiescent or even regulatory state (*11*). Naïve WAVE2-deficient T cells showed clear evidence of overactivity of both pathways through which mTOR signals: mTOR complex 1 (mTORC1) and mTORC2 (*1*). Administration of an mTOR inhibitor reversed these biochemical abnormalities, normalized cellular responses to TCR stimulation, and rescued mice from lethal autoimmunity and lymphoproliferation.

Liu *et al.* provide strong evidence that WAVE2 interacts directly with mTOR, which appears to sequester mTOR away from regulatory-associated protein of mTOR (RAPTOR; mTORC1) and rapamycin-insensitive companion of mTOR (RICTOR; mTORC2). This raises the possibility that WAVE2 functions as an endogenous competitive inhibitor of both pathways. Indeed, loss of WAVE2 led to inappropriate mTOR activity and its overexpression inhibited mTOR. This suggests that WAVE2 influences mTOR "tone" within a physiologically relevant dynamic range, which is in keeping with a role in the metabolic restraint required for peripheral T cell quiescence and immune homeostasis. How WAVE2-mTOR interaction might be modulated by cellular activation status—in particular, the impact of posttranslational modification and relocalization within the cell—remains to be determined. One model would be that T cell activation releases mTOR from tonic inhibition at least in part by drawing WAVE2 away to participate in actin-remodeling events at the IS.

That activity of mTOR and the cytoskeleton should be linked is perhaps not unexpected. A cooperative relationship between mTORC2 expression and actin remodeling was postulated at the time RICTOR was discovered because reducing RICTOR expression prevented lamellipodia formation and cortical actin polymerization in epithelial cells (*14*, *15*). It would be interesting to investigate whether mTOR-WAVE2 interaction is inappropriately increased in this context, especially in T cells. More recently, human WAVE2 and HEM1 were reported to bind to RICTOR (although not mTOR itself) (*6*). This interaction was proposed to activate mTOR because human HEM1-deficient T lymphoblasts were impaired for overall TCR responsiveness and AKT-Ser^{473} phosphorylation (downstream of mTORC2) (*6*). Reduced AKT activity was also reported in B cells from patients with HEM1 deficiency (*7*).

This lack of congruence between findings in WAVE2-deficient mice and HEM1-deficient humans is unexpected and merits further attention. Although true interspecies differences cannot be excluded, the similarity in phenotype instead suggests a common molecular mechanism. mTOR activity is inherently sensitive to confounding variables such as lymphocyte proliferative history, immunosenescence, and immunosuppressive therapy. It will be interesting, and could have therapeutic importance, to clarify the nature of the mutual interaction between mTOR and the WRC, its modulation by upstream signals, and potential contribution to pathology in a range of human immune disorders. ■

The T cell immunological synapse

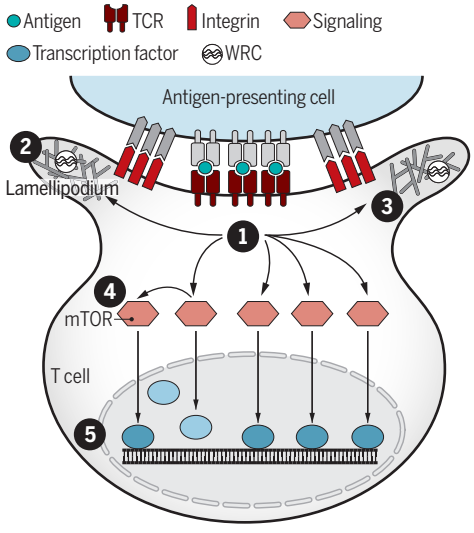

1 TCR engagement initiates signaling, including through phosphoinositide-3-kinase.

2 This activates WAVE2-dependent cytoskeletal remodeling and lamellipodia formation.

3 The immunological synapse matures and becomes stable.

4 Downstream signaling is reinforced, including through mTOR, a master regulator of metabolism.

5 This results in gene expression changes that drive the appropriate T cell response.

mTOR, mechanistic target of rapamycin; TCR, T cell receptor; WRC, Wiskott-Aldrich syndrome protein family (WAVE) regulatory complex.

GRAPHIC: N. CARY/*SCIENCE*

REFERENCES AND NOTES

1. M. Liu *et al.*, *Science* **371**, eaaz4544 (2021).
2. J. C. Nolz *et al.*, *Curr. Biol.* **16**, 24 (2006).
3. D. D. Billadeau, J. C. Nolz, T. S. Gomez, *Nat. Rev. Immunol.* **7**, 131 (2007).
4. J. A. Hammer, J. C. Wang, M. Saeed, A. T. Pedrosa, *Annu. Rev. Immunol.* **37**, 201 (2019).
5. R. Papa, F. Penco, S. Volpi, M. Gattorno, *Front. Immunol.* **11**, 604206 (2021).
6. S. A. Cook *et al.*, *Science* **369**, 202 (2020).
7. E. Salzer *et al.*, *Sci. Immunol.* **5**, eabc3979 (2020).
8. C. N. Castro *et al.*, *J. Exp. Med.* **217**, e20192275 (2020).
9. K. Yang *et al.*, *Immunity* **39**, 1043 (2013).
10. R. A. Saxton, D. M. Sabatini, *Cell* **168**, 960 (2017).
11. C. H. Patel, J. D. Powell, *Curr. Opin. Immunol.* **46**, 82 (2017).
12. C. L. Lucas, A. Chandra, S. Nejentsev, A. M. Condliffe, K. Okkenhaug, *Nat. Rev. Immunol.* **16**, 702 (2016).
13. S. Jung, L. Gámez-Díaz, M. Proietti, B. Grimbacher, *Front. Immunol.* **9**, 966 (2018).
14. D. D. Sarbassov *et al.*, *Curr. Biol.* **14**, 1296 (2004).
15. E. Jacinto *et al.*, *Nat. Cell Biol.* **6**, 1122 (2004).

ACKNOWLEDGMENTS

S.H. is supported by the Wellcome Trust.

10.1126/science.abg8077

PHOTONICS

Gold meets peptides in a hybrid coil

Twisted structures are assembled cooperatively by β-sheet peptides and gold nanorods

By **Ki Tae Nam** *and* **Hyeohn Kim**

Chirality can be transferred and coupled at multiple length scales under the condition that the breaking of mirror symmetry is preserved. Biological systems continue to inspire the design and synthesis of new chiral structures, from the smallest biomolecules to whole organisms (*1*). One hypothesis to understand the transfer of molecular chirality turns to the interplay between cytoskeletons and proteins. The chiral interaction between *Drosophila* myosin and actin cytoskeleton mediates the gliding of actin filaments and determines the handedness of cells, organs, and the organism (*2*). On p. 1368 of this issue, Lu *et al.* (*3*) harness a peptide assembly to induce the chiral assembly of synthetic gold nanomaterials, substantially enhancing the optical chiral response.

The key idea adopted by the authors is to use the helical structures of the human islet amyloid polypeptide (hIAPP). The major biological role of hIAPP is as a hormone that regulates physiological glucose concentrations, but it also induces fiber formation in the brain. The secondary structure of hIAPP forms a β-sheet, which assembles upon stacking into a one-dimensional, long tape-like structure. This tape-like structure is gradually twisted with a regular pitch, owing to the chiral center at the alpha carbon in the peptide. Lu *et al.* put this platform fully into effect by exploring chiral-selective and molecule-specific interfaces, along with uniform and anisotropic nanorods (see the figure).

In this sense, further emphasis can be placed on the coassembly of the amyloid peptides and uniform gold nanorods where the structural ordering of peptides is well transferred to the hybrid structures. Although conjugation of gold nanorods with the already assembled peptides showed a very low asymmetry factor (*g*-factor) because of the lack of coupling between individual nanorods, coassembly of uniform gold nanorods and peptides simultaneously induced a high asymmetry factor of 0.1. The authors claimed that the hydrophobic confinement of hIAPP with cetyltrimethylammonium bromide surfactant at the gold surfaces induced peptide folding into a well-defined β-sheet rather than a random coil conformation. Thus, determining the coassembly conditions is necessary to maximize the synergistic coupling in a coiled hybrid of peptide fibers and gold nanorods. Owing to the geometric specificity, the response of circular dichroism, or the differential absorption of left and right circularly polarized light, can be precisely controlled by the gold nanorod size, gap distance between individual nanorods, number of helical turns, and nanohelix pitch length.

A twisted chain of nanorods

Human islet amyloid polypeptides (blue) and gold nanorods (yellow) are cooperatively assembled into a chiral hybrid coil structure. The nanogaps between nanorods twisted along the fibril come from the structural ordering of the peptide sheets.

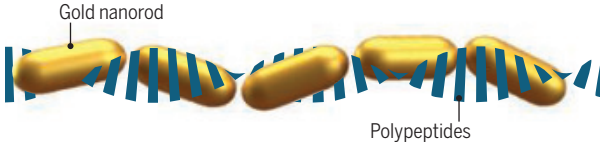

The asymmetry (*g*) factor of 0.1 is itself as important as previous examples (*4*) of spherical gold nanoparticles on a DNA helix that were closer to a *g*-factor of 0.01. The well-defined nanosized gap between the two edges of the uniform nanorods that were twisted along the peptide fibril enhanced the chiroptic response. A *g*-factor higher than 0.1 for a singular gold nanoparticle was achieved by controlling the edges and gaps using chiral peptides (*5*) and micellar organization (*6*). However, the authors' use of multiple gold nanoparticles along with the rotational symmetry of multiple nanogaps in a peptide fibril generated with a precise pitch along the longitudinal direction is a much different demonstration. The collective oscillation of magnetic dipoles through plasmonic resonance becomes rotational, depending on the polarization state of the incident light. The size of the nanorods and the pitch of the assembled structure without being precisely matched will not allow for a high *g*-factor generation because of the lack of symmetry of the magnetic dipoles.

The authors' proposed hybrid coil structure provides a versatile platform for studying exotic phenomena, such as phase-controlled optical devices, hologram films, responsive devices, and nonlinear chiral plasmonic devices (*7*). One strategy in this direction could be the coupling of dielectric materials, such as silica or titanium dioxide (TiO_2), because they could lower the optical loss and broaden the applicability scope to even practical optical communication devices, such as flat lenses and displays. Another challenge would be the application of a coassembly strategy by using DNA, polysaccharides, proteins, and viruses as the other chiral inducers. Furthermore, exploring the implications of achiral peptide-mimetic peptoid polymers (*8*), multiple peptides, or other organic molecules would be interesting.

The authors also demonstrated a sensory application monitoring the chiroptic response according to amyloid-fiber inhibitor concentrations. The gradual assembly of chiral nanostructures may open up opportunities to modulate the assembly kinetics and pathways, enabling time-dependent structural changes (*9*) even under in vivo conditions. This requires a precise stereochemical design of biomolecules. And dynamic chiroptical modulations could facilitate the realization of practical applications for sensitivity-enhanced detection of cancer markers and genetic mutations, or other reactions with molecular precision in actual cellular environments. ■

Department of Materials Science and Engineering, Seoul National University, 1 Gwanak-ro, Gwanak-gu, Seoul 08826, Republic of Korea. Email: nkitae@snu.ac.kr

REFERENCES AND NOTES

1. M. C. Fernandes, J. Aizenberg, J. C. Weaver, K. Bertoldi, *Nat. Mater.* **20**, 237 (2021).
2. G. Lebreton *et al.*, *Science* **362**, 949 (2018).
3. J. Lu *et al.*, *Science* **371**, 1368 (2021).
4. A. Kuzyk *et al.*, *Nature* **483**, 311 (2012).
5. H.-E. Lee *et al.*, *Nature* **556**, 360 (2018).
6. G. González-Rubio *et al.*, *Science* **368**, 1472 (2020).
7. L. Gui *et al.*, *ACS Photonics* **6**, 3306 (2019).
8. S.-T. Wang *et al.*, *Proc. Natl. Acad. Sci. U.S.A.* **117**, 6339 (2020).
9. H.-Y. Ahn *et al.*, *Accounts of Chemical Research* **52**, 2768 (2019).

ACKNOWLEDGMENTS

The authors appreciate the support from the Creative Materials Discovery Program through the National Research Foundation of Korea (NRF-2017M3D1A1039377)

10.1126/science.abg9901

GRAPHIC: N. DESAI/*SCIENCE*

A live Iberá Seedeater male (left) challenges a painted male model that is delivering a song playback (right), whom he sees as a threat in his territory.

PHOTO: SHEELA TURBEK/UNIVERSITY OF COLORADO, BOULDER

EVOLUTION

At the beginning of speciation

Appearance and song are sexually selected factors to maintain a new bird species

By **Erich D. Jarvis**

Understanding how one population of individuals can split into two species has remained a challenge, especially when the newly emerging species lives inside the geographic area of the older one (*1*). One possible answer is offered by Turbek *et al.* (*2*) on page 1337 of this issue. They studied two songbird species belonging to the Southern capuchino seedeater lineage, where the Iberá Seedeater (*Sporophila iberaensis*) lives entirely within the territory of the Tawny-bellied Seedeater (*S. hypoxantha*) in Iberá National Park, Argentina. Despite having similar genomes and the ability to form viable hybrids, the two species maintain mating isolation from each other, based on male plumage and learned song. These pre-mating barriers are proposed as the mechanism that maintains the beginning of speciation within the past million years, and which is expected to eventually lead to post-mating barriers where their genomes will sufficiently diverge to prevent viable offspring.

The authors found that the two species differ in only three genomic regions, each no more than 50,000 base pairs in length, out of their 1.2 billion–base pair genomes. Two of these regions contain mutations in regulatory regions of plumage coloration genes, which could explain the male plumage differences. One of these two was on the Z sex chromosome, indicating a link to sexual selection. In birds, sex chromosome organization is the inverse of that in mammals, where females have ZW chromosomes (instead of XX) and males have ZZ (instead of XY).

To show that sexual selection was driving speciation, Turbek *et al.* used an ingenious experimental setup. Model birds were painted to look like real male birds (Iberá models with an off-white belly and chest; tawny-bellied models with an orange chest), mounted on branches in the wild in a male's territory, in the presence of a female. A male's song was played through a speaker placed beneath the model. Iberá males responded with a high-intensity territorial response to the Iberá model playing the Iberá song, but they largely ignored tawny-bellied males with tawny-bellied song. The opposite result occurred when the models and songs were switched. Hybrid mixes of plumage and song received territorial responses of intermediate intensity.

For the females, using a genetic test, Turbek *et al.* found (like for some other songbird species) that there was a high degree of secret extra-pair mating, where ~52% of the offspring were fathered by another male. But extra-pair mating occurred entirely within each species. Thus, despite a <0.1% difference in their genomes, males and females of each species mostly stay with their own species (based on appearance and song). This finding was determined from genotyping DNA sequencing of parents and their offspring and analysis of single-nucleotide polymorphisms that can distinguish genetic parentage and species.

Some unanswered questions include whether species selection for song is cultural only, or cultural and genetic. Songbirds are one of the rare groups of species that have vocal learning, the ability to imitate sounds and culturally pass them on from one generation to another (*3*, *4*). The other vocal learning lineages (apart from humans) are parrots and hummingbirds among birds, and cetaceans (whales/dolphins), pinnipeds (e.g., seals), elephants, and bats among mammals. Theoretically it should be possible for a young Iberá male to learn to imitate the song of a tawny-bellied male and vice versa. If given the choice, with all factors being equal, would isolated young Iberá males have a preference for which song they imitate? If they show no preference, it would indicate that selection for how they "talk" has been purely cultural. But if a preference exists, it would indicate a genetic predisposition, perhaps controlled by genes potentially involved in vocal learning in one of the three genomic regions with differences. Another potential issue is that these are draft genomes generated with short reads, which have difficulty sequencing through regions rich in guanine-cytosine (GC) base pairs (which include many regulatory regions), as well as difficulty resolving repetitive regions (which could also include regulatory regions and recent gene duplications). High-quality de novo genome assemblies, as done with the Vertebrate Genomes Project (*5*), could reveal additional genomic regions as candidates contributing to recent speciation.

The findings of Turbek *et al.* prompt the question of how widespread this pre-mating mechanism of speciation might be. Perhaps it can give rise to local population differences within a species. Humans are vocal learners, which is necessary for spoken language (*3*). People take for granted that their apparent mate preferences are for others of the same culture who speak the same language. But perhaps these choices could be part of a broader, genetically determined recognition mechanism that influences mate selection and speciation. Answers to these questions can be gained in future studies in genomics, behavior, and ecology, following the model of Turbek *et al.*, to assess the beginning of population divergence and speciation. ■

Laboratory of Neurogenetics of Language and Howard Hughes Medical Institute, The Rockefeller University, New York, NY 10065, USA. Email: ejarvis@rockefeller.edu

REFERENCES AND NOTES

1. Marie Curie SPECIATION Network, *Trends Ecol. Evol.* **27**, 27 (2012).
2. S. P. Turbek *et al.*, *Science* **371**, 1337 (2021).
3. E. D. Jarvis, *Science* **366**, 50 (2019).
4. J. H. Bruno *et al.*, *Annu. Rev. Linguist.* **7**, 449 (2021).
5. A. Rhie *et al.*, bioRxiv 2020.05.22.110833 [preprint]. 23 May 2020.

ACKNOWLEDGMENTS

Supported by the Howard Hughes Medical Institute and the National Institutes of Health.

10.1126/science.abg5454

CHEMISTRY

Getting excited about cycloadditions

Photoactivation to long-lived triplet excited states enables cycloadditions with heteroarenes

By **Valerie A. Schmidt**

Synthetic chemists use photochemistry to achieve challenging or unusual chemical transformations, but not all compounds are photoactive. Photosensitization is a process by which a molecule that is incapable of efficiently absorbing a particular wavelength of light directly is promoted to its triplet excited state (T_1) by an intermolecular triplet energy transfer from a photosensitizer, which is a compound that ideally has a large extinction coefficient, rapid rate of intersystem crossing, and a long-lived T_1. A particular advantage of photosensitization is that distinctive reactivity profiles not accessible through ground states become facile from corresponding excited states (*1*). The use of photosensitizers in chemical synthesis has paralleled the rise in popularity and use of various photoredox catalysts (*2*). On page 1338 of this issue, Ma *et al.* (*3*) report a photosensitized dearomative [4 + 2] cycloaddition that converts simple, unsaturated building blocks into products of increased molecular complexity using visible light.

Cycloaddition reactions are one of a limited number of fundamental reaction types that exemplify several ideals of chemical synthesis and that have divergent reactivity when carried out under thermal versus photochemical conditions. These reactions have the ability to bring together multiple molecular fragments in a convergent manner and can create several new covalent bonds with well-established predictability and often with control over the chemo-, regio-, and diastereoselectivity of the addition products. As a result of their utility in the synthesis of complex molecules and their well-studied mechanistic pathways, cycloadditions have been a cornerstone for demonstrating key principles in organic chemistry classes for many years. Notably, [4 + 2] cycloadditions require two unsaturated reaction components that trade two double (π) bonds for two single (σ) bonds to form a six-membered ring structure. The first unsaturated component, known as the "diene," contains two π bonds connected by a single σ bond.

Arenes similarly contain alternating double bonds (as a result of conventions of chemical structure drawing), but their use in cycloaddition reactions presents additional challenges as a result of their increased stabilization conferred by aromaticity. Although aromatic compounds are a diverse, abundant set of chemical building blocks, these flat molecules are limited in their three-dimensional structural complexity and, for applications as pharmaceutical agents, possible interactions with biological receptors (*4*). Thus, the development of new synthetic methods that may simultaneously take advantage of abundant arene starting materials while increasing stereochemical and functional group density is highly attractive.

Several heteroarenes, such as furans and pyrroles, have long been used as "dienes" in [4 + 2] cycloadditions to produce multicyclic, bridged compounds, enabled largely by their lower degree of aromaticity created by electronegative oxygen and nitrogen atoms in their rings, compared with more stabilized all-carbon arenes such as benzene. Whereas thermally promoted dearomative cycloadditions of benzene, pyridine, or quinoline are plagued with challenges caused by high kinetic barriers and unfavorable thermodynamic profiles, photochemical activation has been successfully used (*5*).

Given that pyridine is one of the most commonly found nitrogen heterocycles in drugs approved by the U.S. Food and Drug Administration (*6*), synthetic strategies to access them from readily available starting materials is an attractive conceptual approach. Ma *et al.* chose to combine established photosensitizing reactivity of octahedral iridium photocatalysts with Lewis and Brønsted acid T_1 energy-lowering coordination (*7*) to activate azaarenes and direct excellent chemo-, regio-, and stereoselective dearomative [4 + 2] cycloadditions with a range of functionalized terminal olefins (see the figure). In this process, the valuable heteroarene is retained in the product, and molecular complexity is increased with full atom economy.

Given nature's ability to perform highly complex and energetically demanding photochemical processes, there are likely few limits to chemical transformations that can be enabled by photochemistry. With increased interest in rational design and application of triplet energy transfer catalysts that has been facilitated by continued advances in computational chemistry (*8*, *9*), it is likely that we are at the earliest stages of seeing the bright future photosensitization has in store for chemical synthesis. ■

Acting like a diene

Aromatic molecules are usually too stable to serve as conjugated diene substrates (which contain two double bonds separated by one single bond) in cycloadditions through thermal routes. Ma *et al.* show that energy transfer from an iridium photosensitizer allows heteroaromatics (azaarenes) to react with alkenes bearing a functional group R.

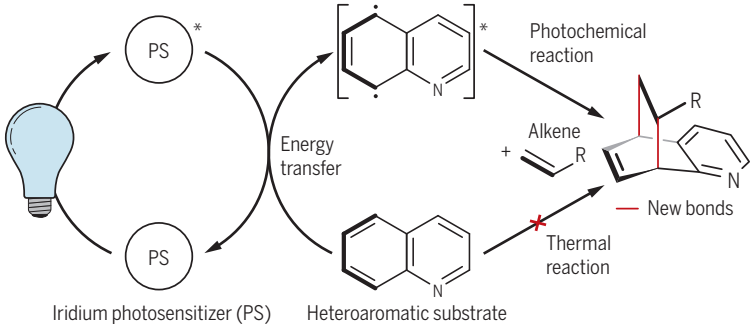

GRAPHIC: JOSHUA BIRD/*SCIENCE*

Department of Chemistry and Biochemistry, University of California San Diego, La Jolla, CA 92093, USA.
Email: vschmidt@ucsd.edu

REFERENCES AND NOTES

1. G. S. Hammond, N. J. Turro, *Science* **142**, 1541 (1963).
2. F. Strieth-Kalthoff, M. J. James, M. Teders, L. Pitzer, F. Glorius, *Chem. Soc. Rev.* **47**, 7190 (2018).
3. J. Ma *et al.*, *Science* **371**, 1338 (2021).
4. F. Lovering, J. Bikker, C. Humblet, *J. Med. Chem.* **52**, 6752 (2009).
5. R. Remy, C. G. Bochet, *Chem. Rev.* **116**, 9816 (2016).
6. E. Vitaku, D. T. Smith, J. T. Njardarson, *J. Med. Chem.* **57**, 10257 (2014).
7. T. R. Blum, Z. D. Miller, D. M. Bates, I. A. Guzei, T. P. Yoon, *Science* **354**, 1391 (2016).
8. J. Zhao, W. Wu, J. Sun, S. Guo, *Chem. Soc. Rev.* **42**, 5323 (2013).
9. L. D. Elliott, S. Kayal, M. W. George, K. Booker-Milburn, *J. Am. Chem. Soc.* **142**, 14947 (2020).

ACKNOWLEDGMENTS

V.A.S. is supported by the National Science Foundation (CAREER award CHE-1945463) and the American Chemical Society Petroleum Research Fund (60135-DNI1).

10.1126/science.abg7834

POLICY FORUM

AIR POLLUTION

Raising standards to lower diesel emissions

California policies protect vulnerable communities the most and should be adopted nationwide

By **Megan Schwarzman[1], Samantha Schildroth[1]*, May Bhetraratana[2], Álvaro Alvarado[2]†, John Balmes[1,3]**

Air pollution from fine particulate matter ($PM_{2.5}$) is increasingly driving the global burden of disease (*1*), and diesel-powered vehicles are substantial contributors. Recognizing the public health impacts of diesel $PM_{2.5}$ (DPM) (*2*), many countries have reduced emissions of DPM from both on- and off-road mobile sources over the past three decades. The previous US federal administration, however, changed course by eliminating or weakening policies and standards that govern these emissions. In contrast, the State of California has continued to reduce mobile-source DPM emissions using the state's long-standing authority under the Clean Air Act (CAA) to regulate air pollution more stringently than the federal government. Our analysis of mobile-source DPM emissions suggests that many California sector-based policies have been highly effective relative to the rest of the US. To improve health in communities disproportionately affected by these emissions, we point to opportunities to further reduce DPM emissions in California, in the US more broadly, and in parts of the world where countries have less aggressive vehicle emissions policies than the US (*3*).

The US has targeted emissions of nitrogen oxides (NO_x) and DPM from diesel trucks and buses, railway locomotives, marine vessels, and off-road engines used in construction and agriculture through successively tighter emissions standards phased in since 1994 (table S1). These standards require low- and ultralow-sulfur diesel fuels (LSDF and ULSDF), establish emissions limits, and institute systems for portable emissions measurement and onboard diagnostics (table S1).

The US Environmental Protection Agency (EPA) estimated that full implementation of Obama-era US emissions standards by 2030 would prevent some 12,000 premature deaths annually (*4*). Despite this, EPA leadership disbanded the PM review panel ahead of the scheduled 2020 update of federal PM standards; it also rolled back, or attempted to roll back, 85 federal air pollution policies (*5*) and moved to restrict the ability of states to set more stringent emissions standards (*6*).

CALIFORNIA VERSUS THE REST OF THE UNITED STATES

California, whose economy would rank fifth largest in the world if it were a sovereign nation, hosts the country's two largest ports and moves 60% of its container cargo (see supplementary materials). With the associated truck and rail traffic, California stands out as the largest emitter of DPM in the country. At the same time, California has also led the nation with the largest overall reduction in metric tons of DPM emissions from mobile sources. Over the past three decades, California's policies have systematically targeted high-emitting sectors, reducing mobile-source DPM emissions by, for example, substituting electric for diesel power where feasible, tightening emissions limits for new and existing diesel engines, and requiring ULSDF, which emits substantially less $PM_{2.5}$ than higher-sulfur fuels upon combustion and can be combined with particle filters to further reduce emissions.

To understand the impact of California's portfolio of policies, we used DPM emissions data from the EPA National Emissions Inventory (NEI), which assembles a comprehensive estimate of air pollution emissions using data reported by states, combined with modeled and measured inputs. We compared mobile-source DPM emissions in California versus the rest of the US for the period 1990 to 2014, the earliest and most recent year for which consistent NEI data are available (*7*). During that time, California reduced overall mobile-source DPM emissions by 78% while the rest of the US saw only a 51% reduction. These reductions came despite a concurrent steady rise in diesel fuel consumption: 20% in California and 28% in the rest of the US (data S1).

Emissions reductions from heavy-duty diesel vehicles (HDDVs)—commercial trucks and buses—caused most of this decline, accounting for 67% of DPM emissions reductions in California and 57% in the rest of the US. Although the federal phase-in of ULSDF, off-road emissions standards, and the Heavy-Duty Engine and Vehicle Rule has reduced HDDV emissions across the US, California's reductions from HDDVs have been steeper and contribute even more to the overall reductions than would be predicted from the sector's size. Analyses of DPM emissions over time and the relative contributions made by each sector point to the effectiveness of California's policies that require diesel engine retrofits (adding emissions controls to existing HDDVs) and early replacement of older engines with newer, cleaner engines.

DIFFERENT ERAS, DIFFERENT OUTCOMES

Our analysis identifies three distinct phases in mobile-source DPM emissions between 1990 and 2014. Emissions fell overall from 1990 to 2001 in California and from 1990 to 2005 in the rest of the country. Reduced emissions from HDDVs contributed the largest share of the overall drop (see the figure and data S1). These changes are attributable to the introduction of LSDF nationwide, and to California's new requirements for vehicle inspections (table S2).

Then, from 2001 to 2005 in California and from 2005 to 2008 in the rest of the country, emissions rose during an economic boom, driven primarily by increasing emissions from HDDVs and marine sources. Finally, overall DPM emissions once again fell, beginning in California in 2005 and in the rest of the US in 2008. The recession played a role in the early part of this drop (*8*), but emissions reductions continued through 2014 despite the economic recovery and the corresponding upturn in diesel use. During this final phase, California's 67% drop in DPM emissions outpaced the 40% reduction seen in the rest of the country (see the figure and data S1). Our analysis of individual sectors and each state's HDDV emissions suggests that California policies specifically targeting emissions from HDDVs and marine sources drove this decline.

[1]School of Public Health, University of California, Berkeley, CA, USA. [2]California Air Resources Board, Sacramento, CA, USA. [3]Department of Medicine, University of California, San Francisco, CA, USA. Email: mschwarzman@berkeley.edu
*Present address: Boston University School of Public Health, Boston, MA, USA. †Present address: Office of Environmental Health Hazard Assessment, Oakland, CA, USA.

SECTOR-BASED POLICY: CALIFORNIA

The later phases of California's emissions reductions correspond to the implementation of two overarching plans by the California Air Resources Board (CARB): the Diesel Risk Reduction Plan and the Emission Reduction Plan for Ports and Goods Movement (Goods Movement Plan), both of which encompassed multiple policies governing emissions from trucks and buses, ports, and off-road engines (table S2). Key policies targeting on-road HDDVs took effect in 2006 and 2007, further lowering the sulfur content of diesel fuel to 15 ppm (table S2) and tightening DPM emissions standards by 90% for new HDDVs (table S2). Beginning in 2010, with a rolling compliance period starting in 2015, all on-road HDDVs that operate in California were required to either retrofit existing engines with particle filters or replace engines older than the 2007 model year (table S2).

By comparison, federal policies do not require retrofit or replacement of old diesel engines to meet emission standards, and HDDV engines typically operate for almost two decades, or about a million miles, before retirement. Our state-level analysis shows that by 2014 California HDDVs were emitting 139 metric tons of DPM for every billion vehicle-miles traveled (VMT), far less than the next-closest state (Oklahoma, 250 metric tons DPM per billion VMT) and the average in the rest of the country (345 metric tons DPM per billion VMT) (data S1). Although HDDVs remain California's largest source of DPM emissions, regulatory actions by CARB (over and above federal standards) have reduced HDDV emissions by 85% since 1990. If California's HDDV sector had followed the trajectory of other US states and DC, HDDV emissions in the state would have dropped only 58% (95% confidence interval, 52 to 64%) in that period (data S1).

Also notable is the impact of two key CARB policies targeting marine sources. The 2007 At-Berth rule requires that ocean-going vessels switch to electric shore power while in port or use alternative control technologies to reduce emissions by an equivalent amount (table S2). The Cleaner Ocean Vessel fuel policy, finalized in 2008, requires that ships within 24 nautical miles of California's shoreline replace heavy fuel oil in their main engines with lower-sulfur fuels (table S2). Between 2008 and 2014, marine DPM emissions in the state dropped 51% overall (see the figure and data S1), and by 2018 emissions measured at the Port of Los Angeles had declined by 37% (fig. S3, A and B, and data S1).

By contrast, California has struggled to target diesel emissions from agriculture (table S2). The sector is responsible for up to 18% of the state's total DPM emissions from mobile sources, but it accounted for less than 1% of the total emissions reductions in California between 1990 and 2014. Although these figures do not reflect gains from voluntary tractor engine replacements that are reported differently, opportunities remain to reduce off-road farm emissions in the nation's leading agricultural state.

Voluntary programs have further reduced DPM emissions beyond California's regulatory requirements. Incentives to bring engines and equipment to a standard cleaner than required by law are estimated to have reduced DPM emissions by more than 6000 metric tons since 2001 (table S2). A program established in 2006 has provided $1 billion in grants to update trucks, locomotives, and ships at berth, eliminating an estimated 2200 metric tons of DPM emissions (table S2). Like other policies targeting emissions along goods-movement corridors, this program particularly benefits neighboring communities, which tend to be lower-income communities of color (table S4).

Taken together, CARB's policies reduced emissions to the extent that by 2014 California was emitting less than half the DPM that would be expected had the state followed the same trajectory as the rest of the US (fig. S2 and data S1). Correspondingly, we estimate that more than twice as many Californians would have died from DPM-attributable cardiopulmonary disease in 2014 alone if the state had not so markedly reduced emissions (data S1).

SECTOR-BASED POLICY: THE REST OF THE UNITED STATES

The impact of targeted emissions regulation is also evident nationally, but it has come later and never as meaningfully as in California. Farming and construction emissions fell following the 2007 EPA Heavy Duty Engine and Vehicle Rule and the 2008–2015 phase-in of Tier 4 standards targeting off-road emissions from farm and construction equipment (table S1). Federal requirements for LSDF in the 1990s and ULSDF beginning in 2006 reduced HDDV emissions from both nonroad and on-road sources (table S1).

In the marine sector, US coastal areas caught up to California's fuel standards in 2012 when ULSDF was required for smaller marine engines (table S1) and in 2015 for the largest vessels when requirements for lower-sulfur marine diesel came into effect in the North American Emissions Control Area established by the International Maritime Organization (table S1). By contrast, California has taken not only earlier action on marine emissions but also aggressive steps to target emissions from the many engines that pollute the air near ports, including marine auxiliary engines, short-haul trucks, cargo-

California versus the rest of the United States: Mobile-source DPM emissions declined differently

Mobile-source diesel $PM_{2.5}$ (DPM) emissions by sector in California versus the rest of the US from 1990 to 2014. HDDV, heavy-duty diesel vehicle; LDDV, light-duty diesel vehicle. All percentage changes reflect values relative to 1990 values.

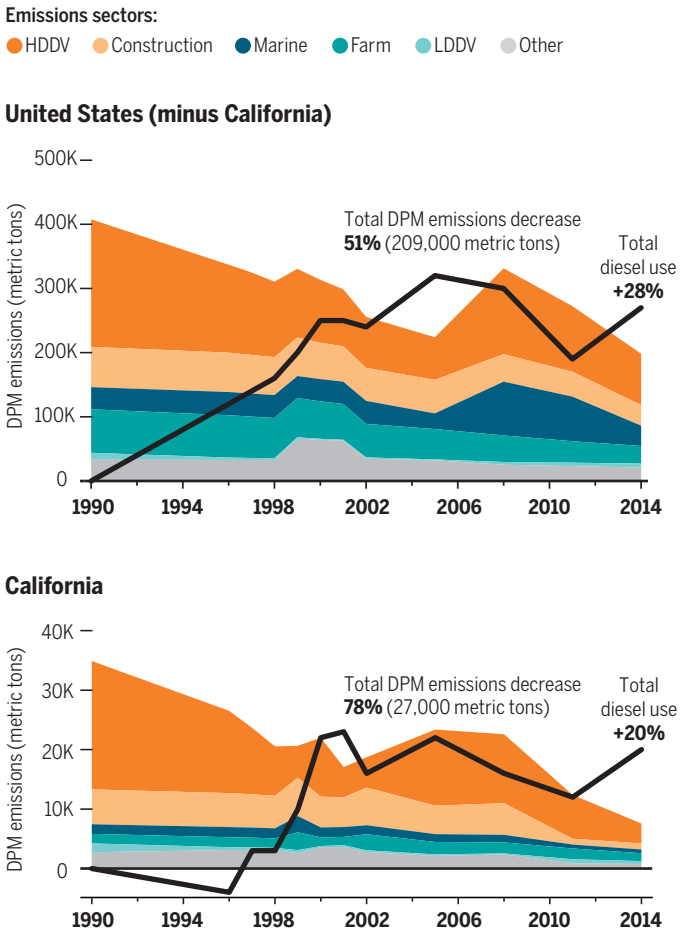

GRAPHIC: N. CARY/SCIENCE

handling cranes, and yard trucks (table S2).

Individual states that have reduced HDDV emissions more than the national average are more likely to have adopted California's standards, as permitted under the CAA (table S5 and data S1), and the rest of the US could do the same.

GROUND-TRUTHING EMISSIONS REDUCTIONS

Coordination across states and between state and federal agencies means that methodological differences in data collection are unlikely to account for the observed differences in DPM emissions between California and the rest of the US (see supplementary materials). But how do we know that emission inventories are accurate and, furthermore, that CARB policies are responsible for the observed reductions?

Field studies measuring changes in concentrations of DPM serve to ground-truth emissions inventories and substantiate the link between policy interventions and observed outcomes (table S4). For example, following the suite of interventions under the 2006 Goods Movement Plan, California communities in close proximity to goods-movement corridors saw significantly greater air quality improvements relative to non–goods-movement corridors and control areas monitored during the same time period (table S4). These findings show specific, local impacts of regulations targeting high-emitting sectors, distinguishing those changes from secular trends in air pollution and demonstrating their potential to advance environmental justice.

The 2007 CARB regulation requiring retrofit or replacement of older HDDV engines for short-haul "drayage trucks" that operate at ports and railyards corresponded to a 70% reduction in black carbon emissions (a DPM proxy) and a 75% reduction in PM mass specific to drayage trucks measured in and around the ports of Oakland and Los Angeles between 2009 and 2011 (table S4). These changes mirror the emissions reductions measured in laboratory testing of the low-sulfur fuels and retrofit technologies used to meet the drayage truck standards (table S3).

Likewise, the 2009 CARB requirement for low-sulfur fuels in oceangoing vessel engines operating within 24 nautical miles of the California coastline was associated with a measured 64% drop in San Francisco Bay Area concentrations of vanadium, a marker for combustion of heavy fuel oil (table S4). Sampling conducted by aircraft flying in the exhaust plume of a container ship approaching the coast showed that the fuel switch, combined with a required speed reduction, dropped DPM emissions by 90% (table S4). That these changes all occurred in the setting of continued growth in California's population, gross state product, and diesel consumption (figs. S4 and S5) further supports the assertion that the observed reductions track to the policies targeting DPM emissions. Observed emissions reductions are further corroborated by epidemiological data that link specific CARB policies to regional reductions in children's exposure to particle pollution and show corresponding improvements in both lung function and development in children with and without asthma (*9*).

Finally, comparing HDDV sector emissions in California to the rest of the country likely underestimates the actual impact of CARB policies, which apply not only to the nearly half-million trucks and buses registered in California but also to the same number of out-of-state HDDVs estimated to drive California's highways each year (*10*). This requirement reduces emissions outside of California as well, although those reductions are attributed to federal policy.

IMPLICATIONS FOR FUTURE STANDARDS

In California, cleaner air has not come at the expense of the state's economy, which in recent years has grown at double the average national rate (*11*). CARB estimates that every dollar the state has spent controlling air pollution has generated $38 in benefits attributable to reduced air pollution–related illness, premature death, and lost productivity. California's overall economic gain from health benefits linked to air pollution reduction, including CARB rules and programs, is estimated to have exceeded $250 billion between 1973 and 2014 (*12*). The link between $PM_{2.5}$ exposure and increased risk of hospitalization and death from COVID-19 (*13*) further underscores the public health importance of cleaner air, particularly for communities of color that are disproportionately affected by both.

California could benefit from additional measures to reduce emissions from off-road sectors, such as construction and agriculture, which CARB has not tackled as aggressively (*14*). Indeed, the nation as a whole could reduce mobile-source DPM emissions by requiring ships at berth to use shore power, and by requiring replacement or retrofit of existing on-road and off-road HDDVs in advance of fleet turnover. Given the long service life of older, dirty diesel engines, the current federal policy of mandating engine upgrades only with vehicle turnover is simply too slow.

As the US initiates new federal rule-making on the proposed Cleaner Trucks Initiative to reduce NO_x emissions from HDDVs, industry and environmental groups are calling on EPA to address NO_x and DPM emissions in tandem and to create consistent "50-state" standards (*15*). In doing so, the EPA should align with CARB rules. EPA should also remove federal preemption of state emissions limits for off-road engines used in construction and agriculture. Even absent more aggressive federal policy, states' authority to set and implement their own stricter emissions standards must be protected. ■

REFERENCES AND NOTES

1. GBD 2017 Risk Factor Collaborators, *Lancet* **392**, 1923 (2018).
2. California Air Resources Board, "Overview: Diesel Exhaust & Health"; ww2.arb.ca.gov/resources/overview-diesel-exhaust-and-health.
3. European Union Directorate-General for Internal Policies, *Comparative Study on the Differences Between the EU and US Legislation on Emissions in the Automotive Sector* (2016); www.europarl.europa.eu/RegData/etudes/STUD/2016/587331/IPOL_STU(2016)587331_EN.pdf.
4. DieselNet, "Emission Standards, United States"; www.dieselnet.com/standards/us/index.php.
5. J. M. Samet, T. A. Burke, *Annu. Rev. Public Health* **41**, 347 (2020).
6. C. Davenport, "Trump to Revoke California's Authority to Set Stricter Auto Emissions Rules." *New York Times*, 17 September 2019; www.nytimes.com/2019/09/17/climate/trump-california-emissions-waiver.html.
7. US Environmental Protection Agency, "National Emissions Inventory (NEI)"; www.epa.gov/air-emissions-inventories/national-emissions-inventory-nei.
8. D. Q. Tong *et al.*, *Atmos. Environ.* **107**, 70 (2015).
9. F. Gilliland *et al.*, "The Effects of Policy-Driven Air Quality Improvements on Children's Respiratory Health" (2017); www.healtheffects.org/system/files/GillilandRR190.pdf.
10. California Air Resources Board, "Staff Report: Initial Statement of Reasons for Proposed Rulemaking: Proposed Regulation for In-Use On-Road Diesel Vehicles" (2008); https://westrk.org/CARBdocs/ARB_CDTOA/InitialStatementofReasons.pdf.
11. Next10, 2017 California Green Innovation Index (2017); www.next10.org/publications/2017-gii.
12. California Air Resources Board, Fifty Year Air Quality Trends and Health Benefits; ww3.arb.ca.gov/board/books/2018/020818/18-1-2pres.pdf.
13. X. Wu, R. C. Nethery, M. B. Sabath, D. Braun, F. Dominici, *Sci. Adv.* **6**, eabd4049 (2020).
14. California's construction emissions declined markedly from 2008 to 2011. Although industry likely lowered emissions in anticipation of deadlines in the 2008 In-Use Off-Road Diesel-Fueled Fleet Regulation (table S2), the majority of the decline is likely attributable to CARB's 2011 construction inventory revision prompted by the regulated industry. In that year, the regulation was also amended to delay implementation by 4 years and to lower required emission reductions.
15. US Environmental Protection Agency, "Control of Air Pollution From New Motor Vehicles: Heavy-Duty Engine Standards" [proposed rule]; www.federalregister.gov/documents/2020/01/21/2020-00542/control-of-air-pollution-from-new-motor-vehicles-heavy-duty-engine-standards#citation-4-p3307.

ACKNOWLEDGMENTS

We thank K. Peterson (University of California, Berkeley) for data visualization; K. Karparos, C. Parmer, and B. Holmes-Gen (CARB) for manuscript review; M. Houyoux, J. Godfrey, and M. Aldrich (EPA) for assistance with NEI data; and J. Austin, R. Boyd, T. Brasil, J. Cao, M. Diaz, R. Furey, J. Herner, S. Huber, M. Komlenic, R. Krieger, T. Kuwayama, N. Lowery, N. Motallebi, S. Pournazeri, S. Yoon, S. Zelinka, and L. Zhou (CARB) for assistance with CARB regulations and data. This research was supported in part by California Breast Cancer Research Program grant 23QB-1881. J.B. serves as the Physician Member of CARB. A.A. is a former employee of CARB.

SUPPLEMENTARY MATERIALS

science.sciencemag.org/content/371/6536/1314/suppl/DC1

10.1126/science.abf8159

BOOKS *et al.*

A caretaker stands watch over one of the world's last living northern white rhinos in 2018.

PHOTO: JAN HUSAR/SOPA IMAGES/LIGHTROCKET/GETTY IMAGES

ECOLOGY

The conservationists

Passionate advocates have helped humanity rethink its relationship with Earth's other species

By **Christopher Kemp**

By 1963, the number of bald eagles—long a symbol of American exceptionalism—had dwindled to a staggering low of 417 known nesting pairs in the contiguous United States, having been decimated by a combination of habitat destruction, DDT poisoning, and illegal hunting. With the passage and enforcement of sturdy conservation laws, however, the species has steadily recovered. There are currently around 10,000 breeding pairs in the lower 48 states and more than 100,000 individual birds, making the bald eagle one of a number of profoundly satisfying success stories of the modern conservation movement.

The quest to save endangered species has been a journey of gains and losses, with many wrong turns and dead ends. Michelle Nijhuis's *Beloved Beasts* is a definitive and informative history of this journey, from its conflicted and noisy beginning at the dawn of the 20th century to the present day. A writer for *National Geographic* and editor for *The Atlantic*, Nijhuis deftly reminds readers of some of humanity's greatest conservation achievements and disappointments. Along the way, we meet towering figures in the conservation movement, including the militant socialite conservationist Rosalie Edge and the father of wildlife ecology, Aldo Leopold. We are also reminded of the determination of individuals such as *Silent Spring* author Rachel Carson, one of the better angels of our nature.

Beloved Beasts: Fighting for Life in an Age of Extinction
Michelle Nijhuis
Norton, 2021. 352 pp.

In some respects, the title of the book is misleading: This is more of a human story than a tale about animals. Humans, after all, are the reason the dodo disappeared from Mauritius in the space of a few short and bloody decades (the last one was killed in 1662). The bird was joined in extinction by the great auk (1852); the Falkland Islands wolf (1876); the passenger pigeon (1914); the thylacine, or Tasmanian tiger (1936); and an unknown number of unnamed species that disappeared before we even got around to cataloging them. Since the 1500s, Nijhuis writes, humans have driven more than 150 bird species alone to extinction.

Nijhuis's detailed account is clear-eyed and unvarnished in its honesty. She readily acknowledges that many of the early figures of the conservation movement were deeply flawed. William Temple Hornaday, for example, almost single-handedly repopulated the North American Plains with bison, which had dwindled from 20 million to 30 million in the 1700s to an estimated 300 in 1886, when Hornaday headed out west to shoot some for a museum diorama. In 1907, Hornaday, who was the director of what is now the Bronx Zoo, transported zoo-bred bison by rail to Oklahoma and released them into a bison preserve that he had pressured Congress to designate. However, his motivation for protecting the bison population did not come from a desire to protect the animals for their own sake. Hornaday wanted to rescue the bison so that hunters could continue shooting them for sport. And while he imagined vast herds of bison re-darkening the plains, his dreams did not include the Comanche, the Blackfoot, the Lakota, or any of the other Indigenous people whose way of life depended on the bison.

To this day, Nijhuis writes, the conservation movement has maintained its awkward ties with hunters. In Africa, for example, dwindling populations of lions, giraffes, and elephants are protected using funds raised via trophy hunting auctions. If the contemporary conservationists Nijhuis interviews in *Beloved Beasts* have any say in it, this too will eventually change.

As Nijhuis reminds readers, the late 19th century marked the dawn of a new way of thinking, and ecology was a new concept—the word having only just been minted in 1866 by zoologist Ernst Haeckel. Before Charles Darwin published *On the Origin of Species* in 1859 (and afterward too), many people thought that God had made each species for humanity's convenience. Nevertheless, the conservation movement grew, as important ideas tend to do, one organization at a time: from the Royal Society for the Protection of Birds, established in 1889, to the Sierra Club (1892), the Wildlife Conservation Society (1895), the National Audubon Society (1905), and Birdlife International (1922).

The effects of the Anthropocene will remain for millennia in the form of species extinctions, habitat destruction, and the uncountable fragments of plastic floating in our oceans. But the moral evolution that Nijhuis recounts in *Beloved Beasts* is part of our legacy as well—one worth documenting and worth celebrating. ■

10.1126/science.abg4886

The reviewer is the author of *The Lost Species: Great Expeditions in the Collections of Natural History Museums* (University of Chicago Press, 2017).
Email: cjkemp@gmail.com

ECOLOGY

A planet remade in our image

As Anthropocene impacts accumulate, a sometimes-unrecognizable Earth emerges

By **Mary Ellen Hannibal**

The essays in *Second Nature* can be sorted into roughly two categories: powerful investigative pieces, and stories that intersect with author Nathaniel Rich's philosophical musings and consider the boundaries between human-made and nature-made. The latter of these is a categorical quagmire, because humans are inherently inseparable from nature, but, as Rich notes, there are arenas in which we are exceeding prior limits.

Readers learn about so-called "de-extinction" efforts, which seek to bring back the woolly mammoth, among other species. Rich focuses mostly on efforts to bring back the passenger pigeon, flocks of which were once so dense that they blackened skies on the East Coast of the United States. This work is supported by a nongovernmental organization led by entrepreneur Ryan Phelan and her husband, writer Stewart Brand—Brand's conservation bona fides can be traced back to his counterculture publication, the *Whole Earth Catalog* (1968–1998). The time frame for this project is years and perhaps decades, but the organization's efforts are already yielding results in other species (*1*).

Rich ventures into the kitchen, where adventurous chefs are making meals out of molecules, and then on to the exclusive enclave of Aspen, Colorado, where wealthy fossil fuel guzzlers attend high-priced "ideas festivals" to discuss ambitious carbon-reducing efforts for the world. In nearby Gothic, Colorado, he meets Billy Barr, a citizen-scientist exemplar, who has painstakingly documented the disappearance of the region's snow for more than 40 years.

In an investigative piece called "Dark Waters," a farmer in West Virginia enlists the help of a corporate attorney to uncover what is poisoning his cows and his water. The ensuing saga stretches over decades and revolves around the production of perfluorooctanoic acid (PFOA) used to make Teflon. The Environmental Protection Agency eventually reached a $16.5 million settlement with Teflon producer DuPont in 2017, but as Rich dryly observes, despite being the largest civil administrative penalty ever obtained by the agency, "The fine represented less than two percent of the profits earned by DuPont on PFOA that year." Today, he notes, thousands of PFOA knockoffs pervade everyday products, from computer cables to implantable medical devices.

Billy Barr has traced the disappearance of Colorado's snow for decades.

In "Here Come the Warm Jets," an otherwise beautiful Southern California landscape is invisibly marred by suffocating fumes emanating from a gas well in Aliso Canyon. Local Porter Ranch residents seal their windows and doors, but many continue to experience troubling symptoms, including severe headaches, problems with balance, and shortness of breath. The natural gas provider impedes efforts to investigate the potential leak, which eventually results in the release of 109,000 metric tons of methane into the atmosphere.

"Engineering is clearly the dominant idea of the industrial age," wrote conservation icon Aldo Leopold in 1938. He wondered whether ecology might contend with the human proclivity for building things and help characterize "a new order." The unsteady tension between nature's mechanisms of growth and humanity's command and control of these processes is expressed in reporting on an unruly panoply of plants and animals that quickly recolonize a neighborhood razed by Hurricane Katrina.

In the three-part centerpiece of the book, entitled "Bayou Bonjour," Rich recounts the geomorphological relationship of the Mississippi River and the spit of land that it simultaneously creates and erases. Southern Louisiana's racial and social history are intertwined with dubious decisions about how to grapple with the oil and gas industry, which takes as much as, if not more than, it gives to the region. Rich reports on herculean engineering plans to bulwark coastal wetlands despite the scientific consensus that the Gulf of Mexico will inevitably wash over the lower third of the state.

The essays in *Second Nature* reveal important truths that gather power when they are read together. In ranging across so many fields, Rich makes implicit connections between the way we treat nature and the way we treat each other. Although shortsighted geoengineering and corporate malfeasance ultimately affect everyone, not all of us are currently bearing the consequences equally. "Ecological degradation, by exacerbating the inequalities that poison our society, degrades democracy itself," cautions Rich. ■

Second Nature: Scenes from a World Remade
Nathaniel Rich
Farrar, Straus and Giroux, 2021. 304 pp.

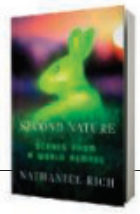

The reviewer is the author of *Citizen Scientist: Searching for Heroes and Hope in an Age of Extinction* (The Experiment, 2016). Email: maryellenhannibal@gmail.com

REFERENCES AND NOTES

1. S. Imbler, "Meet Elizabeth Ann, the first cloned black-footed ferret," *New York Times*, 18 February 2021; www.nytimes.com/2021/02/18/science/black-footed-ferret-clone.html.

10.1126/science.abg6862

PHOTO: HELEN H. RICHARDSON/*THE DENVER POST*/GETTY IMAGES

LETTERS

PHOTO: DIEGO MÉNDEZ

Edited by **Jennifer Sills**

Vulnerable Andean condors in steep decline

Despite being an iconic species and the national bird of Bolivia, Chile, Colombia, and Ecuador, the Andean condor (*Vultur gryphus*) is moving fast toward extinction. Its world population, which probably does not exceed 6700 individuals (*1*, *2*), is worryingly declining throughout its range, particularly due to massive poisoning events (*1*) to which the species is especially prone because of its highly gregarious behavior at carcasses (*3*). In 2018, 34 individuals in western Argentina died after consuming a deliberately poisoned carcass placed to eliminate mammals perceived as livestock predators (*4*). On 6 February, another 34 condors died in southern Bolivia, in similar conditions (*5*). Because of events like these, the Andean condor was recently uplisted to a designation of globally Vulnerable (*1*).

Poisoning is the most grievous threat to the Andean condor, with incidents reported across the Andes (*1*, *6*), but the species faces other challenges as well. Condors have fallen victim to lead intoxication, illegal capture, and shooting (*6*). They compete with other scavenger birds (*7*) and with feral and free-roaming domestic dogs for carrion resources (*5*). Complicating conservation efforts, these hazards vary regionally in nature and intensity (*6*).

To address the roots of the complex threats faced by Andean condors, the conservation response must leverage international and multi-sectoral collaboration. Those working toward protecting the species must base all actions on scientific evidence and assess each step taken to evaluate its effectiveness. Only with coordinated efforts at local, national, and international levels can we halt the Andean condor's decline (*2*).

Diego Méndez[1,2,3]*, Pedro P. Olea[1,4], José Hernán Sarasola[5,6], Félix Hernán Vargas[3], Vanesa Astore[7,8], Víctor Escobar-Gimpel[9,10], Rayen Estrada-Pacheco[7,11], Sandra Gordillo[12], N. Luis Jácome[7], Sebastián Kohn-Andrade[13,14], Alejandro Kusch[10,15], Adrián Naveda-Rodríguez[16], Fabricio Narváez[13,14], María Alejandra Parrado-Vargas[3,17,18], Renzo P. Piana[19], Juan Sebastian Restrepo-Cardona[20], Robert B. Wallace[21]

[1]Departamento de Ecología, Universidad Autónoma de Madrid, Madrid, Spain. [2]Museo Nacional de Historia Natural, La Paz, Bolivia. [3]The Peregrine Fund, Boise, ID 83709, USA. [4]Centro de Investigación en Biodiversidad y Cambio Global, Universidad Autónoma de Madrid, Madrid, Spain. [5]Centro para el Estudio y Conservación de las Aves Rapaces en Argentina, Universidad Nacional de La Pampa, Santa Rosa, La Pampa, Argentina. [6]Instituto de las Ciencias de la Tierra y Ambientales de La Pampa– Consejo Nacional de Investigaciones Científicas y Técnicas (CONICET), Santa Rosa, La Pampa, Argentina. [7]Fundación Bioandina Argentina, Ciudad Autónoma de Buenos Aires, Argentina. [8]Ecoparque de la Ciudad de Buenos Aires, Ciudad Autónoma de Buenos Aires, Argentina. [9]Corporación Amigos del Cóndor– Chile, Santiago, Chile. [10]Grupo de Investigación y Estudio del Cóndor en Chile, Santiago, Chile. [11]Centro de Investigación Científica y de Transferencia Tecnológica a la Producción, Universidad Autónoma de Entre Ríos, Provincia de Entre Ríos (CONICET), Diamante, Entre Ríos, Argentina. [12]Instituto de Antropología de Córdoba– CONICET, Universidad Nacional de Córdoba, Córdoba, Argentina. [13]Fundación Cóndor Andino, Quito, Ecuador. [14]Grupo Nacional de Trabajo del Cóndor Andino, Quito, Ecuador. [15]Far South Expeditions, Punta Arenas, Chile. [16]Department of Wildlife, Fisheries and Aquaculture, Mississippi State University, Mississippi State, MS 39762, USA. [17]Fundación Neotropical, Bucaramanga, Santander, Colombia. [18]Universidad Industrial de Santander, Laboratorio de Conservación, Santander, Colombia. [19]Centro de Ornitología & Biodiversidad, Lima, Perú. [20]Programa de Maestría en Conservación y Uso de Biodiversidad, Pontificia Universidad Javeriana, Bogotá, Colombia. [21]Wildlife Conservation Society, Andes-Amazon-Orinoquia Region, La Paz, Bolivia.
*Corresponding author.
Email: diemndez@gmail.com

The Andean condor (*Vultur gryphus*) faces an array of threats throughout its range.

REFERENCES AND NOTES

1. The IUCN Red List of Threatened Species, "Andean Condor: *Vultur gryphus*" (2020); www.iucnredlist.org/species/22697641/181325230.
2. R. Wallace *et al.*, *Saving the Symbol of the Andes: A Range Wide Conservation Priority Setting Exercise for the Andean Condor* (Vultur gryphus) (Wildlife Conservation Society, La Paz, Bolivia, 2020); https://bolivia.wcs.org/Portals/14/Libro%20Condor_ingles.pdf.
3. D. Méndez, P. P. Olea, J. H. Sarasola, F. H. Vargas, *J. Raptor Res.* **55**, 10.3356/JRR-20-26 (2021).
4. P. A. E. Alarcón, S. A. Lambertucci, *Science* **360**, 612 (2018).
5. Y. Sierra Praeli, "Amenaza latente: 34 cóndores mueren envenenados en Bolivia" (2021); https://es.mongabay.com/2021/02/condor-andino-envenenamiento-bolivia/ [in Spanish].
6. P. I. Plaza, S. A. Lambertucci, *Biol. Conserv.* **251**, 108782 (2020).
7. F. Sáenz-Jiménez, O. Rojas-Soto, J. Pérez-Torres, J. Shepard, *Bird Conserv. Int.* 10.1017/S0959270920000271 (2020).

10.1126/science.abh3358

Banned pesticide still poisoning EU raptors

Carbofuran is a highly toxic carbamate pesticide used in agriculture for pest control (*1*). The European Union banned its use in 2008 (*2*). However, because the pesticide is still available in countries outside the European Union, it continues to threaten vulnerable species. The European Union should work with neighboring countries to enact consistent policies that limit the use of toxic pesticides such as carbofuran.

Despite the EU ban, acute cases of carbofuran poisoning have recently been

reported in Hungary and in Poland. The victims were raptors with high conservation priority such as the eastern imperial eagle (*Aquila heliaca*) and the white-tailed eagle (*Haliaeetus albicilla*) (*3*–*5*). The raptor species were poisoned when they fed on predators that had been illegally exterminated by farmers, such as the red fox (*Vulpes vulpes*) (*4*). The illegal carbofuran was likely smuggled from nearby countries where it has not been banned, such as Ukraine, Moldova, and Turkey (*6*).

To protect these species, Eastern European countries should collaborate and implement regional strategies that address the use and transport of hazardous pesticides. All of these countries should improve their detection and reporting of raptor poisoning cases, as the scale of this problem may be underestimated (*3*). National governments should also intensify educational activities to raise public awareness about the environmental hazards of banned pesticides (*4*).

Ignacy Kitowski[1], Rafał Łopucki[2]*, Anna Stachniuk[3], Emilia Fornal[3]
[1]State School of Higher Education in Chełm, 22-100 Chełm, Poland. [2]The John Paul II Catholic University of Lublin, 20-708 Lublin, Poland. [3]Medical University of Lublin, 20-090 Lublin, Poland.
*Corresponding author. Email: lopucki@kul.pl

REFERENCES AND NOTES

1. P. Otieno *et al.*, *Bull. Environ. Contam. Toxicol.* **84**, 536 (2010).
2. Commission of the European Communities, "2007/416/EC: Commission Decision of 13 June 2007 concerning the non-inclusion of carbofuran in Annex I to Council Directive 91/414/EEC and the withdrawal of authorisations for plant protection products containing that substance" (2007); https://eur-lex.europa.eu/legal-content/GA/TXT/?uri=CELEX%3A32007D0416.
3. G. Deak *et al.*, *J. Vertebr. Biol.* **69**, 20110 (2021).
4. I. Kitowski *et al.*, *Environ. Conserv.* **47**, 310 (2020).
5. Anonymous, "The eagle could not be saved" (2021): www.lublin112.pl/bielika-nie-udalo-sie-uratowac-wszystko-wskazuje-na-to-ze-ptak-zostal-otruty/ [in Polish].
6. UN Environment Programme and GRID-Arendal, "The Illegal trade in chemicals" (2020).

10.1126/science.abh0840

The rise and fall of the "warrior gene" defense

Since a 1993 study suggested that a single gene might predispose an individual to violence (*1*), criminal defendants have argued that their genes made them commit the crime. Through genome-wide association studies, we now understand that thousands of gene variants each contribute a very small amount to behavioral variation between individuals, and the idea that a single gene could cause violent behavior has been rejected. In February, the so-called "warrior gene" theory as a criminal defense was dealt a blow by the New Mexico Supreme Court in the case of *State* v. *Yepez* (*2*), but the ruling did not go far enough. By failing to address the current scientific consensus, the court missed an opportunity to create the much-needed persuasive authority for other courts on this issue. We must improve communication between scientists and the legal system to ensure that courts can access and understand the most current science.

The defendant in the recent court case, Anthony Blas Yepez, sought to introduce expert testimony that he had a genetic predisposition to violence that prevented him from being able to form the intent necessary to commit second-degree murder. The trial court excluded the testimony—which linked Yepez's "warrior gene" and childhood maltreatment to his ability to form the intent to kill—as scientifically unproven. On appeal, the appellate court upheld his conviction but found that the trial court had acted wrongly in excluding the testimony (*3*). The New Mexico Supreme Court disagreed. It found that the trial court acted reasonably in excluding the testimony as scientifically unfounded.

The New Mexico Supreme Court reached the right conclusion but used the wrong analysis. Their opinion ignored the scientific consensus, reached by 2011 and articulated in 2019 (*4*), which rejects a candidate-gene approach that identifies single genes responsible for variations in human behavior. The court wrongly endorsed the trial court's conclusion that findings from research like the original 1993 study had achieved "general acceptance…in the relevant scientific communities" (*2*). The court's mistake sets a dangerous legal precedent and threatens justice itself.

The genetic predisposition defense has been used in other cases with starkly diverging results (*5*). Some defendants have been convicted on lesser charges, whereas others have been punished more harshly on the mistaken belief that the defendant was programmed to kill [e.g., (*6*)]. This case could have set the record straight and established a precedent on which other courts could rely. We need better engagement between scientists, lawyers, and judges to help our legal institutions move beyond outdated science that wrongly labels defendants as genetically programmed to offend.

Nita A. Farahany[1,2]* and Gene E. Robinson[3,4]
[1]Duke Law School, Durham, NC 27708, USA. [2]Duke Initiative for Science & Society, Durham, NC 27708, USA. [3]Carl R. Woese Institute for Genomic Biology, Urbana, IL 61801, USA. [4]College of Liberal Arts & Sciences, University of Illinois at Urbana-Champaign, Urbana, IL 61801, USA.
*Corresponding author. Email: farahany@duke.edu

REFERENCES AND NOTES

1. H. G. Brunner *et al.*, *Science* **262**, 578 (1993).
2. *State* v. *Yepez*, NO. S-1-SC-37216 C/W NO. S-1-SC-37217, 2021 WL 732668 (N.M. Supreme Court, 25 February 2021)
3. *State* v. *Yepez*, 428 P.3d 301 (Ct. App. New Mexico, 24 July 2018)
4. National Institute of Mental Health, "Report of the National Advisory Mental Health Council Workgroup on Genomics: Opportunities and challenges of psychiatric genetics" (2019); www.nimh.nih.gov/about/advisory-boards-and-groups/namhc/reports/report-of-the-national-advisory-mental-health-council-workgroup-on-genomics.shtml.
5. W. Bernet *et al.*, *J. Foren. Sci.* **52**, 1362 (2007).
6. *Schriro* v. *Landrigan*, 550 US 465 (2007).

COMPETING INTERESTS

G.E.R. served on the National Advisory Mental Health Council Workgroup on Genomics.

10.1126/science.abh4479

TECHNICAL COMMENT ABSTRACTS

Comment on "Large-scale GWAS reveals insights into the genetic architecture of same-sex sexual behavior"

Dean Hamer, Brian Mustanski, Randall Sell, Stephanie A. Sanders, Justin R. Garcia

The phenotypic measures used by Ganna *et al.* (Research Articles, 30 August 2019, p. 882) lump together predominantly heterosexual, bisexual, and homosexual individuals, including those who have experimented with a same-sex partner only once. This may have resulted in misleading associations to personality traits unrelated to understood categories of human sexuality. Scientific studies of human sexuality should use validated and reliable measures of sexual behaviors, attractions, and identities that capture the full spectrum of complexity.

Full text: dx.doi.org/10.1126/science.aba2941

Response to Comment on "Large-scale GWAS reveals insights into the genetic architecture of same-sex sexual behavior"

Andrea Ganna, Karin J. H. Verweij, Michel G. Nivard, Robert Maier, Robbee Wedow, Alexander S. Busch, Abdel Abdellaoui, Shengru Guo, J. Fah Sathirapongsasuti, 23andMe Research Team, Paul Lichtenstein, Sebastian Lundström, Niklas Långström, Adam Auton, Kathleen Mullan Harris, Gary W. Beecham, Eden R. Martin, Alan R. Sanders, John R. B. Perry, Benjamin M. Neale, Brendan P. Zietsch

Hamer *et al.* argue that the variable "ever versus never had a same-sex partner" does not capture the complexity of human sexuality. We agree and said so in our paper. But Hamer *et al.* neglect to mention that we also reported follow-up analyses showing substantial overlap of the genetic influences on our main variable and on more nuanced measures of sexual behavior, attraction, and identity.

Full text: dx.doi.org/10.1126/science.aba5693

AAAS ANNUAL MEETING

2021 AAAS Student E-poster Competition Winners

The AAAS Student E-poster Competition recognizes the individual efforts of students who are actively working toward an undergraduate, graduate or doctoral-level degree. The winners' presentations displayed originality and understanding that set them apart from their peers.

BIOCHEMISTRY AND MOLECULAR BIOLOGY

Graduate Student First Place: Christina Roman, University of Chicago, *Structures of Viral RNA Elements Solved with Chaperone Assisted RNA Crystallography*

Graduate Student Second Place: Anirudh Gaur, University of California, Davis, *Effects of Natural Genetic Variations in Incretin Receptors on Glucose Homeostasis*

Graduate Student Third Place: Collin Jugler, Arizona State University, *Plant-Made Immunotherapeutics; A Potential Treatment for Severe Covid-19*

Undergraduate First Place: Simon Ng, University of California, Los Angeles, *Engineering Carbonic Anhydrase for Spacecraft CO2 Removal Using Machine Learning*

Undergraduate Second Place: Kimberly Hane, Cedar Crest College, *qPCR and Microbe Identification for Forensic Blood Pattern Analysis*

Undergraduate Third Place: Zhela Sabir, Arizona State University, *Vitamin D Impacts Nrf-2 and Antioxidation Pathways that Modulate Cellular Aging*

BRAIN AND BEHAVIOR

Graduate Student First Place: Faheem Handoo, Indiana University School of Medicine, *Phenotyping Obstructive Sleep Apnea and Heart Failure*

Graduate Student Second Place: Divyesh Doddapaneni, FAU College of Medicine, *Characterization of a Novel Inhibitory Cell Cluster within the Amygdala*

Undergraduate First Place: Joshua Martinez, University of California, Irvine, *In Vivo Imaging of 2-AG Induced Xenopus Laevis Retinal Ganglion Cell Development*

Undergraduate Second Place: Rosa Serrano, University of California, Irvine, *Focal Deletion of BAF53b in the Adult Brain is Sufficient to Impair Long Term Memory*

Undergraduate Third Place: Marina Edward, University of California, Irvine, *Upregulated 2-AG and AEA Affect Synaptic Plasticity In Xenopus Laevis Visual Circuit*

CELL BIOLOGY

Graduate Student First Place: DeQuantarius Speed, University of Chicago, *The Role and Regulation of Plastid Targeting of the Systemic Defense Signal AZI1*

Graduate Student Second Place: Austin E.Y.T. Lefebvre, University of California, Irvine, *Tracking Mitochondria Reveals Metabolic and Dynamic Heterogeneity in Breast Cancers*

Graduate Student Third Place: Aya Hanzawa, Iwate University, *Actin Isovariant ACT8 Regulates the Cold Response in Arabidopsis Root*

Undergraduate First Place: Nafis Eghrari, Arizona State University, *Ozanimod Preserves Contractile Human Brain VSM Phenotype Against Ischemic Insult*

Undergraduate Second Place: Casadora Boone, University of California, Irvine, *Multidrug Resistance Conjugative Plasmid in an Environmental Escherichia Coli*

Undergraduate Third Place: Christian Checkcinco, University of California, Irvine, *Assessment of Possible Metabolic Disrupting Compounds through Optimized Protocol*

DEVELOPMENTAL BIOLOGY GENETICS AND IMMUNOLOGY

Graduate Student First Place: Luz Milbeth Cumba Garcia, Mayo Clinic Graduate School of Biomedical Sciences, *Identifying Glioblastoma or Monocytic Cells Extracellular Vesicles via Flow Cytometry*

Graduate Student Second Place: Kenji Sugita, Iwate University, *RIC2 and RIC4 Act Redundantly to Regulate the Actin Mediated Developmental Process*

Graduate Student Third Place: Amanda Wacker, University of California, San Diego, *Uncovering Patterns of Methylation in Microbial Astronauts*

Undergraduate First Place: Lucy Moore, Saint Mary's College of California, *Differentiation of Human and Rat Stem Cells to Neuroglial Support Cells*

Undergraduate Second Place: Angelique Cortez, University of California, Irvine, *Studying the Chromatin States in Alzheimer's Disease Derived Microglia*

Undergraduate Third Place: Rachell Quarles, Morgan State University, *Potential Genetic Biomarkers Located in Preeclampsia Patients*

ENVIRONMENT AND ECOLOGY

Graduate Student First Place: Wenjuan Liu, Arizona State University, *Li Mining-Community-Aquifer Interactions in Salar De Atacama: An Agent-Based Model*

Graduate Student Second Place: Kimberly Colgan, University of Minnesota, *Mitigating Food System Emissions Could Impede Achieving Sustainable Development Goals*

Graduate Student Third Place: Lyydia Leino, University of Turku, *Potential Effect of The*

aaas.org/2021-eposter-sessions

AAAS

ANNUAL MEETING

Herbicide Glyphosate on the Human Gut Microbiome

Undergraduate First Place: Clarisa Martinez, University of California, Irvine, *Beta-Lactam Resistance in an Avian Escherichia Coli from California*

Undergraduate Second Place: Michael Marvin, Arizona State University, *Effectiveness of Foredune Restoration in High-Energy Coastal Environments*

Undergraduate Third Place: Joanne Villagrana, University of California, Irvine, *First U.S. Report of Escherichia Coli St1193 Collected from an Aquatic Environment*

MEDICINE AND PUBLIC HEALTH

Graduate Student First Place: Emily Kaelin, Arizona State University, *Convergence of The Preterm Infant Gut Virome Prior to Necrotizing Enterocolitis*

Graduate Student Second Place: Kazune Pax, Ohio State University, *Infant Oral Microbiome Influenced by Maternal Habits*

Graduate Student Third Place: Michelle Scott, Ohio State University, *E-Cigarettes Differentially Alter Microbial Metabolism and Colonization Dynamics*

Undergraduate First Place: Marize Rizkalla, University of California, Irvine, *Multidrug Resistant and Virulent Environmental Escherichia Coli St38*

Undergraduate Second Place: Sydney Skeie, Capital University, *Reliability of "Gluten-Free" Labels Found on Food Products in the United States*

PHYSICAL SCIENCES

Graduate Student First Place: Ekaterina Selivanovitch, Indiana University, *Molecular Exclusion Limits for Diffusion Across a Porous Capsid*

Graduate Student Second Place: Sindhu Nathan, Stanford University, *Bridging Electro- and Thermal Catalysis by Converting CO2 with Carbon-Based Materials*

Graduate Student Third Place: Jacob Garcia, Arizona State University, *Femtosecond Pump-Probe Spectroscopy of Neutral Transition Metal Oxide Clusters*

Undergraduate First Place: Dolapo Nurudeen, Morgan State University, *The Synthesis of FAC-(CO)3 (A-Diimine)ReOC(O) O(CH2)4CH3 Compound*

Undergraduate Second Place: Avram Bar-Meir, Northwestern University, *Novel Approaches for In Situ Analysis in the Search for Extraterrestrial Life*

SCIENCE AND SOCIETY

Graduate Student First Place: Dina Ziganshina, Arizona State University, *Why Does Russia Have a Higher Abortion Rate Than Other Post-Soviet Countries?*

Graduate Student Second Place: Amie Sommers, University of Nebraska, Lincoln, *Salient Experiences in Undergraduate Development Via Chickering's Vector Framework*

Graduate Student Third Place: Alex Hsain, North Carolina State University, *Paid Parental Leave to Strengthen the STEM Workforce*

Undergraduate First Place: Julie Roberts, Arizona State University, *Perceptions of Evolution Among Muslim Undergraduate Biology Students in the USA*

Undergraduate Second Place: Arya Natarajan, University of California, San Diego, *The Symbiologist: Examining the Power of Storytelling in Science Communication*

Undergraduate Third Place: Estefania Arellano, Arizona State University, *Get Excited!: Using Anime to Rethink Adolescent Science Education*

SOCIAL SCIENCES

Graduate Student First Place: Erika Nadile, Arizona State University, *Call On Me! Science Undergraduates' Perceptions of Voluntarily Asking Questions*

Graduate Student Second Place: Jacy Anthis, University of Chicago, *Emergent Trends in Public Opinion on Animal Farming and Animal Product Alternatives*

Graduate Student Third Place: Emily Santora, Arizona State University, *The Impact of Menstrual Education on the Treatment of Gynecological Conditions*

Undergraduate First Place: Kenna McRae, Arizona State University, *Cultural Health Navigator Strategies to Guide Refugee Patients through Covid-19*

Undergraduate Second Place: Puja Chhetri, Arizona State University, *The Effect of Variation in Features Of Exam Questions from Biology Instructors*

Undergraduate Third Place: Alyssa Hart, Arizona State University, *Arizona University Student Perceptions to Covid-19 and the Campus' Measures Taken*

TECHNOLOGY, ENGINEERING AND MATH

Graduate Student First Place: Jessica LaLonde, Duke University, *A Machine Learning Approach to Investigate Degradation of Poly(Hydroxyalkanoates)*

Graduate Student Second Place: Jenna Ott, Princeton University, *To Biofilm or Not to Biofilm: A Competition Between Accumulation and Dispersa*

Graduate Student Third Place: Rongjiao Ji, University of Milan, *Meet My Avatar*

Undergraduate First Place: Ada Kanapskyte, Ohio State University, *Biolead: Biological Exploration Via Autonomous Detection Using Dielectric Spectroscopy*

Undergraduate Second Place: Myka Terry, Morgan State University, *Rainbow Cells: Tracking Trends in Cell Division Using Motzkin Paths*

Undergraduate Third Place: Francisco Brenes, University of California, Irvine, *Relational Database for the Analysis of Quantified Cardiac Muscle Tissue Stud*

aaas.org/2021-eposter-sessions

AAAS
ANNUAL MEETING

We appreciate the time and commitment from the judges and reviewers of the 2021 AAAS E-posters

STUDENT E-POSTER COMPETITION JUDGES

Allison Truhlar, U.S. Department of Energy

Amy Gilson, California State Senate Committee on Transportation

Beverly Lindsay, University of California

Björn Johansson, Chalmers University of Technology

Cecily Steppe, USNA Oceanography Department

Chenyu Li, Paragon Genomics

Deborah Stine, Science, Technology, and Innovation Policy Analysis & Education, LLC

Dominic Benford, NASA

Kenneth Michael Beck, Scientists for Future

Edgar Meyer, University of Arkansas for Medical Sciences

Edward Van Opstal, American Association for the Advancement of Science

Elizabeth Day, Michigan State University

Erdogan Memili, Department of Animal and Dairy Sciences, Mississippi State University

Eve Granatosky, Lewis-Burke Associates LLC

Felix Acheampong, Pharmaceutical Product Development Inc

Ildoo Kim, Konkuk University

Jacquelyn Cragg, Univeristy of British Columbia

Jaswinder Sharma, Oak Ridge National Laboratory

Jennifer Rubin, Rochester Community and Technical College

K. Joy Karnas, Cedar Crest College

Kaelin Cawley, National Ecological Observatory Network, operated by Battelle

Kathryn Meier, Washington State University

Kimberly DiGiovanni, Quinnipiac University

Laurie Stepanek, American University

Luiz Galvao, FIOCRUZ

Marjan Assefi, UNCG

Mark Seielstad, UCSF

Mary Ann Ottinger, University of Houston

Miriam Bocarsly, National Institute on Alcohol Abuse and Alcoholism/NIH

Mohammad Russel, Dalian University of Technology

Niveen AbiGhannam, American University of Beirut

NseAbasi Etim, Akwa Ibom State University

Nsikak-Abasi Etim, University of Uyo

Paul Dent, Virginia Commonwealth University

Pooja Sharma, The Catholic University of America

Prajwal MohanMurthy, University of Chicago

Pushpanathan Muthuirulan, Harvard University

Rafael J Veraza, Vascular Perfusion Solutions, Inc.

Rajamani Selvam, FDA

Sarala Padi, NIST

Stavana Strutz, Intergovernmental Panel on Climate Change / University of Texas at Austin

Stephanie Deppe

Swati Agrawal, University of Mary Washington

Zoe Pettway Unno, NNLM Pacific Southwest Regional Medical Library

The AAAS team appreciates the help of reviewers, who evaluated scientific sessions of the 2021 Annual Meeting.

Full list of reviewers can be seen here:

meetings.aaas.org/2021-reviewers

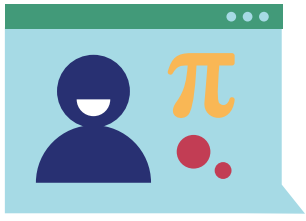

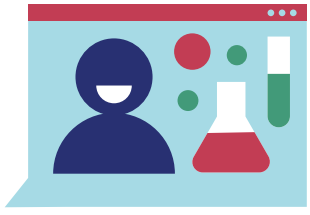

CONNECT WITH US:

aaas.org/meetings | #AAASmtg

aaas.org/2021-eposter-sessions

EMPOWER WITH EVIDENCE

AAAS | ANNUAL MEETING

SUBMIT A SCIENTIFIC SESSION OR WORKSHOP PROPOSAL FOR THE 2022 AAAS ANNUAL MEETING!

Theme of the 2022 AAAS Annual Meeting—Empower With Evidence—focuses on science literacy, evidence-based decision making, and the use of validated knowledge to drive public policy for the benefit of all.

CONNECT WITH US:

aaas.org/meetings | #AAASmtg

AAAS NEWS & NOTES

Scientific excellence and diversity at Annual Meeting

Showcasing diverse speakers requires a deliberate commitment to inclusion from decision-makers

By **Andrea Korte**

When members of the scientific community gathered at the AAAS Annual Meeting in February, they did so in front of laptops and tablets from their home offices and dining tables. They presented over Zoom, submitted questions via chat, and caught up with colleagues over social media. The 2021 AAAS Annual Meeting was unlike any other in the meeting's 187-year history, but the fully virtual setting did not dampen enthusiasm for sharing science in keeping with the "Understanding Diverse Ecosystems" meeting theme.

Dozens of scientific sessions shared new research in areas ranging from microbiomes to space travel. More than 40 workshops offered attendees the opportunity to discuss strategies for working in the ecosystems of academia and science policy. Plenary and topical lecturers covered timely topics, including Ruha Benjamin on how technology can deepen inequities, Anthony Fauci on the next steps for COVID-19 response, Mary Gray on research ethics, and Yalidy Matos on immigration policies.

"The quality of the speakers was absolutely undeniable, and the diversity of the speakers—across gender, race, region—was just extraordinary," said Sudip Parikh, chief executive officer of AAAS and executive publisher of the *Science* family of journals. "That is what our vision of the world looks like in a place where science is done with creativity and innovation and excellence."

Selecting a diverse meeting program is grounded in AAAS's values, but it is not without concerted effort, according to Claire Fraser. Fraser, who served as AAAS president through February and now serves as chair of the AAAS Board of Directors, selected the meeting theme and led the AAAS Meeting Scientific Program Committee, which oversees selection of the meeting's speakers.

"The diversity doesn't happen by accident. I think it reflects the very strong commitment on the part of the Scientific Program Committee to make sure that not only is the science presented timely and excellent, but the diversity of speakers and participants is as broad as it possibly can be," said Fraser, director of the Institute for Genome Sciences at the University of Maryland School of Medicine.

Diversity isn't an afterthought—it's a deliberate part of the very first review of potential scientific sessions, according to Andrew Black, chief of staff and chief public affairs officer. When hundreds of volunteer reviewers evaluate the quality of the submissions before sending the best for consideration by the Scientific Program Committee, they are also looking for diversity across many dimensions, Black said. Among those dimensions are diversity of scientific discipline—befitting AAAS's multidisciplinary membership—but also gender, race and ethnicity, geographic diversity, career stage, and type of institution, including all types and sizes of universities, industry, and government.

"Who do you see, who do you hear, and what kind of voices are in dialogue with each other? That's part of our assessment process," said Agustín Fuentes, professor of anthropology at Princeton University and a member of the Scientific Program Committee.

The review process offers opportunities for applicants to diversify their sessions. Applicants are often encouraged to look beyond their own networks to add a range of voices to their presentation to best communicate their ideas to the broader scientific community, Fuentes said.

"We need to think very carefully in this moment in time about how do we not only redress past biases and discriminatory practices but how do we create a space, a voice, and a suite of presenters that is very inviting to a diverse audience," Fuentes said.

Added Fraser, "What you end up with is even better because you have such broad perspectives represented."

The committee also emphasized the importance of ensuring that a diverse group of decision-makers have a seat at the table. Members of the Scientific Program Committee, who are nominated from across AAAS and its 26 disciplinary sections and approved by the AAAS Board, represent a broad range of groups and perspectives, Fraser said.

PHOTOS: AAAS

"What I firmly believe is that you can't come up with a diverse program like we had this year and like we've had in previous years without that diversity in the program committee," Fraser said.

Commitment to diversity across many axes is part of AAAS Annual Meeting history. In the 1950s, AAAS refused to hold meetings in the segregated South. In 1976, under one of AAAS's first female presidents, Margaret Mead, the Annual Meeting was fully accessible to people with disabilities for the first time. According to the AAAS Project on Science, Technology, and Disability, wheelchair ramps were added to the conference hall, programs were made accessible for hearing-impaired and visually impaired attendees, and Mead's presidential address was simultaneously interpreted in sign language. In 1978, AAAS's Board of Directors voted to move the following year's Annual Meeting out of Chicago because Illinois had not ratified the Equal Rights Amendment. In 1993, AAAS moved its 1999 meeting from Denver after Colorado voters adopted a constitutional amendment to deny residents protection from discrimination based on sexual orientation.

Leaders at AAAS note that there is always more work to be done in the present and future—both at the Annual Meeting and year-round. AAAS continues to focus on its own systemic transformation in areas of diversity, equity, and inclusion and on the breadth of initiatives in its new Inclusive STEM Ecosystems for Equity & Diversity program, all to ensure that the scientific enterprise reflects the full range of talent.

That goal resonated with many 2021 AAAS Annual Meeting speakers, too.

A more diverse group of scientists creating artificial intelligence systems can improve those systems, said Ayanna Howard, a roboticist who leads The Ohio State University's College of Engineering, during her topical lecture, "Demystifying AI Through the Lens of Fairness and Bias."

Said Howard, "We as people are diverse and we're different and it makes us unique and beautiful, and our AI systems should be designed in such a way."

Nalini Nadkarni, a University of Utah biologist who delivered a topical lecture on "Forests, the Earth, and Ourselves: Understanding Dynamic Systems Through an Interdisciplinary Lens," shared how she reaches young girls to let them know that science—and her own scientific specialty—is a space where they can thrive. She and her students created and distributed "Treetop Barbie," dressing a doll in fieldwork clothes and creating a doll-sized booklet about canopy plants.

The Annual Meeting offers a chance to show that science is best when it is for everyone, regardless of background or perspective, whether they're a kid or just a kid at heart.

Said Parikh, "The AAAS Annual Meeting is where the pages of *Science* literally come alive. It's a place where scientists, no matter what discipline or industry they decided to pursue, can pull back and just fall in love with the idea of science again—like we did when we were kids."

Becky Ham contributed to this article.

2020 election results

The AAAS 2020 elections for President-Elect, members of the Board of Directors, and the Committee on Nominations were held from 8 February to 22 February 2021. The following elected candidates began their terms on 24 February 2021.

General Election
President-Elect: Gilda A. Barabino, *Olin College of Engineering*

Board of Directors
Kaye Husbands Fealing, *Georgia Institute of Technology;* Janine Austin Clayton, *U.S. National Institutes of Health*

RESEARCH

IN *SCIENCE* JOURNALS

Edited by **Michael Funk**

Cave deposits collected in northern Greenland provide a record of climate in the Arctic ~560,000 years ago.

PHOTO: ROBBIE SHONE

CLIMATOLOGY

Arctic response to a warming world

Regional studies of paleoclimate provide important insights into how different parts of the Earth system respond to global climate change. Geochemical data gathered for cave deposits from northeast Greenland have now provided the first paleoclimate record for the High Arctic during an interglacial warming event extending from 588 to 549 thousand years ago. Moseley *et al.* show that the High Arctic at that time was at least 3.5°C warmer than today during that interval, with extensive permafrost thaw and markedly increased precipitation. Comparisons with datasets for that interval from elsewhere in the world suggest that the Arctic regions were affected more substantially during this warming event, and the same can be anticipated as anthropogenic global warming continues into the future. —KVH

Sci. Adv. 10.1126/sciadv.abe1260 (2021).

PALEOCEANOGRAPHY

Carbon cycle history

Marine carbon includes organic and inorganic components, both of which must be accounted for to understand the global carbon cycle. Paytan *et al*. assembled a record of stable strontium isotopes (^{88}Sr and ^{86}Sr) derived from pelagic marine barite and used it to reconstruct changes in the deposition and burial of biogenic calcium carbonate in marine sediments. These data, when combined with measurements of $^{87}Sr/^{86}Sr$, can help to reveal past changes in the sources and sinks of strontium, as well as variations in carbonate deposition that affect the carbon cycle. —HJS

Science, this issue p. 1346

PLANT SCIENCE

Cell cycle regulation

The hormone cytokinin regulates various aspects of plant development and physiology, largely by managing cell proliferation. Yang *et al*. show that cytokinin promotes nuclear localization of the transcription factor MYB3R4, which activates the expression of two importins and genes that tip the cell into the next phase of the cell cycle. The importins facilitate further MYB3R4 accumulation within the nucleus, accelerating the progression into mitosis. MYB3R4 and the importins dissipate when the nuclear membrane dissolves at prometaphase, so there is only one round of mitotic activation per cell cycle. —PJH

Science, this issue p. 1350

CANCER

The STAR of the show

Chimeric antigen receptor T (CAR-T) cells have revolutionized treatment for hematological cancers, but this success has not translated to solid tumors. To address this challenge, Liu *et al.* engineered a synthetic T cell receptor and antigen receptor (STAR) that combines the specificity of a CAR and the internal signaling machinery of an endogenous T cell receptor. STAR-T cells outperformed their CAR-T cell counterparts in controlling multiple murine tumors and did not display evidence of the exhaustion frequently observed in CAR-T cells. These results suggest that STAR-T cells may be an attractive option for treating patients with solid tumors. —CSM

Sci. Transl. Med. **13**, eabb5191 (2021).

CORONAVIRUS

Targeting the SARS-CoV-2 main protease

Vaccines are an important tool in the fight against COVID-19, but developing antiviral drugs

is also a high priority, especially with the rise of variants that may partially evade vaccines. The viral protein main protease is required for cleaving precursor polyproteins into functional viral proteins. This essential function makes it a key drug target. Qiao *et al*. designed 32 inhibitors based on either boceprevir or telaprevir, both of which are protease inhibitors approved to treat hepatitis C virus. Six compounds protected cells from viral infection with high potency, and two of these were selected for in vivo studies based on pharmokinetic experiments. Both showed strong antiviral activity in a mouse model. —VV

Science, this issue p. 1374

SPECTROSCOPY

Mapping nanostructure surface excitations

Atomic vibrations (phonons) govern many physical properties of materials, especially those related to heat and thermal transport. They also provide fingerprints of the chemistry of a wide variety of materials, from solids to molecules. The behavior of phonons in nanostructures can be appreciably modified because of confinement effects. Li *et al*. combined several electron microscopy techniques to map out the phonon-polariton excitations across the surface of magnesium oxide nanostructures with high spatial, spectral, and angular resolution. The reconstruction of the surface excitation maps in three dimensions will be useful for understanding and optimizing the properties of the nanostructured materials for advanced functionality. —ISO

Science, this issue p. 1364

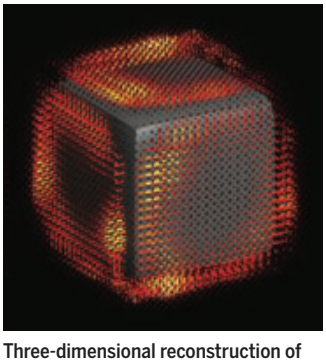

Three-dimensional reconstruction of electromagnetic local density of states in a magnesium oxide cube

CREDITS (LEFT TO RIGHT): LI *ET AL*.; LOSSADA *ET AL*., *ACS NANO* 10.1021/ACSNANO.0C10001 (2021)

QUANTUM CONTROL

Dynamic stabilization of an array

Large-scale systems comprising one-dimensional chains and two-dimensional arrays of excited atoms held in a programmable optical lattice are a powerful platform with which to simulate emergent phenomena. Bluvstein *et al*. built an array of up to 200 Rydberg atoms and subjected the system to periodic excitation. Under such driven excitation, they found that the array of atoms stabilized, freezing periodically into what looked like time crystals. Understanding and controlling the dynamic interactions in quantum many-body systems lies at the heart of contemporary condensed matter physics and the exotic phenomena that can occur. —ISO

Science, this issue p. 1355

SOLAR CELLS

Perovskite synthesis out in the open

Although methods have been developed that create the photoactive black perovskite phase of formamidinium lead iodide (α-$FAPbI_3$), these routes are temperature and humidity sensitive and less compatible with large-scale solar cell production. Hui *et al*. report an alternative route in which vertically aligned lead iodide thin films are grown from the ionic liquid methylamine formate. Nanoscale channels in the films lower the barrier to permeation of formamidinium iodide and enable transformation to α-$FAPbI_3$, even at high humidity and room temperature. Solar cells made with these films have power conversion efficiencies as high as 24.1% that display high stability. —PDS

Science, this issue p. 1359

IN OTHER JOURNALS

Edited by **Caroline Ash** *and* **Jesse Smith**

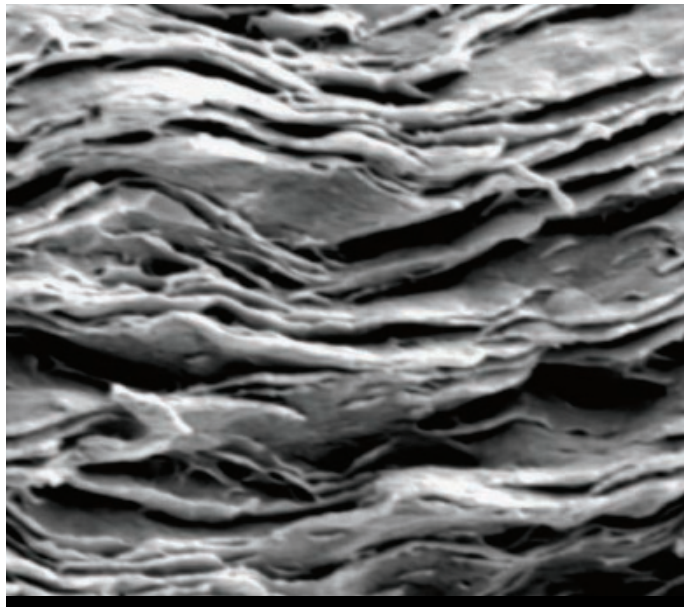

MATERIALS SCIENCE

Recyclable nacre-like composites

The brick-and-mortar structure of nacre combines stiffness and exceptional toughness far in excess of the properties of the constituent materials and has thus been used as an inspiration for making tough composites. Lossada *et al.* combined nanoclay (the bricks) with a methacrylate-methacrylamide vitrimer polymer and some catalyst (the mortar) in aqueous solution. Vitrimers contain chemical cross-links, but the structure can be modified at elevated temperatures through bond-shuffling mechanisms. Thus, the properties of the nanocomposite can be tuned and the material can even be recycled by grinding and hot-pressing. The addition of a small amount of reduced graphene oxide enabled localized heating of the nanocomposites using laser irradiation. —MSL *ACS Nano* 10.1021/acsnano.0c10001 (2021).

Scanning electron micrograph of a fractured cross-section of a nacre-mimetic nanocomposite

NEURODEGENERATION

It takes tau to tangle

In Alzheimer's disease and in other neurodegenerative diseases known as tauopathies, misfolded tau protein forms filamentous aggregates, known as tangles, in the brain. These tangles have often been considered end-stage features that will remain indefinitely within the brain once formed. Croft *et al.* studied the formation and potential clearance dynamics of tau inclusions in brain slices from tauopathy model mice. Initially, inclusions formed relatively rapidly, within a day or two, and turned over with a half-time of about a week. This turnover slowed down as the slices aged in culture. After 2 months in culture, deposited tau took ~3 weeks to turn over and its half-life had tripled. Thus, although they can be long-lived, tau inclusions may not necessarily be permanent. —SMH

Acta Neuropathol. **141**, 359 (2021).

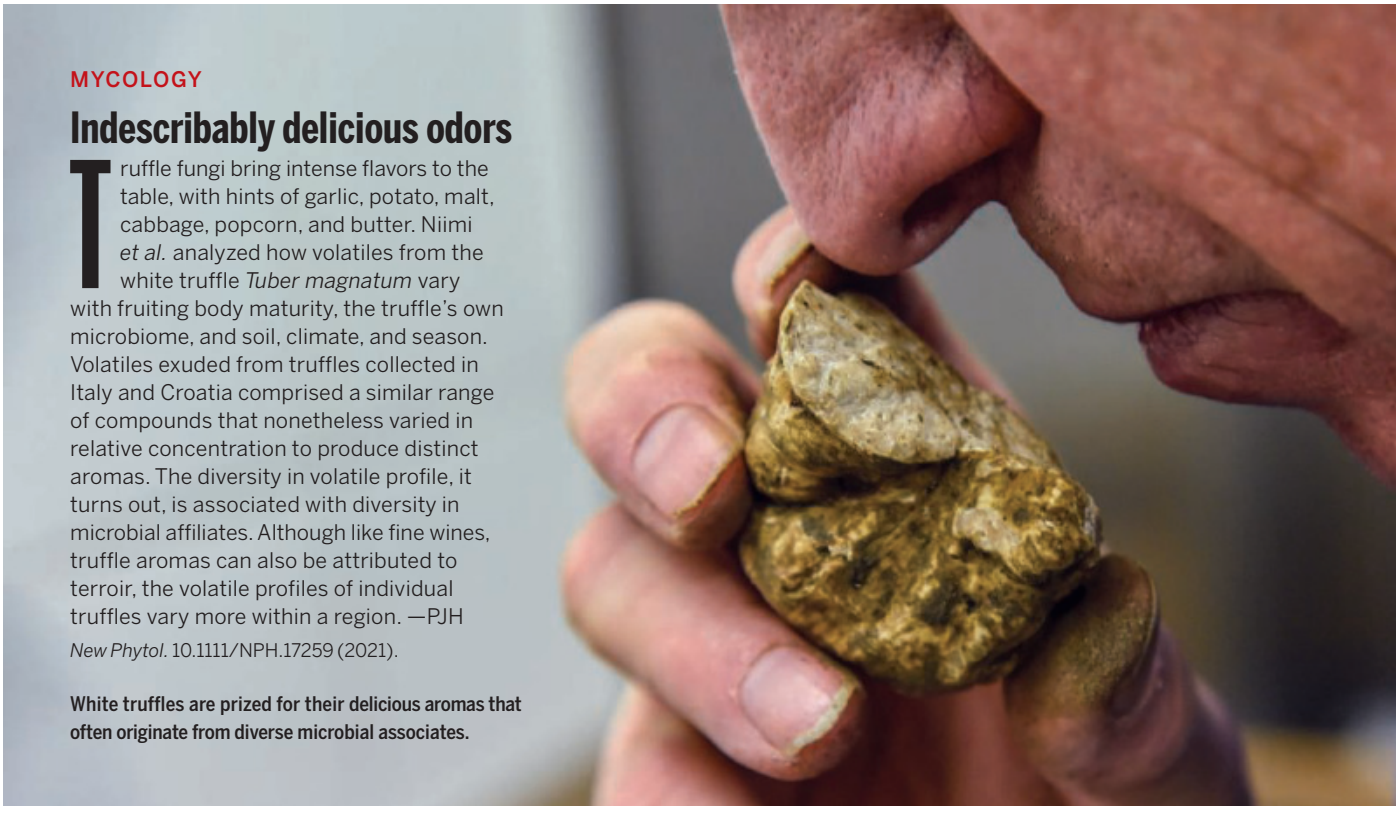

MYCOLOGY

Indescribably delicious odors

Truffle fungi bring intense flavors to the table, with hints of garlic, potato, malt, cabbage, popcorn, and butter. Niimi *et al.* analyzed how volatiles from the white truffle *Tuber magnatum* vary with fruiting body maturity, the truffle's own microbiome, and soil, climate, and season. Volatiles exuded from truffles collected in Italy and Croatia comprised a similar range of compounds that nonetheless varied in relative concentration to produce distinct aromas. The diversity in volatile profile, it turns out, is associated with diversity in microbial affiliates. Although like fine wines, truffle aromas can also be attributed to terroir, the volatile profiles of individual truffles vary more within a region. —PJH

New Phytol. 10.1111/NPH.17259 (2021).

White truffles are prized for their delicious aromas that often originate from diverse microbial associates.

EDUCATION

Social justice meets STEM education

It is critical that STEM students learn how science has been implicated in creating social inequities over time. Ali *et al.* describe a method for incorporating social justice themes into an organic chemistry curriculum. Instructors deliberately infused social justice themes into a standard curriculum by including key compounds that have had important social, cultural, and environmental impacts. Students then predicted products and identified functional groups of compounds now placed in a historical and social context. Although most of the students agreed that this method made the material more relevant, only 4% reported social justice discussions in other STEM courses, highlighting a plethora of missed opportunities. STEM instructors across disciplines are encouraged to emulate this approach and infuse social justice into their courses. —MMc

J. Chem. Educ. **97**, 3984 (2020).

COSMOLOGY

Curvature with interacting dark energy

Some analyses of the cosmic microwave background (CMB) imply that the Universe probably has a closed geometry (positive curvature). This disagrees with several other cosmological observations indicating a flat (zero curvature) Universe. Di Valentino *et al.* investigated whether this discrepancy can be alleviated in cosmologies that allow dark energy to interact with dark matter. They found that these more general models strengthen the arguments for a closed Universe and lessen the tension with the large-scale galaxy distribution. However, the authors caution that the discrepancy in the Hubble constant becomes worse, and that a flat Universe cannot be ruled out. —KTS

Mon. Not. R. Astron. Soc. **502**, L23 (2021).

SIGNAL TRANSDUCTION

Target for antidepressants

Antidepressants are clinically effective and widely used but their mechanisms of action are not fully understood. Casarotto *et al.* propose that several different types of antidepressants all act directly on the neuronal receptor tyrosine kinase receptor 2 (TRKB). TRKB is the receptor for brain-derived neurotrophic factor, regulates activity-dependent synaptic plasticity, and has been implicated in antidepressant actions. The authors found three different types of antidepressant bound with relatively low affinity to the transmembrane domain of TRKB. Mutation of the site impaired antidepressant action in cellular and animal studies. The authors propose that the low-affinity binding can help to explain the known slow time course of antidepressant action, which might reflect slow accumulation of the drugs in the brain to reach a dose that enhances TRKB signaling. —LBR

Cell **184**, P1299 (2021).

MALARIA

Forest-going risks

Forest malaria occurs among economically driven migrants working in the Amazon. However, in the literature, conclusions about the role of forest activities in relation to malaria incidence are conflicting. Rerolle *et al.* investigated the risk of forest malaria in Lao People's Democratic Republic (PDR) in the context of a nationwide malaria elimination program. High-resolution Landsat remote-sensing imagery of forest cover and malaria incidence data were systematically gathered from four northern and four southern districts of Lao PDR between 2013 and 2016. Deforestation in a 30-kilometer radius around villages was associated with higher malaria incidence within a year, particularly of *Plasmodium falciparum* malaria, but declined over 3 years. In Lao PDR, unlike the Amazon, it is resident not migrant populations who suffer from forest malaria. —CA

eLife **10**, e56974 (2021).

PHOTO: GIUSEPPE CACACE/GETTY IMAGES

REVIEW SUMMARY

CANCER MICROBIOME

The microbiome and human cancer

Gregory D. Sepich-Poore, Laurence Zitvogel, Ravid Straussman, Jeff Hasty, Jennifer A. Wargo, Rob Knight*

BACKGROUND: Historical accounts linking cancer and microbes date as early as four millennia ago. After establishment of the germ theory of infectious diseases, clinical research of microbial influences on cancer began in 1868, when William Busch reported spontaneous tumor regressions in patients with *Streptococcus pyogenes* infections. Over the next century, poor reproducibility, erroneous microbiological claims, and severe toxicity led many to discount the role of bacteria in carcinogenesis and cancer therapy. However, these studies provided the first crude demonstrations of cancer immunotherapy. Contemporaneously, the viral theory of cancer flourished, spurred by the 1911 discovery of Rous sarcoma virus, which transformed benign tissue into malignant tumors in chickens. The decades-long search to find viruses behind every human cancer ultimately failed, and many cancers have been linked to somatic mutations. Now the field is encountering intriguing claims of the importance of microbes, including bacteria and fungi, in cancer and cancer therapy. This Review critically evaluates this evidence in light of modern cancer biology and immunology, delineating roles for microbes in cancer by examining advances in proposed mechanisms, diagnostics, and modulation strategies.

ADVANCES: Few microbes directly cause cancer, but many seem complicit in its growth, often acting through the host's immune system; conversely, several have immunostimulatory properties. Mechanistic analyses of gut microbiota–immune system interactions reveal powerful effects on antitumor immunity by modulating primary and secondary lymphoid tissue activities. Many of these pathways invoke Toll-like receptor–initiated cytokine signaling, but microbial metabolic effects and antigenic mimicry with cancer cells are also important. In preclinical models, microbial metabolites also regulate phenotypes of tumor somatic mutations and modulate immune checkpoint inhibitor efficacy.

Emerging evidence suggests that intratumoral bacteria exist and are active, with overlapping immunohistochemistry, immunofluorescence, electron microscopy, and sequencing data in ~10 cancer types. Preliminary studies further suggest that fungi and bacteriophages contribute to gastrointestinal cancers. However, the abundance of intratumoral microbial cells is low relative to cancer cells, and knowledge of their functional repertoire and potency remains limited. Further validation of their prevalence and impact is needed in diverse cohorts and therapeutic contexts.

The immunomodulatory effects of host microbiota have reinvigorated efforts to change their composition as a form of immunotherapy. Despite extensive preclinical evidence, translation of microbiota modulation approaches into humans has not yet materialized into commercialized therapies. Synthetic biology approaches are also gaining traction, with engineered bacterial cancer therapies in preclinical and clinical trial settings.

OUTLOOK: A better understanding of the roles of microbes in cancer provides an opportunity to improve each stage of the cancer care cycle, but major challenges remain. Concerted efforts to characterize cancer-associated microbiota among tumor, stool, and blood samples with gold-standard contamination controls would tremendously aid this progress. This would be analogous to The Cancer Genome Atlas's role in characterizing the cancer somatic mutation landscape. Large-scale clinical trials are currently testing the efficacy of microbiota modulation approaches, ranging from dietary modifications to intratumorally injected, engineered bacteria. These bacterial cancer therapies, if safe and effective, could tremendously expand the cancer therapy armamentarium. Altogether, integrating the host-centric and microbial viewpoints of cancer may improve patient outcomes while providing a nuanced understanding of cancer-host-microbial evolution. ■

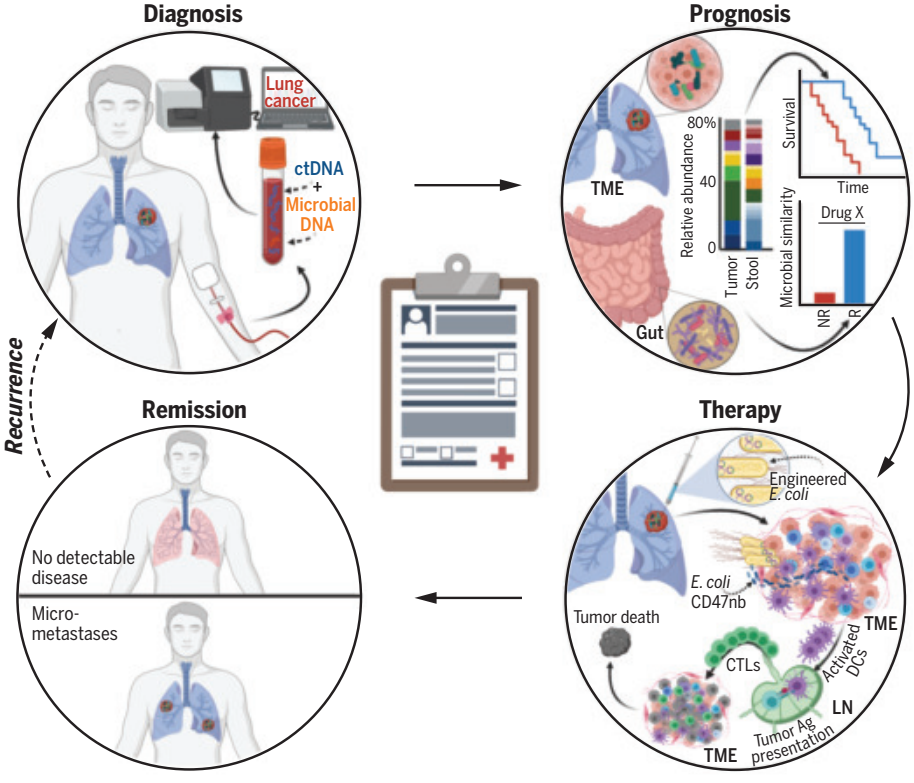

Opportunities for microbes to affect cancer care. Diagnosis: Cancer-specific, blood-borne microbial DNA may complement cell-free tumor DNA (ctDNA). Prognosis: Gut and intratumoral microbiota may stratify patient outcomes (NR, nonresponder; R, responder; TME, tumor microenvironment). Therapy: Intratumor injection of CD47 nanobody (CD47nb)–producing *Escherichia coli* may create systemic antitumor immunity by enhancing dendritic cell (DC) phagocytosis, lymph node (LN) antigen (Ag) presentation, and cytotoxic T lymphocyte (CTL) activity.

The list of author affiliations is available in the full article online.
*Corresponding author. Email: robknight@eng.ucsd.edu
Cite this article as G. D. Sepich-Poore *et al.*, *Science* 371, eabc4552 (2021). DOI: 10.1126/science.abc4552

READ THE FULL ARTICLE AT
https://doi.org/10.1126/science.abc4552

RESEARCH ARTICLE SUMMARY

IMMUNOLOGY

Liver type 1 innate lymphoid cells develop locally via an interferon-γ–dependent loop

Lu Bai*, Margaux Vienne*, Ling Tang*, Yann Kerdiles*, Marion Etiennot, Bertrand Escalière, Justine Galluso, Haiming Wei, Rui Sun†‡, Eric Vivier†‡, Hui Peng†‡, Zhigang Tian†‡

INTRODUCTION: The predominant sites where hematopoiesis occurs change during the course of mammalian development. Bone marrow (BM) hematopoiesis has long been considered the major source of mature blood cells during adulthood, but extramedullary hematopoiesis in other adult organs can occur under certain circumstances and makes a particularly important contribution when the BM is not functional. In particular, the adult liver environment remains compatible with hematopoiesis and contains a few hematopoietic stem cells (HSCs) with long-term capacity for hematopoietic reconstitution.

RATIONALE: The pathways leading to the development of tissue-resident lymphocytes, including liver type 1 innate lymphoid cells (ILC1s), remain unclear. The adult mouse liver ILCs include $CD49a^{-}CD49b^{+}$ conventional natural killer (cNK) cells and $CD49a^{+}CD49b^{-}$ ILC1s. Given the tissue-resident status of $CD49a^{+}CD49b^{-}$ ILC1s in the liver and their impaired reconstitution in mice receiving BM transplants, we investigated whether liver ILC1s could develop from local hematopoietic progenitors during adulthood.

RESULTS: Previous studies have demonstrated that fetal liver HSCs are enriched in a lineage (Lin)-negative population expressing both Mac-1 and Sca-1. We found that the adult mouse liver also contains $Lin^{-}Sca\text{-}1^{+}Mac\text{-}1^{+}$ (LSM) HSCs derived from the fetal liver. An analysis of parabiotic mice showed that adult liver LSM cells were strictly tissue resident at steady state. LSM cells purified from adult mouse liver and transferred into sublethally irradiated immmunodeficient mice by portal vein injection were able to generate multiple hematopoietic lineages but preferentially differentiated into ILC1s rather than cNK cells in the recipient liver. Single-cell RNA sequencing analysis showed that LSM cells represented a complex population of various cell subsets and revealed $Lin^{-}CD122^{+}CD49a^{+}$ cells as a heterogeneous precursor population downstream from LSM cells, with a differentiation potential restricted to liver ILC1s rather than cNK cells. Mechanistically, we could show that deficiency in the gene encoding interferon-γ (*Ifng*) or one of its receptors (*Ifngr1*) selectively reduced the frequency and number of ILC1s and not cNK cells in the liver. Delivery of a plasmid containing the interferon-γ (IFN-γ) cDNA to *Ifng*-deficient mice via hydrodynamic tail-vein injection selectively increased the frequency and number of liver ILC1s but not of liver cNK cells. Moreover, IFN-γ signaling promoted the expansion and differentiation of LSM cells but not of ILC1s, supporting a model in which IFN-γ acts on these local progenitors to promote liver ILC1 development. Previous studies have shown a strict requirement of the transcription factor T-bet for ILC1 development. We showed that T-bet is not required for LSM cell development but is key for the LSM cell differentiation into ILC1s. We then explored the cellular source of IFN-γ that affects liver ILC1 production. ILC1 numbers were unaffected in the absence of T or B cells. By contrast, $Ncr1^{Cre/+}$ $Ifng^{fl/fl}$ mice, in which *Ifng* expression is conditionally abolished on $NKp46^{+}$ cells, harbored a selective deficiency of liver ILC1s. We previously demonstrated that conditional deficiency of the transcription factor Eomes in $NKp46^{+}$ ILCs leads to an absence of cNK cells, with no impact on liver ILC1s, ruling out a role for cNK cells in liver ILC1 development. Because all $NKp46^{+}$ ILCs producing IFN-γ are either cNK cells or ILC1s, IFN-γ production by ILC1s therefore promotes the development of ILC1s in the liver through its action on their progenitors.

CONCLUSION: We identified an IFN-γ–dependent loop that amplifies the development of liver ILC1s but not cNK cells locally. Our findings reveal the contribution of extramedullary hematopoiesis to a distinctive regional immune feature within the liver. These results are reminiscent of the local development of macrophages from embryonic precursors that selectively seed the tissues and of the in situ differentiation of lung ILC2s from tissue-resident progenitors. They advance our knowledge of the importance of extramedullary hematopoiesis to cells of lymphoid origin. ■

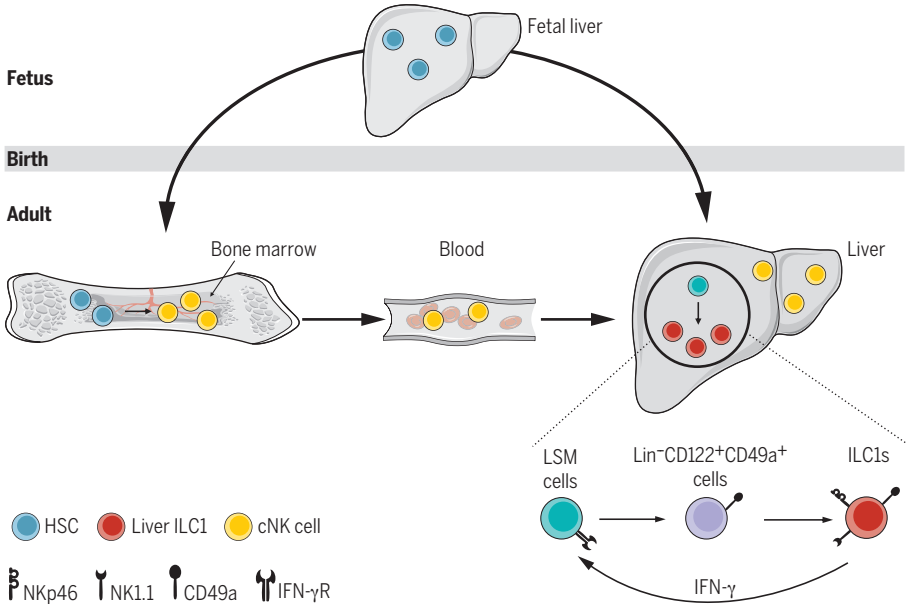

Liver ILC1s develop in situ during adulthood. In contrast to cNK cells (yellow) derived from the HSCs (blue) in adult BM, tissue-resident liver ILC1s (red) develop locally during adulthood from LSM HSCs (green) derived from the fetal liver. The IFN-γ production by the liver ILC1s themselves promotes their development in situ, through effects on their $IFN\text{-}\gamma R^{+}$ liver progenitors.

The list of author affiliations is available in the full article online.
*These authors contributed equally to this work.
†These authors contributed equally to this work.
‡Corresponding author. Email: vivier@ciml.univ-mrs.fr (E.V.); huipeng@mail.ustc.edu.cn (H.P.); sunr@ustc.edu.cn (R.S.); tzg@ustc.edu.cn (Z.T.)
Cite this article as L. Bai *et al.*, *Science* **371**, eaba4177 (2021). DOI: 10.1126/science.aba4177

READ THE FULL ARTICLE AT
https://doi.org/10.1126/science.aba4177

RESEARCH ARTICLE SUMMARY

IMMUNOLOGY

WAVE2 suppresses mTOR activation to maintain T cell homeostasis and prevent autoimmunity

Ming Liu*, Jinyi Zhang*, Benjamin D. Pinder, Qingquan Liu, Dingyan Wang, Hao Yao, Yubo Gao, Aras Toker, Jimin Gao, Alan Peterson, Jia Qu†, Katherine A. Siminovitch†

INTRODUCTION: The essential role of actin cytoskeletal regulatory proteins in expression of effective immune responses is exemplified by the impaired immunity manifested by patients deficient for the Wiskott-Aldrich syndrome actin modulatory protein (WASp). Among other WASp-related drivers of actin rearrangement, the WASp family verprolin homologous protein 2 (WAVE2) is predominantly expressed in hematopoietic cells and has been implicated in the cytoskeletal remodeling required for T cell adhesion and organization of the immunological synapse. However, the precise roles of WAVE2 in modulating T cell functions that govern immunity remain unknown.

RATIONALE: WAVE2 stability and subcellular localization depend on its constitutive association with the ABI1/2 (Abelson interactor 1/2), HEM1 (hematopoietic protein 1), HSPC300 (haematopoietic stem/progenitor cell protein 300), and CYFIP1 (cytoplasmic FMR1 interacting protein 1) proteins, which together constitute a pentameric WAVE regulatory complex (WRC) that supports WAVE2 activation by the Rac guanosine triphosphatase and other stimulatory signals that trigger WAVE2-driven actin-related protein-2/3 (Arp2/3)–dependent actin nucleation. Genetic data implicating several WAVE2-associated WRC proteins in autoimmune disease and the established link between cytoskeletal regulator dysfunction and immune deficiency raise the possibility that WAVE2 represents an important effector of T cell contributions to immune competence. Thus, we derived WAVE2 T cell conditional knockout (*Wave2*^{cKO}) mice to enable investigation of WAVE2 influence on T cell homeostasis and function.

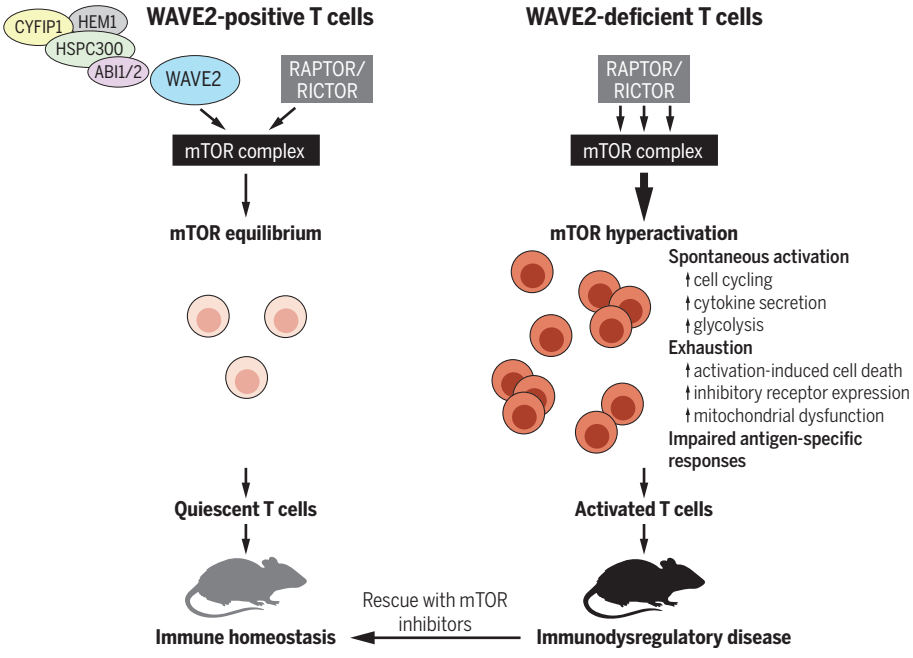

WAVE2 suppresses mTOR activity to maintain immune homeostasis. Mice expressing WAVE2-deficient T cells develop severe immunodysregulatory disease. In normal T cells, WAVE2 represses mTOR activation by restricting RAPTOR/RICTOR recruitment to mTOR. In the absence of WAVE2, enhanced mTOR signaling engenders spontaneous T cell activation, hyperproliferation, and accelerated differentiation, along with impaired antigen-evoked responses and an exhaustion phenotype. These T cell aberrancies and the concomitant autoimmune phenotype are ameliorated by pharmacological inhibition of mTOR.

RESULTS: Characterization of *Wave2*^{cKO} mice expressing WAVE2-deficient T cells revealed numbers of peripheral T cells to be reduced in young (<4 weeks old) mice but progressively increased and surpassed those of control mice by age 8 weeks. Although thymic T cell development appeared normal, *Wave2*^{cKO} mice manifested progressive severe autoimmune and inflammatory disease characterized by splenomegaly, lymphadenopathy, multiorgan lymphocyte infiltration, and early death. Significant increases in proinflammatory cytokine and autoantibody expression were also detected in these mice and were accompanied by spontaneous activation and accelerated differentiation of peripheral T cells. *Wave2*^{cKO} mice also exhibited markedly impaired antigen-specific immune responses associated with exhausted T cells, showing increases in T cell inhibitory receptor expression, dysregulated mitochondrial function, and increased activation-induced cell death. T cell antigen receptor (TCR)–driven actin polymerization and chemotaxis were also impaired in WAVE2-deficient T cells, with aberrant trafficking of these cells to nonlymphoid organs. WAVE2 deficiency had negligible effects on proximal TCR signaling but was associated with significantly increased activation of the mammalian target of rapamycin (mTOR) in response to antigen receptor or cytokine stimulation. Mechanistically, WAVE2 bound mTOR and constrained mTOR binding to RAPTOR (regulatory-associated protein of mTOR) and RICTOR (rapamycin-insensitive companion of mTOR), key components of the mTOR complexes 1 and 2, respectively. Consistent with WAVE2's suppressive effect on mTOR activation, pharmacologic inhibition of mTOR ameliorated the T cell anomalies and the immunodysregulatory phenotypes manifested in *Wave2*^{cKO} mice.

CONCLUSION: Our findings identify a critical role for WAVE2 in restraining T cell activation and effector differentiation, with T cell–selective WAVE2 ablation leading to combined immunodeficiency and autoimmune disease. The enhanced mTOR activation observed in WAVE2-deficient T cells and the suppression of disease in *Wave2*^{cKO} mice treated with an mTOR inhibitor establish WAVE2 restriction of mTOR activity as a critical mechanistic pathway supporting T cell quiescence so as to maintain immune homeostasis and prevent inflammation and autoimmunity. ■

The list of author affiliations is available in the full article online.
*These authors contributed equally to this work.
†Corresponding author. Email: katherine.siminovitch@sinaihealthsystem.ca (K.A.S); jqu@mail.eye.ac.cn (J.Q.)
Cite this article as M. Liu *et al.*, *Science* 371, eaaz4544 (2021). DOI: 10.1126/science.aaz4544

READ THE FULL ARTICLE AT
https://doi.org/10.1126/science.aaz4544

RESEARCH ARTICLE SUMMARY

SIGNAL TRANSDUCTION

Photoinduced receptor confinement drives ligand-independent GPCR signaling

M. Florencia Sánchez, Sylvia Els-Heindl, Annette G. Beck-Sickinger, Ralph Wieneke, Robert Tampé*

INTRODUCTION: Lateral membrane organization and receptor cluster formation are implicated in signal transduction and regulation of cellular responses. The physiological relevance of clustering or confinement of heterotrimeric guanine nucleotide–binding protein (G protein)–coupled receptors (GPCRs) is not well understood, and methods to study how the spatial distribution and location of receptor clusters affect cell responses are limited. However, the urgency of these questions is substantiated by the fact that several receptor families show cell responses that depend on the topology of the stimulus. Neuropeptide Y (NPY) hormone receptors, which belong to the class A GPCR rhodopsin family, contribute to a large variety of physiological processes, ranging from the regulation of cell migration to memory retention, fear extinction, and disorders such as epilepsy. Confinement of Y_2 receptors (Y_2Rs) is of high relevance because spatially restricted ligand-receptor interactions have been observed in vivo. Therefore, new approaches are needed to modulate receptor confinement in a rapid and noninvasive manner.

RATIONALE: To better understand how the location and dynamics of GPCR clustering influence cell responses, we developed a system to precisely control the lateral membrane organization of neuropeptide Y_2Rs in living cells by light. Light triggers photoreactions within seconds and can in turn be modulated in time, space, and intensity. We used ultrasmall, high-affinity lock-and-key pairs; a light-controllable multivalent chelator on a two-dimensional matrix; and histidine-tagged Y_2Rs. This system enables in situ induction of receptor clusters of variable size, location, and density upon photoactivation of the multivalent chelator, which is initially inactivated through an intramolecular histidine tag.

RESULTS: We generated a human cell line stably expressing small amounts of histidine-tagged neuropeptide Y_2Rs at the cell surface, comparable to an in vivo setting. Cells over matrices modified with the photoactivatable chelator trivalent nitrilotriacetic acid were illuminated by in situ laser-scanning microscopy. By following the process of cluster formation in real time, we observed a fast receptor assembly within the first 60 s, which increased continuously over the first minutes. Photoactivation of circular regions covering the cell body, edge, and periphery showed an immediate effect on cell spreading and motility. Cells moved toward the photoactivated spots, which resulted in new receptor accumulations in regions that were previously distant from the cell periphery. Photoactivation restricted to the cell leading edge also modulated cell migration. Using live-cell calcium imaging, we found that light-induced receptor clustering provoked a global increase in cytosolic calcium concentration. Changes in cell motility and calcium concentration were also observed after stimulation with the canonical ligand NPY. Subsequent photoinduced receptor confinement in the same cell triggered further increases in cytosolic calcium and cell motility. By contrast, these effects could be selectively blocked by a Y_2R antagonist.

CONCLUSION: By revealing ligand-independent receptor activation after cluster formation, our results demonstrate that Y_2R clusters locally enhance constitutive receptor activity. High-affinity Y_2R/G protein complexes have been observed in the absence of the ligand. In our system, the high local receptor density may increase the residence time of proximate G proteins and recruit further downstream effectors, which could boost the likelihood of activation. In this regard, our results highlight that confinement of GPCRs can bias their active state and initiate downstream signaling akin to the canonical agonist. This versatile approach, along with the nanotool used, creates new possibilities to study in situ the impact of membrane organization on cell signaling and mechanotransduction. ■

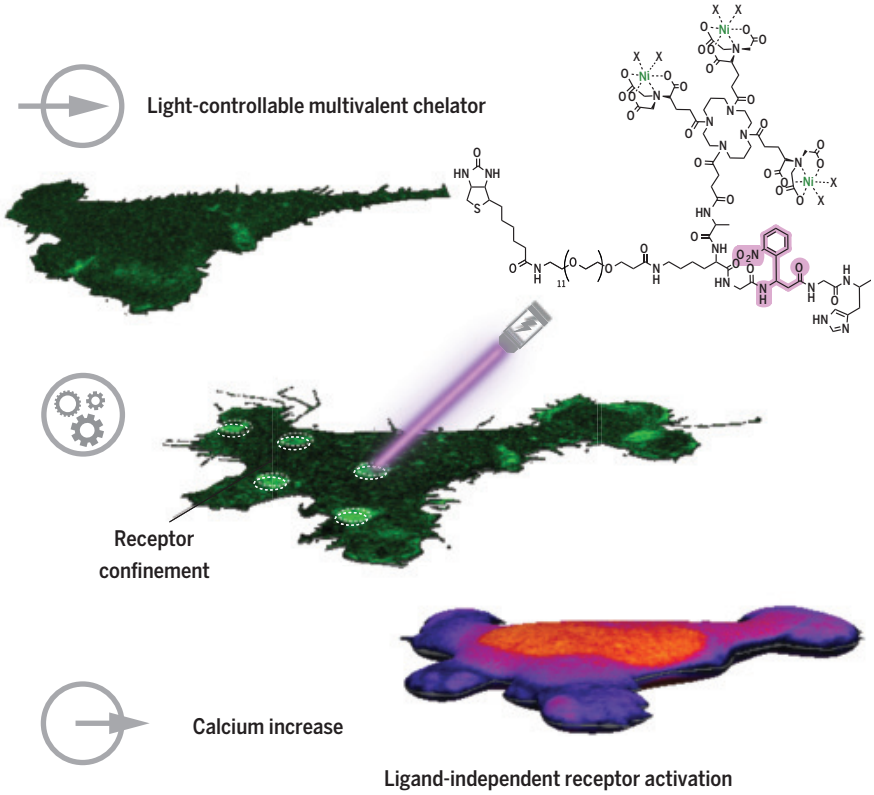

In situ receptor confinement triggered by light. Input (light) activates multivalent chelators displayed on a generic matrix to generate fine-tunable receptor clusters at the cell membrane in a rapid, noninvasive, and reversible manner. Increased cell motility and calcium signals as output reveal ligand-independent receptor activation.

The list of author affiliations is available in the full article online.
*Corresponding author. Email: tampe@em.uni-frankfurt.de
Cite this article as: M. F. Sánchez *et al.*, *Science* 371, eabb7657 (2021). DOI: 10.1126/science.abb7657

RESEARCH ARTICLE SUMMARY

WILDLIFE DISEASE

Hunting the eagle killer: A cyanobacterial neurotoxin causes vacuolar myelinopathy

Steffen Breinlinger*, Tabitha J. Phillips*, Brigette N. Haram, Jan Mareš, José A. Martínez Yerena, Pavel Hrouzek, Roman Sobotka, W. Matthew Henderson, Peter Schmieder, Susan M. Williams, James D. Lauderdale, H. Dayton Wilde, Wesley Gerrin, Andreja Kust, John W. Washington, Christoph Wagner, Benedikt Geier, Manuel Liebeke, Heike Enke, Timo H. J. Niedermeyer†‡, Susan B. Wilde†‡

INTRODUCTION: Vacuolar myelinopathy (VM) is a neurological disease characterized by widespread vacuolization in the white matter of the brain. First diagnosed in 1994 in bald eagles, it has since spread throughout the southeastern United States. In addition to avian species such as waterfowl and birds of prey, VM has also been found to affect amphibians, reptiles, and fish. Despite intense research efforts, the cause of this mysterious disease has been elusive. Neither contagious agents nor xenobiotics were detected in deceased animals, but field and laboratory studies demonstrated that VM can be transferred through the food chain from herbivorous fish and wildlife to birds of prey.

RATIONALE: Occurrence of VM has been linked to a cyanobacterium (*Aetokthonos hydrillicola*) growing on an invasive plant (*Hydrilla verticillata*) in man-made water bodies. Cyanobacteria are known to produce potent toxins, so we hypothesized that a neurotoxin produced by the epiphytic cyanobacterium causes VM.

RESULTS: Field studies in the southeastern United States confirmed that *H. verticillata* was colonized with *A. hydrillicola* in more than half of the watersheds. Wildlife VM deaths occurred only in reservoirs with dense *H. verticillata* and *A. hydrillicola* populations. Laboratory bioassays confirmed the neurotoxicity of crude extracts of *A. hydrillicola*–*H. verticillata* biomass collected during VM outbreaks, but neurotoxicity was not detected in samples from VM-free sites. Laboratory cultures of the cyanobacterium, however, did not elicit VM. *A. hydrillicola* growing on *H. verticillata* collected at VM-positive reservoirs was then analyzed by mass spectrometry imaging, which revealed that cyanobacterial colonies were colocalized with a brominated metabolite. Supplementation of an *A. hydrillicola* laboratory culture with potassium bromide resulted in pronounced biosynthesis of this metabolite. *H. verticillata* hyperaccumulates bromide from the environment, potentially supplying the cyanobacterium with this biosynthesis precursor. Isolation and structure elucidation of the metabolite revealed a structurally unusual pentabrominated biindole alkaloid, which we called aetokthonotoxin (AETX). Genome sequencing of *A. hydrillicola* allowed the identification of the AETX biosynthetic gene cluster. Biochemical characterization of a halogenase detected in the cluster demonstrated that it brominates tryptophan with the expected substitution pattern. AETX is highly toxic to the nematode *Caenorhabditis elegans* [median lethal concentration (LC_{50}) 40 nM] and zebrafish (*Danio rerio*; LC_{50} 275 nM). Leghorn chickens (*Gallus gallus*) gavaged with AETX developed brain lesions characteristic of VM, whereas no lesions were observed in control chickens. VM diagnosis in treated chickens was verified using transmission electron microscopy of brain tissue.

CONCLUSION: We confirmed that AETX is the causative agent of VM. AETX biosynthesis relies on the availability of bromide. Seasonal environmental conditions promoting toxin production of *A. hydrillicola* are watershed specific. The consequences of elevated bromide from geologic and anthropogenic sources (e.g., water treatment and power plants) on VM should be further investigated. Notably, integrated chemical plant management plans to control *H. verticillata* should avoid the use of bromide-containing chemicals (e.g., diquat dibromide). AETX is lipophilic with the potential for bioaccumulation during transfer through food webs, so mammals may also be at risk. Increased monitoring and public awareness should be implemented for *A. hydrillicola* and AETX to protect both wildlife and human health. ■

The list of author affiliations is available in the full article online.
*These authors contributed equally to this work.
†These authors contributed equally to this work.
‡Corresponding author. Email: swilde@uga.edu (S.B.W.); timo.niedermeyer@pharmazie.uni-halle.de (T.H.J.N.)
Cite this article as S. Breinlinger *et al.*, *Science* 371, eaax9050 (2021). DOI: 10.1126/science.aax9050

READ THE FULL ARTICLE AT
https://doi.org/10.1126/science.aax9050

From the cyanobacterium to the bald eagle—toxin transmission through the food chain. *A. hydrillicola*, growing in colonies on aquatic vegetation, produces the neurotoxin AETX. Waterbirds, tadpoles, aquatic turtles, snails, and fish consume this contaminated vegetation and develop VM. Predators develop VM when they consume animals that have been grazing on *A. hydrillicola*–covered plants.

RESEARCH ARTICLE SUMMARY

CORONAVIRUS

Age groups that sustain resurging COVID-19 epidemics in the United States

Mélodie Monod*, Alexandra Blenkinsop*, Xiaoyue Xi*, Daniel Hebert*, Sivan Bershan*, Simon Tietze*, Marc Baguelin, Valerie C. Bradley, Yu Chen, Helen Coupland, Sarah Filippi, Jonathan Ish-Horowicz, Martin McManus, Thomas Mellan, Axel Gandy, Michael Hutchinson, H. Juliette T. Unwin, Sabine L. van Elsland, Michaela A. C. Vollmer, Sebastian Weber, Harrison Zhu, Anne Bezancon, Neil M. Ferguson, Swapnil Mishra, Seth Flaxman†, Samir Bhatt†, Oliver Ratmann*†, on behalf of the Imperial College COVID-19 Response Team

INTRODUCTION: After initial declines, in mid-2020, a sustained resurgence in the transmission of novel coronavirus disease (COVID-19) occurred in the United States. Throughout the US epidemic, considerable heterogeneity existed among states, both in terms of overall mortality and infection, but also in the types and stringency of nonpharmaceutical interventions. Despite these stark differences among states, little is known about the relationship between interventions, contact patterns, and infections, or how this varies by age and demographics. A useful tool for studying these dynamics is individual, age-specific mobility data. In this study, we use detailed mobile-phone data from more than 10 million individuals and establish a mechanistic relationship between individual contact patterns and COVID-19 mortality data.

RATIONALE: As the pandemic progresses, disease control responses are becoming increasingly nuanced and targeted. Understanding fine-scale patterns of how individuals interact with each other is essential to mounting an efficient public health control program. For example, the choice of closing workplaces, closing schools, limiting hospitality sectors, or prioritizing vaccination to certain population groups should be informed by the demographics currently driving and sustaining transmission. To develop the tools to answer such questions, we introduce a new framework that links mobility to mortality through age-specific contact patterns and then use this rich relationship to reconstruct accurate transmission dynamics (see figure panel A).

RESULTS: We find that as of 29 October 2020, adults aged 20 to 34 and 35 to 49 are the only age groups that have sustained SARS-CoV-2 transmission with reproduction numbers (transmission rates) consistently above one. The high reproduction numbers from adults are linked both to rebounding mobility over the summer and elevated transmission risks per venue visit among adults aged 20 to 49. Before school reopening, we estimate that 75 of 100 COVID-19 infections originated from adults aged 20 to 49, and the share of young adults aged 20 to 34 among COVID-19 infections was highly variable geographically. After school reopening, we reconstruct relatively modest shifts in the age-specific sources of resurgent COVID-19 toward younger individuals, with less than 5% of SARS-CoV-2 transmissions attributable to children aged 0 to 9 and less than 10% attributable to early adolescents and teenagers aged 10 to 19. Thus, adults aged 20 to 49 continue to be the only age groups that contribute disproportionately to COVID-19 spread relative to their size in the population (see figure panel B). However, because children and teenagers seed infections among adults who are more transmission efficient, we estimate that overall, school opening is indirectly associated with a 26% increase in SARS-CoV-2 transmission.

CONCLUSION: We show that considering transmission through the lens of contact patterns is fundamental to understanding which population groups are driving disease transmission. Over time, the share of age groups among reported deaths has been markedly constant, and the data provide no evidence that transmission shifted to younger age groups before school reopening, and no evidence that young adults aged 20 to 34 were the primary source of resurgent epidemics since the summer of 2020. Our key conclusion is that in locations where novel, highly transmissible SARS-CoV-2 lineages have not yet become established, additional interventions among adults aged 20 to 49, such as mass vaccination with transmission-blocking vaccines, could bring resurgent COVID-19 epidemics under control and avert deaths. ■

The list of authors and their affiliations is available in the full article online.
*These authors contributed equally to this work.
†Corresponding author. Email: oliver.ratmann@imperial.ac.uk (O.R.); s.bhatt@imperial.ac.uk (S.B.); s.flaxman@imperial.ac.uk (S.F.)

Cite this article as M. Monod *et al.*, *Science* 371, eabe8372 (2021). DOI: 10.1126/science.abe8372

READ THE FULL ARTICLE AT
https://doi.org/10.1126/science.abe8372

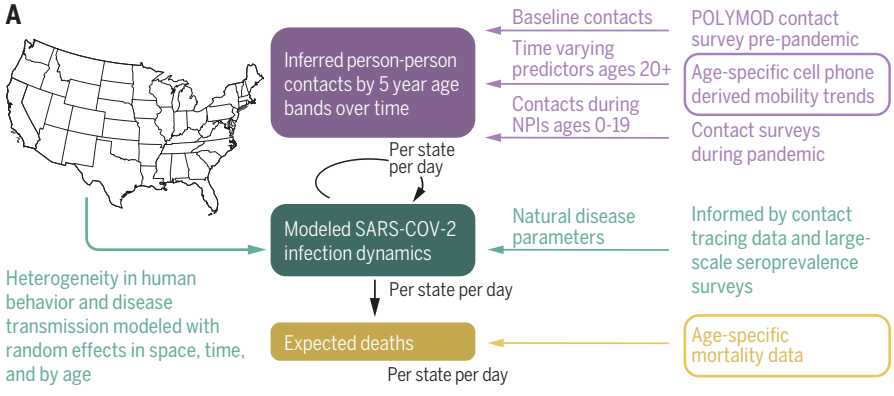

Model developed to estimate the contribution of age groups to resurgent COVID-19 epidemics in the United States. (**A**) Model overview. (**B**) Estimated contribution of age groups to SARS-CoV-2 transmission in October.

RESEARCH ARTICLE SUMMARY

SPECIATION

Rapid speciation via the evolution of pre-mating isolation in the Iberá Seedeater

Sheela P. Turbek*, Melanie Browne, Adrián S. Di Giacomo, Cecilia Kopuchian, Wesley M. Hochachka, Cecilia Estalles, Darío A. Lijtmaer, Pablo L. Tubaro, Luís Fábio Silveira, Irby J. Lovette, Rebecca J. Safran, Scott A. Taylor, Leonardo Campagna*

INTRODUCTION: Organisms in the early stages of speciation provide an opportunity to understand the processes that govern reproductive isolation between taxa. Ecological or behavioral mechanisms can serve as powerful barriers to the interbreeding of co-occurring species at the onset of their divergence. Tracking mating decisions within wild populations early in speciation can improve our understanding of how behavioral isolation promotes divergence.

RATIONALE: The southern capuchino seedeaters (*Sporophila*) are one of the most rapid avian radiations, showing remarkably low ecological and genomic divergence. We took advantage of the recent discovery of a capuchino species, the Iberá Seedeater (*S. iberaensis*), to study the origin and importance of pre-mating barriers early in speciation. By combining genomic and behavioral analyses, we examined (i) the role of assortative mating in the maintenance of species boundaries, (ii) the phenotypic traits underlying species recognition, (iii) the genomic basis of such traits, and (iv) the origin of these genomic variants.

RESULTS: *Sporophila iberaensis* was first observed in 2001 and co-occurs with *S. hypoxantha* throughout its main breeding location in the northern portion of the Iberá wetlands of Argentina. Across two breeding seasons, we located nests and collected genomic samples from both species. We found extremely low genome-wide differentiation, with the exception of three narrow regions located on different chromosomes. These regions contained 12 genes, three of which are involved in plumage coloration (*TYRP1*, *OCA2*, and *HERC2*). *Sporophila hypoxantha* and *S. iberaensis* males differ in coloration and song, but females are indistinguishable in coloration across the avian visual spectrum. We therefore used genomic data to quantify assortative mating. Each female's species-specific genotype always matched the genotype of her mate, demonstrating strong assortative mating despite these two species holding neighboring breeding territories, breeding synchronously, and foraging together on the same grasses. We tested the importance of divergent plumage patterning and song in species recognition and pre-mating isolation through playback experiments in the field. We presented territorial males with combinations of conspecific and heterospecific song and plumage, and assessed their aggressive behavioral responses. Each species responded most aggressively to conspecific song and plumage, confirming that both traits are used to recognize sexual competitors. Finally, we investigated the origin of the novel *S. iberaensis* plumage phenotype by examining genomic differentiation across the broader capuchino radiation. Although multiple species shared variants with *S. iberaensis* in the areas of elevated differentiation, the specific combination of these variants across the divergent regions distinguished *S. iberaensis* from all other capuchinos.

CONCLUSION: Our findings point to pre-mating isolation through assortative mate choice, based on both plumage coloration and song, as a primary mechanism promoting divergence between these co-occurring capuchino species. Although the ultimate fate of the incipient *S. iberaensis* species remains uncertain, our findings illustrate how lineages can form and quickly become reproductively isolated from co-occurring, syntopic species. Our results further suggest that the reshuffling of existing genetic variation can generate novel phenotypes that are then targeted by sexual selection. Assortative mating based on these traits may maintain species boundaries early in speciation while subsequent reproductive barriers accumulate. ■

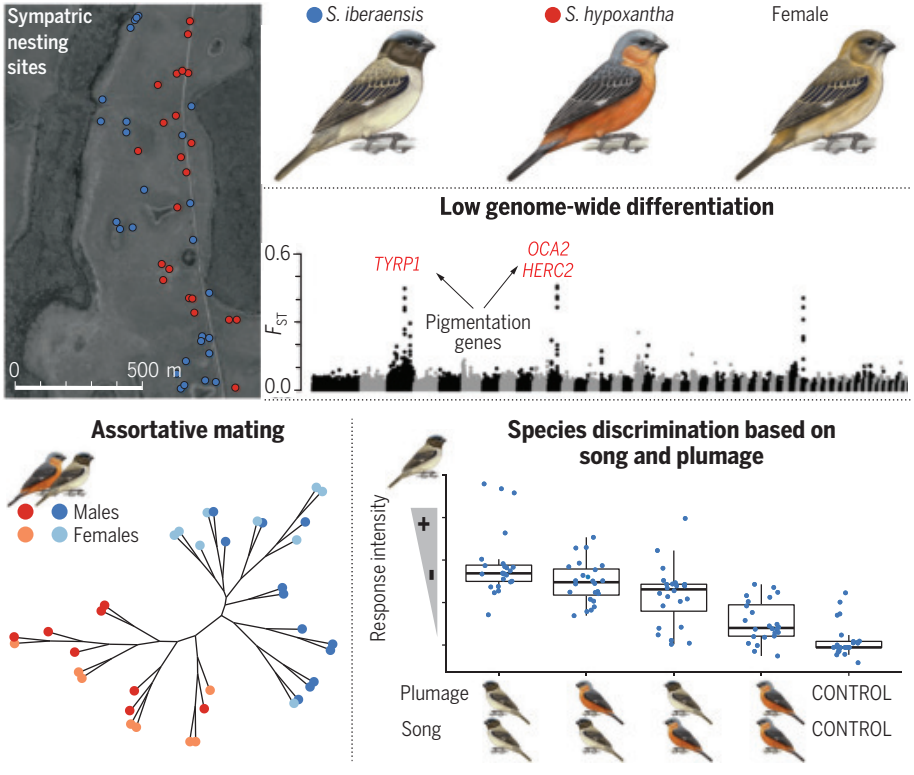

Novel mating signals restrict gene flow between co-occurring bird species. *Sporophila iberaensis* was first observed in 2001 and has a breeding range contained entirely within that of *S. hypoxantha*. Despite extremely low genomic differentiation, both species mate assortatively. Genetic differentiation is concentrated near genes known to be involved in plumage coloration. Field experiments show that both song and plumage are used to recognize sexual competitors.

The list of author affiliations is available in the full article online.
*Corresponding author. Email: sheela.turbek@colorado.edu (S.P.T.); lc736@cornell.edu (L.C.)
Cite this article as S. P. Turbek *et al.*, *Science* **371**, eabc0256 (2021). DOI: 10.1126/science.abc0256

READ THE FULL ARTICLE AT
https://doi.org/10.1126/science.abc0256

RESEARCH ARTICLES

ORGANIC CHEMISTRY

Photochemical intermolecular dearomative cycloaddition of bicyclic azaarenes with alkenes

Jiajia Ma[1]*, Shuming Chen[2]*, Peter Bellotti[1]*, Renyu Guo[3], Felix Schäfer[1], Arne Heusler[1], Xiaolong Zhang[1], Constantin Daniliuc[1], M. Kevin Brown[3]†, Kendall N. Houk[2]†, Frank Glorius[1]†

Dearomative cycloaddition reactions represent an ideal means of converting flat arenes into three-dimensional architectures of increasing interest in medicinal chemistry. Quinolines, isoquinolines, and quinazolines, despite containing latent diene and alkene subunits, are scarcely applied in cycloaddition reactions because of the inherent low reactivity of aromatic systems and selectivity challenges. Here, we disclose an energy transfer–mediated, highly regio- and diastereoselective intermolecular [4 + 2] dearomative cycloaddition reaction of these bicyclic azaarenes with a plethora of electronically diverse alkenes. This approach bypasses the general reactivity and selectivity issues, thereby providing various bridged polycycles that previously have been inaccessible or required elaborate synthetic efforts. Computational studies with density functional theory elucidate the mechanism and origins of the observed regio- and diastereoselectivities.

Advancing efficient and selective catalytic processes to access modular structural complexity is a central theme of modern organic synthesis (*1*, *2*). Cycloaddition reactions are among the most synthetically useful means to meet this end by leveraging the construction of sophisticated architectures from readily available feedstocks and feature excellent step/atom economy with predictable and exclusive stereoselectivity (Fig. 1A) (*3*, *4*). Therefore, cycloaddition reactions have played a prominent role in synthetic chemistry and constitute a major theme in chemistry education (*5*). The classical substrates used in cycloaddition reactions are unsaturated hydrocarbons such as 1,3-butadienes, alkenes, alkynes, and other related compounds. Industrially, these unsaturated hydrocarbons are produced stepwise through petroleum refining to afford saturated hydrocarbons, followed by cracking or dehydrogenation under harsh conditions (*6*). However, the initial refining can also directly afford unsaturated N-heterocycles, such as quinoline, isoquinoline, and quinaldine. Despite containing both latent diene and alkene subunits, these bicyclic azaarenes have shown limited applications in cycloaddition reactions. This phenomenon can be attributed both to the severe reactivity challenges and selectivity issues toward the intermolecular dearomative cycloaddition (DAC) reaction (*7*–*10*). First, overcoming the kinetic barrier of DAC reactions has traditionally required harsh conditions (Fig. 1B, dashed curve) or an extremely reactive or tailored cycloaddend (*11*–*14*). Second, the DACs are endergonic processes that are due to the breaking of aromaticity, 81.0 kcal·mol^{-1} for quinoline and 76.5 kcal·mol^{-1} for quinazoline (*15*); thus, under thermally induced reaction conditions, the starting materials will be favored, and a reverse reaction is feasible (Fig. 1B, dashed curve). Last, even if the kinetic and thermodynamic issues could be overcome, the inherent severe chemo-, regio-, and diastereoselectivity challenges would still diminish the broad utility of such methods (Fig. 1C).

In this context, an energy transfer (EnT) approach paves the way toward the solution of the aforementioned reactivity and selectivity problems (*16*–*18*). Initially, the ground-state azaarene could be selectively excited to a higher energy triplet state by the EnT process, thus leading to a compressed kinetic barrier compared with the thermally controlled pathway (Fig. 1B, solid curve versus dashed curve). Moreover, the combination of notably higher triplet energies in the terminal dearomatization products (which are thus not amenable to further EnT) and the sufficiently mild conditions prevents the reverse reaction. Compared with the conventional ground state chemistry, the unconventional triplet state intermediate could potentially lead to unexpected chemo-, regio-, and diastereoselectivities. Recent works have demonstrated the application of the EnT process for enabling DAC reactions but have faced large limitations. As such, the reaction has mostly been limited to electron-rich arenes or their prefunctionalized derivatives and intramolecular variants (Fig. 1D), which require multistep substrate synthesis and offer limited generality (*19*–*27*). Additionally, inferior selectivity has been observed in both the intra- and intermolecular DAC reactions (Fig. 1D). All these limitations are also commonly encountered under the thermally controlled DAC reactions (*28*–*33*). In this work, we applied the EnT process in combination with Brønsted or Lewis acid mediators to enable the selective DAC reaction of simple quinolines, isoquinolines, and quinazolines with a broad variety of alkenes (Fig. 1E). This reaction features exclusive carbocyclic [4 + 2] cycloaddition, high and divergent regioselectivity, and excellent *endo*-diastereoselectivity.

Evaluation of reaction conditions

The initial experiments involved the reaction of quinoline **1a** and 1-hexene **2a** in the presence of the commercially available photosensitizer [Ir-F] ({Ir[*d*F(CF$_3$) ppy]$_2$[dtbbpy]}{PF$_6$}, 1 or 2 mol %) (CAS No. 870987-63-6) under the irradiation of blue light-emitting diodes (Fig. 2, A and B, and figs. S1 and S2). Under condition A with 1,1,1,3,3,3-hexafluoro-propan-2-ol (HFIP) as the solvent, both regiomers **3a** (syn: R^2 close to the nitrogen of product) and **3b** (anti: the reverse cycloaddition order) were isolated in comparable yields of 41 and 46% but with excellent *endo*-diastereoselectivities (entry 1, Fig. 2B). By applying condition B with CH_2Cl_2 as the solvent and $BF_3{\cdot}OEt_2$ (1.25 equiv) as an additive, **3b** was obtained as the predominant regiomer over **3a** (entry 2, Fig. 2B). Next, when using 6-methyl quinoline **1b**, under condition B, two regiomers **4a** and **4b** were obtained (entry 4, Fig. 2B). Notably, back to condition A, a single regiomer **4a** was isolated in excellent yield (88%) and as a single *endo*-diastereomer (entry 5, Fig. 2B), whereas the other regiomer, **4b**, was not detected by crude ^{1}H nuclear magnetic resonance (NMR) analysis. By using 4-methyl-1-pentene (**2b**), a single regiomer **5a** was also obtained with good outcome (entry 6, Fig. 2B). Styrene (**2c**) was also compatible and provided a single regioisomeric product **6a** with comparable results (entry 7, Fig. 2B). Both the unactivated alkenes, **2a** and **2b**, and the activated one, **2c**, lead to the consistent *endo*-diastereoselectivity of products **3** to **6**. Excluding the acidic components ($BF_3{\cdot}OEt_2$ or HFIP, respectively) completely suppressed product formation (entries 3 and 8, Fig. 2B). Overall, regarding both the reaction efficiency and selectivity, condition A with HFIP as the Brønsted acid mediator was assessed to be optimal for the substituted quinoline **1b**, and condition B with $BF_3{\cdot}OEt_2$ as the Lewis acid mediator was more suitable for the unsubstituted substrate (**1a**).

Mechanistic investigation

The influence of the acidic solvent HFIP (*34*, *35*) and the additive $BF_3{\cdot}OEt_2$ on both the reaction efficiency and selectivities indicates the pivotal role of the Brønsted (*36*) and Lewis (*37*, *38*)

[1]Organisch-Chemisches Institut, Westfälische Wilhelms-Universität Münster, Corrensstraße 40, 48149 Münster, Germany. [2]Department of Chemistry and Biochemistry, University of California, Los Angeles, CA 90095, USA. [3]Department of Chemistry, Indiana University, Bloomington, IN 47405, USA.
*These authors contributed equally to this work.
†Corresponding author. Email: brownmkb@indiana.edu (M.K.B.); houk@chem.ucla.edu (K.N.H.); glorius@uni-muenster.de (F.G.)

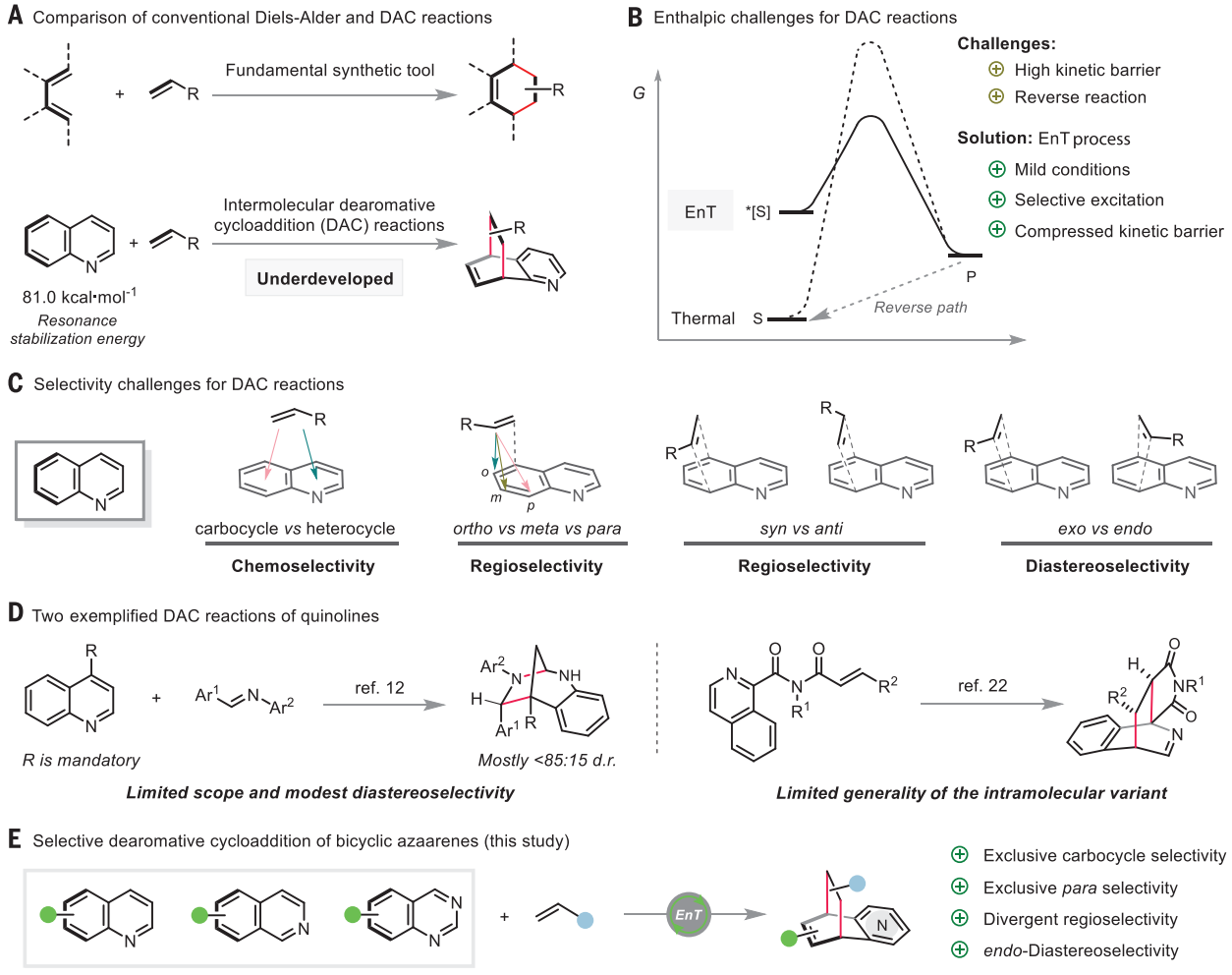

Fig. 1. DAC reactions. (**A**) Comparison of conventional Diels-Alder and DAC reactions. (**B**) Enthalpic challenges for DAC reactions. (**C**) Selectivity challenges for DAC reactions of bicyclic azaarenes. (**D**) Two exemplified DAC reactions of quinolines. (**E**) Selective [4 + 2] DAC of quinolines, isoquinolines, and quinazolines (this study). Ar, aryl; P, product; S, substrate.

acids. Taking this into account, we hypothesized that either the solvent HFIP or the additive $BF_3{\cdot}OEt_2$ was binding to the quinolines **1a** and **1b** through hydrogen bonding or Lewis acid-base interaction, respectively, to give an intermediate **I**, characterized by markedly decreased triplet energy (Fig. 2A). Intermediate **I** can then be selectively excited to the corresponding triplet state (**II**) by an EnT process. The resultant highly reactive biradical intermediate **II** would then add across an alkene in a regio- and stereoselective fashion, thus affording the [4 + 2] DAC products **3** to **6**. A number of mechanistic experiments support this scenario (Fig. 3A) (see supplementary materials for details). First, control experiments that used H-bonding acceptor cosolvents such as 1,4-dioxane, acetonitrile, and *N*,*N*-dimethylacetamide with HFIP led to a notable decrease of the reaction efficiency (table S8). Second, the H-bonding between HFIP and quinoline **1b** in solution is supported by a series of NMR experiments including ^{1}H NMR titration, nuclear Overhauser effect spectroscopy, and Job plot analysis (figs. S3 to S9). Third, in the solid state, a dual H-bonding interaction is directly observed in the cocrystal structure of quinoline-2-carboxylate (**1c**) and HFIP (Fig. 3A and fig. S22). These observations strongly support an H-bonding interaction between the nitrogen atom of quinoline and the alcoholic proton of HFIP. The Lewis acid-base interaction between $BF_3{\cdot}OEt_2$ and quinolines has been previously disclosed (*39*). The proposal of these interactions to decrease the singlet-triplet energy gap was confirmed by density functional theory (DFT) calculations. Accordingly, the triplet energy of **1a** is calculated to be 61.7 kcal·mol^{-1}. By contrast, after complexation with HFIP, protonation by HCl, or interaction with BF_3, decreased triplet energies of 61.2, 57.7, and 58.9 kcal·mol^{-1}, respectively, are predicted, rendering these adducts more amenable to EnT by the photosensitizer [Ir-F] (60.8 kcal·mol^{-1}) (figs. S14 and S15). This effect of Brønsted and Lewis acids on the triplet energy of quinolines is consistent with the experimental results (entries 3 and 8, Fig. 2B). Next, the proposed EnT activation of quinoline **1b** by the excited photosensitizer [Ir-F] was supported by Stern-Volmer luminescence quenching analysis, because a competitive single electron transfer (SET) event was found to be thermodynamically unfeasible by cyclic voltammetry study (figs. S10 to 12). Conversely, the suggested EnT process was further corroborated by the correlation of the reaction rate to triplet energies rather than the redox potentials of various photosensitizers (table S10). Overall, both the experimental and computational studies suggest that the ground-state quinolines can be activated through a Brønsted and Lewis acid–mediated EnT process, which is the key for the success of the [4 + 2] DAC reaction.

The high levels of regio- and stereocontrol observed for unactivated alkenes were of

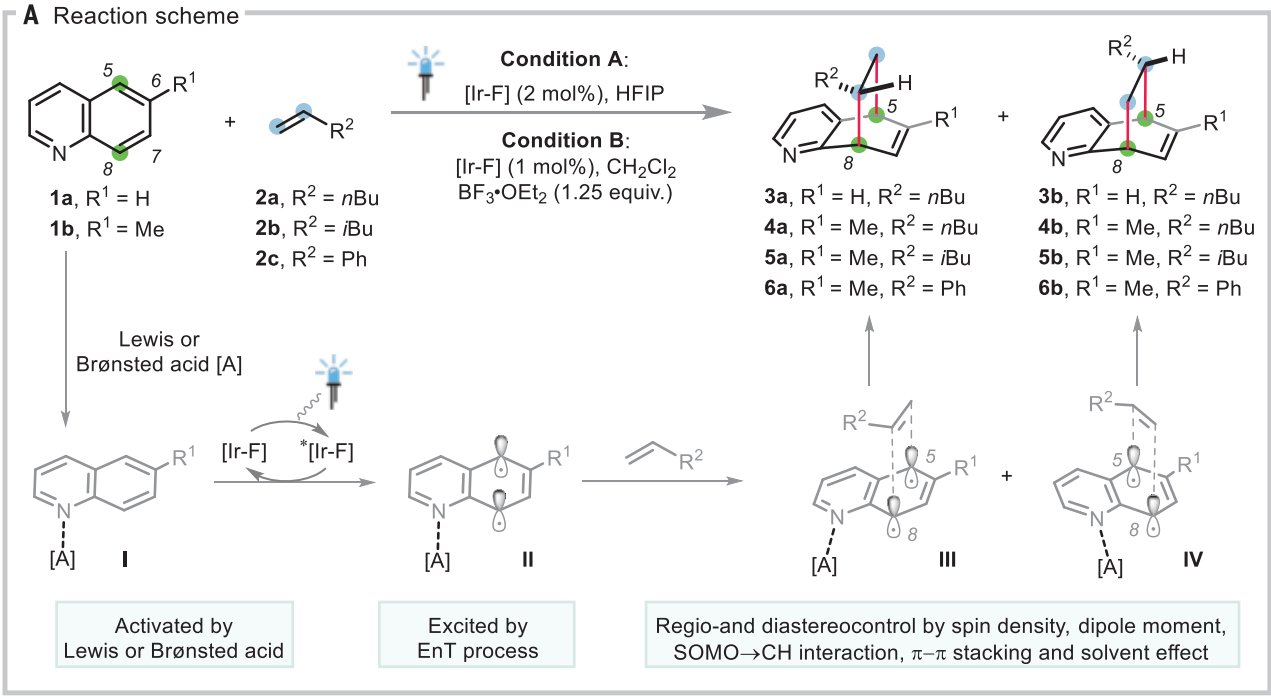

B Evaluation of conditions

Entry	1a/b	2a-c	Condition	Results
1	**1a**	**2a**	**A**	**3a** (41% yield, >95:5 d.r.); **3b** (46% yield, 94:6 d.r.)
2	**1a**	**2a**	**B**	**3a** (18% yield, 92:8 d.r.); **3b** (78% yield, 83:17 d.r.)
3	**1a**	**2a**	**B** (no BF_3•OEt_2)	**No conversion**
4	**1b**	**2a**	**B**	**4a** (75% yield, 95:5 d.r.); **4b** (18% yield, 83:17 d.r.)
5	**1b**	**2a**	**A**	**4a** (88% yield, >95:5 d.r.); **4b** (not detected)
6	**1b**	**2b**	**A**	**5a** (79% yield, >95:5 d.r.); **5b** (not detected)
7	**1b**	**2c**	**A**	**6a** (71% yield, 95:5 d.r.); **6b** (not detected)
8	**1b**	**2a-c**	**A** (MeOH as solvent)	**No conversion**

Fig. 2. Reaction development. (**A**) Reaction scheme. *i*Bu, isobutyl; Me, methyl; *n*Bu, *n*-butyl; Ph, phenyl. (**B**) Conditions evaluation (tables S1 to S7). One representative enantiomer of the racemic product is presented for all throughout the text. MeOH, methanol.

particular interest. We initially hypothesized that spin densities of the substrate in the triplet state would have a major impact on free energy barriers. Although calculated spin densities showed that N-protonation and coordination generally lead to increased spin density at the 5-position for quinoline **1b** in the triplet state (fig. S13), rate-determining C–C bonds forming transition states (TSs) for the formal [4 + 2] reaction between quinoline **1b** and alkene **2b** exhibited low regioselectivity ($\Delta\Delta G^{\ddagger}$ 0.4 to 0.5 kcal·mol^{-1}, difference in activation free energies) when calculated in the gas phase (Fig. 3B), indicating that regiocontrol is not solely due to differences in spin densities. The inclusion of an implicit solvent model for HFIP greatly increases the predicted regioselectivity to levels in good agreement with experimental observations ($\Delta\Delta G^{\ddagger}$ 1.5 to 1.7 kcal·mol^{-1}). These results suggest that TS polarity and solvent stabilization play an important role in enforcing regiocontrol. Calculated TS dipole moments confirm that **TS-1a**, the TS leading to the major product isomer **5a**, is notably more polar (11.4 Debye in HFIP) compared with regioisomeric TSs **TS-1c** (9.1 Debye) and **TS-1d** (9.4 Debye). In all four TSs, a close, stabilizing interaction (2.55 to 2.68 Å) is observed between the developing singly occupied molecular orbital (SOMO) of quinoline **1b** and one of the allylic C–H bonds on **2b**, which anchors the approaching alkene and shapes the lowest-energy TS geometry. As a result, a

A Experimental investigation

Probing H-bonding

i) Intermolecular NOE observed
ii) ^{1}H NMR titration indicates complexation
iii) Job-plot indicates 1:1.5 (**1b**:HFIP) stoichiometry

Probing EnT

i) **1b** as quencher of excited PS *via* Stern-Volmer plots
ii) Exclusion of SET event *via* cyclic voltammetry study
iii) Reaction rate correlates to E_T rather than redox potential of PS

Co-crystal structure of **1c** and HFIP

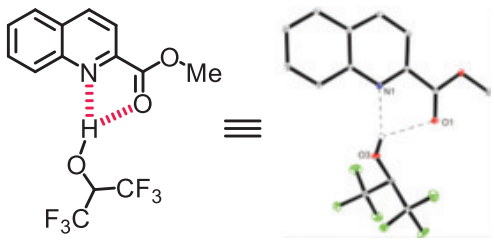

Intermediate **I'** (**1c**+HFIP)

B Computational investigation

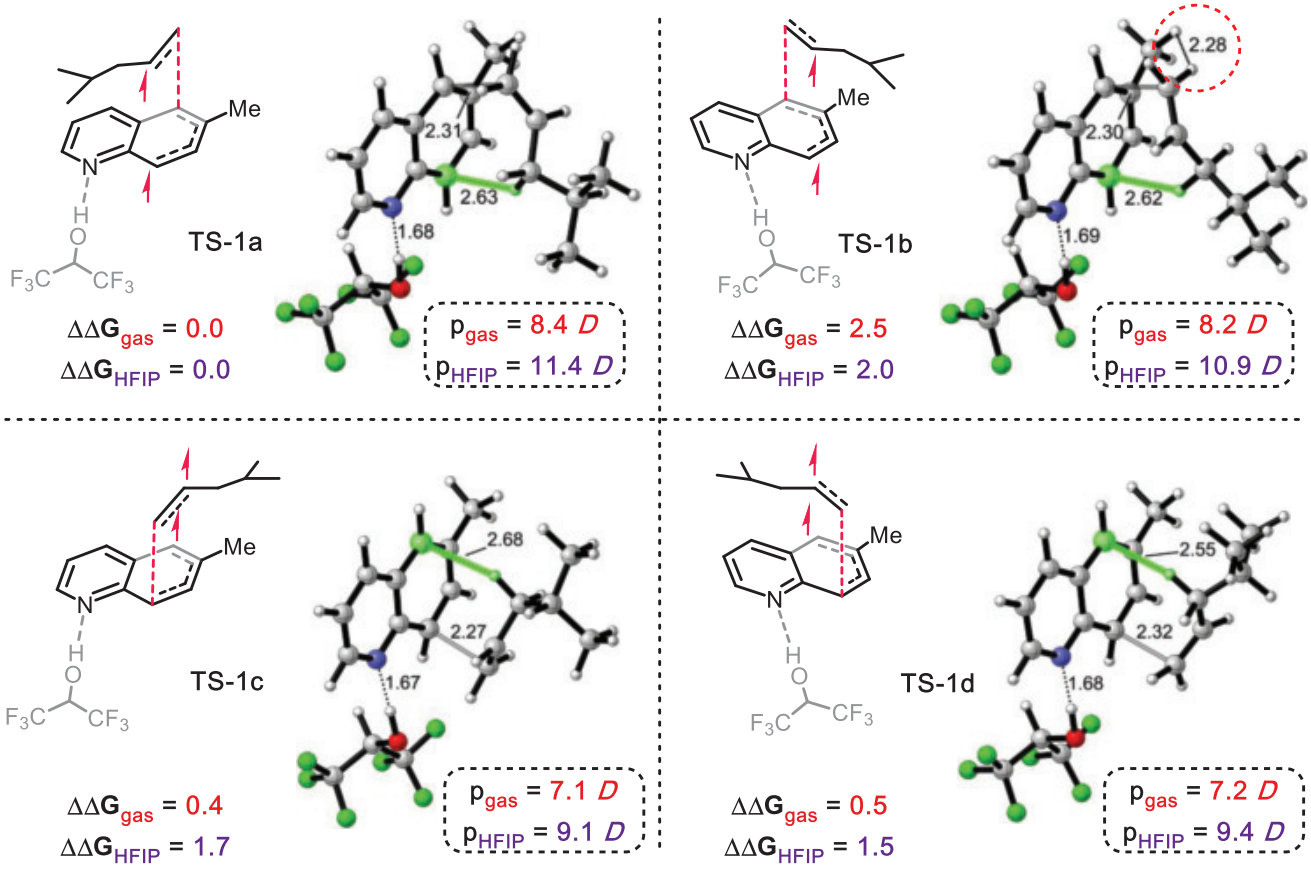

Fig. 3. Mechanistic investigation. (**A**) Experimental investigation (figs. S3 to S12 and tables S8 to S10). (**B**) Computational investigation. Calculated C–C-forming TS geometries, energies, and dipole moments are shown for the [4 + 2] DAC reaction between triplet **1b** and **2b** at the ωB97X-D/6-311++G(d,p.), SMD (HFIP)//ωB97X-D/6-31G(d), SMD (HFIP) level of theory. Energies are in kcal·mol^{-1}. Interatomic distances are in angstroms. Green highlights indicate interactions between developing radical SOMOs and allylic C–H bonds. D, Debye; E_T, triplet state energy; NOE, nuclear Overhauser effect; p, dipole moment; PS, photosensitizer.

destabilizing steric clash (H…H distance 2.28 Å) exists between the approaching alkene and the methyl substituent on quinoline **1b** in **TS-1b**. This steric clash is absent from the **TS-1a**, contributing to the high diastereoselectivity ($\Delta\Delta G^{\ddagger}$ 2.0 kcal·mol^{-1}). The effects of dispersion were calculated to be insignificant for this reaction (see supplementary materials). Calculated selectivities for the reaction between **1b** and styrene (**2c**) found similarly good agreement with experimental observations, with π-π stacking as an important determining factor of TS geometries and energies (fig. S20).

Scope of the [4 + 2] DAC reaction

Having assessed the feasibility of the dearomative approach, we evaluated the reaction scope with respect to the bicyclic azaarenes (Fig. 4). In general, the quinolines bearing substituents at each of the 2 to 8 positions are compatible in this [4 + 2] DAC reaction. Accordingly, under condition B, 2-, 3-, or 4-alkyl–substituted quinolines were converted to the corresponding dearomatization products **7** to **10** in good yields and regio- and diastereoselectivities. Condition A was applied for the 5-, 6-, 7-, or 8-substituted quinolines, thus giving the products **11** to **31** with notable regio- and diastereocontrol. The anti regioselectivity was observed as predominant when using 2-, 3-, 4-, 5-, or 7-substituted quinolines (products **7** to **11**, **13**, and **15**). A reverse order of addition (syn regioselectivity) occurred when

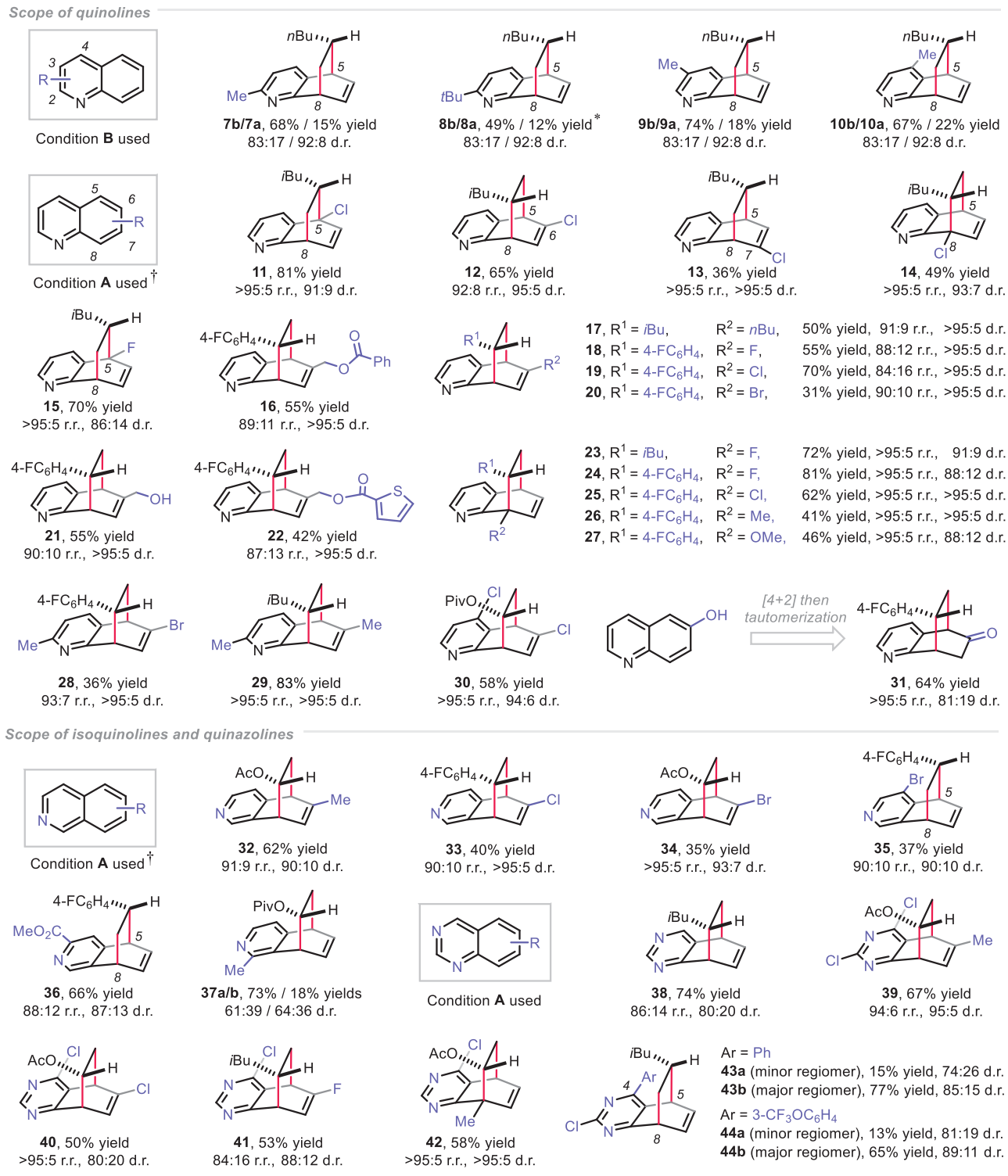

Fig. 4. Scope of bicyclic azaarenes. *NMR yield of minor regiomer **8a** is presented. †HCl (2 equiv) was used. r.r. and d.r. are determined by crude ^{1}H NMR analysis. For experimental details, see supplementary materials. Ac, acetyl; Piv, pivalyl; *t*Bu, tertiary butyl.

using 6- or 8-substituted quinolines (products **12**, **14**, and **16** to **31**). HCl (2 equiv) was added to accelerate the reaction or to promote the conversion of the less reactive 5- or 8-position–substituted quinolines (products **11**, **14**, and **15**) (tables S5 to S7). 6-Hydroxyquinoline proved amenable to the [4 + 2] DAC reaction by providing a ketone **31** through the tautomerization of an enol intermediate. Likewise, both isoquinolines and quinazolines showed good compatibility in the [4 + 2] DAC reaction (products **32** to **44**). As a limitation, when 1-methyl isoquinoline was applied in this transformation, two separable regiomers **37a** and **37b** were afforded with modest levels

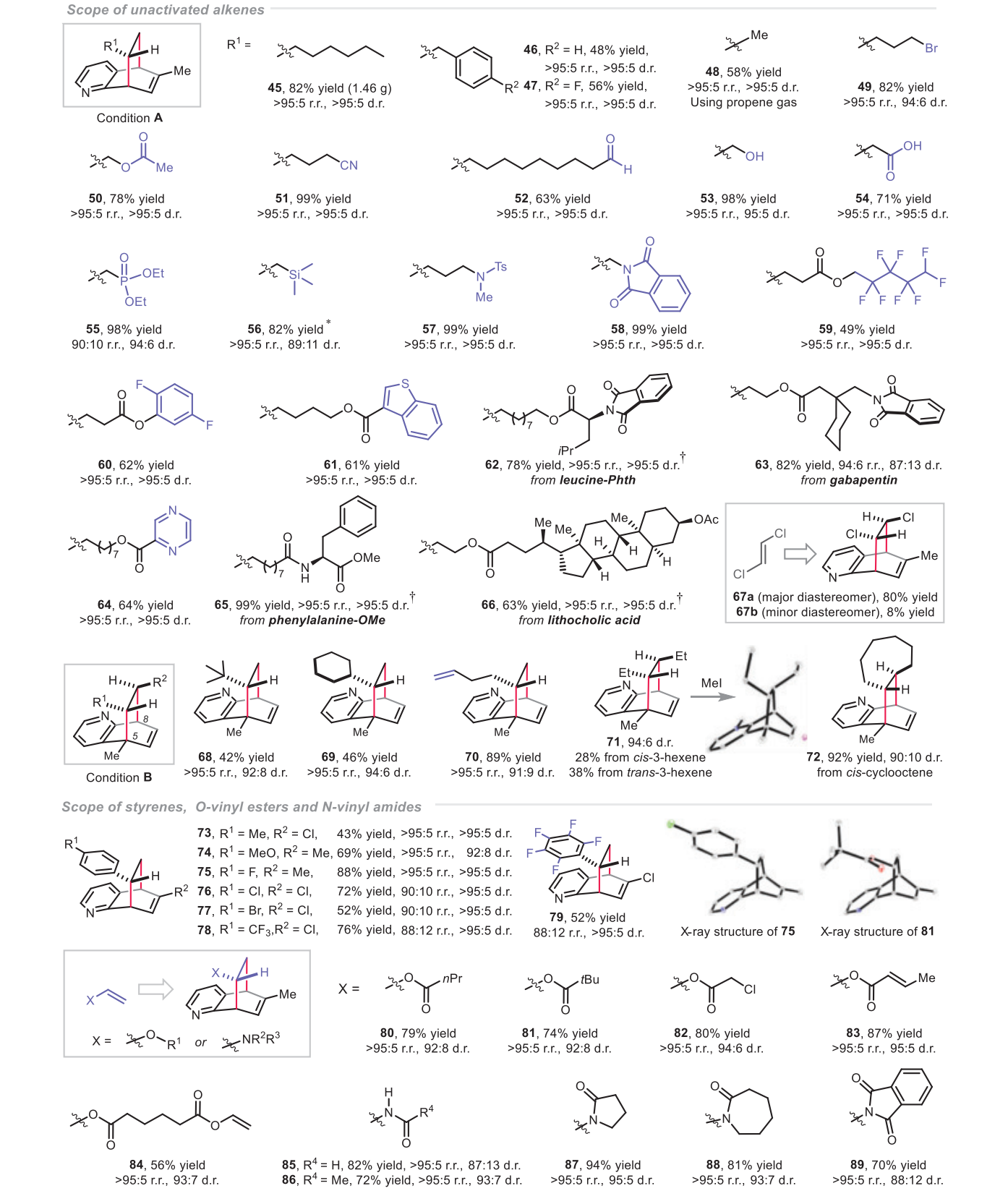

Fig. 5. Scope of alkenes. *Photosensitizer Ir(*d*F-Me-ppy)$_2$(dtbpy)(PF$_6$) was used. †The d.r. value refers to the [4 + 2] cycloaddition resulted motif of the product. HCl (2 equiv) was used for obtaining **46** to **47**, **57** to **60**, **62**, **64** to **65**, **75** to **84**, and **88** to **89**. r.r. and d.r. are determined by crude ^{1}H NMR analysis. For experimental details, see supplementary materials. *i*Pr, isopropyl; Phth, *N*-phthalimido.

of diastereoselectivity. With respect to quinazolines, the syn regioselectivity was commonly observed (products **38** to **42**). However, when 4-aryl quinazolines were used as substrates, the reverse anti regiomers became predominant (**43b** and **44b** versus **43a** and **44a**).

A quite broad scope of unactivated and activated alkenes proved amenable substrates, as presented in Fig. 5. Excellent functional group compatibility was observed, such as bromo (**49**), ester (**50**), nitrile (**51**), aldehyde (**52**), hydroxyl (**53**), carboxylic acid (**54**), phosphate (**55**), silane (**56**), sulfonamide (**57**), phthalimide (**58**), polyfluorinated alkane or arene (**59** and **60**), benzothiophene (**61**), pyrazine (**64**), and many bioactive motifs (**62**, **63**, **65**, and **66**). The [4 + 2] DAC reaction also proceeded efficiently with gaseous propene (2 bar), thus giving **48** in 58% yield as a single regiomer and diastereomer. A gram-scale reaction was performed by using 6-methyl quinoline and 1-octene to afford 1.46 g of **45** [5.73 mmol, 82% yield, >95:5 regioisomeric ratio (r.r.), and >95:5 diastereomeric ratio (d.r.)] (see detailed step-by-step protocol in the

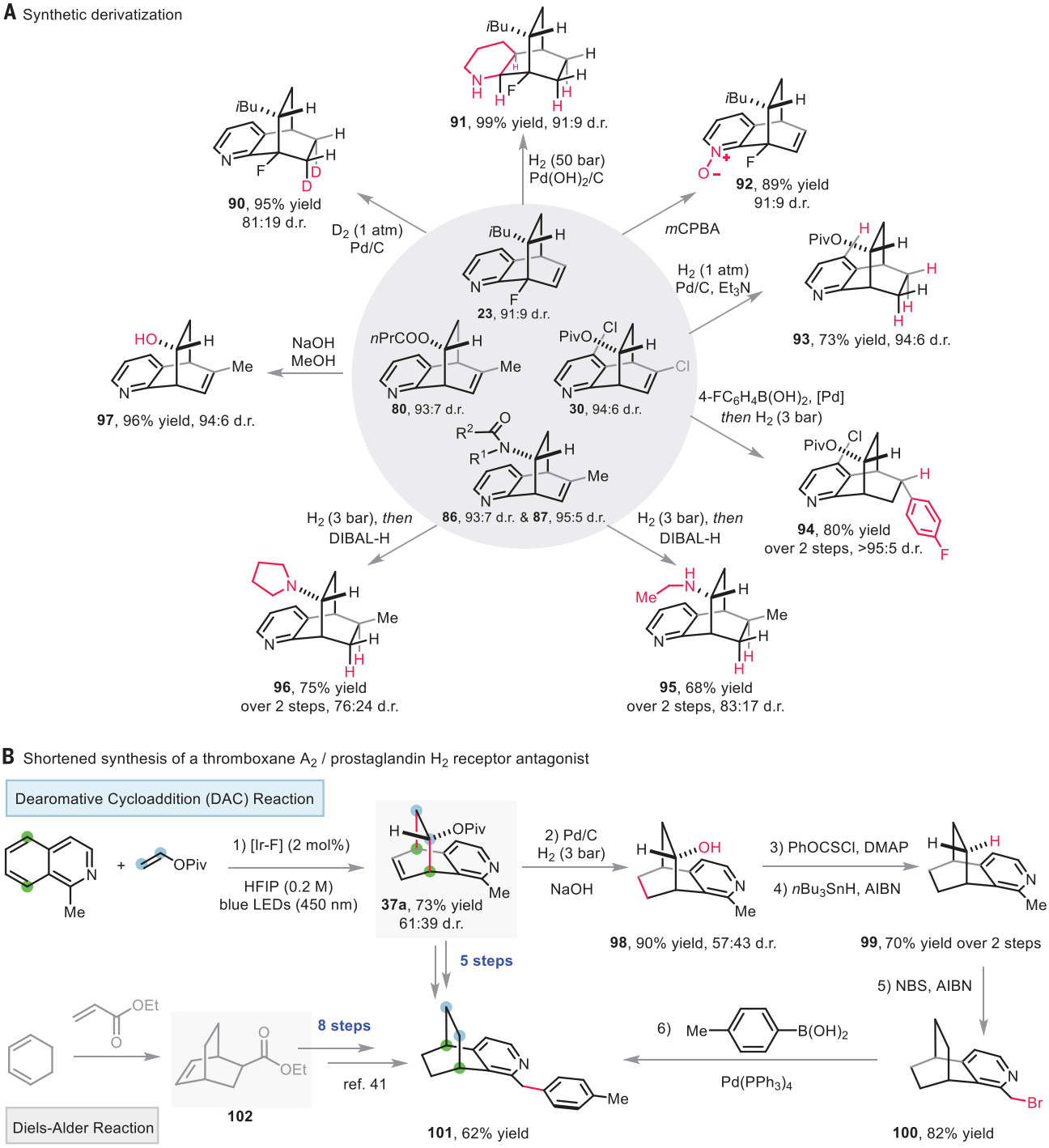

Fig. 6. Synthetic applications. (**A**) Synthetic derivatization of the [4 + 2] DAC products. (**B**) Shortened synthesis of a thromboxane A_2/prostaglandin H_2 receptor antagonist **101**. d.r. displayed here were determined by ^{1}H NMR analysis of purified compounds. AIBN, azobisisobutyronitrile; DIBAL-H, diisobutylaluminum hydride; DMAP, *N*,*N*-4-dimethylaminopyridine; LED, light-emitting diode; *m*CPBA, *meta*-chloroperbenzoic acid; NBS, *N*-bromosuccinimide.

supplementary materials). An internal alkene, *trans*-1,2-dichloroethylene, was also compatible and gave the target product as two separable diastereomers, **67a** and **67b**. Aiming at the construction of challenging all-carbon quaternary stereocenters, 5-methyl quinoline was coupled with a plethora of alkenes under condition B, thus providing the corresponding products (**68** to **70**) with good yields and selectivities. Stereoconvergence was observed when using *trans*- or *cis*-3-hexene, respectively, thus consistently leading to the product **71** with excellent trans diastereoselectivity. *cis*-Cyclooctene was applicable to provide **72** in 92% yield and with good trans diastereoselectivity (90:10). By contrast, unsymmetrical 1,2-disubstituted alkenes displayed decreased selectivity toward the corresponding products. Trisubstituted and tetrasubstituted alkenes proved not compatible with this transformation (tables S11 and S12). Various electronically diverse styrenes, *O*-vinyl esters, and *N*-vinyl amides are also applicable in the [4 + 2] DAC reaction (products **73** to **89**), providing excellent levels of both regio- and diastereocontrol. X-ray structures of **75** and **81** are presented to confirm the configuration of the products. A complementary scope of alkenes is available in the supplementary materials (table S13). Additionally, to improve the user-friendliness and enhance the reproducibility of this method, an assessment of the condition-based sensitivity was performed (*40*). As a result, this reaction was found to be comparatively sensitive to oxygen and high temperature. A slightly decreased yield was observed when the reaction was scaled up by 70 times, albeit under reduced photosensitizer loading. By contrast, the concentration of substrates, moisture, and light intensity did not show any notable influence on the reaction (fig. S21).

Synthetic applications

Next, derivatization of the obtained [4 + 2] DAC products toward relevant three-dimensional scaffolds was conducted (Fig. 6A). Starting from **23**, chemoselective reductions were performed under D_2 atmosphere (1 atm) or H_2 (50 bar), thus affording a deuterated tetrahydro 5,8-ethanoquinoline **90** or a fully saturated decahydro 5,8-ethanoquinoline **91**, respectively. Compound **23** could also be converted to the pyridine *N*-oxide **92** by chemoselective *meta*-chloroperbenzoic acid oxidation, without epoxidation of the remaining C=C double bond. All these motifs are accompanied by a pharmaceutically appealing fluorinated quaternary stereocenter that has been readily introduced by the [4 + 2] DAC reaction using commercial 8-fluoroquinoline. The polychlorinated dearomatization product **30** can undergo a dechlorination-reduction reaction to give **93**. The alkenyl chloride of **30** was chemoselectively coupled with 4-fluorophenylboronic acid, overcoming the presence of the heteroaryl chloride, under palladium catalysis. After facile hydrogenation, **94** was afforded in 80% yield over two steps and as a single diastereomer. Starting from the amide-containing dearomatization products **86** and **87**, a sequential two-step reduction reaction provided a secondary amine **95** and a tertiary one, **96**, respectively. Likewise, an alcohol (**97**) was produced by a convenient hydrolysis of compound **80**. To emphasize the applicability of this [4 + 2] DAC reaction toward biologically active compounds, the shortened synthesis of a thromboxane A_2/prostaglandin H_2 receptor antagonist (**101**) is presented (Fig. 6B) (*41*). Accordingly, the dearomatization product ***37a*** was reduced and hydrolyzed in a one-pot reaction to give **98**. A subsequent Barton-McCombie deoxygenation gave **99** as a single diastereomer. After benzylic bromination, a palladium-catalyzed cross-coupling delivered the target compound **101**. Compared with the original eight-step synthesis from a conventional Diels-Alder reaction product **102**, only five steps are needed by starting from the dearomatization product ***37a*** to access the terminal product **101**. Overall, the [4 + 2] DAC reaction could provide a direct and efficient access to various functionalized bridged polycycles that have previously been inaccessible or required strenuous synthetic efforts.

Given the emerging interest in bridged polycycles in medicinal chemistry (*42*, *43*), we anticipate this method will find substantial use in facilitating the efficient synthesis of such scaffolds.

REFERENCES AND NOTES

1. B. M. Trost, *Science* **254**, 1471–1477 (1991).
2. P. A. Wender, V. A. Verma, T. J. Paxton, T. H. Pillow, *Acc. Chem. Res.* **41**, 40–49 (2008).
3. S. Kobayashi, K. A. Jørgensen, Eds., *Cycloaddition Reactions in Organic Synthesis* (Wiley, 2002).
4. W. Carruthers, *Cycloaddition Reactions in Organic Synthesis*. (Elsevier, 2013).
5. K. C. Nicolaou, S. A. Snyder, T. Montagnon, G. Vassilikogiannakis, *Angew. Chem. Int. Ed.* **41**, 1668–1698 (2002).
6. K. Weissermel, H.-J. Arpe, Eds., *Industrial Organic Chemistry* (Wiley, 2008).
7. J. C. C. Atherton, S. Jones, *Tetrahedron* **59**, 9039–9057 (2003).
8. R. Remy, C. G. Bochet, *Chem. Rev.* **116**, 9816–9849 (2016).
9. C. Zheng, S.-L. You, *Chem* **1**, 830–857 (2016).
10. W. C. Wertjes, E. H. Southgate, D. Sarlah, *Chem. Soc. Rev.* **47**, 7996–8017 (2018).
11. Z. Siddiqi, W. C. Wertjes, D. Sarlah, *J. Am. Chem. Soc.* **142**, 10125–10131 (2020).
12. J. A. Leitch, T. Rogova, F. Duarte, D. J. Dixon, *Angew. Chem. Int. Ed.* **59**, 4121–4130 (2020).
13. J. Preindl, S. Chakrabarty, J. Waser, *Chem. Sci.* **8**, 7112–7118 (2017).
14. Q. Xiong, S. Dong, Y. Chen, X. Liu, X. Feng, *Nat. Commun.* **10**, 2116 (2019).
15. C. W. Bird, *Tetrahedron* **52**, 9945–9952 (1996).
16. F. Strieth-Kalthoff, M. J. James, M. Teders, L. Pitzer, F. Glorius, *Chem. Soc. Rev.* **47**, 7190–7202 (2018).
17. Q.-Q. Zhou, Y.-Q. Zou, L.-Q. Lu, W.-J. Xiao, *Angew. Chem. Int. Ed.* **58**, 1586–1604 (2019).
18. F. Strieth-Kalthoff, F. Glorius, *Chem* **6**, 1888–1903 (2020).
19. F. Strieth-Kalthoff *et al.*, *Chem* **5**, 2183–2194 (2019).
20. M. J. James, J. L. Schwarz, F. Strieth-Kalthoff, B. Wibbeling, F. Glorius, *J. Am. Chem. Soc.* **140**, 8624–8628 (2018).
21. M. Zhu, C. Zheng, X. Zhang, S.-L. You, *J. Am. Chem. Soc.* **141**, 2636–2644 (2019).
22. J. Ma *et al.*, *Chem* **5**, 2854–2864 (2019).
23. M. Zhu *et al.*, *CCS Chem.* **2**, 652–664 (2020).
24. M. S. Oderinde *et al.*, *J. Am. Chem. Soc.* **142**, 3094–3103 (2020).
25. Z. Zhang *et al.*, *ACS Catal.* **10**, 10149–10156 (2020).
26. A. B. Rolka, B. Koenig, *Org. Lett.* **22**, 5035–5040 (2020).
27. M. Zhu, X. Zhang, C. Zheng, S.-L. You, *ACS Catal.* **10**, 12618–12626 (2020).
28. T. Miura, Y. Funakoshi, M. Murakami, *J. Am. Chem. Soc.* **136**, 2272–2275 (2014).
29. B. M. Trost, V. Ehmke, B. M. O'Keefe, D. A. Bringley, *J. Am. Chem. Soc.* **136**, 8213–8216 (2014).
30. H. V. Pham, A. S. Karns, C. D. Vanderwal, K. N. Houk, *J. Am. Chem. Soc.* **137**, 6956–6964 (2015).
31. L. Shen *et al.*, *J. Am. Chem. Soc.* **139**, 13570–13578 (2017).
32. T. Inami, T. Takahashi, T. Kurahashi, S. Matsubara, *J. Am. Chem. Soc.* **141**, 12541–12544 (2019).
33. J. Lee, D. Ko, H. Park, E. J. Yoo, *Chem. Sci.* **11**, 1672–1676 (2020).
34. I. Colomer, A. E. R. Chamberlain, M. B. Haughey, T. J. Donohoe, *Nat. Rev. Chem.* **1**, 0088 (2017).
35. V. Pozhydaiev, M. Power, V. Gandon, J. Moran, D. Lebœuf, *Chem. Commun.* **56**, 11548–11564 (2020).
36. E. M. Sherbrook, H. Jung, D. Cho, M.-H. Baik, T. P. Yoon, *Chem. Sci.* **11**, 856–861 (2020).
37. T. R. Blum, Z. D. Miller, D. M. Bates, I. A. Guzei, T. P. Yoon, *Science* **354**, 1391–1395 (2016).
38. X. Huang, E. Meggers, *Acc. Chem. Res.* **52**, 833–847 (2019).
39. E. Chénard *et al.*, *J. Phys. Chem. C* **120**, 8461–8471 (2016).
40. L. Pitzer, F. Schäfers, F. Glorius, *Angew. Chem. Int. Ed.* **58**, 8572–8576 (2019).
41. S. L. Saha *et al.*, *Bioorg. Med. Chem.* **10**, 2779–2793 (2002).
42. F. Lovering, J. Bikker, C. Humblet, *J. Med. Chem.* **52**, 6752–6756 (2009).
43. P. K. Mykhailiuk, *Org. Biomol. Chem.* **17**, 2839–2849 (2019).

ACKNOWLEDGMENTS

We thank X. Huang (UIUC), J. Li, S. Mondal, T. Pinkert, T. Paulisch, and F. Strieth-Kalthoff (all WWU) for assistance and discussions. **Funding:** Generous financial support by the European Research Council (ERC Advanced Grant Agreement no. 788558) and the Deutsche Forschungsgemeinschaft (SFB 858, Leibniz Award) is gratefully acknowledged. M.K.B. and R.G. thank National Institutes of Health (R35GM131755) for financial support. K.N.H. thanks the National Science Foundation (grant CHE-1764328) for financial support. Calculations were performed on the Hoffman2 cluster at the University of California, Los Angeles, and the Extreme Science and Engineering Discovery Environment, which is supported by the National Science Foundation (grant OCI-1053575). **Author contributions:** F.G., M.K.B., J.M., and R.G. conceived the project. J.M. and R.G. discovered the HFIP and $BF_3{\cdot}OEt_2$ conditions independently. J.M., P.B., R.G., F.S., A.H., and X.Z. performed the synthetic experiments. S.C. performed the DFT calculations. C.D. analyzed the x-ray structures. J.M., S.C., M.K.B., K.N.H., and F.G. supervised the research and wrote the manuscript with contributions from all authors. **Competing interests:** The authors declare no competing interests. **Data and materials availability:** Characterization of compounds and detailed reaction optimization and mechanistic studies are provided in the supplementary materials; crystallographic data are available free of charge under Cambridge Crystallographic Data Centre (CCDC) reference numbers 2041010 (intermediate **I'**), 2060268 (**71**·MeI), 2041012 (**75**), 2041013 (**81**), and 2041014 (**89**·HCl).

SUPPLEMENTARY MATERIALS

science.sciencemag.org/content/371/6536/1338/suppl/DC1
Materials and Methods
Supplementary Text
Figs. S1 to S27
Tables S1 to S16
NMR Spectra
References (*44*–*75*)

8 December 2020; accepted 9 February 2021
10.1126/science.abg0720

PALEOCEANOGRAPHY

A 35-million-year record of seawater stable Sr isotopes reveals a fluctuating global carbon cycle

Adina Paytan[1]*, Elizabeth M. Griffith[2], Anton Eisenhauer[3], Mathis P. Hain[1], Klaus Wallmann[3], Andrew Ridgwell[4]

Changes in the concentration and isotopic composition of the major constituents in seawater reflect changes in their sources and sinks. Because many of the processes controlling these sources and sinks are tied to the cycling of carbon, such records can provide insights into what drives past changes in atmospheric carbon dioxide and climate. Here, we present a stable strontium (Sr) isotope record derived from pelagic marine barite. Our $\delta^{88/86}$Sr record exhibits a complex pattern, first declining between 35 and 15 million years ago (Ma), then increasing from 15 to 5 Ma, before declining again from ~5 Ma to the present. Numerical modeling reveals that the associated fluctuations in seawater Sr concentrations are about ±25% relative to present-day seawater. We interpret the $\delta^{88/86}$Sr data as reflecting changes in the mineralogy and burial location of biogenic carbonates.

Secular variations in seawater radiogenic Sr isotope ratios ($^{87}Sr/^{86}Sr$) reflect changes in the relative input of Sr from weathering and hydrothermal activity and the $^{87}Sr/^{86}Sr$ composition of these fluxes (*1*), providing insights into links between silicate weathering and atmospheric partial pressure of CO_2 (pCO_2) (*2*, *3*). However, changes in seawater $^{87}Sr/^{86}Sr$ arise from multiple processes, complicating the relationship between $^{87}Sr/^{86}Sr$ and silicate weathering (*4*). By contrast, stable Sr isotopes ($\delta^{88/86}$Sr) respond to changes in both the ocean's Sr sources and carbonate sink (Fig. 1). The ocean Sr loss (output) is affected not only by net $CaCO_3$ deposition but also by varying relative proportions of $CaCO_3$ deposited in pelagic or neritic settings, with each environment being dominated by a different $CaCO_3$ mineralogy with differing Sr content. Specifically, changes in the deposition and/or dissolution of Sr-rich neritic $CaCO_3$ (i.e., aragonite) will result in a larger effect on the seawater Sr budget than changes in Sr-poor (calcitic) pelagic $CaCO_3$, such that $\delta^{88/86}$Sr is affected by changes in both the net rate of $CaCO_3$ burial and its neritic-pelagic partitioning (*5*, *6*).

When combined, measurements of $\delta^{88/86}$Sr and $^{87}Sr/^{86}Sr$ thus offer the potential for detecting past changes in sources and sinks of Sr associated with continental weathering, hydrothermal activity, and carbonate deposition (Fig. 1) (*5*–*7*). Here, we reconstructed a 35-million-year (Myr) seawater $\delta^{88/86}$Sr (and $^{87}Sr/^{86}Sr$) record from marine barite, and used a mass balance model (see the materials and methods section in the supplementary materials) to estimate changes in seawater Sr concentration [Sr] resulting from imbalances between the total flux of Sr into and out of the ocean to infer past changes in carbonate deposition that could affect the C cycle.

Results

The measured $^{87}Sr/^{86}Sr$ values in 10 core-top barite samples reflect the present-day seawater value [0.709165 ± 0.000005 (2σ)]. The average $\delta^{88/86}$Sr in these samples is −0.146‰ (relative to SRM987), reflecting an isotopic offset of −0.536‰ from modern seawater (*8*). The core-top samples encapsulate a total (max-min) range in $\delta^{88/86}$Sr of 0.038‰ (table S1), a range larger than the analytical uncertainty in our measurements (±0.02) (*5*). This variability is unlikely to be a temperature effect because the temperature at the depth of barite formation (~700 m) for these samples ranges from 1 to 14°C, and there is no correlation between $\delta^{88/86}$Sr and temperature (see discussion section in the supplementary materials). This offset is consistent with expectations based on previous work on synthetic and continental barite (*9*, *10*) and data reported in Griffith *et al.* (*11*). This variability likely represents the range of $\delta^{88/86}$Sr in seawater during the time span represented by the upper 5 cm of sediments [up to 10,000 years (*12*)]. Therefore, rather than contemporary seawater $\delta^{88/86}$Sr, our core-top average reflects variability in the Holocene seawater composition of a few hundredths of a permille.

Down-core $\delta^{88/86}$Sr shows coherent changes spanning 0.1‰ (Fig. 2 and table S1). This is more than twice the range measured in core tops and more than five times the analytical

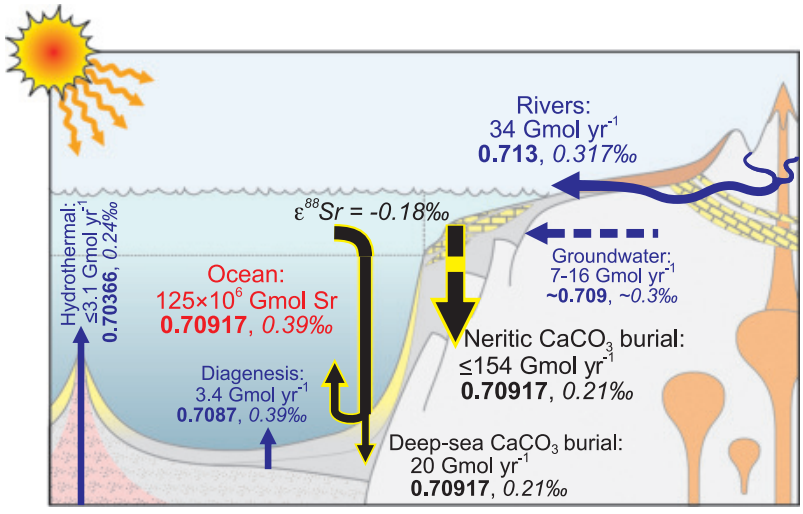

Fig. 1. Schematic diagram of the modern global Sr cycle illustrating the main controlling fluxes (Gmol Sr yr^{-1}) and ocean inventory. Mean isotope values are shown in bold for radiogenic Sr and in italics for stable Sr. The present-day average flux weighted river input to the ocean has an $^{87}Sr/^{86}Sr$ of 0.713 and $\delta^{88/86}$Sr of 0.317‰ (*7*), and this $\delta^{88/86}$Sr value corresponds to an average of different lithologies (silicate 0.58‰ and carbonates 0.18‰). Groundwater inputs have an average $^{87}Sr/^{86}Sr$ ratio of 0.709 and $\delta^{88/86}$Sr of ~0.3‰, and oceanic hydrothermal sources have an average $^{87}Sr/^{86}Sr$ ratio of 0.70366 and $\delta^{88/86}$Sr of 0.24‰ (*7*). The major oceanic Sr sink is the removal of Sr into marine $CaCO_3$, which preferentially incorporates the lighter Sr isotopes with an average isotope offset $\varepsilon(\delta^{88/86}Sr)$ of −0.18‰, resulting in average $CaCO_3$ $\delta^{88/86}$Sr of ~0.21‰ at present (*6*). Seawater $^{87}Sr/^{86}Sr$ at present is 0.70917 and the $\delta^{88/86}$Sr of seawater is 0.39‰, the latter being elevated above the $\delta^{88/86}$Sr of the inputs caused by preferential removal of light Sr isotopes into $CaCO_3$ (i.e., negative ε) driving seawater isotopically heavier. Dashed lines indicate more uncertain fluxes and isotopic compositions. Fluxes are compiled from the literature (see the supplementary materials). Note that available data suggest a large present-day Sr imbalance, so the Sr sink is substantially larger than the combined sources.

[1]Institute of Marine Science, University of California Santa Cruz, Santa Cruz, CA 95064, USA. [2]School of Earth Sciences, The Ohio State University, Columbus, OH 43210, USA. [3]GEOMAR Helmholtz Centre for Ocean Research Kiel, 24148 Kiel, Germany. [4]Department of Earth Sciences and Planetary Sciences, University of California Riverside, Riverside, CA 92521, USA.
*Corresponding author. Email: apaytan@ucsc.edu

uncertainty. Although the range is small, the consistency of the trend produced from samples from different locations offers strong evidence for a global seawater $\delta^{88/86}Sr$ signal and is not an artifact of barite preservation (which would result in a unidirectional change with burial and different signatures at sites with different burial history). Furthermore, our down-core $^{87}Sr/^{86}Sr$ record, measured on the same samples, is consistent with the well-established seawater curve [Fig. 2A and table S1] (*13*). Even if we assume that core-top variability is noise (rather than being signal specific to the past few million years) and that this noise is present throughout the 35-Myr interval, it should be impossible to randomly generate the highly coherent record that we present (Fig. 2B). The temporal coherence in our record strongly argues against a random process.

Past seawater $\delta^{88/86}Sr$ was reconstructed based on the barite record by applying a constant offset of 0.536‰. The resulting record ranges between ~0.3 and 0.4‰, which is within the range of Phanerozoic seawater $\delta^{88/86}Sr$ derived from brachiopods (*6*). The highest values over the past 35 Myr occurred in the Early Oligocene; $\delta^{88/86}Sr$ decreased by ~0.08‰ over the following ~20 million years, reaching a minimum in the Middle Miocene at ~15 Myr ago (Ma), after which time the $\delta^{88/86}Sr$ increased by ~0.06‰ to a high in the Early Pliocene (~5 to 3.5 Ma), sharply decreasing by ~0.04‰ thereafter. These $\delta^{88/86}Sr$ changes suggest that the marine Sr cycle since the Oligocene has been very dynamic, and that fluctuations were not unidirectional, as seen for the $^{87}Sr/^{86}Sr$, which increased over this time interval.

Holocene and Pleistocene seawater Sr

Holocene core-top barites have a higher $\delta^{88/86}Sr$ value (−0.146‰) than the average value of all down-core samples representing the past ~2.5 Myr (−0.186‰, corresponding to an average seawater value of 0.35‰), which themselves represent a range of −0.147 to −0.229‰ (table S1). In other words, seawater $\delta^{88/86}Sr$ fluctuated considerably during the Holocene-Pleistocene (between ~0.31 and 0.39‰), with peak values around the core-top $\delta^{88/86}Sr$. Previous work based on the deviation of seawater $^{87}Sr/^{86}Sr$ from that expected from the total Sr input to the ocean measured in modern sources (terrestrial and hydrothermal) showed that seawater Sr sources and sinks are out of balance at present, which was attributed to intensified weathering related to Northern Hemisphere glaciation (*5*, *7*, *14*, *15*) (fig. S1). The observed difference between our core-top $\delta^{88/86}Sr$ and the long-term Pleistocene average directly documents this imbalance. Our record of the past 2.5 Ma, although documenting considerable fluctuations in $\delta^{88/86}Sr$, is only aliasing rather than fully resolving the likely frequency of variability. Higher-resolution data from additional sites over this time interval are needed to better understand the nature of these fluctuations and their relationship to glacial-interglacial cycles. We suggest that these fluctuations are specific to the Pleistocene and stem from the rapid and large sea-level fluctuations resulting from Northern Hemisphere glaciations (see discussion section in the supplementary materials).

A 35-Myr record of seawater Sr

For most of the past 35 Myr, changes in seawater $\delta^{88/86}Sr$ did not systematically correspond to changes in $^{87}Sr/^{86}Sr$ (Fig. 2), suggesting that the two records are largely controlled by different processes and implying that they can be modeled independently to the first order. Specifically, the most important processes that control oceanic $\delta^{88/86}Sr$ (the uptake or release of Sr from neritic carbonates) impose only a secondary and small impact on $^{87}Sr/^{86}Sr$ by changing the bulk Sr inventory of the ocean. This is because the $^{87}Sr/^{86}Sr$ signature of neritic carbonates is nearly identical to that of seawater $^{87}Sr/^{86}Sr$ (Fig. 1).

To explain the variations in seawater $\delta^{88/86}Sr$, we derived the expression for seawater $\delta^{88/86}Sr$ change over time, without making any steady-state assumption, as follows (see derivation in the supplementary materials):

$$\frac{\Delta\delta_{SW}}{\Delta t} = \left(\frac{\delta_{IN} - \varepsilon - \delta_{SW}}{\tau}\right) + \left(\frac{\varepsilon}{Sr} * \frac{\Delta Sr}{\Delta t}\right)$$

where δ_{SW} and δ_{IN} are the $\delta^{88/86}Sr$ of seawater and of Sr input to the ocean, respectively, ε is the isotopic offset during Sr incorporation into $CaCO_3$, τ is the e-folding time scale for δ_{SW} to relax toward isotopic steady state (i.e., if Sr inventory is at steady state, then τ equates to the residence time of Sr in the ocean), and $\Delta\delta_{SW}/\Delta t$ and $\Delta Sr/\Delta t$ are the time derivatives of δ_{SW} and the ocean's Sr inventory, respectively. This expression separates $\delta^{88/86}Sr$ changes caused by isotope mass balance when the Sr budget is in balance (the first term) from the $\delta^{88/86}Sr$ change caused by an imbalance in the ocean's Sr budget (the second term). Any change in seawater $\delta^{88/86}Sr$ may be the result of either of two end-member explanations, changes in δ_{IN} or [Sr], which we consider separately below.

The first end-member explanation posits a balanced Sr budget (i.e., $\Delta Sr/\Delta t = 0$), such that seawater $\delta^{88/86}Sr$ change is entirely caused by the first term in Eq. 1, which describes how δ_{SW} relaxes toward a value at which $\delta^{88/86}Sr$ of $CaCO_3$ burial (i.e., $\delta_{SW} + \varepsilon$) is equal to δ_{IN}. Therefore, if δ_{IN}, Sr input flux (F_{IN}), and [Sr]

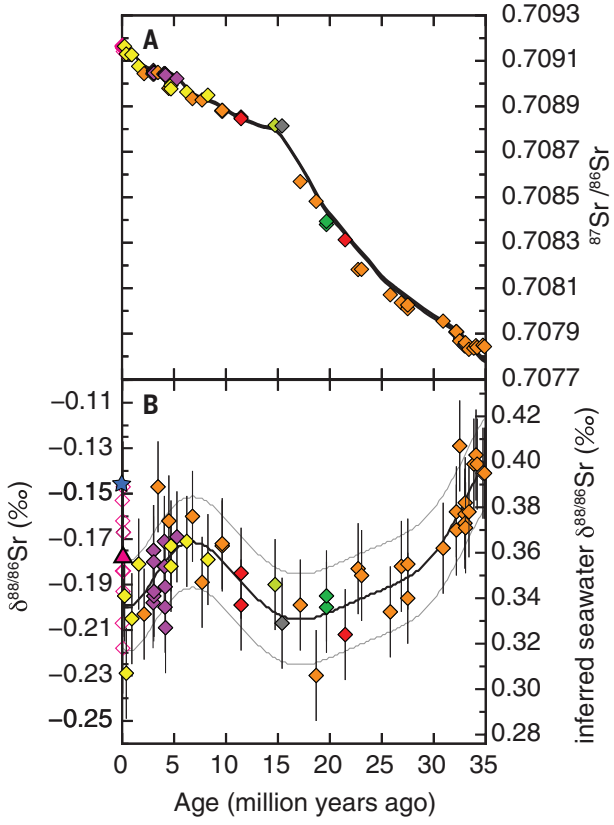

Fig. 2. Sr isotope records over the past 35 Myr. (**A**) Radiogenic Sr isotope record in marine barite separated from several sites over the past 35 Myr (errors are smaller than the symbol size), along with the seawater Sr isotope curve (gray line) from McArthur *et al.* (*13*). Slight differences between the curves are likely due to differences in the age models used. (**B**) Stable Sr isotope record of these down-core marine barite samples with a polynomial curve fit (black line) ± 0.02‰ analytical uncertainty (gray lines). All data are provided in table S1. The inferred seawater $\delta^{88/86}Sr$ was determined by adding the constant isotopic offset (fractionation) of 0.536‰ based on core-top data. Site 572 is shown in yellow; Site 573, red; Site 574, orange; Site 575, green; Site 849, purple; Site 1218, dark green; and Site 1219, gray. The average $\delta^{88/86}Sr$ core top value (−0.146‰) is marked with a blue star, and the average PC72 value (−0.178‰) is marked with a pink triangle (individual measurements are shown as open pink diamonds because they were not used in the fit); the core-top average is not included in the polynomial fit (see discussion section in the supplementary materials).

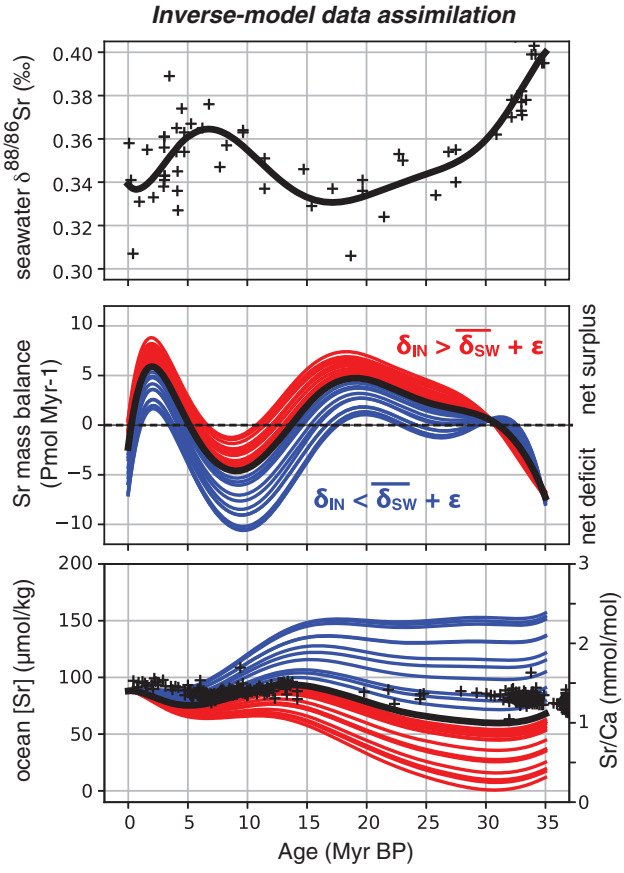

Fig. 3. Sr isotope mass balance model results under the simplifying assumption of constant Sr input to the ocean. The symbols for $\delta^{88/86}$Sr include all down-core data and the average PC72 value (−0.178‰, as the pink triangle in Fig. 2). The reconstructed seawater Sr/Ca data from Lear *et al.* (*16*) are included as + symbols in the bottom panel for comparison. These inverse model results are obtained when Eq. 1 is recast to yield Sr flux imbalance as a function of reconstructed δ_{SW} and then integrated backward in time. This approach demonstrates that the δ_{SW} data are a strong constraint on the fluctuations in the Sr mass balance, but that the integrated long-term trend in the Sr inventory depends mainly on the values chosen for δ_{IN} and for ε. Uncertainties in δ_{IN} and ε were propagated using a Monte Carlo approach, with individual runs shown in red or blue when $\delta_{IN} - \varepsilon$ was either greater or less than the long-term mean of our δ_{SW} record, respectively. See fig. S2 for more details and for the results of a forward model in which δ_{SW} is calculated from Eq. 1 using the time-varying Sr imbalance adjusted to a mean of zero to remove the long-term trend in the Sr inventory. The key outcome of this model-based analysis is that our seawater $\delta^{88/86}$Sr record is a strong constraint on changes in seawater Sr mass balance even if the secular Sr inventory trend cannot be reconstructed on the basis of our data alone.

were taken to be constant, then δ_{SW} would adjust over a few million years (i.e., 2 to 3 e-folding τ) and then remain constant at a value of $\delta_{IN} - \varepsilon$. This is in stark contrast to the observed variations in the $\delta^{88/86}$Sr record. If, however, δ_{IN} is continuously changing, then the $\delta^{88/86}$Sr record could be explained by the resulting continuous adjustments of δ_{SW}. This scenario would result in a strong, positively coupled signal in $^{87}Sr/^{86}Sr$, which we do not see. Such hypothetical changes in δ_{IN} are plausible given the spread in $\delta^{88/86}$Sr from weathering of silicate rocks or limestone [typical $\delta^{88/86}$Sr of 0.58 and 0.18‰, respectively (*7*)], the relative contribution of which may have changed over time. This hypothetical end-member scenario posits neither constant weathering Sr flux nor constant Sr burial but instead requires that Sr input and output be equal, yielding a balanced Sr budget.

The second end-member explanation posits that seawater $\delta^{88/86}$Sr changes reflect transient imbalances in the ocean's Sr budget represented by the second term in Eq. 1. If Sr input exceeds outputs (i.e., $\Delta Sr/\Delta t > 0$), then δ_{SW} will transiently decline toward δ_{IN}, whereas if Sr output exceeds input (i.e., $\Delta Sr/\Delta t < 0$), then δ_{SW} will transiently increase because of the isotopic fractionation during Sr incorporation into $CaCO_3$ and the associated isotopic Rayleigh distillation of the residual ocean Sr inventory. Because the magnitude of fractionation is large, even modest Sr budget imbalances will impart substantial transient changes in δ_{SW}. Given that Sr input and output are expected to change independently with changing climate and sea level, we regard this explanation (transient changes caused by budget imbalance) as the likely dominant driver of the seawater $\delta^{88/86}$Sr changes.

Seawater Sr and carbonate deposition

To illustrate the power of seawater $\delta^{88/86}$Sr in constraining carbonate deposition, we make the simplifying assumption that the bulk Sr input flux and its stable isotopic composition are constant through time to solve for Sr output and numerically integrate the Sr budget back through time (Fig. 3). We applied a Monte Carlo approach to assess the impact of uncertainty in the value of both δ_{IN} (2σ of 0.02‰) and ε (2σ of 0.01‰) (see the supplementary materials for details). Our analysis yields Sr budget imbalances that coherently oscillate by ±5 Pmol Myr^{-1} (10^{15} mol Myr^{-1}) to create the oscillations in our $\delta^{88/86}$Sr data, but the integrated secular [Sr] cannot be determined within simulated uncertainty (Fig. 3). Taking existing seawater Sr/Ca reconstructions (*16*) as evidence that there was no secular [Sr] trend over the past ~35 Myr, the oscillating Sr budget imbalance still integrates to up to ±25% Sr inventory oscillations (±25 Pmol; fig. S2B), with a maximum during the Middle Miocene and minima during the Oligocene and Pliocene. If these Sr budget changes were all due to changes in net $CaCO_3$ deposition, then our model results would imply fluctuations in the order of ±13% in the rate of net $CaCO_3$ burial [calculated relative to a rate of 38 Pmol Myr^{-1} (*6*)]; however, this value can vary considerably depending on the ratio of aragonite to calcite deposition. For example, if we attribute all of the change to deposition or weathering and/or diagenesis of aragonitic shelf carbonates with 8000 ppm Sr (*17*), then our modeled imbalance fluxes of ±5 Pmol Myr^{-1} would correspond to ±7.5 TgC yr^{-1} changes in net burial [i.e., only about ±5% of the mean Holocene estimated shelf burial flux, assuming 150 TgC yr^{-1} total shelf burial; see (*18*) and references therein].

Considering that changes in $^{87}Sr/^{86}Sr$ and $\delta^{88/86}$Sr do not vary uniformly over time (Fig. 4) (i.e., the records do not correlate), this is consistent with the high sensitivity of $\delta^{88/86}$Sr compared with $^{87}Sr/^{86}Sr$ to neritic carbonate deposition and/or recrystallization. As diagnosed by our model, changes in the $\delta^{88/86}$Sr of seawater respond mainly to changes in the ocean's Sr inventory, such as through changing carbonate burial, whereas the $^{87}Sr/^{86}Sr$ system is insensitive to Sr inventory changes. Conversely, increased weathering of granitic (or basaltic) rocks on land will have a large effect on $^{87}Sr/^{86}Sr$, with relatively little impact on $\delta^{88/86}$Sr as long as the weathering change does not drive a large Sr budget imbalance. Thus, the paired records of $\delta^{88/86}$Sr and $^{87}Sr/^{86}Sr$ provide an invaluable constraint in assessing changes in both continental weathering and the rate and extent of global carbonate burial (*6*).

Our record demonstrates that between 35 and ~25 Ma, when $\delta^{88/86}$Sr of seawater decreased from −0.406 to −0.336‰ but the change in $^{87}Sr/^{86}Sr$ was small, the dominant process affecting seawater [Sr] and isotope ratios was a decrease in neritic carbonate deposition possibly because of a drop in sea level over the Oligocene (*19*). Over the following 10 million years (~25 to 15 Ma), $^{87}Sr/^{86}Sr$ increased (from 0.7082 to 0.7088), whereas $\delta^{88/86}$Sr changes were small, suggesting an increase in the input of Sr from rocks with more radiogenic $^{87}Sr/^{86}Sr$ relative to input from basaltic weathering or seafloor hydrothermal sources. This is consistent with some estimates for increased erosion in the Western Greater Himalaya, as well as the

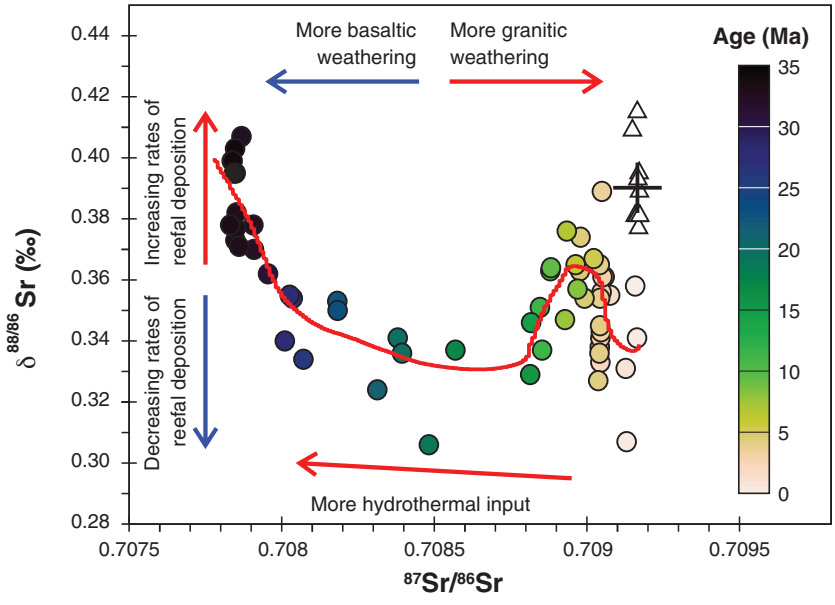

Fig. 4. Observed evolution of the Sr system in radiogenic versus stable Sr isotope space over the past 35 Myr. Circles reflect down-core barite measurements and are color-coded by sample age, and triangles reflect the core-top measurements. The cross indicates modern seawater Sr isotopic composition. All barite data are corrected for the isotopic fractionation offset of 0.536‰, and the *x*- and *y*-axis scales reflect inferred seawater Sr isotopic composition rather than measured $^{87}Sr/^{86}Sr$ and $\delta^{88/86}Sr$ of barite. The red line represents the polynomial fit to the data presented in Fig. 2. The colored arrows illustrate the approximate direction in $^{87}Sr/^{86}Sr$ and $\delta^{88/86}Sr$ space of the seawater Sr response to some of the key controlling factors: the proportion of basaltic versus granitic weathering, the hydrothermal Sr input flux to the ocean, and rates of reef $CaCO_3$ deposition.

initiation (or intensification) of the Asian monsoon in the Early Miocene (*20*, *21*). In the Middle to Late Miocene (~15 to 5 Ma), $\delta^{88/86}Sr$ increased, indicating an increase in carbonate deposition coincident with the proliferation of coral reefs (*22*) and an increase in pelagic carbonate sedimentation in the Middle Miocene (*23*). This was likely accompanied by a decrease in the rate of erosion in the Himalaya and Alps (*24*, *25*) (because $^{87}Sr/^{86}Sr$ increases at a slower rate). Finally, the last 5 Myr of the record saw a decrease in $\delta^{88/86}Sr$ to the Pleistocene average of about −0.186‰, suggesting a decrease in neritic carbonate burial (or increase in shelf carbonate diagenesis) associated with a drop in sea level and the development of Northern Hemisphere glaciation (potentially with large short-term fluctuations, as indicated by the large range of $\delta^{88/86}Sr$ in the Pleistocene and the present-day Sr imbalance). One implication of this coupled record is that we do not see a continuous increase in carbonate deposition (which would be manifested in a continuous increase in $\delta^{88/86}Sr$), as would be expected from a monotonous increase in chemical weathering and increased delivery of weathering products (alkalinity) to the ocean over the past 35 Myr.

Although changes in seawater $\delta^{88/86}Sr$ provide important insights into the Sr cycle and suggest that $CaCO_3$ burial and [Sr] have fluctuated considerably over the past 35 Myr, the system is underconstrained. Interpretations of the Sr isotope records can be refined if seawater [Sr] or the carbonate deposition history were known. Previous attempts to reconstruct seawater [Sr] (*16*, *26*–*32*), however, yielded conflicting records. Moreover, most of these records reported Sr/Ca ratios, and converting Sr/Ca in mineral deposits to seawater [Sr] involves many assumptions (e.g., unchanging or known seawater Ca concentrations) and corrections (e.g., vital effects and post deposition alteration). The record with highest resolution over the past 35 Myr (*16*) shows fluctuations in Sr/Ca that generally correspond in timing with changes in the $\delta^{88/86}Sr$, although with smaller magnitude (Fig. 3). Specifically, Lear *et al.* (*16*) showed that seawater Sr/Ca rose gradually through the Oligocene and Early Miocene, followed by a decrease until the Late Miocene and a subsequent increase toward the present day. If this Sr/Ca record is representative of seawater [Sr], then it is consistent with measurable fluctuations in seawater $\delta^{88/86}Sr$, as described above. On the basis of our model, the total Sr inventory in the ocean could have changed by up to 25%, fluctuating between ~66 and 110 μM around the present-day concentration of ~88 μM (fig. S2B). Although these changes are much larger than those calculated by Lear *et al.* (*16*), which were based on benthic foraminifera Sr/Ca ratios, some of this discrepancy may be related to the many assumptions involved in both our model and those associated with the conversion of foraminifera Sr/Ca ratios to [Sr]. We note that a change in [Sr] in the range of 25 μM over 10 to 20 million years is easily attainable considering the vast amount of Sr stored in neritic carbonates and changes in sea level that subject these deposits to deposition or recrystallization processes. These changes in [Sr] have some implications to the $^{87}Sr/^{86}Sr$ as well. The sensitivity to any changes in the input flux of Sr depends on the [Sr] in the ocean; the larger the reservoir, the more difficult it is to change, so any response to perturbation will be smaller (lower sensitivity). Therefore, [Sr] will modulate the slope of change in $^{87}Sr/^{86}Sr$. For example, between 35 and 25 Ma, when the seawater $\delta^{88/86}Sr$ decreased and thus [Sr] increased, it gradually becomes more difficult to change the Sr isotope ratios in seawater (both $^{87}Sr/^{86}Sr$ and $\delta^{88/86}Sr$). The reasonable agreement between our inferred Sr inventory changes and completely independent estimates from the Sr/Ca dataset by Lear *et al.* (*16*) is strong evidence that these (independent) records are consistent. That means that we now have internally consistent and orthogonal constraints on $\delta^{88/86}Sr$ and [Sr] through much of the Cenozoic, reducing by one the degrees of freedom of the system for the purpose of data assimilation.

Conclusions and implications

Because seawater $\delta^{88/86}Sr$ is sensitive to shallow water carbonate deposition and/or recrystallization (*33*), it provides a globally integrated estimate for the extent of reef and associated changes in carbonate depositional rates (e.g., *34*-*35*) (see the supplementary materials). Thus, if the global rate of carbonate burial in deep-sea sediments is also known, for example, by interpreting changes in the calcite compensation depth (CCD) [(*36*–*38*) but see (*39*) for a discussion of how CCD and global deep-sea burial rates can be decoupled], then combining records of changes in the CCD with $\delta^{88/86}Sr$ could give a measure of the total global carbonate burial rate. At steady state, this must equal total global terrestrial carbonate plus silicate weathering and net seafloor input of Ca^{2+} and/or Mg^{2+}; (hereafter, "alkalinity"), thus resolving the entire inorganic carbon budget of surficial Earth. The $\delta^{88/86}Sr$ record could be explained by fluctuations in the total amount and location of carbonate deposition, and the associated alkalinity changes (if any) may be derived from carbonate weathering or deposition of shelf carbonates (*23*, *35*), thus not necessarily requiring large changes in silicate weathering (*40*, *41*). Overall, $\delta^{88/86}Sr$ data provide constraints and insights into the inner workings of the global carbon cycle, and in conjunction with radiogenic Sr and other proxies raise the prospect of quantifying changes

in global carbonate burial through time. This in turn enables, with more detailed modeling of the coupled stable and radiogenic Sr, constraining the silicate weathering feedback that links atmospheric pCO_2 and temperature and thus unraveling the explanation for the generally declining trends in global temperature and atmospheric pCO_2 that have occurred over the Late Cenozoic.

REFERENCES AND NOTES

1. H. Elderfield, *Treatise on Geochemistry, Volume 6: The Oceans and Marine Geochemistry* (Elsevier, 2006).
2. R. A. Berner, *Am. J. Sci.* **294**, 56–91 (1994).
3. G. E. Ravizza, J. C. Zachos, "Records of Cenozoic ocean chemistry," in *Treatise on Geochemistry, Volume 6: The Oceans and Marine Geochemistry* (Elsevier, 2006), pp. 551–582.
4. G. Li, H. Elderfield, *Geochim. Cosmochim. Acta* **103**, 11–25 (2013).
5. A. Krabbenhöft *et al*., *Geochim. Cosmochim. Acta* **74**, 4097–4109 (2010).
6. H. Vollstaedt *et al*., *Geochim. Cosmochim. Acta* **128**, 249–265 (2014).
7. C. R. Pearce *et al*., *Geochim. Cosmochim. Acta* **157**, 125–146 (2015).
8. J. Fietzke, A. Eisenhauer, *Geochem. Geophys. Geosyst.* **7**, Q08009 (2006).
9. I. H. Widanagamage, E. A. Schauble, H. D. Scher, E. M. Griffith, *Geochim. Cosmochim. Acta* **147**, 58–75 (2014).
10. I. H. Widanagamage *et al*., *Chem. Geol.* **411**, 215–227 (2015).
11. E. M. Griffith, A. Paytan, U. G. Wortmann, A. Eisenhauer, H. D. Scher, *Chem. Geol.* **500**, 148–158 (2018).
12. W. Broecker, K. Matsumoto, E. Clark, I. Hajdas, G. Bonani, *Paleoceanography* **14**, 431–436 (1999).
13. J. M. McArthur, R. J. Howarth, G. A. Shields, "Strontium isotope stratigraphy," in *The Geologic Time Scale*, F. M. Gradstein, J. G. Ogg, M. Schmitz, G. Ogg, G. Eds. (Elsevier 2012), pp. 127–144.
14. A. C. Davis, M. J. Bickle, D. A. H. Teagle, *Earth Planet. Sci. Lett.* **211**, 173–187 (2003).
15. D. Vance, D. A. H. Teagle, G. L. Foster, *Nature* **458**, 493–496 (2009).
16. C. H. Lear, H. Elderfield, P. A. Wilson, *Earth Planet. Sci. Lett.* **208**, 69–84 (2003).
17. D. J. J. Kinsman, H. D. Holland, *Geochim. Cosmochim. Acta* **33**, 1–17 (1996).
18. O. Cartapanis, E. D. Galbraith, D. Bianchi, S. L. Jaccard, *Clim. Past* **14**, 1819–1850 (2018).
19. M. A. Kominz, W. A. Van Sickel, K. G. Miller, J. V. Browning, "Sea-level estimates for the latest 100 million years: One-dimensional backstripping of onshore New Jersey borehole," in *Sequence Stratigraphic Models for Exploration and Production: Evolving Methodology, Emerging Models and Application Case Histories*, J. M. Armentrout, N. C. Rosen, Eds. (SEPM Society for Sedimentary Geology, 2002), vol. 22, pp. 303–315.
20. P. D. Clift *et al*., *Nat. Geosci.* **1**, 875–880 (2008).
21. A. A. Webb *et al*., *Lithosphere* **9**, 637–651 (2017).
22. W. Kiessling, *Annu. Rev. Ecol. Evol. Syst.* **40**, 173–192 (2009).
23. B. N. Opdyke, B. H. Wilkinson, *Paleoceanography* **3**, 685–703 (1988).
24. N. S. Vögeli, P. van der Beek, P. Huyghe, Y. Najman, *J. Geol.* **125**, 515–529 (2017).
25. S. D. Willett, *Annu. Rev. Earth Planet. Sci.* **38**, 411–437 (2010).
26. D. W. Graham, M. L. Bender, D. F. Williams, L. D. Keigwin Jr., *Geochim. Cosmochim. Acta* **46**, 1281–1292 (1982).
27. T. Steuber, J. Veizer, *Geology* **30**, 1123–1126 (2002).
28. L. C. Ivany *et al*., *J. Sediment. Res.* **74**, 7–19 (2004).
29. A. K. Tripati, W. D. Allmon, D. E. Sampson, *Earth Planet. Sci. Lett.* **282**, 122–130 (2009).
30. R. M. Coggon, D. A. H. Teagle, C. E. Smith-Duque, J. C. Alt, M. J. Cooper, *Science* **327**, 1114–1117 (2010).
31. V. Balter, C. Lécuyer, J.-A. Barrat, *Palaeogeogr. Palaeoclimatol. Palaeoecol.* **310**, 133–138 (2011).
32. S. M. Sosdian *et al*., *Geochem. Geophys. Geosyst.* **13**, Q10014 (2012).
33. H. M. Stoll, D. P. Schrag, *Geochim. Cosmochim. Acta* **62**, 1107–1118 (1998).
34. A. B. Ronov, *Stratisphere or Sedimentary Envelope of the Earth: A Quantitative Study* [in Russian] (Nauka, 1993).
35. B. N. Opdyke, J. C. G. Walker, *Geology* **20**, 733–736 (1992).
36. T. H. Van Andel, *Earth Planet. Sci. Lett.* **26**, 187–194 (1975).
37. H. Pälike *et al*., *Nature* **488**, 609–614 (2012).
38. S. M. Campbell, R. Moucha, L. A. Derry, M. E. Raymo, *Geochem. Geophys. Geosyst.* **19**, 1025–1034 (2018).
39. S. E. Greene *et al*., *Paleoceanogr. Paleoclimatol.* **34**, 930–945 (2019).
40. J. K. Willenbring, F. von Blanckenburg, *Nature* **465**, 211–214 (2010).
41. J. K. Caves, A. B. Jost, K. V. Lau, K. Maher, *Earth Planet. Sci. Lett.* **450**, 152–163 (2016).

ACKNOWLEDGMENTS

A.P. was supported by National Science Foundation (NSF) grant 1259440. E.M.G. was supported by NSF grant 1053312. A.R. was supported by NSF grants 1658024 and 1702913 and by the Heising Simons Foundation. M.H. was supported by NERC IRF fellowship NE/K00901X/1. A.E. was supported by the Helmholtz Association and the German Science Funding Agency (DFG). **Author contributions:** A.P. and E.M.G. conceived the research idea and designed the study. A.P., E.M.G., and A.E. separated the barite and conducted the isotope analyses. M.H., K.W., and A.R. modeled the data. A.R. prepared Figs. 1 and 4, E.M.G. prepared Fig. 2, M.H. prepared Fig. 3 and fig. S2, and A.E. prepared fig. S1. All authors discussed and interpreted the data and contributed to writing the manuscript. **Competing interests:** The authors declare no competing interests. **Data and materials availability:** All data are available in the main text or the supplementary materials. All modeling code used can be found at https://github.com/MathisHain/StableSr.

SUPPLEMENTARY MATERIALS

science.sciencemag.org/content/371/6536/1346/suppl/DC1
Materials and Methods
Supplementary Text
Figs. S1 and S2
Table S1
References (*42*–*55*)

27 December 2019; accepted 17 February 2021
10.1126/science.aaz9266

PLANT SCIENCE

Molecular mechanism of cytokinin-activated cell division in *Arabidopsis*

Weibing Yang[1]*, Sandra Cortijo[1]†, Niklas Korsbo[1,2], Pawel Roszak[1], Katharina Schiessl[1], Aram Gurzadyan[1,2], Raymond Wightman[1], Henrik Jönsson[1,2,3]‡, Elliot Meyerowitz[1,4]‡

Mitogens trigger cell division in animals. In plants, cytokinins, a group of phytohormones derived from adenine, stimulate cell proliferation. Cytokinin signaling is initiated by membrane-associated histidine kinase receptors and transduced through a phosphorelay system. We show that in the *Arabidopsis* shoot apical meristem (SAM), cytokinin regulates cell division by promoting nuclear shuttling of Myb-domain protein 3R4 (MYB3R4), a transcription factor that activates mitotic gene expression. Newly synthesized MYB3R4 protein resides predominantly in the cytoplasm. At the G2-to-M transition, rapid nuclear accumulation of MYB3R4—consistent with an associated transient peak in cytokinin concentration—feeds a positive feedback loop involving importins and initiates a transcriptional cascade that drives mitosis and cytokinesis. An engineered nuclear-restricted MYB3R4 mimics the cytokinin effects of enhanced cell proliferation and meristem growth.

Organ morphogenesis in plants is largely determined by the rate and patterns of cell division (*1*) occurring primarily in meristematic tissues, such as the shoot and root meristems, and vascular cambium (*2*). The plant hormone cytokinin stimulates cell proliferation (*3*, *4*) and acts with auxin to coordinate the balance between stem cell division and differentiation (*5*, *6*). Although the molecular mechanisms underlying plant cell cycle progression (*7*) and cytokinin signal transduction (*8*–*11*) have been well characterized, it is unclear how cytokinin signals activate mitotic cell division.

The *Arabidopsis* shoot apical meristem (SAM) harbors stem cells that undergo active proliferation (*12*). Reduced cytokinin levels (*13*, *14*) or impaired cytokinin signaling (*15*) results in smaller meristems with fewer cells. Exogenous cytokinin application promotes cell division, leading to enlarged meristems in wild-type (Col-0) plants that closely resemble those in the cytokinin oxidase mutant *ckx3 ckx5* (*16*) in which endogenous cytokinin levels are elevated owing to reduction in cytokinin degradation (fig. S1).

Two MYB3R transcription factors regulate cytokinin response

A family of three-repeat R1R2R3 MYB transcription factors have been implicated in the control of mitotic gene expression (*17*–*20*). Among the five *MYB3R* genes in *Arabidopsis*, only *MYB3R1* and *MYB3R4* are highly expressed in the SAM, and their mRNAs are enriched in dividing cells, as assayed by in situ hybridization (fig. S2A). Compared with wild type, the *myb3r1 myb3r4* double mutant (*20*) has a

[1]Sainsbury Laboratory, University of Cambridge, Bateman Street, Cambridge CB2 1LR, UK. [2]Department of Applied Mathematics and Theoretical Physics, University of Cambridge, Cambridge CB3 0WA, UK. [3]Department of Astronomy and Theoretical Physics, Lund University, SE22362 Lund, Sweden. [4]Howard Hughes Medical Institute and Division of Biology and Biological Engineering, California Institute of Technology, 1200 East California Boulevard, Pasadena, CA 91125, USA.
*Present address: National Key Laboratory of Plant Molecular Genetics, CAS Center for Excellence in Molecular Plant Sciences, Chinese Academy of Sciences (CAS), and CAS-JIC Center of Excellence for Plant and Microbial Sciences (CEPAMS), Shanghai 200032, China. †Present address: BPMP, Univ Montpellier, CNRS, INRAE, Institut Agro, Montpellier, France.
‡Corresponding author. Email: meyerow@caltech.edu (E.M.); henrik.jonsson@slcu.cam.ac.uk (H.J.)

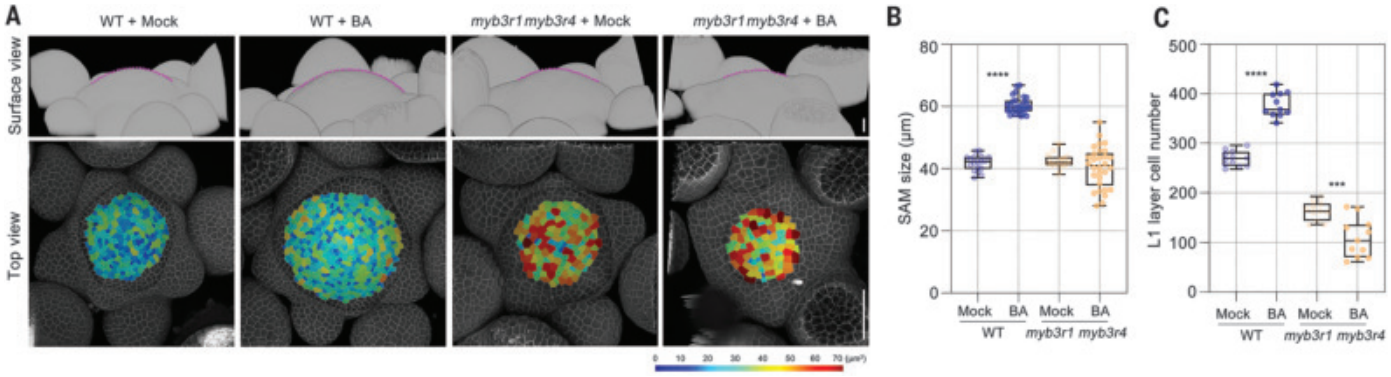

Fig. 1. A pair of MYB3R transcription factors regulate cytokinin-activated cell division in the *Arabidopsis* shoot meristem. (**A**) The morphologies of wild-type (WT, Col-0) and *myb3r1 myb3r4* shoot apical meristems (SAMs) in response to cytokinin treatment. The shoot apices collected shortly after bolting (with stem length of 1 cm) were treated with BA (100 μM) three times at 2-day intervals. The SAMs (top panels) are outlined with magenta dashed lines and are surrounded by developing flower primordia. Bottom panels show segmented L1 (epidermal) cells. The cell walls were stained using propidium iodide (PI, shown in gray). Scale bars, 20 μm (top panel) and 50 μm (bottom panel). (**B** and **C**) The effect of cytokinin treatment on meristem size (B) and cell number (C) in wild-type and *myb3r1 myb3r4* SAMs. ***$P < 0.001$, ****$P < 0.0001$ (two-tailed *t* test). Data in (B) and (C) are displayed as box and whisker plots with individual data points. The error bars represent maximum and minimum values. Center line, median; box limits, 25th and 75th percentiles.

reduced number of cells in both the shoot and root meristems (Fig. 1 and fig. S3). After cytokinin treatment, a large proportion (~60 to 70%) of *myb3r1 myb3r4* SAMs terminated prematurely (fig. S2, B to F). In *myb3r1 myb3r4* SAMs that did not terminate, the meristem size decreased and the number of epidermal (L1) cells was reduced from 164 ± 19 (n = 11 SAMs) in mock-treated controls to 109 ± 39 (n = 11) after 100 μM 6-benzylaminopurine (BA) treatment (three external applications spaced 2 days apart), whereas in wild-type SAMs, the same cytokinin treatment increased the number of L1 cells from 269 ± 15 (n = 12) to 378 ± 24 (n = 11) (Fig. 1, B and C). Therefore, instead of sustaining cell proliferation activity, high levels of cytokinin increase the relative ratio of stem cell differentiation to division in a *myb3r1 myb3r4* genetic background, suggesting that cytokinin-activated cell division in the shoot meristem requires MYB3R1 and/or MYB3R4.

MYB3R1 and MYB3R4 activate core cell cycle gene expression

Genomic binding targets of MYB3R1 and MYB3R4 were identified using chromatin immunoprecipitation sequencing (ChIP-seq). Because expression of *MYB3R1* and *MYB3R4* is restricted to dividing cells (fig. S2A), and because of the low stability of these proteins (*21*), we applied the Maximized Objects for Better Enrichment (MOBE)–ChIP method, a strategy designed to detect low signals (*22*). We dissected and pooled ~1000 shoot meristems from *pMYB3R1::GFP-MYB3R1* and *pMYB3R4::GFP-MYB3R4* plants. MYB3R1- and MYB3R4-bound DNA fragments were purified using an anti–green fluorescent protein (GFP) antibody and sequenced. From three biological replicates (i.e., ~3000 meristems for each MYB3R protein), we identified 5477 and 171 gene regions that were bound by MYB3R1 and MYB3R4, respectively (table S1). Ninety-seven percent of the MYB3R4 targets were shared by MYB3R1 (Fig. 2A); their binding regions also largely overlapped at the gene promoters (fig. S4A). Compared with wild type, the expression levels of the 166 MYB3R1 and MYB3R4 common target genes were mildly increased in *myb3r1* inflorescence meristems, whereas most were down-regulated in the *myb3r4* single or the *myb3r1 myb3r4* double mutants (Fig. 2B and fig. S4, B and C). Thus, MYB3R4 predominantly activates gene expression, consistent with a dual luciferase assay showing that the promoter activity of target genes was enhanced markedly by MYB3R4 (fig. S4D). The overlap of MYB3R1 and MYB3R4 targets and their proximity when bound at gene promoters suggest the possibility of cooperative action in transcriptional control, as for MYB3R1 interacting with MYB3R3 and MYB3R5 in inhibition of cell division in postmitotic or DNA-damaged cells (*21*, *23*–*25*) and with TSO1 in regulation of flower morphogenesis (*26*). Indeed, through bimolecular fluorescence complementation (BiFC) and co-immunoprecipitation (CoIP) assays, it was found that MYB3R1 associates with MYB3R4 (fig. S5).

In synchronized *Arabidopsis* tissue culture cells (*27*), the expression levels of most MYB3R1 target genes remain constant during the cell cycle (fig. S6A), in line with their broad roles in developmental and metabolic processes (fig. S6B). In contrast, MYB3R4 targets exhibit a sharp increase in RNA expression at the G2-to-M transition (fig. S6, A and C). RNA fluorescence in situ hybridization (FISH) for 19 tested targets detected their mRNAs only in dividing cells (Fig. 2C and fig. S6, D and E). MYB3R1 and MYB3R4 targets are involved in all key steps of mitotic progression, including cyclin-dependent kinase activation and inhibition, chromosome reorganization and segregation, and assembly of the phragmoplast structure (Fig. 2D). We previously showed that the mRNAs of *CELL DIVISION CYCLE 20* (*CDC20*) and *CELL CYCLE SWITCH 52B* (*CCS52B*), encoding coactivators of the anaphase-promoting complex/cyclosome (APC/C) that targets cell cycle proteins for degradation (*28*), are expressed in dividing cells but sequestered in the nucleus before nuclear envelope breakdown (NEBD) (*29*). Both *CDC20* and *CCS52B* are direct binding targets of MYB3R1 and MYB3R4. We also observed enrichment of genes that modulate transcription, signal transduction, cell wall synthesis and modification, and cell wall signaling (Fig. 2D and table S2).

Nucleocytoplasmic dynamics of MYB3R4 during cell division

Both GFP-MYB3R1 and GFP-MYB3R4 fusion proteins are functional in genetic complementation assays (fig. S7A). Similarly to typical transcription factors, GFP-MYB3R1 is localized in the nucleus (fig. S7B and movie S1). For MYB3R4, exclusive nuclear localization is only seen in a small proportion (~6%) of cells, whereas in most GFP-MYB3R4–expressing cells, GFP fluorescence is present in both the cytoplasm and nucleus (Fig. 2E, fig. S7C, and movies S2 and S3). This is the case in both shoot and root meristem cells (fig. S8, A and B) as well as in nondividing cells in which GFP-MYB3R4 is ectopically expressed from the *Arabidopsis UBIQUITIN10* (*UBQ10*) promoter (fig. S8, C and D). Leptomycin B treatment, which blocks nuclear export (*30*), results in redistribution of GFP fluorescence signals into the nucleus (fig. S8A and movie S4), demonstrating that MYB3R4 is actively transported from the nucleus.

Time-lapse observations of individual cells undergoing division revealed a recurrent pattern of rapid changes in GFP-MYB3R4 protein

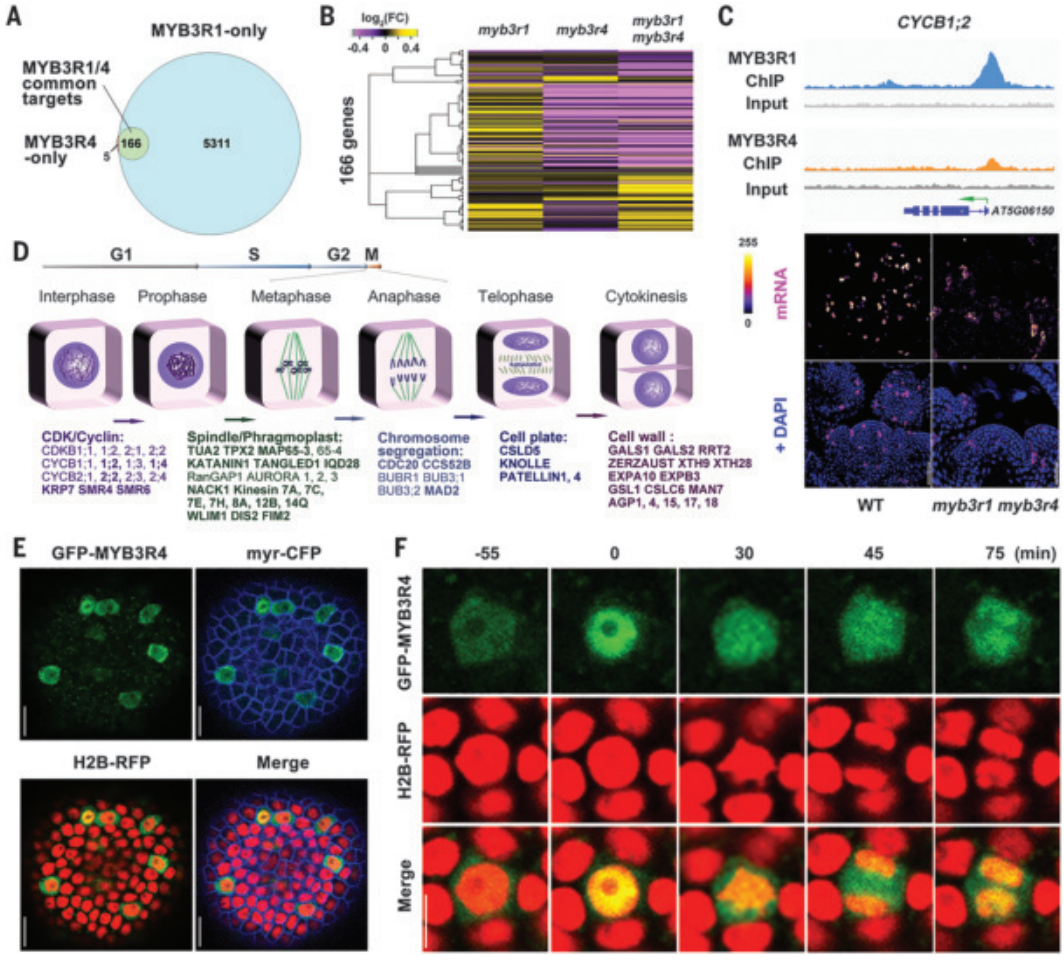

Fig. 2. MYB3R4 transiently localizes in the nucleus to activate the expression of mitotic cell cycle genes. (**A**) Venn diagram showing the number of gene regions bound by MYB3R1 and MYB3R4, as detected by ChIP-seq. (**B**) Hierarchical clustering of 166 MYB3R1 and MYB3R4 common target genes based on their relative expression levels, as detected by RNA sequencing in shoot apices of single and double mutants compared with wild type. Yellow indicates increased expression, and purple indicates decreased expression. FC, fold change. (**C**) MYB3R1 and MYB3R4 bind to target gene promoters and activate their expression in dividing cells. The top panels show genome-browser tracks of MYB3R1 and MYB3R4 ChIP-seq coverage at a representative target gene *CYCB1;2*. The bottom panels show *CYCB1;2* expression in wild-type and *myb3r1 myb3r4* SAMs, as revealed by RNA FISH. FISH signals are displayed using the Fire lookup table of Fiji (ImageJ) software. DAPI, 4′,6-diamidino-2-phenylindole. Scale bars, 50 μm. (**D**) Classification of MYB3R1 and MYB3R4 targets based on their molecular functions. MYB3R1- and MYB3R4-regulated genes are involved in all key steps of mitotic progression. The common targets are shown in bold text. (**E**) Nucleocytoplasmic shuttling of MYB3R4. Shown are SAM cells expressing GFP-MYB3R4 (green) together with a plasma membrane marker myr-CFP (blue) and a nuclear reporter H2B-RFP (red). Scale bars, 20 μm. (**F**) The dynamic localization of GFP-MYB3R4 protein during cell division. MYB3R4 shows rapid translocalization from the cytoplasm to the nucleus at the onset of mitosis (time zero). Scale bar, 5 μm. Data in (A) and (C) are displayed as box and whisker plots with individual data points. The error bars represent maximum and minimum values. Center line, median; box limits, 25th and 75th percentiles.

localization (Fig. 2F and fig. S9). Prior to cell division, the GFP-MYB3R4 fluorescence signal was detected predominantly in the cytoplasm. At the onset of mitosis, shortly before NEBD, a rapid nuclear accumulation of GFP-MYB3R4 led to the highest nuclear concentration of the protein observed in the cell cycle. During the subsequent steps of mitotic division, GFP-MYB3R4 was enriched in the cellular domains corresponding to spindles and phragmoplast. After nuclear envelope reformation at the end of cytokinesis, GFP-MYB3R4 protein showed a second phase of nuclear accumulation but was soon exported back to the cytoplasm. Constitutively expressed GFP-MYB3R4 also exhibits transient nuclear localization in prophase cells (fig. S8C).

Cytokinin promotes MYB3R4 nuclear shuttling

To characterize the factors that regulate MYB3R4 nucleocytoplasmic trafficking, we first changed photosynthetic activity (light-dark shift) or nutrient status, both of which affect cell division (*31*). Light slightly increased the nuclear proportion of MYB3R4, whereas the other changes had no effect (fig. S10). Because MYB3R4 is required for cytokinin-activated cell division, we next tested whether cytokinin modulates MYB3R4 subcellular dynamics. A series of different concentrations of trans-zeatin (tZ), the most prevalent cytokinin in plants, was applied to the *GFP-MYB3R4* SAMs. High concentrations of tZ (≥100 μM) led to relocalization of GFP-MYB3R4 into the nucleus in all of the cells where the protein was present (Fig. 3A and fig. S11, A and B). Similar effects were observed for isopentenyladenine (iP) and BA (Fig. 3A and movies S5 and S7), but auxin had no effect (fig. S11C). Cytokinin action on MYB3R4 nuclear accumulation was not inhibited by cycloheximide (CHX, a protein synthesis inhibitor) (fig. S11D), indicating the movement of preexisting MYB3R4 protein into the nucleus and that MYB3R4 nuclear trafficking is a direct response to cytokinin.

To dissect how cytokinin promotes MYB3R4 nuclear localization, we analyzed the expression patterns of all importin and exportin genes (*32*) at the shoot apex. Most display a uniform distribution or are partially enriched in flower primordia. However, the mRNAs of *IMPORTIN ALPHA 3* (*IMPA3*), encoding the importin subunit α-3 also known as *MOS6* (*MODIFIER OF SNC1, 6*) (*33*), and *IMPA6*, exhibit a patchy pattern resembling the expression of cell cycle–regulated genes (Fig. 3B and fig. S12). We confirmed their expression in dividing cells by RNA FISH (fig. S13, A and B) and by fluorescence reporter live imaging (fig. S13C). Both *IMPA3* and *IMPA6* were direct targets of MYB3R1 and MYB3R4 in the ChIP-seq experiments (fig. S13D). IMPA3 and IMPA6 are α family importins that function as adaptors to recognize target proteins for nuclear import. To examine the possible impact of importins on MYB3R4 nuclear translocation, we coexpressed red fluorescent protein (RFP)–IMPA3 and GFP-MYB3R4 in *Nicotiana benthamiana* leaf cells. In the absence of RFP-IMPA3, GFP-MYB3R4 shows a nuclear and cytoplasmic distribution similar to that in *Arabidopsis* cells. After coexpression with RFP-IMPA3, the nuclear

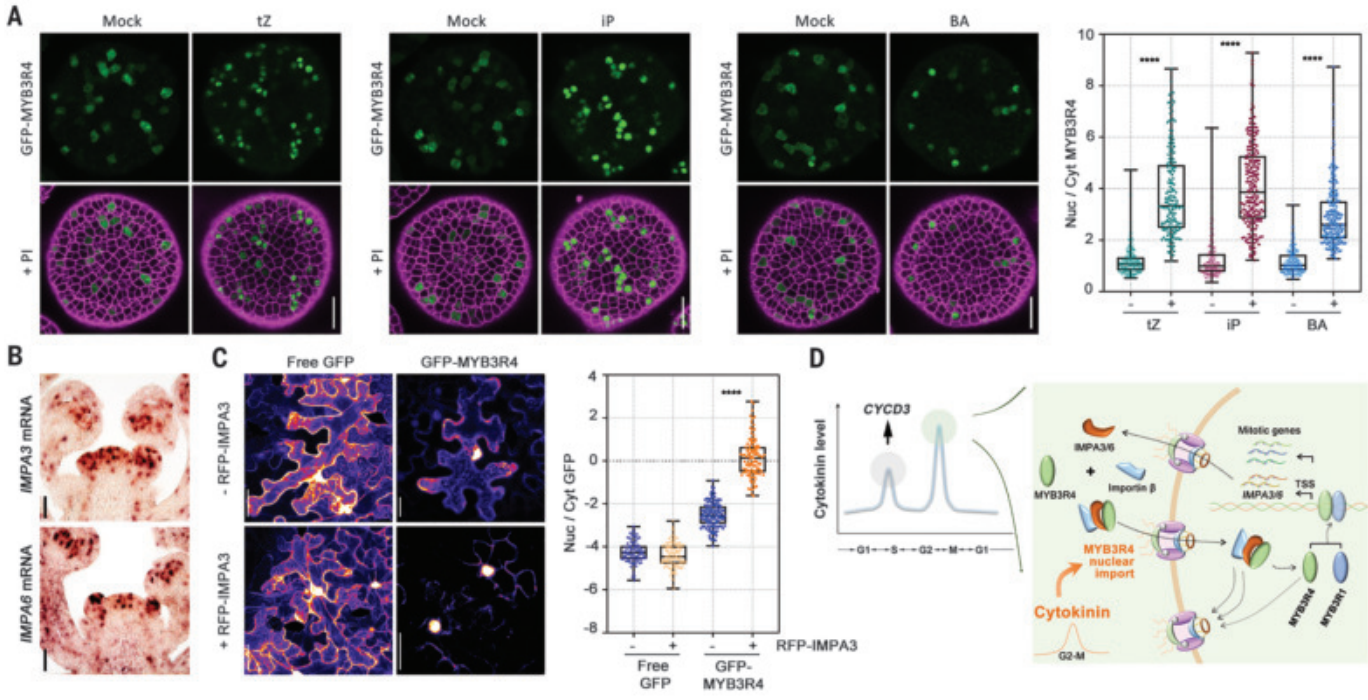

Fig. 3. Cytokinins promote MYB3R4 nuclear localization. (**A**) The subcellular localization patterns of GFP-MYB3R4 after mock treatment or cytokinin treatment. GFP-MYB3R4 protein was predominantly nuclear after 6 hours of 100 μM cytokinin treatment. The nuclear-to-cytoplasmic (Nuc/Cyt) ratio of MYB3R4 was measured by quantifying the GFP fluorescence intensities in Fiji. Scale bars, 20 μm. ****$P < 0.0001$ (two-tailed t test). (**B**) The expression of MYB3R1 and MYB3R4 target genes *IMPA3* and *IMPA6* in dividing cells of the SAM. *IMPA3* and *IMPA6* mRNAs were detected by in situ hybridization. Scale bars, 50 μm. (**C**) IMPA3 facilitates MYB3R4 nuclear import. GFP-MYB3R4 was expressed in the absence (upper panel) or presence (lower panel) of RFP-IMPA3 in the tobacco leaf cells. Free GFP serves as a control. The *Arabidopsis UBQ10* promoter was used for expression of all genes. Scale bars, 50 μm. ****$P < 0.0001$ (two-tailed t test). (**D**) A schematic illustration of cytokinin-activated cell division and the feedback between importin and MYB3R4. A relatively high level of cytokinin induces *CYCD3* expression to promote G1-to-S transition (*37*). As the cell cycle proceeds, a further increase in cytokinin abundance promotes MYB3R4 nuclear translocation. Inside the nucleus, MYB3R4 interacts with MYB3R1 to activate the expression of mitotic cell cycle genes as well as *IMPA3* and *IMPA6*. IMPA3 and IMPA6 subsequently facilitate MYB3R4 nuclear import, thus generating a positive feedback loop. TSS, transcription start site.

proportion of GFP-MYB3R4 protein was significantly increased (Fig. 3C). In contrast, in the *Arabidopsis impa3-1* and *impa6-2* mutant SAMs, the relative amount of GFP-MYB3R4 in the nucleus was reduced compared with the wild-type plants (fig. S13, E and F). Therefore, it seems likely that MYB3R1 and MYB3R4 activate *IMPA3* and *IMPA6* expression, facilitating MYB3R4 nuclear importation. This interplay between MYB3R4 and importins could represent a positive feedback loop that would enable more-rapid nuclear import of MYB3R4 proteins. To test the feasibility of this hypothesis, we established a mathematical model to simulate MYB3R4 dynamics during the cell cycle. When using experimentally derived parameter values, we found that a peak of cytokinin input induces nuclear translocation of MYB3R4 (fig. S14, A to D). Incorporating the positive feedback with IMPA3 and IMPA6 causes MYB3R4 nuclear trafficking to become both faster and stronger (fig. S14, E to G).

The level of cytokinins, like the expression of mitotic genes, fluctuates during the plant cell cycle: Endogenous cytokinin content slightly increases in the middle of S phase and exhibits a sharp peak at the G2-to-M transition (*34*–*36*). The first peak of cytokinins is in line with the report that cytokinin induces *CYCLIN D3* (*CYCD3*) expression for the G1-to-S transition (*37*). It has also been shown that inhibiting cytokinin synthesis at G2 blocks mitotic entry in tobacco Bright Yellow 2 (BY-2) cells (*38*). Our data demonstrate that (i) the second peak of cytokinin levels coincides with rapid MYB3R4 nuclear accumulation and (ii) cytokinin promotes MYB3R4 nuclear relocalization but requires high hormone concentration. On the basis of these observations, we postulate that the high concentration of cytokinins at the G2-to-M transition promotes MYB3R4 nuclear localization to activate mitotic cell cycle gene expression (Fig. 3D).

MYB3R4 constitutive nuclear localization mimics cytokinin response

Finally, we tested whether perturbing MYB3R4 nucleocytoplasmic shuttling would influence cell division activity. To localize a nuclear export signal (NES), we generated a series of 11 truncated GFP-tagged MYB3R4 derivatives and expressed them in a wild-type background under control of the *MYB3R4* promoter (fig. S15A). Subcellular localization analysis identified a sequence within the MYB3R4 C-terminal region that is necessary and sufficient for cytosolic targeting (fig. S15B and movie S8). Sequence comparison between MYB3R4 orthologs in different plant species identified a conserved sequence that could act as an NES (Fig. 4A). When the Phe and Leu residues were simultaneously mutated to Ala, nuclear export was abolished, and the GFP-MYB3R4^{mNES} protein was exclusively nuclear (Fig. 4B and movie S9).

GFP-MYB3R4^{mNES} shows transcriptional activity (fig. S15C) and exhibits a similar DNA binding profile as the natural GFP-MYB3R4 (fig. S15D). Transcriptomic analysis showed an opposite trend in the *pMYB3R4::GFP-MYB3R4^{mNES}* meristems compared with the *myb3r4* mutant, with the expression of most MYB3R4 target genes greatly up-regulated (fig. S15E). RNA FISH showed that in *pMYB3R4::GFP-MYB3R4^{mNES}*, the number of cells expressing MYB3R4 targets such as *CDC20* is increased (Fig. 4C). These plants showed enlarged SAMs (Fig. 4D) and expanded *WUSCHEL* (*WUS*) expression (Fig. 4E). These phenotypes

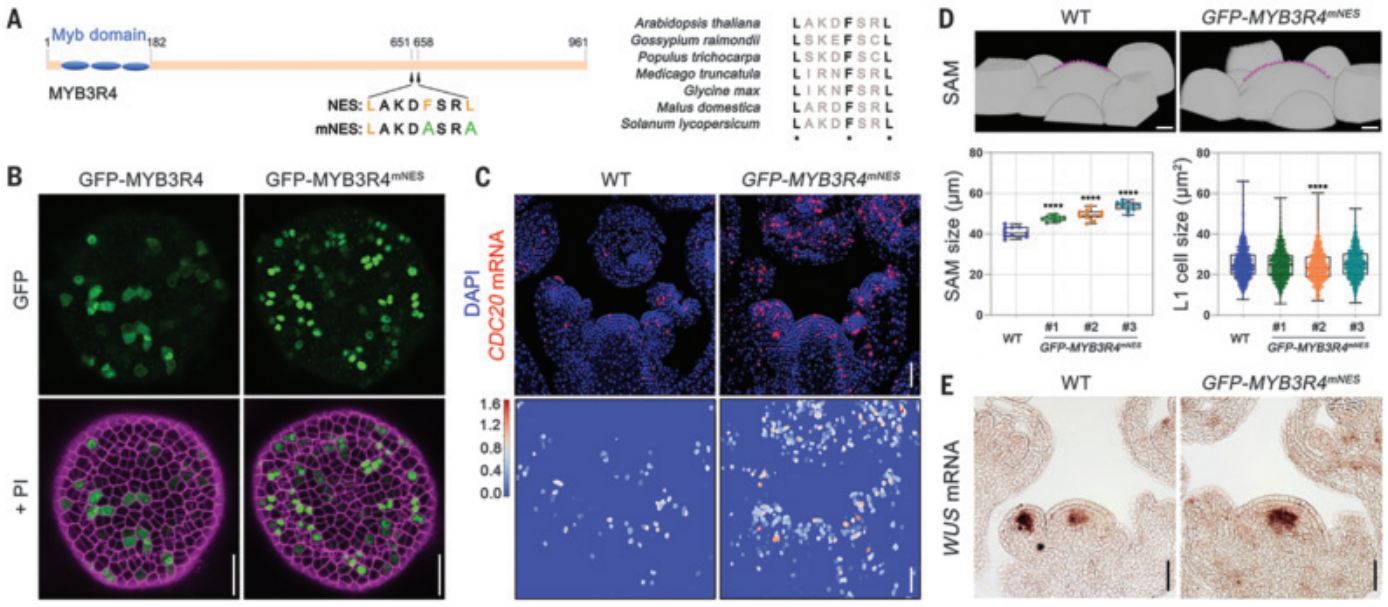

Fig. 4. MYB3R4 nuclear localization stimulates cell division and meristem growth. (**A**) Analysis of MYB3R4 NES. The conserved hydrophobic residues of MYB3R4 NES are substituted with alanine in the mutated NES (mNES). Single-letter abbreviations for the amino acid residues are as follows: A, Ala; C, Cys; D, Asp; F, Phe; I, Ile; K, Lys; L, Leu; N, Asn; R, Arg; and S, Ser. (**B**) Protein localization of GFP-MYB3R4 and GFP-MYB3R4^{mNES} expressed under *MYB3R4* promoter. GFP-MYB3R4^{mNES} protein could be detected only in the nucleus. Scale bars, 20 μm. (**C**) Increased expression of the target gene *CDC20* in wild type and *pMYB3R4::GFP-MYB3R4*^{mNES}. Bottom panels show heatmap of the segmented *CDC20* RNA FISH signals. Scale bars, 50 μm. (**D**) Enhanced meristem growth in *pMYB3R4::GFP-MYB3R4*^{mNES}. Top panels are three-dimensional surface views of wild-type and *pMYB3R4::GFP-MYB3R4*^{mNES} SAMs. The SAMs are outlined with magenta dashed lines. Three representative *pMYB3R4::GFP-MYB3R4*^{mNES} transgenic lines were used for quantification of meristem size and L1 cell size. Scale bars, 20 μm. ****$P < 0.0001$ (two-tailed *t* test). Data are displayed as box and whisker plots with individual data points. The error bars represent maximum and minimum values. Center line, median; box limits, 25th and 75th percentiles. (**E**) Comparison of *WUS* expression in wild-type and *pMYB3R4::GFP-MYB3R4*^{mNES} SAMs, as revealed by mRNA in situ hybridization. Scale bars, 50 μm.

resemble, but are weaker than, those of wild-type plants treated with cytokinin. Furthermore, the growth retardation phenotypes of cytokinin-deficient plants of genotype *35S::CKX1* (*13*) or of cytokinin receptor mutant plants of genotype *ahk2 ahk3* (*15*) could be rescued by *pMYB3R4::GFP-MYB3R4*^{mNES} (fig. S15, F and G). Thus, by engineering a constitutively nuclear-localized form of MYB3R4, we were able to partially recapitulate cytokinin action.

Discussion

Underlying the many aspects of cytokinin-regulated developmental and physiological processes (*11*, *39*) is the fundamental role of cytokinin in stimulating cell proliferation. Here we report that cytokinin directly promotes MYB3R4 nuclear localization to activate mitosis. Our data, together with that on cytokinin-induced *CYCD3* expression (*37*), have revealed a mechanistic framework underlying cytokinin-regulated cell division. The dual regulatory modes of cytokinin in *CYCD3* transcription and MYB3R4 nucleocytoplasmic shuttling ensure precise control of cell cycle transitions in response to different levels of cytokinin input, consistent with the dose-dependent action of cytokinin in plant cell division (*4*). Cytokinin-triggered MYB3R4-IMPA3/6 positive feedback leads to rapid MYB3R4 nuclear accumulation shortly before mitosis, but the transience of MYB3R4 presence in the nucleus is guaranteed by the dissolution of the nuclear membrane at prometaphase, which eliminates the possibilities of importin activity and nuclear localization. This allows for only one round of mitotic activation during the cell cycle. Variation of cytokinin levels in meristem cells, likely perceived by intracellular cytokinin receptors (*40*, *41*), acts by changing the nuclear concentration of a transcription factor, thereby regulating cell numbers in the shoot stem cell niche.

REFERENCES AND NOTES

1. E. M. Meyerowitz, *Cell* **88**, 299–308 (1997).
2. T. Greb, J. U. Lohmann, *Curr. Biol.* **26**, R816–R821 (2016).
3. C. O. Miller, F. Skoog, M. H. Von Saltza, F. M. Strong, *J. Am. Chem. Soc.* **77**, 1392 (1955).
4. G. E. Schaller, I. H. Street, J. J. Kieber, *Curr. Opin. Plant Biol.* **21**, 7–15 (2014).
5. G. E. Schaller, A. Bishopp, J. J. Kieber, *Plant Cell* **27**, 44–63 (2015).
6. L. Moubayidin, R. Di Mambro, S. Sabatini, *Trends Plant Sci.* **14**, 557–562 (2009).
7. L. De Veylder, T. Beeckman, D. Inzé, *Nat. Rev. Mol. Cell Biol.* **8**, 655–665 (2007).
8. A. P. Mähönen *et al.*, *Genes Dev.* **14**, 2938–2943 (2000).
9. T. Inoue *et al.*, *Nature* **409**, 1060–1063 (2001).
10. I. Hwang, J. Sheen, *Nature* **413**, 383–389 (2001).
11. J. J. Kieber, G. E. Schaller, *Development* **145**, dev149344 (2018).
12. G. V. Reddy, M. G. Heisler, D. W. Ehrhardt, E. M. Meyerowitz, *Development* **131**, 4225–4237 (2004).
13. T. Werner *et al.*, *Plant Cell* **15**, 2532–2550 (2003).
14. K. Miyawaki *et al.*, *Proc. Natl. Acad. Sci. U.S.A.* **103**, 16598–16603 (2006).
15. M. Higuchi *et al.*, *Proc. Natl. Acad. Sci. U.S.A.* **101**, 8821–8826 (2004).
16. I. Bartrina, E. Otto, M. Strnad, T. Werner, T. Schmülling, *Plant Cell* **23**, 69–80 (2011).
17. M. Ito, *J. Plant Res.* **118**, 61–69 (2005).
18. M. Umeda, S. S. Aki, N. Takahashi, *Curr. Opin. Plant Biol.* **51**, 1–6 (2019).
19. N. Haga *et al.*, *Development* **134**, 1101–1110 (2007).
20. N. Haga *et al.*, *Plant Physiol.* **157**, 706–717 (2011).
21. K. Kobayashi *et al.*, *EMBO J.* **34**, 1992–2007 (2015).
22. O. S. Lau *et al.*, *Science* **345**, 1605–1609 (2014).
23. P. Chen *et al.*, *Nat. Commun.* **8**, 635 (2017).
24. N. Takahashi *et al.*, *eLife* **8**, e43944 (2019).
25. C. Bourbousse, N. Vegesna, J. A. Law, *Proc. Natl. Acad. Sci. U.S.A.* **115**, E12453–E12462 (2018).
26. W. Wang, P. Sijacic, P. Xu, H. Lian, Z. Liu, *Proc. Natl. Acad. Sci. U.S.A.* **115**, E3045–E3054 (2018).
27. M. Menges, S. M. de Jager, W. Gruissem, J. A. Murray, *Plant J.* **41**, 546–566 (2005).
28. W. Yang, R. Wightman, E. M. Meyerowitz, *Mol. Cell* **68**, 1108–1119.e3 (2017).
29. J. Heyman, L. De Veylder, *Mol. Plant* **5**, 1182–1194 (2012).
30. M. Fornerod, M. Ohno, M. Yoshida, I. W. Mattaj, *Cell* **90**, 1051–1060 (1997).
31. A. R. Jones *et al.*, *Nat. Commun.* **8**, 15060 (2017).
32. I. Meier, E. J. Richards, D. E. Evans, *Annu. Rev. Plant Biol.* **68**, 139–172 (2017).
33. K. Palma, Y. Zhang, X. Li, *Curr. Biol.* **15**, 1129–1135 (2005).
34. N. Nishinari, K. Syōno, *Plant Cell Physiol.* **27**, 147–153 (1986).
35. P. Redig, O. Shaul, D. Inzé, M. Van Montagu, H. Van Onckelen, *FEBS Lett.* **391**, 175–180 (1996).
36. P. Dobrev *et al.*, *Plant Physiol. Biochem.* **40**, 333–337 (2002).
37. C. Riou-Khamlichi, R. Huntley, A. Jacqmard, J. A. Murray, *Science* **283**, 1541–1544 (1999).
38. F. Laureys *et al.*, *FEBS Lett.* **426**, 29–32 (1998).
39. B. Wybouw, B. De Rybel, *Trends Plant Sci.* **24**, 177–185 (2019).
40. K. Wulfetange *et al.*, *Plant Physiol.* **156**, 1808–1818 (2011).
41. K. Caesar *et al.*, *J. Exp. Bot.* **62**, 5571–5580 (2011).

ACKNOWLEDGMENTS

We thank M. Ito, Y. Helariutta, P. Tarr, H. Liu, and the Nottingham Arabidopsis Stock Centre for materials; J. Gruel for help with the computational modeling; K. Jaeger for assistance with DNA library preparation; G. Evans for assisting with the confocal microscopy

analysis; and D. Bergmann for helpful discussions. **Funding:** This work was supported by the Gatsby Charitable Foundation (GAT3395/DAA and GAT3395/PR4B to E.M. and H.J.). The laboratory of E.M. is supported by the Howard Hughes Medical Institute. R.W. received funding from Leverhulme Trust grant RPG-2015-285. The microscopy facility at the Sainsbury Laboratory is supported by the Gatsby Charitable Foundation. **Author contributions:** W.Y. and E.M. initiated and designed the study. W.Y., S.C., P.R., K.S., A.G., and R.W. performed the experiments. N.K. and H.J. performed modeling and simulation. A.G. analyzed the RNA FISH data. W.Y. and E.M. wrote the manuscript. All authors discussed and commented on the manuscript. **Competing interests:** The authors declare no competing interests.

Data and materials availability: All data are available in the main text or the supplementary materials. Sequencing data are available at the NCBI Gene Expression Omnibus (GEO; www.ncbi.nlm.nih.gov/geo/) under accession number GSE144049. Scripts used for image analysis and modeling are available via the Sainsbury Laboratory Gitlab Repository (https://gitlab.com/slcu/teamhj/publications/yang_etal_2021). Please contact E.M. for material requests.

SUPPLEMENTARY MATERIALS

science.sciencemag.org/content/371/6536/1350/suppl/DC1
Materials and Methods
Mathematical Modeling
Figs. S1 to S15
Tables S1 to S4
References (*42*–*56*)
MDAR Reproducibility Checklist
Movies S1 to S9

7 August 2020; accepted 9 February 2021
Published online 25 February 2021
10.1126/science.abe2305

REPORTS

QUANTUM CONTROL

Controlling quantum many-body dynamics in driven Rydberg atom arrays

D. Bluvstein[1], A. Omran[1,2], H. Levine[1], A. Keesling[1], G. Semeghini[1], S. Ebadi[1], T. T. Wang[1], A. A. Michailidis[3], N. Maskara[1], W. W. Ho[1,4], S. Choi[5], M. Serbyn[3], M. Greiner[1], V. Vuletić[6], M. D. Lukin[1]*

The control of nonequilibrium quantum dynamics in many-body systems is challenging because interactions typically lead to thermalization and a chaotic spreading throughout Hilbert space. We investigate nonequilibrium dynamics after rapid quenches in a many-body system composed of 3 to 200 strongly interacting qubits in one and two spatial dimensions. Using a programmable quantum simulator based on Rydberg atom arrays, we show that coherent revivals associated with so-called quantum many-body scars can be stabilized by periodic driving, which generates a robust subharmonic response akin to discrete time-crystalline order. We map Hilbert space dynamics, geometry dependence, phase diagrams, and system-size dependence of this emergent phenomenon, demonstrating new ways to steer complex dynamics in many-body systems and enabling potential applications in quantum information science.

Dynamics of complex, strongly interacting many-body systems have broad implications in quantum science and engineering, ranging from understanding fundamental phenomena (*1*, *2*) to realizing robust quantum information systems (*3*). Such dynamics typically lead to a rapid growth of quantum entanglement and a chaotic spreading of the wave function throughout an exponentially large Hilbert space, a phenomenon associated with quantum thermalization (*1*, *2*, *4*). Recent advances in the controlled manipulation of isolated, programmable many-body systems have enabled detailed studies of nonequilibrium states in strongly interacting quantum matter (*4*–*6*), in regimes inaccessible to numerical simulations on classical machines. Identifying nontrivial states for which dynamics can be stabilized or steered by external controls is a central question explored in these studies. For instance, it has been shown that strong disorder, leading to many-body localization (MBL), allows systems to suppress entanglement growth and retain memory of their initial state for long times (*7*, *8*). Another example involves quantum many-body scars, which manifest as periodic entanglement and disentanglement dynamics for special initial states that avoid rapid thermalization within an otherwise chaotic system (*9*–*11*). Further, periodic driving in strongly interacting systems can give rise to exotic nonequilibrium phases of matter, such as the discrete time crystal (DTC), which spontaneously breaks the discrete time-translation symmetry of the underlying drive (*12*, *13*). Here, we report the discovery of a new type of nonequilibrium dynamics associated with many-body scarring trajectories stabilized by periodic driving. The driven scars result in an emergent phenomenon akin to discrete time-crystalline order that can be harnessed to steer entanglement dynamics in complex many-body systems.

In our experiments, neutral ^{87}Rb atoms are trapped in optical tweezers and arranged into arbitrary two-dimensional patterns generated by a spatial light modulator (*14*, *15*). This programmable system allows us to explore quantum dynamics in systems ranging from chains and square lattices to exotic decorated lattices, with sizes up to 200 atoms. All atoms are initialized in an electronic ground state $|g\rangle$ and coupled to a Rydberg state $|r\rangle$ by a two-photon optical transition with an effective Rabi frequency $\Omega(t)$ and detuning $\Delta(t)$ (Fig. 1A). When excited into Rydberg states, atoms interact through a strong, repulsive van der Waals interaction $V \sim 1/d^6$, where d is the interatomic separation, resulting in the many-body Hamiltonian (*10*)

$$\frac{H}{\hbar} = \frac{\Omega(t)}{2}\sum_i \sigma_i^x - \Delta(t)\sum_i n_i + \sum_{i<j} V_{ij} n_i n_j \quad (1)$$

where $\hbar$ is the reduced Planck constant, $n_i = |r_i\rangle\langle r_i|$ is the projector onto the Rydberg state at site i, and $\sigma_i^x = |g_i\rangle\langle r_i| + |r_i\rangle\langle g_i|$ flips the atomic state. We choose lattice spacings where the nearest-neighbor (NN) interaction $V_0 > \Omega$ results in the Rydberg blockade (*14*, *16*, *17*), preventing adjacent atoms from simultaneously occupying $|r\rangle$. For large negative detunings, the many-body ground state is $|gggg\ldots\rangle$, and at large positive detunings on bipartite lattices, the ground state is antiferromagnetic, of the form $|rgrg\ldots\rangle$. Starting with all atoms in $|g\rangle$, adiabatically increasing Δ from large negative values to large positive values thus prepares antiferromagnetic initial states $|\mathrm{AF}\rangle$ (*10*, *18*–*21*); we choose array configurations (e.g., odd numbers of atoms) such that one of the two classical orderings, $|\mathrm{AF}_1\rangle$, is energetically preferred.

To explore quantum scarring in two-dimensional systems, we prepare $|\mathrm{AF}_1\rangle$ on an 85-atom honeycomb lattice and then suddenly quench at fixed Ω to a small positive detuning (Fig. 1B). The system quickly evolves from $|\mathrm{AF}_1\rangle$ into a disordered state as expected from a thermalizing system, but then notably the opposite order $|\mathrm{AF}_2\rangle$ emerges at a later time (*11*). Through the same process, the system evolves back to $|\mathrm{AF}_1\rangle$, consistent with previous observations of quantum scars in one-dimensional chains (*10*, *11*). These scarring dynamics can be seen in the evolution of sublattice A and B populations as a function of quench duration (Fig. 1C), where disordered configurations arise when the sublattice populations are approximately equal. These observations are surprising

[1]Department of Physics, Harvard University, Cambridge, MA 02138, USA. [2]QuEra Computing Inc., Boston, MA 02135, USA. [3]IST Austria, Am Campus 1, 3400 Klosterneuburg, Austria. [4]Department of Physics, Stanford University, Stanford, CA 94305, USA. [5]Department of Physics, University of California Berkeley, Berkeley, CA 94720, USA. [6]Department of Physics and Research Laboratory of Electronics, Massachusetts Institute of Technology, Cambridge, MA 02139, USA.
***Corresponding author. Email: lukin@physics.harvard.edu**

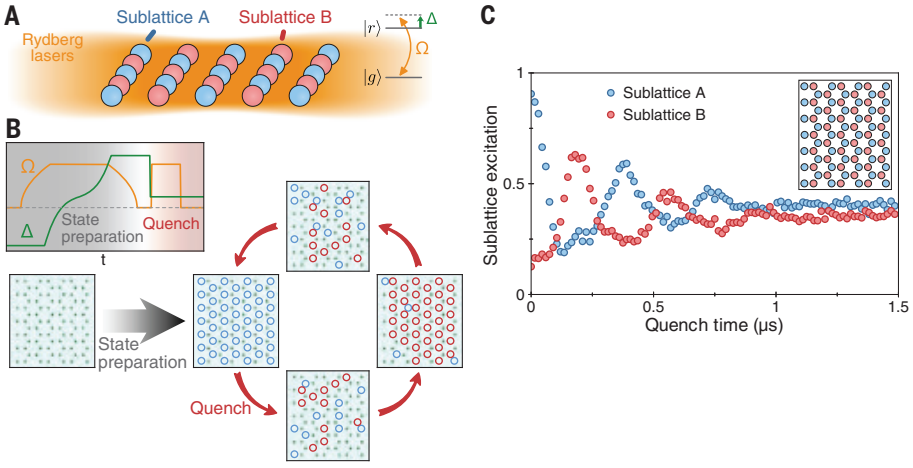

Fig. 1. Experimental investigations of quantum many-body scars. (**A**) Two-dimensional atom array subject to global Rydberg lasers with Rabi frequency Ω and detuning Δ. (**B**) A quasi-adiabatic ramp of Δ and Ω prepares an antiferromagnetic state $|\mathrm{AF}_1\rangle$ with sublattice A excited, and a detuning quench launches nonequilibrium dynamics. Atoms in $|g\rangle$ are imaged in optical tweezers by fluorescence, whereas atoms in $|r\rangle$ (empty circles) are expelled and detected as atom loss. (**C**) The Rydberg population on sublattices A and B undergoes periodic oscillations. The inset shows the geometry used here.

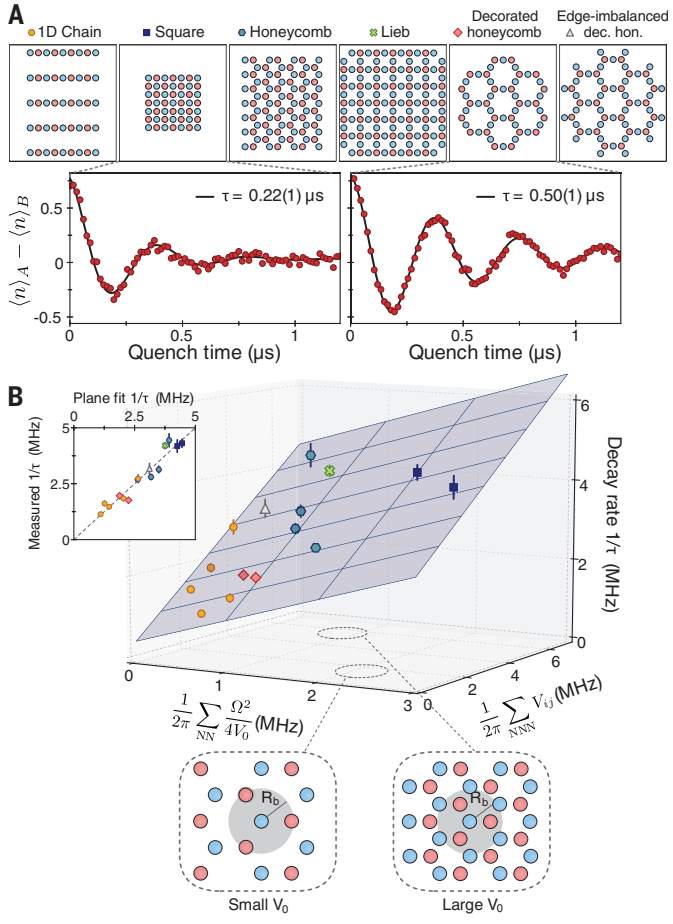

Fig. 2. Universal empirical description of scar lifetime. (**A**) Different geometries used in this study. The lifetime τ of the sublattice excitation difference depends strongly on the geometry. 1D stands for one-dimensional. (**B**) As a function of coupling to blockade-violating states ($\propto\Omega^2/V_0$) and NNN interactions, the scar decay rate $1/\tau$ displays a bilinear dependence. The inset shows a cross section of the plane. Schematics depict regimes where the two different decay processes dominate. Symbols are defined in (A). Error bars represent the standard error of the fit of τ.

in a strongly interacting system and indicate a special dynamical behavior as well as a form of ergodicity breaking (*11*, *22*). This scarring behavior is captured by the so-called "PXP" model of perfect NN blockade, in which V_0 is infinite and interactions beyond NN are zero: $H_{\mathrm{PXP}} = (\Omega/2)\sum_i P_{i-1}\sigma_i^x P_{i+1}$, where $P_i = |g_i\rangle\langle g_i|$ is the projector onto the ground state at site i. (*11*, *22*–*26*). In this model, the coherent oscillations of the sublattice population difference $\langle n\rangle_A - \langle n\rangle_B$ are understood as the oscillations of an emergent "large spin" (*27*).

We observe this oscillatory behavior in a wide variety of bipartite lattices (Fig. 2A). (We do not observe scarring on the nonbipartite lattices that we measure.) As an example, we plot the difference between the sublattice A and B populations $\langle n\rangle_A - \langle n\rangle_B$ for a 49-atom square and a 54-atom decorated honeycomb (*28*), with Rabi frequency $\Omega/2\pi = 4.2$ MHz and interaction strength $V_0/2\pi = 9.1$ MHz. We note a marked difference in the lifetime of periodic revivals for these two different lattices. Quantitatively, we find that dynamics of $\langle n\rangle_A - \langle n\rangle_B$ are well-described by a damped cosine, $y_0 + C\cos(\tilde{\Omega}t)\exp(-t/\tau)$, with oscillation frequency $\tilde{\Omega}$, decay time τ, offset y_0, and contrast C. Although $\tilde{\Omega} \approx 0.6\Omega$ on both the square and decorated honeycomb lattices (and on the other lattices we probe), the fitted τ for these two different configurations are 0.22(1) and 0.50(1) μs, respectively.

To understand this geometry dependence, we consider an empirical model for the decay rate of many-body scars [see (*29*)], parametrized as follows:

$$\frac{1}{\tau} = \alpha\left(\frac{1}{2\pi}\sum\nolimits_{\mathrm{NN}}\frac{\Omega^2}{4V_0}\right) + \beta\left(\frac{1}{2\pi}\sum\nolimits_{\mathrm{NNN}}V_{ij}\right) + \frac{1}{\tau_0} \qquad (2)$$

where the first two terms capture deviations of the Rydberg Hamiltonian from the idealized PXP model, owing to second-order virtual coupling to states violating blockade and next-nearest-neighbor (NNN) interactions, respectively (*29*); α, β, and τ_0 are phenomenological values. In Fig. 2B, we plot the measured $1/\tau$ as a function of the first and second terms in Eq. 2 for all geometries shown in Fig. 2A and varied interaction strengths V_0. We find that the decay rates fit well to a plane with slopes α = 0.72(12) and β = 0.58(5) and offset $1/\tau_0 = 0.4(2)$MHz. Note that $1/\tau_0$, which includes decay contributions inherent to the idealized PXP model (*11*, *28*), is much smaller than $1/\tau$; i.e., the decay of scars is dominated by imperfect blockade and long-range interactions. The observation that long-range fields contribute to decay also motivates quenching to small positive $\Delta_q = \Delta_{q,\mathrm{opt}} = 1/2\sum_{i,j>\mathrm{NN}}V_{ij}$, which cancels the static contribution from the long-range interactions (*29*) and is used throughout this work. These results also suggest an intrinsic limit to the scar lifetime, coming from the trade-off between imperfect blockade ($\propto 1/V_0$) and long-range interactions ($\propto V_0$). For example, we estimate a maximum lifetime $\tau_{\max} \approx 0.9$ μs for a chain and $\tau_{\max} \approx 0.4$ μs for a honeycomb lattice.

We next investigate the effect of parametric driving on many-body scars. To this end, we implement quenches to a time-dependent detuning $\Delta_q(t) = \Delta_0 + \Delta_m\cos(\omega_m t)$, as illustrated

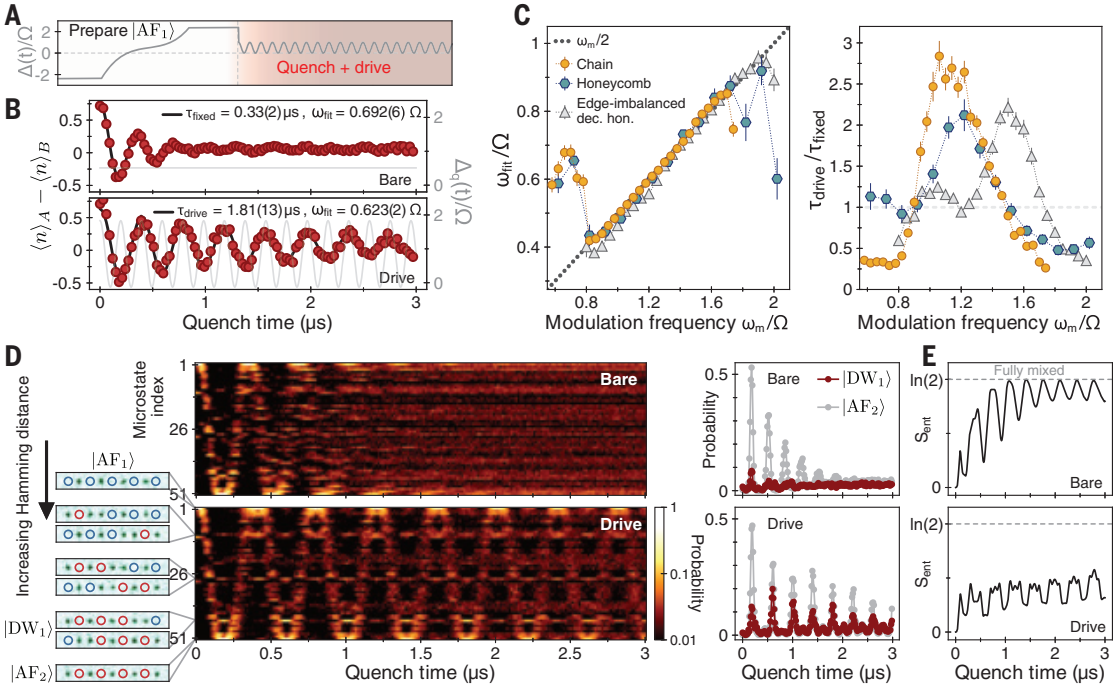

Fig. 3. Emergent subharmonic locking and stabilization. (**A**) Pulse sequence showing state preparation and quench with $\Delta_q(t)$. (**B**) Scar dynamics on a chain during quench to fixed optimal detuning (bare) with lifetime τ_{fixed}, and time-dependent detuning (drive) with modulation frequency $\omega_m = 1.24\Omega$ and lifetime τ_{drive}. The drive increases the scar lifetime and changes its frequency to $\omega_m/2$. (**C**) Scar response frequency and lifetime as a function of ω_m, showing a subharmonic locking and lifetime increase. (**D**) Dynamics of the entire Hilbert space measured with experimental snapshots (0.5 million total bit strings). The microstates of the constrained Hilbert space are ordered by $n_A - n_B$, or equivalently by Hamming distance (number of spin flips) from $|AF_1\rangle$ [see (*29*) for details]. Right subplots highlight $|AF_2\rangle$ and a state with a domain wall $|DW_1\rangle$. (**E**) Reduced density matrix of a single atom in a chain (numerics) shows that driving reduces the growth of entanglement entropy S_{ent}.

in Fig. 3A, and explore a nonperturbative regime of $\Delta_m, \Delta_0, \omega_m \sim \Omega$. Notably, in Fig. 3B, we find that such a quench results in a fivefold increase of scar lifetime compared with the fixed-detuning case, for properly chosen drive parameters (modulation frequency $\omega_m = 1.24\Omega$, offset $\Delta_0 = 0.85\Omega$, and amplitude $\Delta_m = 0.98\Omega$ for this nine-atom chain). Further, we find that the drive changes the oscillation frequency $\tilde{\Omega}$ to $\omega_m/2$, apparent in the synchronous revival of $\langle n\rangle_A - \langle n\rangle_B$ every two drive periods of $\Delta_q(t)$.

Figure 3C shows the scar lifetime and oscillation frequency as a function of modulation frequency ω_m, for a nine-atom chain (with different V_0 than Fig. 3A), a 41-atom honeycomb, and a 66-atom edge-imbalanced decorated honeycomb [tabulation of system and drive parameters in (*29*)]. For all three lattices, a robust subharmonic locking of the scar frequency is observed at $\omega_m/2$ over a wide range of ω_m, accompanied by a marked increase in the scar lifetime. The optimal driving frequency roughly corresponds to twice the natural scar oscillation frequency for the chain and honeycomb lattice (with an apparent ~10% shift toward lower ω_m), whereas the imbalanced lattice exhibits an unexpected double-peak structure (*29*). We note that sizable lifetime enhancements are found even when $\Delta_m, \Delta_0 \gg \sum_{NNN} V_{ij}$, and even in numerics for the idealized PXP model (*29*), indicating that the physical origin of the enhancement is not simply a mean-field-interaction cancellation akin to fixed $\Delta_{q,opt}$.

Figure 3D shows the experimentally observed distribution of microscopic many-body states across the entire Hilbert space of the nine-atom chain, as a function of quench time (see also movie S1). For the fixed detuning quench, oscillations between $|AF_1\rangle$ and $|AF_2\rangle$ product states are observed, before the quantum state spreads and thermalizes to a near-uniform distribution across the many-body states (*1*, *2*). Notably, parametric driving not only delays thermalization but also alters the actual trajectory being stabilized: The driven case also shows periodic, synchronous occupation of several other many-body states (emphasized in the right panels of Fig. 3D), seemingly dominated by those with near-maximal excitation number (indicated in the left panels). This suggests that rather than enhancing oscillations between the $|AF\rangle$ states, the parametric driving actually stabilizes the scar dynamics to oscillations between entangled superpositions composed of various product states. Figure 3E further illustrates the change in trajectory with numerical simulations of the local entanglement entropy, revealing that driving stabilizes the periodic entangling and disentangling of an atom with the rest of the system.

We observe this emergent subharmonic stabilization for a wide range of system and drive parameters. Figure 4, A and B, shows the time dynamics of $\langle n\rangle_A - \langle n\rangle_B$ and the normalized intensity of its associated Fourier transform $|S(\omega)|^2$ as a function of the drive frequency for a nine-atom chain. A response is observed at $\omega = \omega_m$ for $\omega_m < 0.8\Omega$, before suddenly transitioning into a subharmonic response $\omega = \omega_m/2$ for $\omega_m > 0.8\Omega$. For different drive parameters, a weak fourth subharmonic response at $\omega = \omega_m/4$ is also observed (*29*). To quantify the robustness of the observed response, we evaluate the subharmonic weight, $|S(\omega = \omega_m/2)|^2$, which encapsulates both the $\omega_m/2$ response and enhanced lifetime (*30*, *31*). Figure 4C shows the corresponding results for a nine-atom chain and a 41-atom honeycomb as a function of the modulation frequency ω_m and the lattice spacing a [in units of the blockade radius R_b defined by $V(R_b) = \Omega$]. A wide plateau in the subharmonic weight is clearly observed for both lattices, as a function of both modulation frequency and interaction strength (range 0.6 to $0.9a/R_b$ corresponds to $V_0/2\pi \approx 8$ to 80 MHz). To quantify the many-body nature of this stable region (*13*), we make use of the subharmonic rigidity, defined as the sum of the subharmonic weights measured at each modulation frequency: $\sum_{\omega_m} |S_{\omega_m}(\omega = \omega_m/2)|^2$ for $\omega_m = 0.75, 0.85, ..., 1.75\Omega$. The subharmonic rigidity quantifies robustness of the subharmonic response, where large values imply a large subharmonic response over a wide range of modulation frequencies. Figure 4D shows that subharmonic rigidity increases with system size until saturating at roughly 13 atoms for both a chain and a honeycomb lattice and appearing stable for the honeycomb lattice even to 200 atoms.

The emergent subharmonic response and its rigidity are strongly reminiscent of those

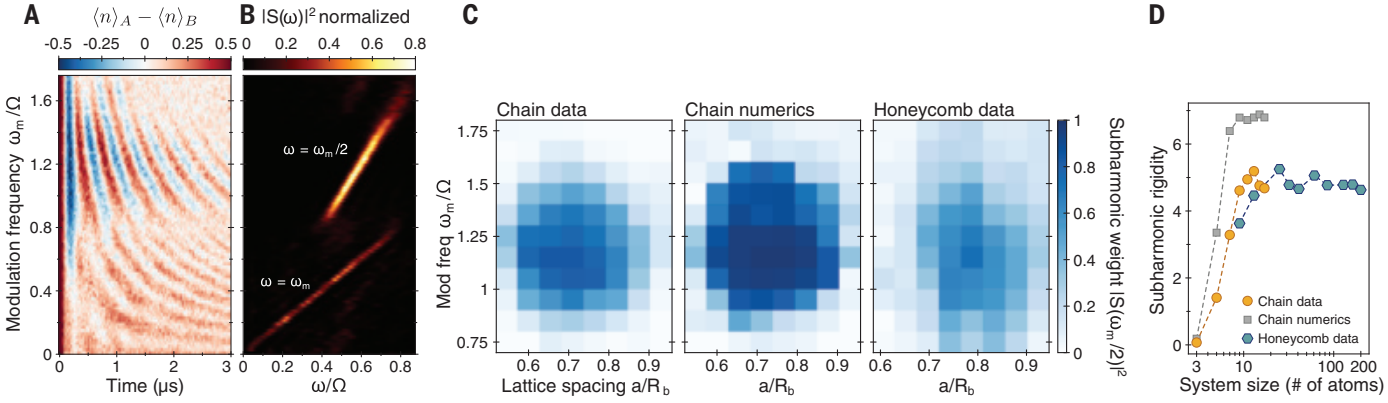

Fig. 4. Robustness of the subharmonic response. (**A**) Dynamics of sublattice population difference after quench, as a function of modulation frequency. (**B**) Fourier transform intensity $|S(\omega)|^2$ of data in (A), showing a harmonic locking for $\omega_m < 0.8\Omega$ and a subharmonic locking for $\omega_m > 0.8\Omega$. (**C**) Phase diagram of the subharmonic response $|S(\omega = \omega_m/2)|^2$ in chain data (left), chain numerics (middle) from perfectly initialized $|AF_1\rangle$ without experimental imperfections, and honeycomb data (right). (**D**) Increase of subharmonic rigidity (sum of subharmonic weights measured over a range of modulation frequencies) with increasing system size.

associated with discrete time-crystalline order (*12*, *13*, *30*–*32*). Yet, there are clear distinctions. Specifically, this behavior is observed only for antiferromagnetic initial states, whereas other initial states such as $|ggg\ldots\rangle$ thermalize and do not show subharmonic responses (*29*). This sharp state dependence distinguishes these observations from conventional MBL or prethermal time crystals (*33*), where subharmonic responses are not tied to special initial states. Moreover, it is surprising that our drive, whose frequency is resonant with local energy scales, enhances quantum scarring and ergodicity breaking instead of rapidly injecting energy into the system, as would generally be expected in many-body systems (*34*).

To gain intuition into the origin of the observed subharmonic stabilization of many-body scars, we consider a toy, pulsed model with Floquet unitary $U_F(\theta,\tau) = e^{-i\theta\sum_i n_i} e^{-iH_{PXP}\tau}$, where rotation angle θ arises from an infinitesimal, strong detuning pulse [see the follow-up theoretical work (*35*)]. Owing to the particle-hole symmetry of the PXP Hamiltonian, for $\theta = \pi$, the time evolution $e^{-iH_{PXP}\tau}$ during one pulse is canceled by the time evolution $e^{iH_{PXP}\tau}$ in a subsequent pulse, generating an effective many-body echo and subharmonic response (*29*, *35*). Interestingly, for small deviations ε from perfect π rotations, giving rotation angles $\theta = \pi + \varepsilon$, revivals vanish for generic initial states but persist robustly for an initial $|AF\rangle$ state (*29*, *35*). This behavior can be understood as follows: Owing to the scarring character of the antiferromagnetic initial states, the PXP evolution approximately realizes an effective π-pulse from $|AF_1\rangle$ to $|AF_2\rangle$ but results in ergodic spreading for other initial states. Accordingly, for $\theta = \pi + \varepsilon$, evolution still approximates an effective many-body echo for the scarred $|AF\rangle$ but does not reverse the chaotic evolution of generic initial states. Finally, the additional $\varepsilon\sum_i n_i$ serves as a "stabilizing Hamiltonian" by creating an effective gap between the $|AF\rangle$ states (which have maximal atomic excitations $n_{max} = \sum_i n_i$) from the rest of the spectrum. In practice, the $|AF\rangle$ states will be dressed by other states with near-maximal atomic excitations, consistent with the dynamics in Fig. 3D. Although the above arguments involve an idealized pulsed model, neglect large NNN interactions, and do not explicitly explain the observations in imbalanced lattices (Fig. 3C), this analysis already offers useful insight by connecting the observed subharmonic response to DTC physics (*35*) and warrants further study.

These considerations indicate that the observed subharmonic stabilization of many-body scars constitutes a new physical phenomenon that can be used for steering quantum dynamics in complex systems. Our observations challenge conventional understandings of quantum thermalization, warranting further investigation to understand the exact nature and conditions for this stabilization, its relationship to dynamical phases of matter such as the DTC, and the special role of the many-body scar states. Such studies could be extended to systems with more complex geometry, control, and topology, ranging from other initial states (*36*) and nonbipartite arrays (*14*, *21*) to the implementation of these techniques in other controllable many-body systems. These results open new possibilities for robust control of complex entangled states in many-body systems, with potential applications in areas such as quantum metrology and quantum information science (*3*).

REFERENCES AND NOTES

1. M. Srednicki, *Phys. Rev. E Stat. Phys. Plasmas Fluids Relat. Interdiscip. Topics* **50**, 888–901 (1994).
2. M. Rigol, V. Dunjko, M. Olshanii, *Nature* **452**, 854–858 (2008).
3. F. Arute *et al.*, *Nature* **574**, 505–510 (2019).
4. A. M. Kaufman *et al.*, *Science* **353**, 794–800 (2016).
5. M. Schreiber *et al.*, *Science* **349**, 842–845 (2015).
6. T. Langen *et al.*, *Science* **348**, 207–211 (2015).
7. D. A. Abanin, E. Altman, I. Bloch, M. Serbyn, *Rev. Mod. Phys.* **91**, 021001 (2019).
8. R. Nandkishore, D. A. Huse, *Annu. Rev. Condens. Matter Phys.* **6**, 15–38 (2015).
9. E. J. Heller, *Phys. Rev. Lett.* **53**, 1515–1518 (1984).
10. H. Bernien *et al.*, *Nature* **551**, 579–584 (2017).
11. C. J. Turner, A. A. Michailidis, D. A. Abanin, M. Serbyn, Z. Papić, *Nat. Phys.* **14**, 745–749 (2018).
12. V. Khemani, A. Lazarides, R. Moessner, S. L. Sondhi, *Phys. Rev. Lett.* **116**, 250401 (2016).
13. D. V. Else, B. Bauer, C. Nayak, *Phys. Rev. Lett.* **117**, 090402 (2016).
14. H. Labuhn *et al.*, *Nature* **534**, 667–670 (2016).
15. S. Ebadi *et al.*, arXiv:2012.12281 [quant-ph] (22 December 2020).
16. D. Jaksch *et al.*, *Phys. Rev. Lett.* **85**, 2208–2211 (2000).
17. E. Urban *et al.*, *Nat. Phys.* **5**, 110–114 (2009).
18. T. Pohl, E. Demler, M. D. Lukin, *Phys. Rev. Lett.* **104**, 043002 (2010).
19. P. Schauß *et al.*, *Science* **347**, 1455–1458 (2015).
20. E. Guardado-Sanchez *et al.*, *Phys. Rev. X* **8**, 021069 (2018).
21. V. Lienhard *et al.*, *Phys. Rev. X* **8**, 021070 (2018).
22. W. W. Ho, S. Choi, H. Pichler, M. D. Lukin, *Phys. Rev. Lett.* **122**, 040603 (2019).
23. C. Ates, J. P. Garrahan, I. Lesanovsky, *Phys. Rev. Lett.* **108**, 110603 (2012).
24. I. Lesanovsky, H. Katsura, *Phys. Rev. A* **86**, 041601 (2012).
25. C. J. Lin, O. I. Motrunich, *Phys. Rev. Lett.* **122**, 173401 (2019).
26. V. Khemani, C. R. Laumann, A. Chandran, *Phys. Rev. B* **99**, 161101 (2019).
27. S. Choi *et al.*, *Phys. Rev. Lett.* **122**, 220603 (2019).
28. A. A. Michailidis, C. J. Turner, Z. Papić, D. A. Abanin, M. Serbyn, *Phys. Rev. Res.* **2**, 022065 (2020).
29. Materials and methods are available as supplementary materials.
30. J. Zhang *et al.*, *Nature* **543**, 217–220 (2017).
31. S. Choi *et al.*, *Nature* **543**, 221–225 (2017).
32. N. Y. Yao, C. Nayak, L. Balents, M. P. Zaletel, *Nat. Phys.* **16**, 438–447 (2020).
33. D. V. Else, B. Bauer, C. Nayak, *Phys. Rev. X* **7**, 011026 (2017).
34. P. Ponte, A. Chandran, Z. Papić, D. A. Abanin, *Ann. Phys.* **353**, 196–204 (2015).
35. N. Maskara *et al.*, arxiv:2102.13160 [quant-ph] (25 February 2021).
36. B. Mukherjee, A. Sen, D. Sen, K. Sengupta, *Phys. Rev. B* **102**, 075123 (2020).

ACKNOWLEDGMENTS

We thank many members of the Harvard AMO community, particularly E. Urbach, S. Dakoulas, and J. Doyle for their efforts enabling safe and productive operation of our laboratories during

2020. We thank D. Abanin, I. Cong, F. Machado, H. Pichler, N. Yao, B. Ye, and H. Zhou for stimulating discussions. **Funding:** We acknowledge financial support from the Center for Ultracold Atoms, the National Science Foundation, the Vannevar Bush Faculty Fellowship, the U.S. Department of Energy (LBNL QSA Center and grant no. DE-SC0021013), the Office of Naval Research, the Army Research Office MURI, the DARPA DRINQS program (grant no. D18AC00033), and the DARPA ONISQ program (grant no. W911NF2010021). The authors acknowledge support from the NSF Graduate Research Fellowship Program (grant DGE1745303) and The Fannie and John Hertz Foundation (D.B.); a National Defense Science and Engineering Graduate (NDSEG) fellowship (H.L.); a fellowship from the Max Planck/Harvard Research Center for Quantum Optics (G.S.); Gordon College (T.T.W.); the European Research Council (ERC) under the European Union's Horizon 2020 research and innovation program (grant agreement no. 850899) (A.A.M. and M.S.); a Department of Energy Computational Science Graduate Fellowship under award number DE-SC0021110 (N.M.); the Moore Foundation's EPiQS Initiative grant no. GBMF4306, the NUS Development grant AY2019/2020, and the Stanford Institute of Theoretical Physics (W.W.H.); and the Miller Institute for Basic Research in Science (S.C.). **Author contributions:** D.B., A.O., H.L., A.K., G.S., S.E., and T.T.W. contributed to the building of the experimental setup, performed the measurements, and analyzed the data. A.A.M., N.M., W.W.H., S.C., and M.S. performed theoretical analysis. All work was supervised by M.G., V.V., and M.D.L. All authors discussed the results and contributed to the manuscript. **Competing interests:** M.G., V.V., and M.D.L. are co-founders and shareholders of QuEra Computing. A.O. is a shareholder of QuEra Computing. **Data and materials availability:** All data needed to evaluate the conclusions in the paper are present in the paper and the supplementary materials.

SUPPLEMENTARY MATERIALS

science.sciencemag.org/content/371/6536/1355/suppl/DC1
Materials and Methods
Figs. S1 to S13
Tables S1 and S2
References (*37*–*46*)
Movie S1

21 December 2020; accepted 12 February 2021
Published online 25 February 2021
10.1126/science.abg2530

SOLAR CELLS

Stabilizing black-phase formamidinium perovskite formation at room temperature and high humidity

Wei Hui[1]*, Lingfeng Chao[2]*, Hui Lu[1]*, Fei Xia[1], Qi Wei[3], Zhenhuang Su[4], Tingting Niu[2], Lei Tao[1], Bin Du[1], Deli Li[2], Yue Wang[2], He Dong[2], Shouwei Zuo[5], Bixin Li[6], Wei Shi[1], Xueqin Ran[1], Ping Li[1], Hui Zhang[1], Zhongbin Wu[2], Chenxin Ran[2], Lin Song[2], Guichuan Xing[3], Xingyu Gao[4], Jing Zhang[5], Yingdong Xia[1], Yonghua Chen[1]†, Wei Huang[1,2,7]†

The stabilization of black-phase formamidinium lead iodide (α-$FAPbI_3$) perovskite under various environmental conditions is considered necessary for solar cells. However, challenges remain regarding the temperature sensitivity of α-$FAPbI_3$ and the requirements for strict humidity control in its processing. Here we report the synthesis of stable α-$FAPbI_3$, regardless of humidity and temperature, based on a vertically aligned lead iodide thin film grown from an ionic liquid, methylamine formate. The vertically grown structure has numerous nanometer-scale ion channels that facilitate the permeation of formamidinium iodide into the lead iodide thin films for fast and robust transformation to α-$FAPbI_3$. A solar cell with a power-conversion efficiency of 24.1% was achieved. The unencapsulated cells retain 80 and 90% of their initial efficiencies for 500 hours at 85°C and continuous light stress, respectively.

The high power-conversion efficiency (PCE) of lead halide perovskite solar cells (PSCs) is attributed to their high carrier mobility and diffusion length and adjustable bandgap of the active-layer materials (*1*, *2*). Black-phase formamidinium lead iodine (α-$FAPbI_3$) has the narrowest bandgap (1.45 to 1.51 eV in thin films) (*3*, *4*). This phase easily transforms into a wide-bandgap yellow nonperovskite phase (δ-$FAPbI_3$) under ambient conditions because the large size of FA^+ induces lattice distortion (*5*, *6*), so routes have been developed to stabilize α-$FAPbI_3$ perovskite thin films. Some of these approaches involve mixing alternative cations, anions, or both to form hybrid formamidinium perovskites, such as the FA_xMA_{1-x} double cation (*7*); the $FA_{1-x-y}MA_xCs_y$ triple cation (*8*); and even FA^+, MA^+, Rb^+, Cs^+, SCN^-, and Br^- multiple cation-anion hybrids (*5*, *9*, *10*). Although these modifications improve the stability and enhance PCEs (*10*, *11*), high-quality perovskite and perovskite intermediate thin films must be processed in an inert atmosphere with strict control of both the temperature and relative humidity (RH). These requirements greatly limit production and applications of PSCs (*12*). The stability issues result from interactions of the precursors in their common solvents and their thin films. These interactions control the assembly of perovskite segments and affect the stability and performance of the frameworks (*13*).

We report a synthesis of stable black-phase α-$FAPbI_3$ that is insensitive to environmental conditions during its preparation. Vertically aligned thin films of lead iodide (PbI_2) are prepared from the ionic liquid methylamine formate (MAFa). Unlike commonly used solvents, such as *N*,*N*-dimethylformamide (DMF) and dimethyl sulfoxide (DMSO), strong interactions with PbI_2 through C=O···Pb chelation and N-H···I hydrogen bonds in the MAFa solvent promoted the vertical growth with respect to the substrate. Formamidinium iodide (FAI) could enter the PbI_2 thin films through in situ formation of ion channels, which notably reduced the formation energy barriers. A fast transformation to stable black-phase α-$FAPbI_3$ was observed irrespective of RH (20 to 90%) and temperature (25° to 100°C). We achieved a PCE of >24% in ambient air, with 93% of the initial efficiency retained up to 5000 hours (under nitrogen-filled glove box), thermal stability for 500 hours (80% of the initial efficiency retained at 85°C), and stability under continuous light stress (90% of the initial efficiency retained over 500 hours of operation at maximum power point).

We dissolved 1.5 M PbI_2 in two different solvents: MAFa (fig. S1) and DMF:DMSO (9:1, v/v) (Fig. 1A). The PbI_2 in DMF:DMSO (PbI_2@DMF:DMSO) solution was a deep yellow, whereas a yellow-green solution formed in the MAFa solvent. Proton nuclear magnetic resonance (^1H NMR) spectra of the two solutions before and after dissolution of PbI_2 (Fig. 1B) (*12*, *14*) showed that the amino hydrogen spectrum in the MAFa solution shifted from 8.46 to 9.04 parts per million (ppm) because of amino hydrogen forming a strong N-H···I hydrogen bond with an I^- ion in solution (*14*–*16*). However, no similar hydrogen-bond interactions were observed in the PbI_2@DMF:DMSO solution (fig. S2). Moreover, the peak of C=O in the ^{13}C NMR spectra moved from 167.2 ppm for pure MAFa to 167.6 ppm for the PbI_2 in MAFa (PbI_2@MAFa) solution (Fig. 1C), which is indicative of a strong interaction of the C=O group in MAFa with Pb^{2+} (*15*, *17*), but no clear

[1]Key Laboratory of Flexible Electronics (KLoFE) and Institute of Advanced Materials (IAM), Nanjing Tech University, 30 South Puzhu Road, Nanjing 211816, Jiangsu, China. [2]Frontiers Science Center for Flexible Electronics, Xi'an Institute of Flexible Electronics (IFE) and Xi'an Institute of Biomedical Materials and Engineering, Northwestern Polytechnical University, 127 West Youyi Road, Xi'an 710072, China. [3]Joint Key Laboratory of the Ministry of Education, Institute of Applied Physics and Materials Engineering, University of Macau, Avenida da Universidade, Taipa, Macau 999078, China. [4]Shanghai Synchrotron Radiation Facility (SSRF), Zhangjiang Lab, Shanghai Advanced Research Institute, Chinese Academy of Sciences, 239 Zhangheng Road, Shanghai 201204, China. [5]Beijing Synchrotron Radiation Facility, Institute of High Energy Physics, Chinese Academy of Sciences, Beijing 100049, China. [6]Department of Educational Science, Laboratory of College Physics, Hunan First Normal University, Changsha 410205, Hunan, China. [7]Key Laboratory for Organic Electronics and Information Displays and Institute of Advanced Materials, Nanjing University of Posts and Telecommunications, Nanjing 210023, China.
*These authors contributed equally to this work.
†Corresponding author. Email: iamyhchen@njtech.edu.cn (Y.C.); iamwhuang@nwpu.edu.cn (W.H.)

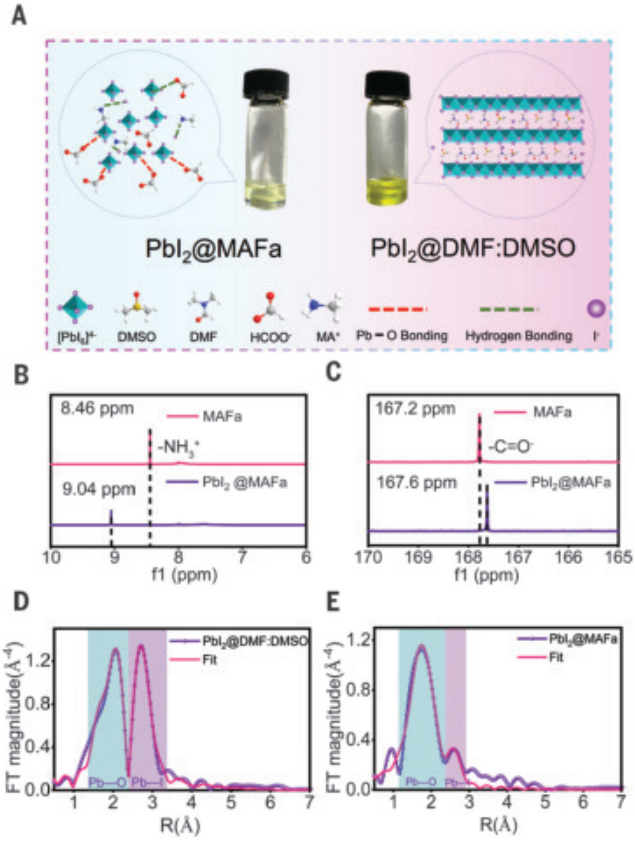

Fig. 1. Chemical environment for precursors in different solvents. (**A**) Images of PbI_2@MAFa and PbI_2@DMF:DMSO solutions and schematic diagram of interactions in the solutions. (**B**) ^1H NMR spectra of the two solutions before and after dissolution of PbI_2. f1, magnetic intensity. (**C**) ^{13}C NMR spectra of the two solutions before and after dissolution of PbI_2. (**D** and **E**) Extended x-ray absorption fine structure spectra and fits in R-space at the Pb L_3-edge of PbI_2@DMF:DMSO (D) and PbI_2@MAFa (E). The green area represents the Pb···O bond, and the purple area represents the Pb–I bond. FT, Fourier transform.

Table 1. Parameters of champion devices based on $FAPbI_3$@MAFa and $FAPbI_3$@DMF:DMSO perovskite thin films.

Solvents	V_{oc} (V)	J_{sc} (mA cm^{-2})	FF (%)	PCE (%)
MAFa	1.17	25.34	81.36	24.1
DMF:DMSO	1.15	24.72	77.85	22.1

shift was observed before and after the dissolution of PbI_2 in DMF:DMSO (fig. S3).

We used x-ray absorption near-edge structure to determine the coordination environment of the Pb atoms in the two solvents. Both Pb···O and Pb–I bonds were observed in DMF:DMSO (Fig. 1D), which we attributed to the coordination of both S=O in DMSO and C=O in DMF with Pb^{2+} (fig. S4) (*13*). Strong Pb–I bonds originated from the layered PbI_2 molecules, which indicated relatively weak interactions between the solvent and PbI_2 molecules. By contrast, the PbI_2@MAFa solution had stronger Pb···O coordination and weaker Pb–I bonding (Fig. 1E). Moreover, the length of the Pb···O bond decreased from 2.48 to 2.35 Å (table S1) compared with that of the PbI_2@DMF:DMSO solution. This observation indicated an extremely strong C=O···Pb interaction in the PbI_2@MAFa solution, which plays an important role in affecting the layered structure of PbI_2 (*14*, *18*).

Free I^- formed hydrogen bonds with the amino groups of MAFa that could protect I^- in solution from oxidization (*12*, *14*, *19*). We exposed the two solutions to the atmosphere (RH > 80%) for 6 hours; the PbI_2@DMF:DMSO solution formed considerable amounts of precipitate (fig. S5) and had absorption characteristics of I^{3-} (fig. S6), whereas a clear solution and no absorption of I^{3-} were observed for the PbI_2@MAFa solution (fig. S7) (*14*). We attributed the improved solution stability to strong interactions of MAFa and PbI_2 through C=O···Pb chelation and N-H···I hydrogen bonds.

We systematically investigated the PbI_2 thin film formation and crystallization processes from these solutions. The PbI_2@MAFa thin films were prepared in air under ambient humidity, but the PbI_2@DMF:DMSO thin films were prepared in a N_2-filled glove box. A needlelike surface morphology of PbI_2 was observed after spin coating (0 s) from PbI_2@DMF:DMSO solution (Fig. 2A), consistent with previous reports (*13*, *20*). The needlelike initial grains provided multiple nucleation sites, which caused the grains to contract during the growth process and form undesirable pinholes.

To further understand the crystallization behavior of the PbI_2 thin films, we used in situ grazing-incidence wide-angle x-ray scattering (GIWAXS). The precursor phase (near $q \approx 7$ nm^{-1}, where q is the scattering vector) was the main component of the PbI_2@DMF:DMSO thin films in the initial stage of crystallization (Fig. 2B and fig. S8A). As the annealing time was prolonged, a PbI_2 signal near $q \approx 9.25$ nm^{-1} appeared (*21*). Although the diffraction intensity of PbI_2 increased as the annealing time was prolonged, most of the precursor structures had a strong signal. The strong Debye-Scherrer ring with an isotopic intensity distribution indicated that the grain orientation was completely random. This result was further confirmed by the disordered integration lines, as shown by the azimuthal integration of the PbI_2 diffraction ring (Fig. 2C) (*8*, *22*).

In contrast to DMF:DMSO, the use of MAFa as a solvent promoted the formation of uniform and PbI_2 grains larger than 1 μm after spin coating (Fig. 2D). Notably, diffraction from $MAPbI_3$ was observed given the presence of methylamine ions in the MAFa solution (fig. S9). When the annealing time was prolonged, full coverage of pinhole-free PbI_2 thin films with large grains was achieved. The initial strong diffraction signal of PbI_2 and weak $MAPbI_3$ signal near $q \approx 10$ nm^{-1} (Fig. 2E and fig. S8B) corresponded to the features in the x-ray diffraction (XRD) spectra. Although a certain precursor structure was produced at the beginning of spin coating, the precursor gradually transformed into a stable PbI_2 phase through a solid-solid conversion during annealing (*22*).

After the annealing process, the resulting PbI_2 thin films had a strong degree of preferential orientation with respect to the contact, as evident from sharp and discrete Bragg spots (Fig. 2E, 240 s), and the only pole figures of the azimuth angle were at 90° without noticeable peaks along the same rings (Fig. 2F) (*23*). Moreover, we found the random orientation of PbI_2 domains in the PbI_2@DMF:DMSO thin films from the high-resolution transmission electron microscopy (HRTEM) (fig. S10) (*24*), whereas the (001)-oriented PbI_2 domains have a high degree of orientation and show a very regular arrangement in the PbI_2@MAFa thin films (fig. S11). This allows the formation of a regular mesoporous structure of ~5 to 10 nm between the oriented domains of PbI_2 with the evaporation of MAFa (fig. S11, A and B) because MAFa remains in the thin films (fig. S12). Moreover, a clear hole was observed in the side view of the PbI_2@MAFa sample (fig. S11C). This structure led to vertically aligned growth of the PbI_2 thin films with formation of nanometer-scale ion channels between the layered PbI_2, which provides a direct reaction

channel for cations. This differs from the previously reported pore formation in PbI_2 films (*25*–*27*). Most notably, the PbI_2@MAFa thin films were more stable under high humidity than the PbI_2@DMF:DMSO thin films as a result of the strong Pb···O and hydrogen-bond interactions between residual MAFa and the PbI_2 framework (figs. S13 and S14) (*14*).

We prepared perovskite thin films under ambient conditions in air. The $FAPbI_3$@DMF:DMSO thin films (prepared from PbI_2@DMF:DMSO thin films at room temperature in a N_2-filled glove box) had a weak α phase at ~13.9° with a strong δ-phase signal (~11.8°) because of the low formation barrier of the δ phase (Fig. 3A) (*3*, *21*). By contrast, no δ phase was observed in the $FAPbI_3$@MAFa thin films (prepared by using PbI_2@MAFa thin films at room temperature in air), but a very strong α-$FAPbI_3$ perovskite signal was observed together with the PbI_2 peak at ~12.7° (*21*). This can be attributed to the fact that MAFa prevents the transformation of PbI_2 to δ-phase perovskite by the strong interactions of MAFa and PbI_2 through C=O···Pb chelation and N-H···I hydrogen bonds. The phase transition temperature of α-$FAPbI_3$ through the PbI_2@MAFa thin films decreased considerably and allowed for the transition to take place at room temperature and in air.

This result was further confirmed by a strong absorption with a band edge at ~820 nm and steady-state photoluminescence emission at ~820 nm for the $FAPbI_3$@MAFa film (fig. S15) (*2*). The PbI_2 peak intensity gradually weakened and crystallization of α-$FAPbI_3$ was further promoted when the substrate temperature was increased. Moreover, the surface roughness of the perovskite films decreased from 20.5 to 10.3 nm (fig. S16) together with an increase in grain size (fig. S17) (*3*). The δ phase was suppressed in the $FAPbI_3$@MAFa thin films because the vertical crystal orientation of the PbI_2 structure provided nanoscale ion channels for rapid entry of FA^+ and reduced the energy barrier to formation of α-$FAPbI_3$ (Fig. 3B) (*28*). The PbI_2@DMF:DMSO thin films had random orientation distributions (Fig. 2C), which limit the diffusion of FA^+, and this greater energy barrier to form α-$FAPbI_3$ favored the formation of a low-energy yellow phase (*29*).

The crystallization process of the $FAPbI_3$ perovskite thin films was further monitored by in situ GIWAXS measurement in real time. Crystals of the $FAPbI_3$@DMF:DMSO perovskite thin film grew in the vicinity of 30° through azimuth integration (fig. S18) and had a large δ-$FAPbI_3$ phase near $q \approx 8.5$ nm^{-1} (Fig. 3C) (*21*). Although the thin film eventually transformed into α-$FAPbI_3$, we could not rule out the possibility of a large amount of δ-$FAPbI_3$ remaining (Fig. 3C, 240 s, and fig. S19). However, for the $FAPbI_3$@MAFa perovskite thin films, stable α-$FAPbI_3$ perovskite thin films formed after the deposition of FAI without annealing (Fig. 3D and fig. S20). A small amount of the intermediates and PbI_2 transformed into α-$FAPbI_3$ perovskite structures during the annealing process, which is consistent with the XRD analysis.

Moreover, one-dimensional (1D) integration diagrams of 2D GIWAXS images (Fig. 3, E to J) indicated competition between the formation of δ-$FAPbI_3$ and α-$FAPbI_3$ phases in the case of the PbI_2@DMF:DMSO thin films (*13*). The peak position of δ-$FAPbI_3$ markedly shifted to a high q value upon annealing (Fig. 3F), which we attribute to the structural transformation. This process resulted in the fluctuation of the α-$FAPbI_3$ peak position over a small range near $q \approx 10$ nm^{-1}. The integrated intensity of δ-$FAPbI_3$ was markedly higher than that of α-$FAPbI_3$ in the early stage of crystallization (Fig. 3G); however, δ-$FAPbI_3$ phases remained inside the final $FAPbI_3$@DMF:DMSO perovskite thin films (*21*). By contrast, the $FAPbI_3$@MAFa perovskite thin films maintained a stable α-$FAPbI_3$ phase from the initial stage of crystallization (Fig. 3H), and the peak position

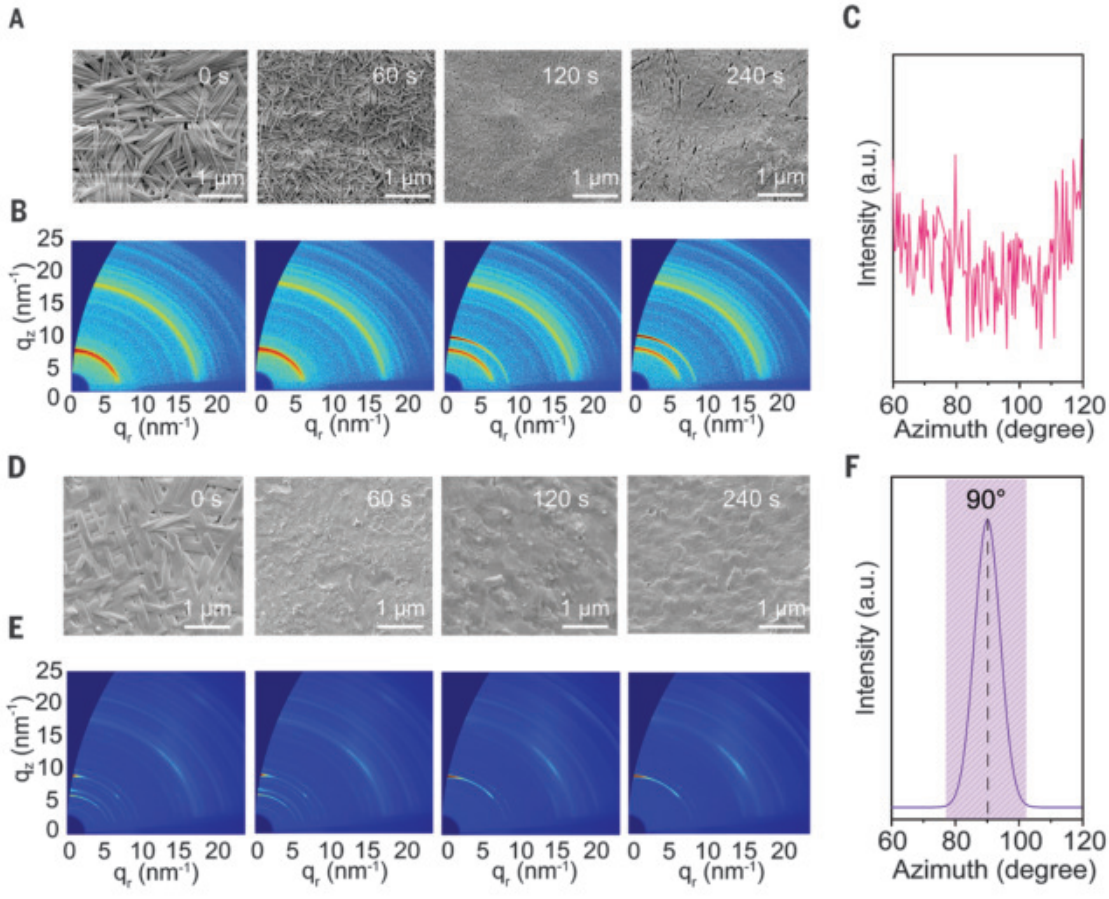

Fig. 2. Morphology and structural characterization of PbI_2@DMF:DMSO and PbI_2@MAFa films. (**A**) Scanning electron microscopy (SEM) images of PbI_2@DMF:DMSO films at different annealing times. (**B**) In situ GIWAXS spectra of PbI_2@DMF:DMSO films at the corresponding annealing time. (**C**) Azimuth integration at $q \approx 9.25$ nm^{-1} for PbI_2@DMF:DMSO thin films. a.u., arbitrary units. (**D**) SEM images of PbI_2@MAFa films at different annealing times. (**E**) In situ GIWAXS spectra of PbI_2@MAFa films at corresponding annealing times. (**F**) Azimuth integration at $q \approx 9.25$ nm^{-1} for PbI_2@MAFa thin films.

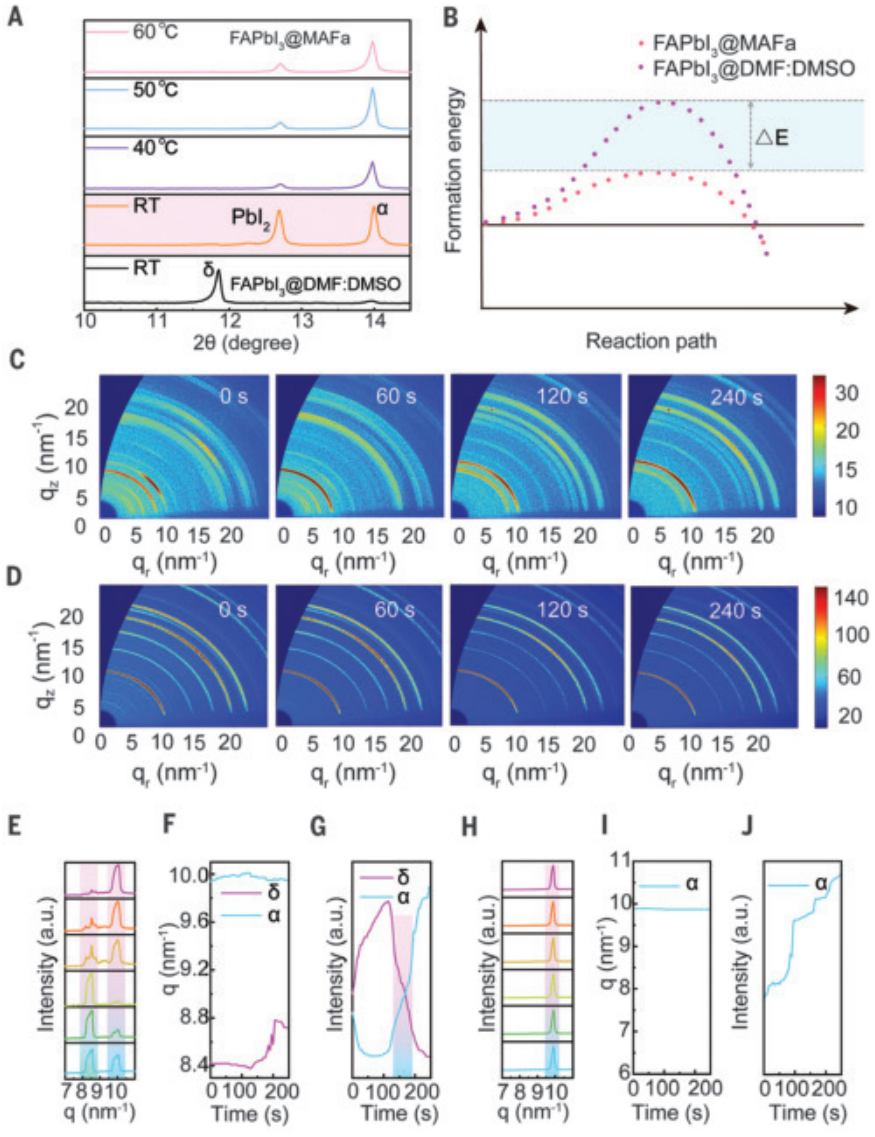

Fig. 3. Structural characterization of $FAPbI_3$ obtained from PbI_2@DMF:DMSO and PbI_2@MAFa films. (**A**) XRD spectra of $FAPbI_3$ perovskite films prepared from PbI_2@MAFa and PbI_2@DMF:DMSO films at room temperature (RT). The $FAPbI_3$@MAFa film was prepared under atmospheric conditions and the humidity exceeded 80%, whereas the $FAPbI_3$@DMF:DMSO film was prepared in a nitrogen glove box because it cannot be prepared under such high humidity conditions. (**B**) Schematic diagram of perovskite crystallization kinetics of $FAPbI_3$ film under PbI_2@MAFa (pink) and PbI_2@DMF:DMSO (purple) films, respectively. ΔE, change in energy barrier. (**C** and **D**) In situ GIWAXS spectra of $FAPbI_3$@DMF:DMSO perovskite films (C) and $FAPbI_3$@MAFa films (D) under different annealing times. (**E**) 1D GIWAXS integral spectra of $FAPbI_3$@DMF:DMSO at different annealing times. (**F**) Variation of the diffraction ring of α-$FAPbI_3$ and δ-$FAPbI_3$ with annealing time for the case of PbI_2@DMF:DMSO films. (**G**) Competition of the integrated intensity of α-$FAPbI_3$ and δ-$FAPbI_3$ with annealing time for the case of PbI_2@DMF:DMSO films. (**H**) 1D GIWAXS integral spectra of $FAPbI_3$@MAFa at different annealing times. (**I**) Variation in the diffraction ring of α-$FAPbI_3$ with annealing time for the case of PbI_2@MAFa films. (**J**) Evolution of black-phase $FAPbI_3$@MAFa perovskite with annealing time.

remained stable (Fig. 3I). This result indicates that the $FAPbI_3$@MAFa perovskite thin films had excellent crystallinity and a stable structure, as reflected by the increasing trend of the integrated peak intensity (Fig. 3J) (*8*).

Generally, the I–Pb–I ionic bonds are strong in the layered structure of PbI_2, whereas the van der Waals between adjacent sandwiched layers is weak. This allows a successfully insertion of different guest molecules, bringing about the expansion of interlayer distance along the *c* axis (*13*, *30*). Because of the large size of FA ions, it is difficult to insert them into the layered structure of PbI_2. However, FAI has a high affinity for PbI_2 (*31*), and it is easy to interact with PbI_2 at the edge of the crystal to form a δ-phase perovskite with a low formation energy barrier (*32*). The randomly arranged PbI_2 structure formed by the DMF:DMSO solvent could further affect the FAI diffusion process, thus resulting in the easy formation of δ-$FAPbI_3$ perovskite. In the PbI_2@MAFa thin films, ion channels are constructed that notably improve the diffusion path of FAI in the PbI_2 thin films, providing direct reaction channels for ions and greatly reducing the energy required to transform PbI_2 into α-$FAPbI_3$ perovskite. In addition, because of the strong chemical effect of MAFa, the structure of PbI_2 changes from the original Pb–I–Pb line structure to a corner-sharing layered structure, which consists of the initial preparation of $FAPbI_3$ and $MAPbI_3$ by $HPbI_3$ (*33*). This corner-sharing structure prevents the transformation of PbI_2 into δ-$FAPbI_3$ perovskite but facilitates the transformation of PbI_2 into α-$FAPbI_3$ perovskite.

Moreover, because of the different growth directions of the PbI_2@DMF:DMSO thin films, the diffraction peak positions of the generated α-$FAPbI_3$ were located near q = 9.95 nm^{-1}, compared with the α-$FAPbI_3$ prepared from PbI_2@MAFa thin films, which were fixed at q = 9.80 nm^{-1} (fig. S21). The large FA^+ anion did not fit well with such a smaller interplanar spacing. This mismatch was not conducive to structural stability of the thin films and contributed to their sensitivity to humidity (figs. S22 and S23) (*32*, *34*, *35*). Because the PbI_2@MAFa thin films have excellent vertically oriented crystallization, the FA^+ quickly enters the interior of the crystal in the second step and immediately reacts with PbI_2 to form a stable α-$FAPbI_3$ structure. Moreover, the interaction between the perovskite framework and MAFa can probably reduce the elastic modulus of the perovskite film, which alleviates the lattice strain inside the film and relieves the tensile stress on the surface (fig. S24). These could help to improve the stability of the $FAPbI_3$ perovskite film under high humidity (movie S1).

We prepared PSCs with a planar structure of indium tin oxide/SnO_2 (20 nm)/perovskite (~950 nm)/spiro-OMeTAD (80 nm)/MoO_3 (5 nm)/Au (100 nm). A device based on $FAPbI_3$@MAFa perovskite thin films with a champion PCE of 24.1% was achieved, with an open-circuit voltage (V_{oc}) of 1.17 V, a short-circuit current (J_{sc}) of 25.34 mA cm^{-2}, and a fill factor (FF) up to 81.36% at an RH of 80%, and the PCE was much higher than that for a PSC based on $FAPbI_3$@DMF:DMSO perovskite thin films under a N_2-filled glove box (22.12%) (Table 1). The steady-state output efficiency had a PCE close to 23.7%, and the steady-state output photocurrent density was 25.23 mA cm^{-2} (fig. S25), which is near that obtained from the *J-V* curve measurements (Fig. 4A).

We compared the performance of PSCs prepared under an RH of 30, 50, 70, and 90%. Devices based on $FAPbI_3$@DMF:DMSO perovskite thin films had an efficiency >20% at an RH of 30%, which decreased to 18% at an RH of 50%, and no photovoltaic performance was observed at an RH > 70% (fig. S26 and table S2). However, a PCE of ~23% with negligible hysteresis was achieved by the $FAPbI_3$@MAFa thin films regardless of RH (figs. S26 to S28 and table S2). Moreover, a high PCE of 20.76% for a large-area device was achieved (1 cm by 1 cm) (fig. S29).

The trap density of the $FAPbI_3$@MAFa perovskite thin films (4.74×10^{15} cm^{-3}) was lower than that of $FAPbI_3$@DMF:DMSO perovskite thin films (1.36×10^{16} cm^{-3}) (fig. S30), which is also conducive to lower carrier recombination. This result was confirmed by the dependence of the V_{oc} on the light intensity (fig. S31) and the dependence of J_{sc} on the light intensity (fig. S32). Trap-assisted recombination and bimolecular recombination were negligible in the $FAPbI_3$@MAFa perovskite thin films, which is consistent with its longer carrier lifetime (312.13 ns) than that of the $FAPbI_3$@DMF:DMSO perovskite thin films (9.82 ns) (fig. S33). Moreover, the $FAPbI_3$@MAFa thin films had more balanced carrier transport and a prolonged average lifetime owing to their high crystalline quality and low defect state density (figs. S34 and S35 and table S3), which contributed to the improved stability and current density of the devices.

The long-term stability of the PSCs was tested under various conditions without encapsulation. The $FAPbI_3$@MAFa device retained 93% of its original PCE after storage in the N_2-filled glove box for 5000 hours. This result contrasts with that of the $FAPbI_3$@DMF:DMSO device, which underwent a 30% PCE loss within only 500 hours (Fig. 4B). Moreover, we conducted the device thermal stability at 85°C in a N_2-filled glove box (Fig. 4C) (*36*) and found that the average PCE of the $FAPbI_3$@MAFa device remained at 80% of the initial efficiency for ~500 hours in a N_2-filled glove box, whereas serious PCE decrease was observed in the $FAPbI_3$@DMF:DMSO device, with 45% left after only ~150 hours. In addition, we performed the stability under operational conditions examined at the maximum power point. As seen in Fig. 4D, the $FAPbI_3$@DMF:DMSO device degrades rapidly, with 60% decrease of its initial efficiency within 140 hours. By contrast, the $FAPbI_3$@MAFa device retains 90% of its initial efficiency for 500 hours. We attribute the greater stability of the PbI_2@MAFa thin films to the vertically oriented crystal growth that provides ion channels for the rapid reaction in the second step, which created stable α-$FAPbI_3$ perovskite thin films. Also, residual MAFa protected the thin films from erosion by water

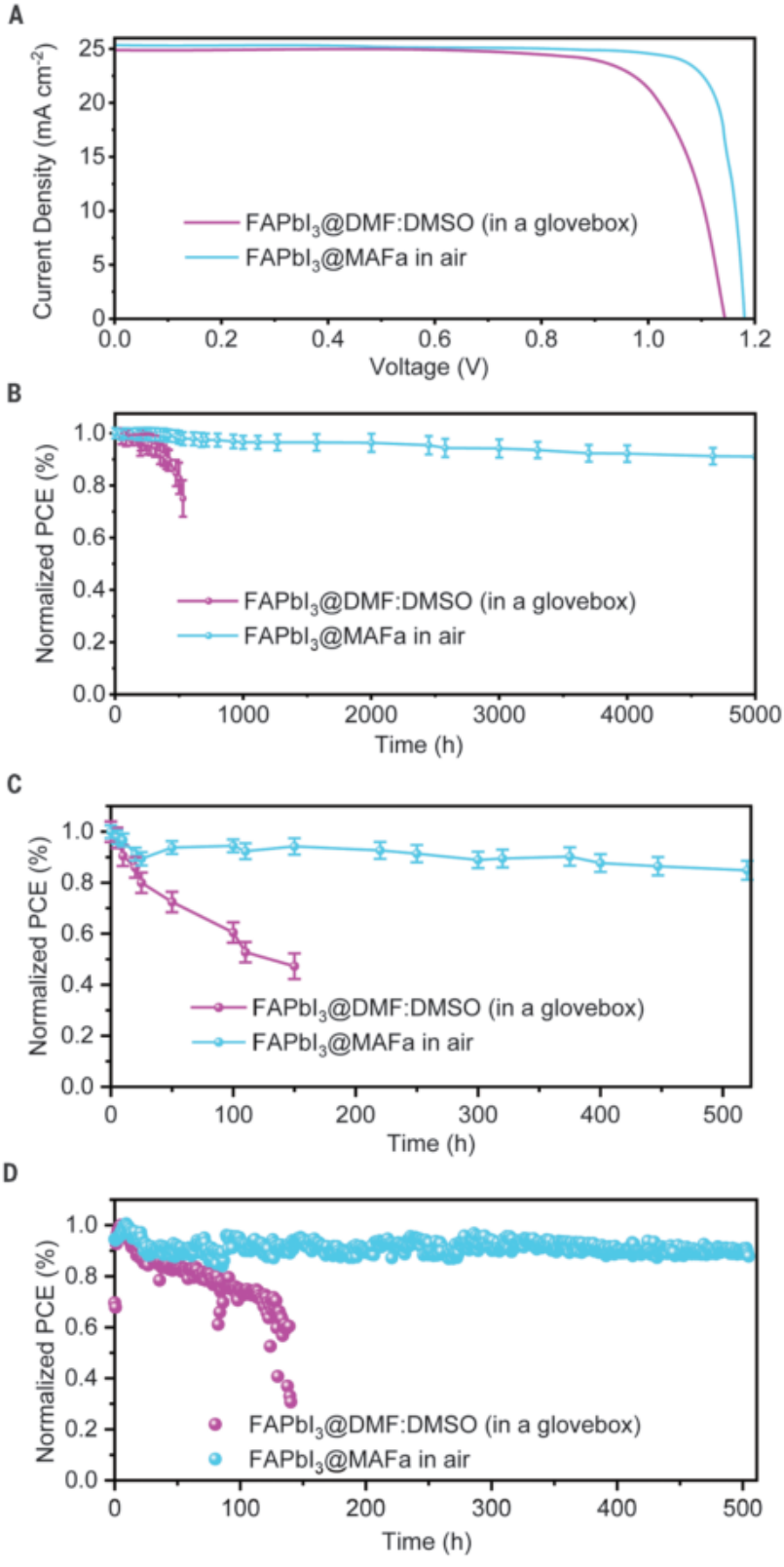

Fig. 4. Photovoltaic device performance. (**A**) *J*–*V* curves of champion device based on $FAPbI_3$@MAFa and $FAPbI_3$@DMF:DMSO films. (**B**) Stability of unencapsulated devices stored in a N_2-filled glove box in the dark. Error bars indicate the error or uncertainty in the reported measurements. (**C**) Comparison of the thermal stability of two unencapsulated devices under continuous heating at 85°C in a N_2-filled glove box. Error bars indicate the error or uncertainty in the reported measurements. (**D**) Operational stability of two unencapsulated devices at maximum power point (0.92 and 0.72 V for $FAPbI_3$@MAFa and $FAPbI_3$@DMF devices, respectively) under a white light-emitting diode lamp in a N_2-filled glove box.

and oxygen and combined with Pb vacancies at grain boundaries to prevent the decomposition of the thin films (fig. S36).

REFERENCES AND NOTES

1. National Renewable Energy Laboratory, Best Research-Cell Efficiency Chart (US Department of Energy, 2021); www.nrel.gov/pv/cell-efficiency.html.
2. H. Min *et al.*, *Science* **366**, 749–753 (2019).
3. G. Kim *et al.*, *Science* **370**, 108–112 (2020).
4. J. M. Frost *et al.*, *Nano Lett.* **14**, 2584–2590 (2014).
5. H. Lu *et al.*, *Science* **370**, eabb8985 (2020).
6. W. S. Yang *et al.*, *Science* **348**, 1234–1237 (2015).
7. N. J. Jeon *et al.*, *Nature* **517**, 476–480 (2015).
8. M. Qin *et al.*, *Adv. Mater.* **31**, e1901284 (2019).
9. T. Duong *et al.*, *Adv. Energy Mater.* **7**, 1700228 (2017).
10. M. Saliba *et al.*, *Science* **354**, 206–209 (2016).
11. M. I. Saidaminov *et al.*, *Nat. Energy* **3**, 648–654 (2018).
12. L. Chao *et al.*, *Chem* **5**, 995–1006 (2019).
13. Y. Guo *et al.*, *J. Am. Chem. Soc.* **137**, 15907–15914 (2015).
14. X. Wang *et al.*, *Angew. Chem. Int. Ed.* **59**, 13354–13361 (2020).
15. B. Li *et al.*, *Nat. Commun.* **9**, 1076 (2018).
16. A. Abate *et al.*, *Nano Lett.* **14**, 3247–3254 (2014).
17. A. Q. Alanazi *et al.*, *J. Am. Chem. Soc.* **141**, 17659–17669 (2019).
18. J. Pan *et al.*, *Adv. Mater.* **28**, 8309–8314 (2016).
19. H. Ren *et al.*, *Nat. Photonics* **14**, 154–163 (2020).
20. Q. Li *et al.*, *Adv. Mater.* **30**, 1803095 (2018).
21. Y. Liu *et al.*, *Angew. Chem. Int. Ed.* **59**, 15688–15694 (2020).
22. T. Miyadera *et al.*, *Nano Lett.* **15**, 5630–5634 (2015).
23. W. Hui *et al.*, *Nano Energy* **73**, 104803 (2020).
24. T. J. Jacobsson *et al.*, *J. Am. Chem. Soc.* **138**, 10331–10343 (2016).
25. X. Duan *et al.*, *Adv. Mater.* **32**, e2000617 (2020).
26. H. Zhang *et al.*, *Adv. Energy Mater.* **5**, 1501354 (2015).
27. C.-H. Chiang, C.-G. Wu, *Nat. Photonics* **10**, 196–200 (2016).
28. Y. Zhao *et al.*, *Adv. Mater.* **32**, e1907769 (2020).
29. Y. Zhao *et al.*, *Nat. Commun.* **9**, 1607 (2018).
30. Y. Jo *et al.*, *Adv. Mater. Interfaces* **3**, 1500768 (2016).
31. A. Binek, F. C. Hanusch, P. Docampo, T. Bein, *J. Phys. Chem. Lett.* **6**, 1249–1253 (2015).
32. B. W. Park, S. I. Seok, *Adv. Mater.* **31**, e1805337 (2019).
33. S. Pang *et al.*, *J. Am. Chem. Soc.* **138**, 750–753 (2016).
34. T. Chen *et al.*, *Sci. Adv.* **2**, e1601650 (2016).
35. Q. Han *et al.*, *Adv. Mater.* **28**, 2253–2258 (2016).
36. Q. Jiang *et al.*, *Nat. Photonics* **13**, 460–466 (2019).

ACKNOWLEDGMENTS

Y.C. acknowledges X. Huang from Nanjing Tech University (China) for assisting with HRTEM sample preparation and measurement and for the discussion of the structure of lead iodide. **Funding:** The authors acknowledge the Natural Science Foundation of China (grants 51602149, 61705102, 91833304, and 91733302); the Natural Science Foundation of Jiangsu Province for Distinguished Young Scholars, China (grant BK20200034); the National Key Research and Development Program of China (grant 2017YFA0403400); Projects of International Cooperation and Exchanges NSFC (51811530018); the Young 1000 Talents Global Recruitment Program of China; the Jiangsu Specially-Appointed Professor Program and the "Six talent peaks" Project in Jiangsu Province, China; and the Scientific Research Fund of Hunan Provincial Education Department (20B121). **Author contributions:** Y.C. and W.Huang conceived the idea and designed the experiments. Y.C. and W.Huang supervised the work. W.Hui, L.C., and H.L. carried out the device fabrication and characterizations. F.X., Q.W., B.L., and Z.S. also contributed to device fabrication. Q.W., G.X., T.N., L.T., W.S., X.R., P.L., and H.Z. conducted the optical spectra measurements. H.L., B.D., and Y.X. synthesized the MAFa. D.L., Y.W., and H.D. carried out the NMR and Fourier transform infrared spectra measurements. S.Z. and J.Z. conducted the x-ray absorption fine structure measurements and analyzed the data. GIWAXS was performed and analyzed by W.Hui, Z.S., C.R., L.S., and X.G., supported by the BL14B beamline of SSRF. W.Hui and L.C. wrote the first draft of the manuscript. Y.C., Y.X., Z.W., and W.Huang participated in data analysis and provided major revisions. All authors discussed the results and commented on the manuscript. **Competing interests:** The authors declare no competing financial or nonfinancial interests. **Data and materials availability:** All data needed to evaluate the conclusions in the paper are present in the paper or the supplementary materials.

SUPPLEMENTARY MATERIALS

science.sciencemag.org/content/371/6536/1359/suppl/DC1
Materials and Methods
Figs. S1 to S36
Tables S1 to S3
References (*37*–*47*)
Movie S1

17 November 2020; accepted 26 February 2021
10.1126/science.abf7652

SPECTROSCOPY

Three-dimensional vectorial imaging of surface phonon polaritons

Xiaoyan Li[1], Georg Haberfehlner[2], Ulrich Hohenester[3], Odile Stéphan[1], Gerald Kothleitner[2,4]*, Mathieu Kociak[1]*

Surface phonon polaritons (SPhPs) are coupled photon-phonon excitations that emerge at the surfaces of nanostructured materials. Although they strongly influence the optical and thermal behavior of nanomaterials, no technique has been able to reveal the complete three-dimensional (3D) vectorial picture of their electromagnetic density of states. Using a highly monochromated electron beam in a scanning transmission electron microscope, we could visualize varying SPhP signatures from nanoscale MgO cubes as a function of the beam position, energy loss, and tilt angle. The SPhPs' response was described in terms of eigenmodes and used to tomographically reconstruct the phononic surface electromagnetic fields of the object. Such 3D information promises insights in nanoscale physical phenomena and is invaluable to the design and optimization of nanostructures for fascinating new uses.

Surface phonon polaritons (SPhPs) are mixed electromagnetic and optical phonon waves that propagate at the surface of ionic materials (*1*). In macroscopic solids, they have little influence on the thermodynamic properties, which are dominated by volume acoustic phonons, and hardly couple to the electromagnetic far-field. Therefore, they have been long seen as a scientific curiosity. Recently, they attracted much attention because of their counterintuitive physical properties and their promising applications in photonics and nanophotonics from the mid–infrared (IR) (3 to 8 μm, 155 to 413 meV) up to the far-IR (15 to 1000 μm, 1.2 to 83 meV) (*2*). Their contribution to the physical properties in this range naturally increases with the surface-to-volume ratio (*3*). At the same time, the nanostructuration dramatically influences near-field enhancement and coupling to the far-field.

Therefore, SPhPs directly affect the thermodynamic properties of nanostructured materials. For example, they are responsible for highly coherent emission of silicon carbide (SiC) upon heating, in stark contrast with the conventional incoherent black-body radiation (*4*). They also induce enhanced thermal conduction in thin membranes (*3*) or heat transfer between two nanosurfaces (*5*). These remarkable properties may be favorably applied to the design of phononic metamaterials acting as extremely efficient passive coolers (*6*).

Beyond that, SPhPs concentrate electromagnetic energy at deep subwavelength scales in the same way as surface plasmons, but up to the far-IR region and with exceptionally high-quality factors (*7*), resulting in further intriguing nanophotonic applications, such as superresolution lenses (*2*) or enhanced vibrational spectroscopies (*2*, *7*).

All of these applications rely on the nanostructured electromagnetic field in the vicinity of surfaces of metamaterials or nanoparticles. However, designing or even engineering the electromagnetic local density of states (EMLDOS) for specific functionalities requires the unambiguous visualization of such field modulations at the nanometer scale. This became accessible by means of near-field IR techniques (*8*, *9*). Also, after pioneer works in electron energy loss spectroscopy (EELS) (*10*, *11*), lacking spatial resolution, EELS in a scanning transmission electron microscope (STEM) made it possible to measure phonon spectra at the nanometer (*12*, *13*) then atomic scales (*14*). Nevertheless, intrinsic to those techniques, they only allow for two-dimensional (2D) imaging and do not provide directional field information from the start. Recently, in the visible range, tomographic tilting of plasmonic EELS data in combination with sophisticated eigenmode-based reconstruction algorithms have led to a series of publications (*15*–*17*), culminating in the full 3D and vectorial reconstruction of a plasmonic field at all frequencies in the visible regime

[1]Université Paris-Saclay, CNRS, Laboratoire de Physique des Solides, 91405 Orsay. France. [2]Institute of Electron Microscopy and Nanoanalysis, Graz University of Technology, Steyrergasse 17, 8010 Graz, Austria. [3]Institute of Physics, University of Graz, Universitätsplatz 5, 8010 Graz, Austria. [4]Graz Centre for Electron Microscopy, Steyrergasse 17, 8010 Graz, Austria.
***Corresponding author. Email: gerald.kothleitner@felmi-zfe.at, mathieu.kociak@universite-paris-saclay.fr**

(*17*, *18*). The possibility to perform such a reconstruction is deeply rooted in the genuine relation between plasmon excitations and their EMLDOS (*19*), which describes the variation of the square modulus of the eigenfields, projected along arbitrary axes, in space and energy.

Given the strong formal analogy between surface plasmons and phonons (*1*), and having shown the theoretical link between EELS and SPhP EMLDOS (*20*), it was speculated whether a 3D reconstruction of SPhPs properties is also feasible (*20*). The high demands for simultaneous nanometer spatial and milli–electron volt spectral resolution and access to the IR regime could recently be met (*21*), and further advancements in EELS tomographic reconstruction algorithms have now paved the way for a full assessment of the 3D phononic EMLDOS. We allied tilted EELS spectral-imaging with a model-constrained approach to give a comprehensive, 3D vectorial view on the EMLDOS of individual nanometer-scale magnesium oxide (MgO) particles.

We describe the experimental set-up in Fig. 1A. A 60-keV electron beam with an initial energy width of ≈350 meV is filtered by a monochromator to obtain a final energy spread around 7 to 10 meV. This monochromator (*12*) efficiently optimizes the current left after monochromation, with a beam current of a few picoamperes in a sample area of ≈1 nm^2. The nano-object presented in Fig. 1 is a MgO cube with edge length of 191 nm deposited on a 20-nm-thin silicon nitride (Si_3N_4) substrate. The back surface of the substrate was covered with a few-nanometers-thin carbon layer to avoid charge-related issues (supplementary materials, materials and methods). By scanning the electron beam, one can collect high-angle annular dark field (HAADF) images that reveal the morphology of the cube. Sample tilting by an angle α allows imaging of the cube under different orientations (Fig. 1B). At each position of the scan, an EELS spectrum was recorded. A complete EELS spectrum (fig. S1) is composed of the zero-loss peak (ZLP), with a strong tail removed (Fig. 1C), and a weak Si_3N_4 phonon around 110 meV, whose left tail can be seen in Fig. 1C. In the reststrahlen band of MgO (upper far-IR), clear spectral responses are extracted at two different tilt angles for two different positions of the electron beam (Fig. 1C). Because the spectral features do change with both the electron beam position and the tilt angle, the selected spectral, spatial, and tilt resolutions of the used setup (materials and methods) has proven adequate to directly resolve signals that are characteristic of the main modes of the cubes (*13*, *20*, *21*). To understand the physical origin of the main spectral features at 68 (experimental mode I), 69 (II), and 78 meV (III), we systematically recorded EELS spectral images (SIs) at different tilt angles. For a first analysis, we present in Fig. 2A intensity maps for the experimental modes I, II, and III for two different tilt angles (full tilt maps are provided in fig. S3). These maps were generated by using a fitting routine for each experimental mode of a SI that has been deconvoluted from the ZLP beforehand (materials and methods) and writing the resulting intensity in the fitted image pixel.

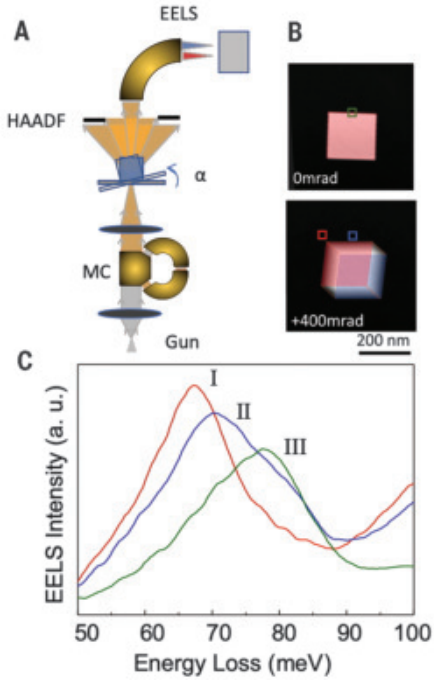

Fig. 1. Tomographic SPhP EELS experiments. (**A**) SPhP tomography set-up. MC, monochromator. (**B**) HAADF images of an MgO cube acquired at two different tilt angles. (**C**) Selected spectra for the two different tilt angles taken at the positions indicated on (B). The ZLP has been removed (materials and methods). Shown is the difference of spectra upon tilt for a fixed beam position (experimental modes II and III). a.u., arbitrary units.

When the electron beam is propagating perpendicular to the faces that are parallel to the substrate (0-mrad tilt), experimental mode I is localized on the four corners. Tilted spectral imaging directly shows a difference in intensity between the signal on corners in vacuum and those on the substrate. The latter is much weaker than the former. The experimental mode II is not directly seen on the 0-mrad map. It is essentially related to the inability of the fitting procedure to resolve experimental mode II because it appears as a weak shoulder on the experimental mode III main peak at zero tilt (*13*). It becomes visible upon tilting (supplementary materials). The signal originates from the edges and again is much weaker for the edges attached to the substrate. Last, the experimental mode III is present at all angles. However, its spatial distribution is more difficult to understand.

As presented in Fig. 2B and in the supplementary materials, we performed simulations for a cube of equal size in vacuum with the boundary element method (*22*) using the MNPBEM package (*23*). The simulations reveal similar features as those in the experimental data and confirm the existence of three different experimental modes (*13*, *20*). The main deviations are the absence of signal inside the cube in the experimental data, owing to the electrons getting scattered out of the spectrometer for large thicknesses, and the obvious absence of asymmetry in the theoretical data because the substrate influence has not been accounted for in the simulations.

To understand the full SPhP response of the cube, we built a tomographic reconstruction method for the EMLDOS inspired by those recently developed in plasmonics (materials and methods and supplementary text) (*17*, *18*). In our approach, we used the quasistatic limit (*24*), which applies because the typical free-space wavelengths of the SPhPs (several tens of micrometers) are much larger than the cube size (fig. S8). The vibrational response of the cube can be described in terms of geometric eigenmodes with spatial distributions $u_k(\mathbf{s})$ of the associated eigencharges, where k labels the eigenmodes and $\mathbf{s}$ is the surface coordinate (*20*, *22*, *24*). Using these eigenmodes, the EELS probability can be cast to the form

$$\mathcal{P}_{\mathrm{EELS}} = \sum\nolimits_k C_k \left| \oint_{\partial\Omega} V_{\mathrm{el}}(\mathbf{s}) u_k(\mathbf{s}) d\mathbf{S} \right|^2 \tag{1}$$

where C_k is a mode-dependent coefficient, $V_{\mathrm{el}}(\mathbf{s})$ is the potential associated with the swift electron, and $\partial\Omega$ is the nanocube boundary. The aim of our tomography scheme is to find for each mode I, II, and III the best coefficients C_k and functions $u_k(\mathbf{s})$ for which the reprojected EELS maps of Eq. 1 resemble as closely as possible the experimental ones. Once C_k and $u_k(\mathbf{s})$ are known, we can compute any linear property of the photonic environment, such as the EMLDOS (*20*, *22*, *25*). We express $u_k(\mathbf{s})$ in terms of a simulated reference basis $u^0_k(\mathbf{s})$

$$u_k(\mathbf{s}) \approx \sum\nolimits_{k'=1}^{n} \mathbb{Q}_{kk'} u^0_{k'}(\mathbf{s}) \tag{2}$$

where $\mathbb{Q}$ is an orthogonal matrix and n is a cutoff for the reference basis states, which is needed for the sake of convergence speed. The basis $u^0_k(\mathbf{s})$ is in principle arbitrary but should be chosen so that the gross features of

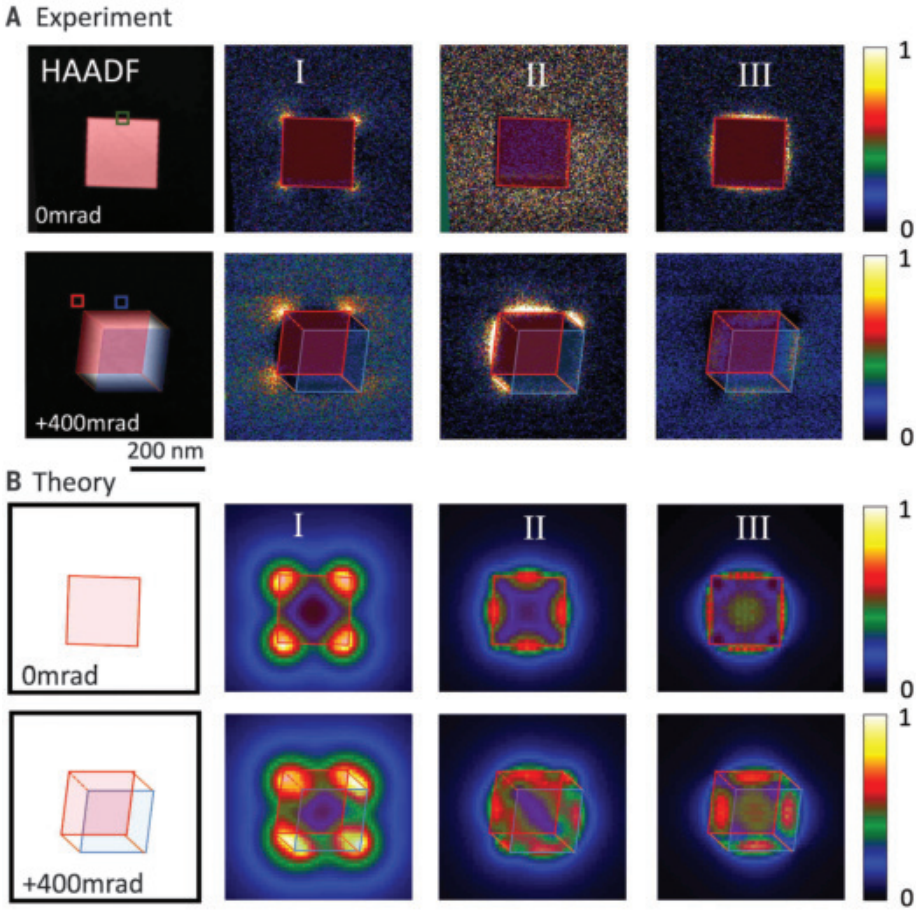

Fig. 2. 2D phonon mapping at different tilt angles. (**A**) (Left) Experimental HAADF images and (right) fitted maps of the main experimental SPhP modes (I, II, and III) for two tilt configurations (0 and 400 mrad) (materials and methods). The face in contact with the substrate is highlighted with a blue square. (**B**) Same for simulations of a cube in vacuum.

the modes, such as enhanced charge distributions localized at the corners or edges of the cube, are already encoded to some degree. We used the eigenmodes of a cube in vacuum (Fig. 2B and figs. S7 and S8), calculated by using the boundary element method (*20*, *22*), as a reference eigenbasis. Through the change-of-basis matrix $\mathbb{Q}$, our approach naturally allows the eigenmodes $u_k(\mathbf{s})$ to be reconstructed through complex combinations of the reference eigenmodes, as needed to accommodate for the presence of strong asymmetry in the experimental data. The applicability of this procedure was validated on synthetic data based on a cube in vacuum.

To perform the reconstruction, we used 12 spectral images (12 tilt angles), consisting on 400 by 400 spectra (materials and methods). Despite the massive amount of data, the signal-to-noise ratio was insufficient to proceed directly to the reconstruction. Data treatment by using the non-negative matrix factorization (NMF), following the pioneer work on 3D non-vectorial surface plasmon reconstruction (*15*), leads to the modal signatures shown in Fig. 3A. The NMF spectra are consisting of several peaks, with the most prominent ones corresponding to the I, II, and III experimental modes pointed out in Fig. 1. This allows to confidently associate each experimental mode to an NMF component. An extra peak is seen for the NMF component I around 90 meV, as the manifestation of the imperfect factorization of the NMF (*15*). The corresponding maps displayed in Fig. 3B reproduce the spatial variation already observed on the raw data. Incidentally, the experimental mode II was hardly visible with a simple fitting (Fig. 2A) but is now clearly disentangled thanks to the NMF procedure. Two other NMF components (fig. S5) correspond to the right tail of the zero-loss peak and the left tail of the 110-meV phonon of Si_3N_4 that does not participate to the strong modification of the MgO modes owing to the high indices of the substrate. The NMF components are fitted against the EELS expression (Eq. 1) to get the reconstructed eigenmodes (Eq. 2). From those, the SPhP EMLDOS can be retrieved as displayed in Fig. 3C and fig. S9. Each reconstructed component (I, II, and III) is made up of a sum of reconstructed eigenmodes that are too close in energy to be experimentally disentangled (fig. S10) (*20*). To assure data integrity, modeled reprojected 2D EELS maps calculated from the reconstruction were directly compared with the experimental ones and show very good agreement (fig. S11). Also, the reconstructed EMLDOS is robust against variations in the input experimental data and in the number of reference eigenmodes (fig. S10).

Mode I can therefore be easily interpreted as being mainly localized at the corner ["corner mode" (*13*, *20*, *26*)]. The presence of a substrate is expected to induce a split in two bands of modes, one localized close to the substrate (proximal) and one close to the vacuum (distal) (*13*, *20*, *26*). The two bands are clearly disentangled spatially, although not spectrally. In particular, the proximal band is strongly damped because of the presence of carbon (*26*) on the substrate (the smaller effect of the substrate in absence of carbon is shown in fig. S4). In addition, some intensity can be seen near the center of some edges. This is because reconstruction includes both resonant [corner localized (*20*)] and nonresonant [edge localized (*20*)] contributions from the different reconstructed modes. This points to the NMF not providing a pure orthogonal decomposition of the different modes. Our reconstruction scheme allows observation of this mixing, although the EELS maps and the reprojection do not. This emphasizes the need to reconstruct a

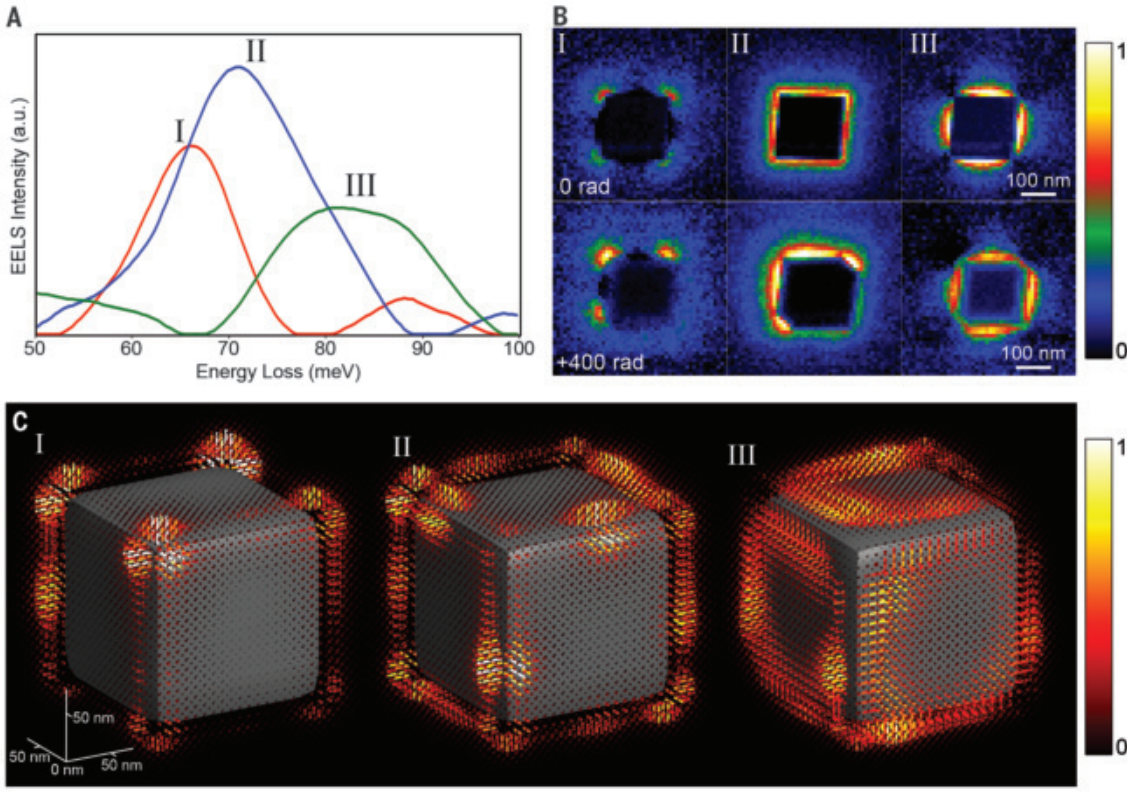

Fig. 3. 3D, fully vectorial reconstruction of the phononic electromagnetic local density of state. (**A**) NMF components extracted from the experimental data. (**B**) Reconstructed NMF maps for the three components at the two angles shown in Fig. 2. (**C**) 3D reconstruction of the EMLDOS seen from the top (the substrate, not shown, is at the bottom of the cube). The polarization of the EMLDOS along three orthogonal directions is shown as needles, in which color and length indicate its intensity.

physical observable—the full EMLDOS—that contains the whole physical content of a peculiar system, in contrast to the EELS data, which cannot always be directly interpreted (*24*). The mode II is localized at the edges ("edge mode") (*20*) and is particularly hard to identify (*13*) because of the small energy difference with mode I and the small coupling of the electrons to the mode II field in usual, nontilted, geometry. Last, mode III can be related to surface modes.

This first proof-of-principle visualization of the SPhP EMLDOS should motivate the development of more systematic reconstruction of the full SPhP optical response. Such mapping should be extended to other situations in which the 3D and vectorial information of the electromagnetic density is of importance. This includes extension of the methodology to anisotropic materials such as graphene analogs and transition-metal dichalcogenides. This also includes the possibility to study consistently strong coupling physics, which has recently been unravelled for plasmons and phonons in EELS (*27*). Last, highly monochromated EELS has triggered much hope for its potential applications in vibrational mapping for biological systems (*28*). However, it is well known that the 3D information is mandatory for this purpose (*29*). Therefore, the present method should be adapted to cryomicroscopy to, for example, make it possible to combine ultrastructure characterization with protein vibrational marking in three dimensions.

REFERENCES AND NOTES

1. K. Kliewer, R. Fuchs, *Theory of Dynamical Properties of Dielectric Surfaces*, vol. 27 (Wiley, 1974).
2. J. D. Caldwell *et al.*, *Nanophotonics* **4**, 44–68 (2015).
3. Y. Wu *et al.*, *Sci. Adv.* **6**, eaba5692 (2020).
4. J. J. Greffet *et al.*, *Nature* **416**, 61–64 (2002).
5. B. Song *et al.*, *Nat. Nanotechnol.* **10**, 253–258 (2015).
6. E. Rephaeli, A. Raman, S. Fan, *Nano Lett.* **13**, 1457–1461 (2013).
7. M. Autore *et al.*, *Light Sci. Appl.* **7**, 17172 (2018).
8. R. Hillenbrand, T. Taubner, F. Keilmann, *Nature* **418**, 159–162 (2002).
9. R. Zhang *et al.*, *Nature* **498**, 82–86 (2013).
10. H. Raether, *Excitation of Plasmons and Interband Transitions by Electrons*, vol. 88 (Springer, 2006).
11. H. Boersch, J. Geiger, W. Stickel, *Phys. Rev. Lett.* **17**, 379–381 (1966).
12. O. L. Krivanek *et al.*, *Nature* **514**, 209–212 (2014).
13. M. J. Lagos, A. Trügler, U. Hohenester, P. E. Batson, *Nature* **543**, 529–532 (2017).
14. F. S. Hage, G. Radtke, D. M. Kepaptsoglou, M. Lazzeri, Q. M. Ramasse, *Science* **367**, 1124–1127 (2020).
15. O. Nicoletti *et al.*, *Nature* **502**, 80–84 (2013).
16. S. M. Collins *et al.*, *ACS Photonics* **2**, 1628–1635 (2015).
17. A. Hörl *et al.*, *Nat. Commun.* **8**, 37 (2017).
18. G. Haberfehlner *et al.*, *Nano Lett.* **17**, 6773–6777 (2017).
19. F. J. García de Abajo, M. Kociak, *Phys. Rev. Lett.* **100**, 106804 (2008).
20. H. Lourenço-Martins, M. Kociak, *Phys. Rev. X* **7**, 041059 (2017).
21. M. J. Lagos *et al.*, *Microscopy (Oxf.)* **67** (suppl_1), i3–i13 (2018).
22. F. J. García de Abajo, J. Aizpurua, *Phys. Rev. B Condens. Matter* **56**, 15873–15884 (1997).
23. U. Hohenester, *Comput. Phys. Commun.* **185**, 1177–1187 (2014).
24. U. Hohenester, *Nano and Quantum Optics* (Springer, 2020).
25. G. Boudarham, M. Kociak, *Phys. Rev. B Condens. Matter Mater. Phys.* **85**, 245447 (2012).
26. S. Mazzucco *et al.*, *Nano Lett.* **12**, 1288–1294 (2012).
27. L. H. G. Tizei *et al.*, *Nano Lett.* **20**, 2973–2979 (2020).
28. P. Rez *et al.*, *Nat. Commun.* **7**, 1 (2016).
29. W. Kukulski, M. Schorb, M. Kaksonen, J. A. Briggs, *Cell* **150**, 508–520 (2012).

ACKNOWLEDGMENTS

X.L., O.S., and M.K. thank M. Walls and A. Gloter for help in preparing the sample and acknowledge the joint effort of the STEM team in Orsay. M.K. thanks F. De La Peña for insightful discussions on the NMF factorization and the physics of the nanocubes plasmons. **Funding:** This work has received support from the National Agency for Research under the program of future investment TEMPOS-CHROMATEM with the reference no. ANR-10-EQPX-50. This project has received funding from the European Union's Horizon 2020 Research and Innovation Program under grant agreements 823717 (ESTEEM3) and 101017720 (EBEAM) and from the Austrian Science fund FWF under project P 31264. **Author contributions:** G.K. and M.K. conceived the project. G.K, M.K., O.S., and X.L. designed the experiments. X.L. and M.K. performed the experiments. X.L. and G.H. performed the data analysis. U.H. designed the theory, and G.H. and U.H. performed the reconstructions. All authors participated in the results analysis and contributed to the preparation of the manuscript. **Competing interests:** The authors declare no competing interests. **Data and materials availability:** All data necessary for evaluating the conclusions of the paper are included in the main text and/or the supplementary materials.

SUPPLEMENTARY MATERIALS

science.sciencemag.org/content/371/6536/1364/suppl/DC1
Materials and Methods
Supplementary Text
Figs. S1 to S11
References (*30*–*36*)

7 December 2020; accepted 12 February 2021
10.1126/science.abg0330

PLASMONICS

Enhanced optical asymmetry in supramolecular chiroplasmonic assemblies with long-range order

Jun Lu[1,2,3], Yao Xue[1], Kalil Bernardino[4], Ning-Ning Zhang[1], Weverson R. Gomes[5], Naomi S. Ramesar[3,6], Shuhan Liu[7], Zheng Hu[7], Tianmeng Sun[7], Andre Farias de Moura[5]*, Nicholas A. Kotov[2,3,6]*, Kun Liu[1,8,9]*

Chiral assemblies of plasmonic nanoparticles are known for strong circular dichroism but not for high optical asymmetry, which is limited by the unfavorable combination of electrical and magnetic field components compounded by strong scattering. Here, we show that these limitations can be overcome by the long-range organization of nanoparticles in a manner similar to the liquid crystals and found in helical assemblies of gold nanorods with human islet amyloid polypeptides. A strong, polarization-dependent spectral shift and the reduced scattering of energy states with antiparallel orientation of dipoles activated in assembled helices increased optical asymmetry *g*-factors by a factor of more than 4600. The liquid crystal–like color variations and the nanorod-accelerated fibrillation enable drug screening in complex biological media. Improvement of long-range order can also provide structural guidance for the design of materials with high optical asymmetry.

Chirality at the nanoscale has an overarching importance that spans several disciplines (*1*–*5*) and fuels intense studies of chiral inorganic nanostructures. Most of the relevant attention in academia and industry has been focused on the high values and spectral dependence of their circular dichroism (CD) (*6*) rather than on their *g*-factors—the dimensionless parameter that describes the ratio of polarized photons to extinct ones. Despite the high polarizability of chiral nanoassemblies from plasmonic nanoparticles (NPs) or nanorods (NRs) that are conducive to strong dichroic effects, most of these assemblies are strong light scatterers with *g*-factors between 10^{-4} and 10^{-2}. These values are much lower than those for liquid crystals (LCs), which have *g*-factors between 0.01 and 1 (*7*–*9*) and scatter light to a much smaller extent. The contribution of scattering to total light extinction in plasmonic particles and their superstructures is particularly strong for the states with the lowest energy (also known as bright states) with parallel orientation of coupled oscillating dipoles (*10*).

[1]State Key Laboratory of Supramolecular Structure and Materials, College of Chemistry, Jilin University, Changchun, China. [2]Department of Chemical Engineering, University of Michigan, Ann Arbor, MI 48109, USA. [3]Biointerfaces Institute, University of Michigan, Ann Arbor, MI 48109, USA. [4]Institute of Chemistry, University of São Paulo, 05508-000, São Paulo, SP, Brazil. [5]Department of Chemistry, Federal University of São Carlos, 13565-905, São Carlos, SP, Brazil. [6]Department of Materials Science and Engineering, University of Michigan, Ann Arbor, MI 48109, USA. [7]Key Laboratory of Organ Regeneration and Transplantation of Ministry of Education, Institute of Immunology, The First Hospital, Jilin University, Changchun, China. [8]Optical Functional Theranostics Joint Laboratory of Medicine and Chemistry, The First Hospital, Jilin University, Changchun, China. [9]Chiral Nanomaterials Research Center, International Center of Future Science, Jilin University, Changchun, China.
*Corresponding author. Email: kotov@umich.edu (N.A.K.); moura@ufscar.br (A.F.d.M.); kliu@jlu.edu.cn (K.L.)

High *g*-factors between 0.02 and 0.2 have been obtained for single plasmonic and magnetic NPs (*11*–*13*) with complex molecular and nanoscale structures, but their origins are fundamentally different from those of LCs. The high optical asymmetry of LC media originates from the long-range order of chiral molecules, whereas the *g*-factors of individual LC molecules are very small—typically below 0.001 (*14*, *15*). Thus, the question emerges: Is it possible to increase the optical asymmetry of plasmonic assemblies by creating the long-range organization of nanoscale constituents that, by themselves, have low *g*-factors?

Current knowledge about chiral organic nanostructures and LCs cannot be directly extended to plasmonic systems. Furthermore, even when microscopy images in the dry state indicate that engineered plasmonic NPs have a degree of helical arrangement—for example, DNA origami (*16*–*19*)—the flexibility of their inter-NP bridges leads to disorder in the liquid state, the condition under which the chiro-optical properties are measured. Theoretical considerations regarding the asymmetry of local electric, **E**, and magnetic, **B**, fields around plasmonic NPs (*20*) are also ambiguous and have provided arguments both for and against the benefits of long-range organization. Helical superstructures from plasmonic NPs with long-range registry will increase the local $|\mathbf{B}|$ values with direct benefits for optical asymmetry (*21*), but the substantial increase of the electrical field between the coupled plasmonic particles (*22*) decreases *g*-factors proportionally to $|\mathbf{E}|^2$ (*20*, *23*). Manifestation of these effects related to magnetic and electrical field components can be vividly traced in a limited increase of optical activity in flexible NP and NR constructs observed experimentally (*24*–*26*).

If the LC-like order could convert low-*g*-factor plasmonic NPs into optical media with high *g*-factors, this method could be applied to a variety of inorganic components with both simple and complex geometries—chiral and achiral—and provide unifying design principles for organic and inorganic optically active media. The low-*g* chiral components used in this study were gold NRs covered by cetyltrimethylammonium bromide (CTAB) molecules with an average length of 50 ± 3.0 nm and average diameter of 19 ± 1.7 nm. These NRs were conjugated to human islet amyloid polypeptides (hIAPPs) that imparted weak chiro-optical activity and a maximal *g*-factor of 2.6×10^{-5} (fig. S1, A to C). The transition from the disorganized to organized state occurred as a result of the self-assembly of randomly coiled hIAPPs into twisted fibrils with β-sheet structures (*27*, *28*). Notably, the assembly of NRs onto the premade hIAPP fibrils (fig. S1, D to F) yielded discrete twisted NR pairs that were similar to those observed in prior studies (*24*, *29*) but without the long-range registry between the plasmonic building blocks.

The assemblies with long-range organization were observed when hIAPP was bound onto NR surfaces via the Au–S bond, as confirmed by Raman spectroscopy (fig. S2). Subsequently, the densely bound peptides with a coverage density of 0.70 chains per square nanometer (fig. S3) were allowed to self-assemble with the free dissolved hIAPP with a bound/free peptide ratio of 1.3/2.7 (fig. S4). Under these conditions, the intensity of the CD spectra (Fig. 1C) rose to as high as 2000 millidegrees (mdeg), which can be compared with the maximal CD intensity of 0.90 mdeg for assemblies templated by mature hIAPP fibrils (fig. S1F). Concomitant with the rise in intensity, the bisignate CD spectra gradually red shifted, which resulted in a positive peak at 658 nm and a negative peak at 737 nm.

With the coassembly of NRs and hIAPPs, the *g*-factors (Fig. 1D) increase substantially, reaching 0.12 at 661 nm, which is markedly higher than those observed for other multiparticle constructs from plasmonic or semiconductor NPs of any geometry (*13*, *30*). Compared with LC optical media, which are generally viscous and anisotropic, these dispersions were fluid and isotropic (fig. S5). In the framework of this study, the *g*-factors of assemblies were more than 4600 times as great as those for single NRs carrying hIAPPs. Also, the *g*-factor was between 10 and 1000 times as great as those of the coassemblies from hIAPPs with gold nanospheres, gold nanoarrows, and silver-coated gold NRs, which generated strongly coupled chain-like nanostructures but lacked long-range registry between the NPs (fig. S6).

Transmission electron microscopy (TEM) images indicated formation of the long chain NRs with end-to-end orientation (Fig. 1E) and long-range periodicity (fig. S7). Tomographic reconstructions revealed that the NRs in these

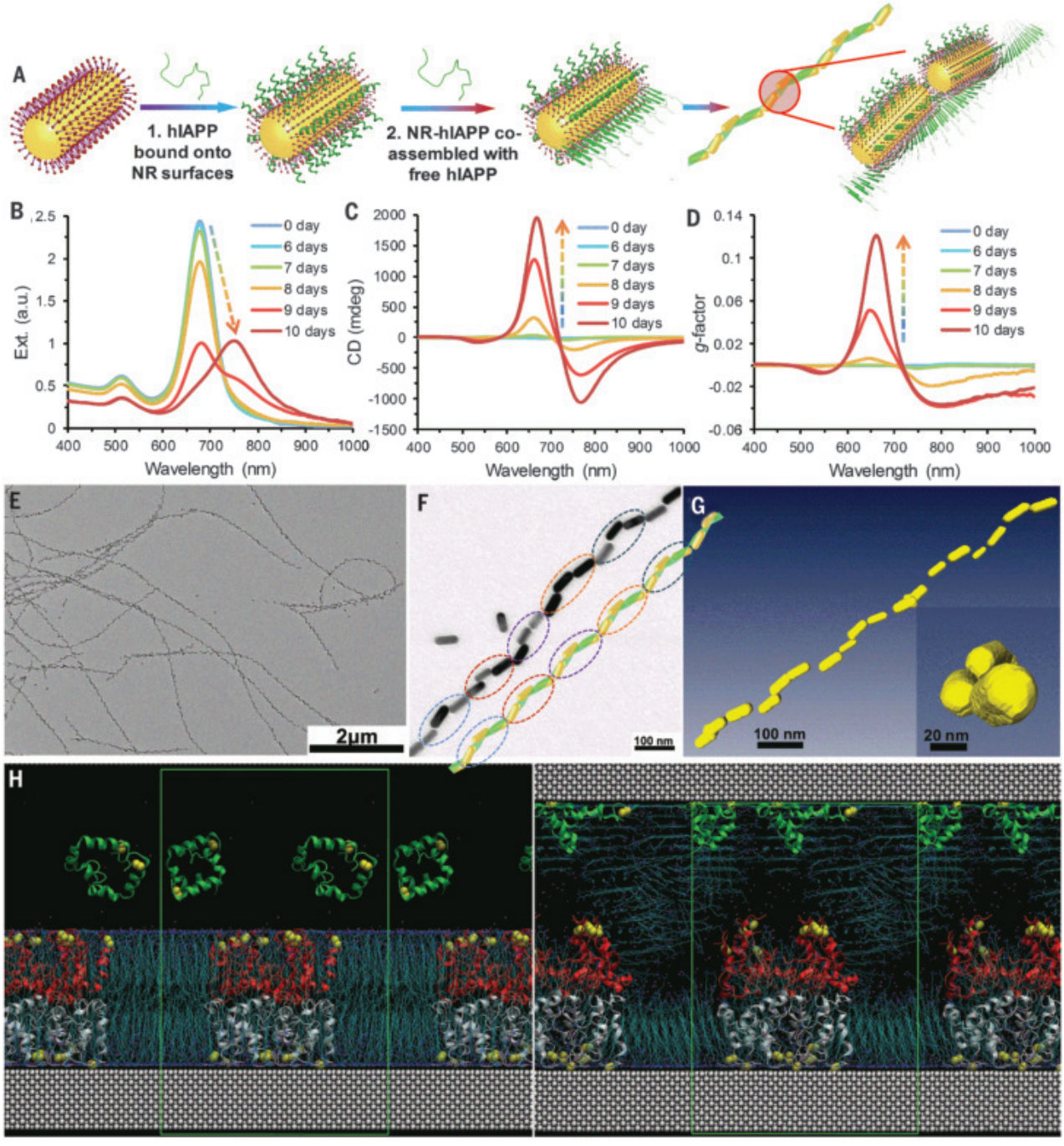

Fig. 1. Assembly of hIAPPs with NRs producing LC-like helices with long-range order. (**A**) Schematics of the assembly process of hIAPP monomers with NRs. (**B** to **D**) Extinction (Ext.) (B), CD (C), and *g*-factor (D) spectra for the coassembly process of 4.0-mM hIAPPs with 0.50-nM gold NRs with average lengths and diameters of 50 and 19 nm, respectively. The attribution of CD peaks to the CD of NR-hIAPP assemblies was verified by negligible linear dichroism (LD) intensity (fig. S5D). a.u., arbitrary units. (**E** and **F**) TEM images of nanohelices. The nanohelices model in (F) was reconstructed from the TEM images at various tilting angles. The circles represent the pitch of the nanohelices. (**G**) Reconstructed cryo-TEM tomography images showing the left-handed helices of the straight hIAPP-NR fibers. (**H**) Initial (left) and final (right) structures for the MD simulations of hIAPPs in the CTAB bilayer. The different hIAPP molecules are depicted as follows: silver ribbons for molecules in the bilayer and in contact with gold, red ribbons for molecules in the bilayer and in contact with the aqueous solution, and green ribbons for the free peptides in solution. The sulfur atoms of hIAPPs are depicted as yellow spheres, the gold atoms as gray spheres, the CTA^+ cations as lines (carbon shown in cyan and nitrogen in dark blue, with hydrogen atoms omitted for clarity), and the Br^- and Cl^- anions as purple dots.

chains were arranged into left-handed nanohelices (Fig. 1F and fig. S8). The average pitch distance, p = 160 ± 16 nm, was consistent with that of hIAPP fibrils (161 ± 10 nm) (fig. S8A) (*28*) and accommodated three NRs per turn. The average number of NRs in a continuous nanohelix was 35 ± 20 (fig. S9), which is between 3 and 15 times as long as those of other plasmonic nanoassemblies (*3*, *16*–*19*, *29*, *31*–*34*). The 5.8 ± 4.4–nm narrow gaps between the NRs (fig. S9) led to strong coupling of the longitudinal plasmons and the gradual red

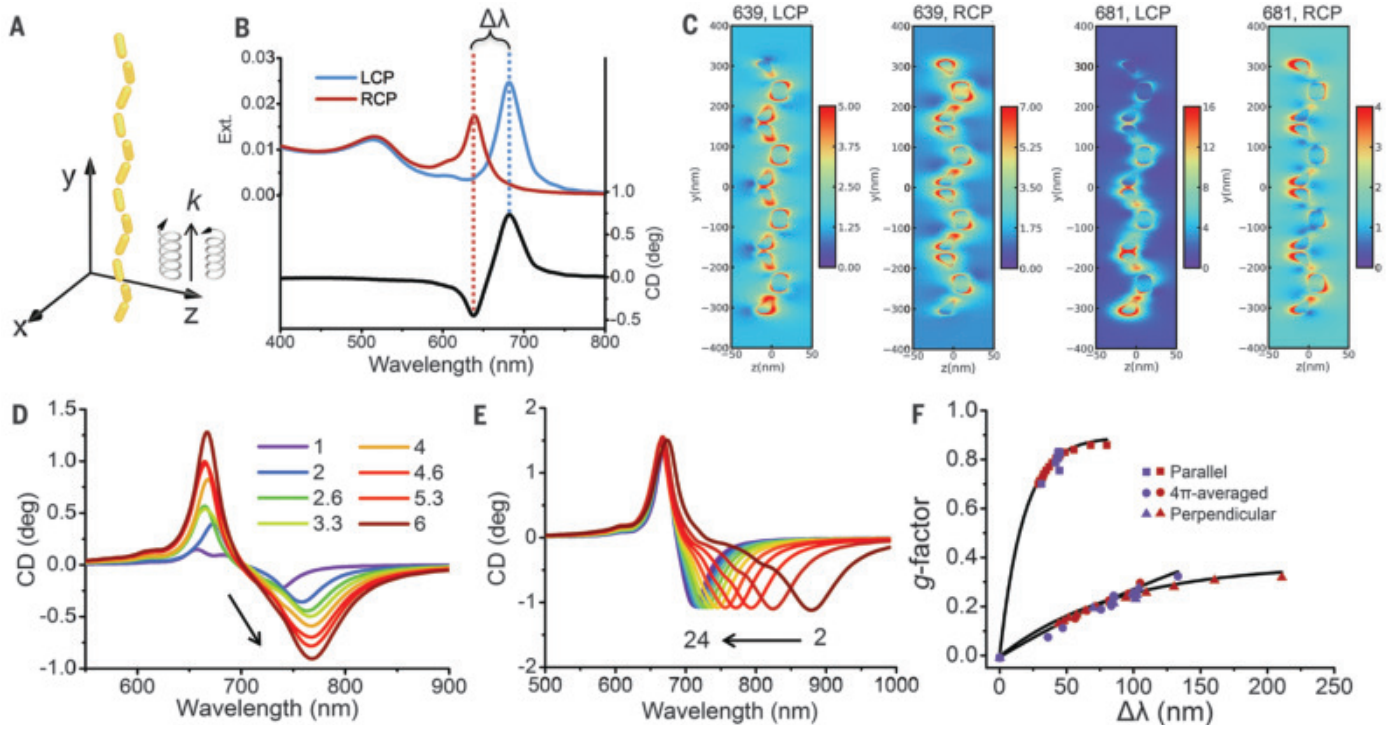

Fig. 2. Optical properties of NR helices with long-range registry. (**A** to **C**) Plasmonic resonances under circularly polarized light (CPL). (A) Nanohelix model with four helical turns and 12 NRs used for FDTD simulations with geometry based on cryo-TEM reconstructions. Extinction and CD spectra (B) are shown for the nanohelix and electric fields (C) irradiated at the extinction peaks under left- and right-handed CPL—i.e., 681 and 639 nm. deg, degrees. (**D** to **F**) Relationship of *g*-factor with Δλ. Simulated CD spectra for nanohelices with variable helical turns *N* (D) and interparticle distances *d* (E). (F) Dependence of *g*-factor on Δλ based on the simulation results for nanohelices with variable *N* (violet) and *d* (red) from the parallel (square), perpendicular (triangle), and 4π-averaged orientation (circle) with respect to the *k*-vector of incident photons.

shift in the CD spectra as the system progressed from individual particles to the assembled state. The NR chains were straight, as observed by cryo–transmission electron microscopy (cryo-TEM) tomography, and as many as 50 NRs were in registry with each other (Fig. 1G and movies S1 and S2 in the supplementary materials). These images display the native state of the nanoassemblies in isotropic dispersions and their distinction from other plasmonic assemblies, for which the long-range registry is not retained.

High fidelity of the long-range organization was related to collective supramolecular interactions between the hIAPPs and the NRs. The peptide monomers were tethered to NR surfaces between cysteine residues 2 and 7, located in the tail region of the polypeptide, which was not directly involved in amyloid packing (fig. S10) (*27*, *35*). Furthermore, the fibril core segment—residues 20 to 29—was partly exposed outside of the CTAB bilayers and interacted with free hIAPPs in solution (Fig. 1H). Thus, the NRs did not hinder hIAPP folding during the process of assembly into fibrils. On the contrary, the NRs accelerated the self-assembly of hIAPPs at least threefold (fig. S11). For comparison, the assembly time of a 10-μM dispersion of hIAPPs was ~12.0 hours without NRs and ~4.0 hours when NRs were added. The shortening of the fibrillation time is essential for both disease diagnostics (*24*) and rapid drug discovery (see below).

It is important to uncover the chemical reasons for the marked acceleration of hIAPP fibrillation by NRs. Recent studies have shown that nanoscale (*36*) and macroscale (*37*) interfaces catalyze the assembly of amyloid peptides; however, the molecular underpinning of this process has not been disclosed. Using CD analysis, we found that the folding of hIAPPs into an α helix was facilitated by the hydrophobicity of the CTAB bilayers coating the NRs when hIAPP monomers interacted with their surfaces (fig. S12). We further used molecular dynamics (MD) simulations to understand the structural stability of hIAPP macromolecules and uncover potential effects of the gold surface on peptide folding (figs. S13 to S15 and movie S3). High-level MD simulations with large numbers of atoms have severe limitation in time scales, which makes the assembly of nanoscale objects difficult to observe computationally unless they are coarse-grained. Nevertheless, we had to carry out the simulations at the atomistic level to correctly describe two things: (i) the chemical bonds at the interface of gold and hIAPPs and (ii) the conformation of the peptide essential for the formation of helices. Our model contained 20 peptide molecules; among those, 16 hIAPP units were in the form of dimers attached to the gold surface covered with a CTAB bilayer via cysteine residues 2 and 7 in the bottom units (Fig. 1H). An additional four reference hIAPP molecules were placed in the aqueous solution outside the surfactant bilayer.

We found that the CTAB layer is essential for the successful fibrillation of hIAPPs on NRs. All peptide dimers imbedded in the CTAB coating maintained well-defined tertiary and quaternary structures. The stable conformation facilitated the fibrillation by lowering the free energy barrier for subsequent peptide pairing (*36*, *37*) and the transition from α helix to β sheet that is typical for amyloid fibrils (*38*, *39*). By contrast, the reference peptides underwent large structural changes, acquiring predominantly random coil conformations, which maximized the contact area with the bare gold surface. In a broader sense, the CTAB layers mimic the natural fibrillation-promoting effect of phospholipid bilayers (*29*, *40*, *41*).

Furthermore, MD simulations showed that the CTAB coating strengthened supramolecular

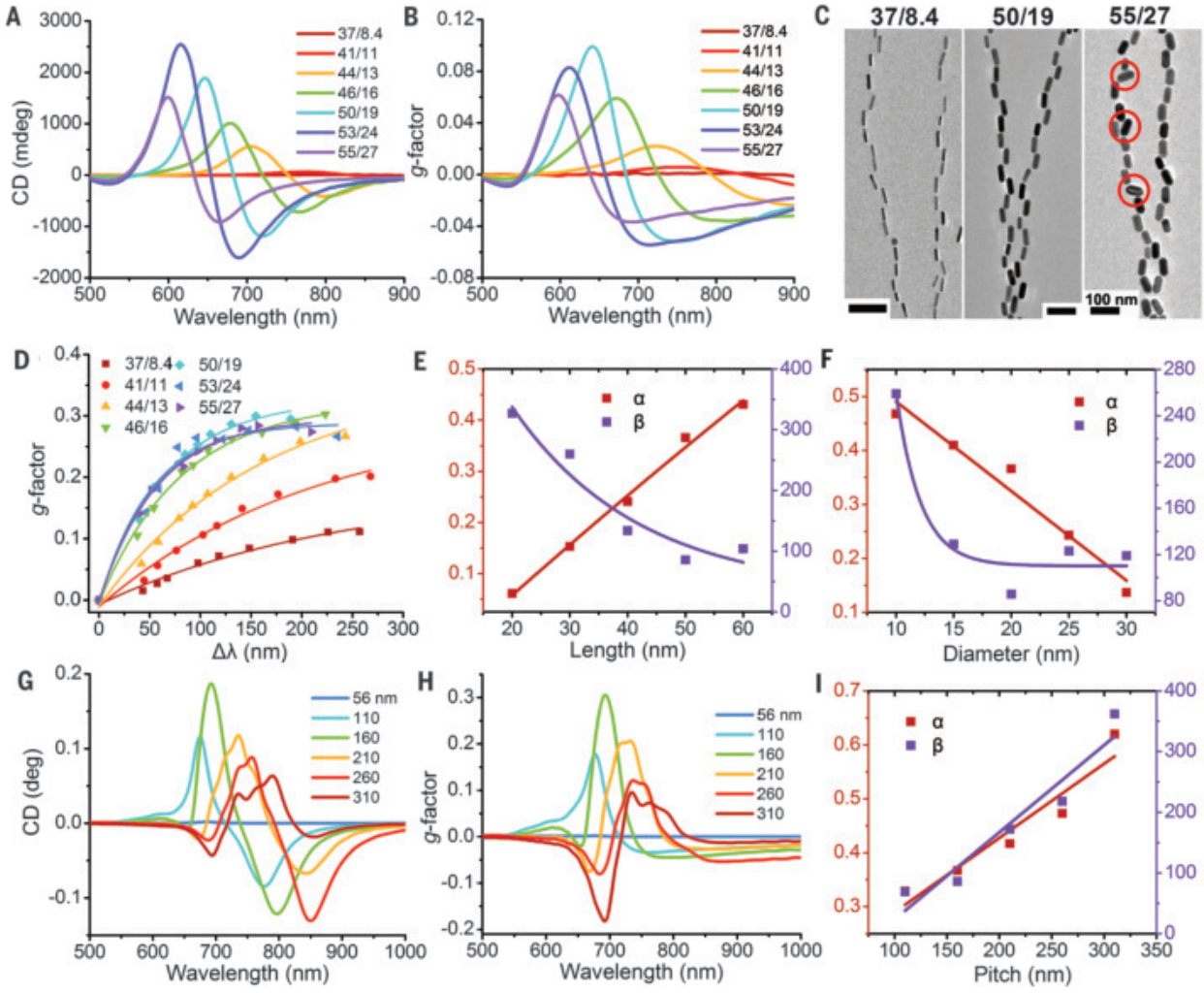

Fig. 3. The influence of NR size and nanohelix pitch on experimentally observed and computationally derived *g*-factors. (**A** to **C**) CD spectra (A), *g*-factor spectra (B), and representative TEM images (C) for helices from various sizes of NRs assembled under identical conditions. The numbers in the legends, e.g., 37/8.4, represent the average length (37 nm) and diameter (8.4 nm) of the NRs. The red circles in the inset of TEM image show the expelled NRs on hIAPP fibers. (**D**) Dependence of simulated *g*-factors on Δλ for nanohelices from NRs of variable sizes. (**E** and **F**) Plot of α and β with NR lengths (E) and diameters (F) based on the *g*-factor dependence on Δλ for NRs and only changing the lengths or diameters, respectively. (**G** to **I**) Chiroptical properties of nanohelices for variable pitch lengths: simulated CD (G), *g*-factor spectra (H), and dependence of α and β on pitch (I).

attractions between peptides (figs. S16 and S17). The average energy of hIAPP-hIAPP interactions within the CTAB coating was −504 kJ/mol, whereas those for peptides on the uncoated gold surface and in the CTAB micelles were −374 kJ/mol and −270 kJ/mol, respectively, which indicates the synergy between the surfactant layer and the solid surface in promoting the fibrillation.

Long-range organization of the NRs in the helices made it possible to establish the dependence of *g*-factors on their structural parameters. The geometry observed for NR-hIAPP assemblies from TEM microscopy and cryo-TEM tomography was transferred to a finite-difference time-domain (FDTD) model for in-depth evaluation of the chiro-optical properties of the helical superstructures.

The plasmonic resonances of an angled NR dimer—the elementary segment of a nanohelix—display high energy (HE) and low energy (LE) states with dipole vectors approaching antiparallel and parallel directions, respectively (*42*). The asymmetry of angled dimers leads to their asymmetric interaction with circularly polarized light (fig. S18). The LE bright state of the left-handed helix was more allowed for left-handed circularly polarized light (LCP) than for right-handed circularly polarized light (RCP) because of the match between the handedness of the nanoassembly and the rotational sense of the incident photons. The reverse was true for the HE state, also known as a dark or optically inactive state, in symmetrical assemblies. As the number of NRs increased while the helical organization was retained, the spectral maxima for the extinction of LCP and RCP photons separated, until the peaks no longer overlapped (figs. S19 and S20). For example, for a nanohelix made of 12 NRs, LCP produced only a peak at 700 nm corresponding to the LE state, whereas RCP resulted in only a peak at 654 nm corresponding to the HE state (Fig. 2, B and C). We note that the optical asymmetry of total extinction in NR assemblies—and therefore the high *g*-factor—primarily originates from absorption of photons (figs. S21 and S22). The contribution of scattering to the optical activity of LE states for the 4π-averaged orientation increased, however, as the length of nanohelices increased, thereby preventing further enhancement of *g*-factors (fig. S21). The relative contribution of scattering

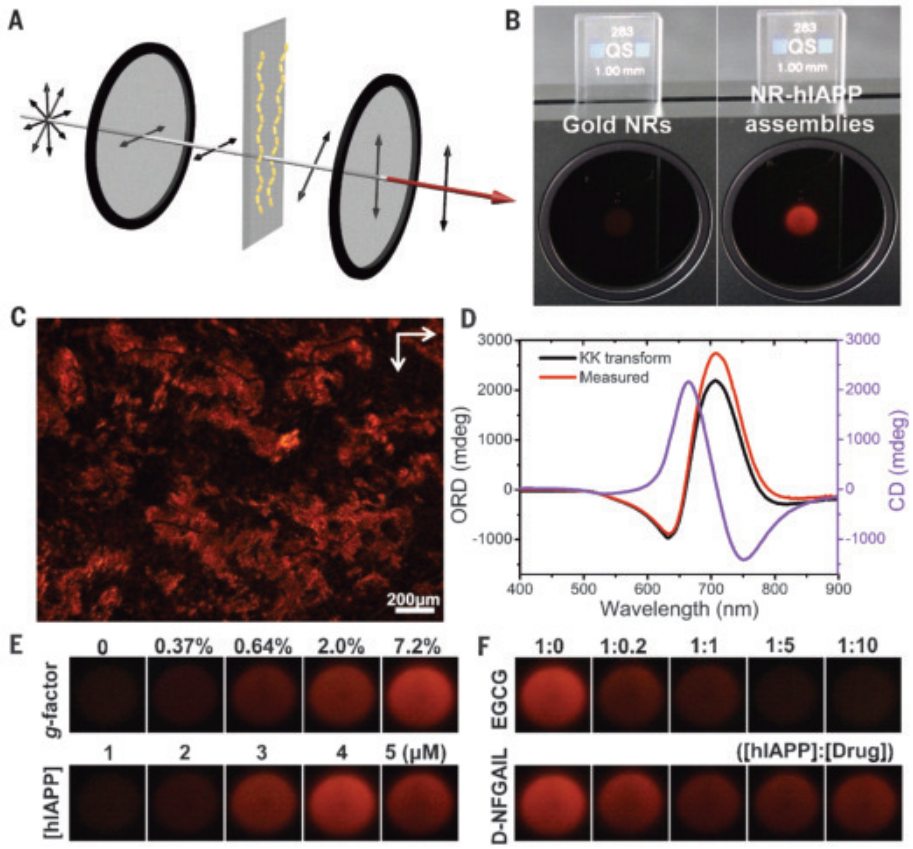

Fig. 4. Accelerated drug screening using high-*g* assemblies. (**A**) Schematics for cross-polarization optical cell being illuminated with LED light. NR-hIAPP assemblies are pictured being oriented perpendicularly to the *k*-vector of photons for simplicity; they form isotropic dispersions in biological media. (**B**) Photographs of pure NR and NR-hIAPP assemblies monitored by a camera and showing the red light transmitted under cross-polarized conditions. (**C**) Polarized optical microscopy (POM) image of NR-hIAPP assemblies. (**D**) Optical rotatory dispersion (ORD) spectrum of NR-hIAPP assemblies from the measurement and Kramers-Kronig (KK) transformation to the corresponding CD spectra. (**E** and **F**) Photographs of the NR-hIAPP assemblies with different *g*-factors and coassembled from variable hIAPP concentrations (E) and coincubated with two typical inhibiting drugs—i.e., EGCG and D-NFGAIL—in different concentrations (F).

to the optical activity of HE states under the same conditions remained small and nearly the same for all of the assemblies (fig. S21). These differences between the HE and LE states enable substantially increased *g*-factors for nanohelices with long-range order because the width of both LE and HE bands in these assemblies remains narrow, which prevents the spillover of scattering from HE to LE bands. Electrical fields generated between the NRs for HE states are also lower than those generated for LE states (fig. S23). Considering that *g*-factors ~$1/|\mathbf{E}|^2$, the optical asymmetry must also increase for partially allowed HE states formed in well-organized and strongly coupled helices.

The asymmetry of optical properties with respect to LCP and RCP was enumerated using the spectral separation ($\Delta\lambda$) of a positive peak (λ_+) and a negative peak (λ_-), which correspond to the HE and LE states, respectively (Fig. 2, B and C). In accord with the considerations above, the simulation data based on the Lorentzian line shape of the peaks and the spectral patterns emerging for split plasmon resonances (fig. S24) revealed a negative exponential relationship between *g*-factors and $\Delta\lambda$

$$g = \alpha\left[1 - e^{\left(-\frac{\Delta\lambda}{\beta}\right)}\right] \quad (1)$$

where α is the maximum optical asymmetry magnitude and β (nm) is the growth rate of the *g*-factor with $\Delta\lambda$. The generality of this dependence could be seen from its validity for extinction peaks consisting of two or more Lorentzian functions (fig. S24, M to P) that were exemplified by the absorbance and scattering of NR assemblies.

Because $\Delta\lambda$, α, and β strongly depend on the order parameters of the helix, we investigated how they changed with the geometrical parameters of the nanohelices, including the number of helical turns (N), the interparticle distance between adjacent NRs (d), helix orientation, NR size, and pitch. The sonication time of the preassembled helices resulted in various N. The sonication time did not affect the helical registry of the shorter NR assemblies (fig. S25), which enabled the comparison of the experimental and computational data for the relationship of *g*-factors with N and $\Delta\lambda$. Simulations showed that *g*-factors and $\Delta\lambda$ increased as N increased, reaching saturation at four helical turns for parallel, perpendicular, and 4π-averaged orientations of the helix with respect to the *k*-vector of photons (Fig. 2D and fig. S26). Although the range of experimental *g*-factors was narrow, the simulated curve matched the experimental trend well (fig. S25). The limited range of optical asymmetry for this and other experimental dependences was a consequence of the high efficiency of polarization rotation in these nanoassemblies and the low β from Eq. 1, resulting from the high *g*-factors observed for all of the structures.

The dependence of *g*-factors on d was experimentally studied by growing additional gold layers on preassembled nanochains (fig. S27). A concomitant simulation study for $2 < d < 24$ nm resulted in progressively decreased *g*-factors as d became larger (Fig. 2E and fig. S28). The negative exponential dependence was similar to that observed for the simulation series for N (Fig. 2F and fig. S29). Additionally, the orientation of the nanohelices parallel to the *k*-vector led to a greater α and smaller β, so the *g*-factors rose higher and faster with $\Delta\lambda$ (Fig. 2F).

We expected the dimensions of NRs to be critical for producing LC-like superstructures with high *g*-factors because they need to match the geometry of the hIAPP helix (Fig. 3, A and B). Nanohelices made from small NRs—for example, 37/8.4 nm (length/diameter) NRs—displayed a low *g*-factor of 0.001, although the NRs retained their helical organization (Fig. 3C). As NR sizes increased, the *g*-factors quickly increased until they reached a maximum of 0.10 with 50/19-nm NRs. Once the size of the NRs became too large (for example, 55 nm), the long-range registry of the NRs in the nanochains was disturbed. Although the approximate helical motif could still be traced in electron microscopy images, it inevitably resulted in stronger scattering and overlap between HE and LE bands. The decreased order led to a strong decline of *g*-factors, which was identical to the effects of intermolecular registry in LCs (*7*–*9*). Computational simulations matched the experimental results very well and identified nanohelices assembled from 50/19-nm NRs as the chiroplasmonic structures with the highest *g*-factor (Fig. 3D and table S1). Computed dependences demonstrated that α was proportional to the aspect ratios of NRs, whereas β was inversely proportional to

the NR sizes (Fig. 3, E and F; fig. S30, A and B; and tables S2 and S3).

Computational models validated by this and other experimental series enabled the consideration of additional geometrical design parameters for these materials. One such parameter is the pitch of the nanohelices; it is not currently possible to control the pitch of hIAPP assemblies, and yet it is likely to be essential for reaching and exceeding the *g*-factors of common LC materials. We found that a nanohelix with a pitch of 160 nm produced high α, small β (Fig. 3I, fig. S30C, and table S4), and the largest *g*-factor for gold NR assemblies (Fig. 3, G and H, and fig. S31). As the pitch increased beyond this value, the nanohelices became flatter, and, thus, their asymmetry decreased. For the nanohelices with smaller pitch, the drop in *g*-factor was caused by reduced plasmonic coupling. The sign of the CD spectra also switched when the pitch was below 110 nm—for example, 80 nm (fig. S32)—which was notable both from fundamental and practical standpoints.

The polypeptide hIAPP is a hallmark pathological feature of type 2 diabetes and an important biomarker for pancreatic cancer. The ability to sense amyloid peptides is pivotal for early diagnosis for all amyloid-related malfunctions, including Parkinson's disease (*24*), Huntington's disease, kidney amyloidosis, lateral sclerosis, and cataracts. Equally important is finding a method for the rapid screening of chemical structures that can inhibit the self-assembly of peptides, which is critical for drug discovery assays. Greatly enhanced intensity of the CD peaks from 0.90 to 2000 mdeg provided a highly precise sensing protocol to monitor the kinetic process of amyloid peptide association even under relatively low peptide concentrations. We observed spectral features in our assemblies that were hundreds of times as strong as the CD peaks in the ultraviolet part of the spectrum for biomolecules (fig. S33). Additionally, high *g*-factors, specific for the LC-like NR-hIAPP nanohelices, combined with their accelerated assembly, enabled rapid sensing and drug discovery protocols based on simple polarization optics (Fig. 4). Chiroptical spectroscopy in the near-infrared part of the spectrum avoided interference from most other biomolecules. Altogether, this combination of optical and biological properties engenders a drug discovery protocol capable of accelerated evaluation of drug candidates in complex media approaching that of the cellular environments of target organs. Until now, it was nearly impossible to realize this capability with other peptide fibrillation protocols and optical methods, including traditional CD spectroscopy (*43*, *44*).

A dispersion of isolated NRs placed in a standard cross-polarization optical cell allows little or no light to pass through it (Fig. 4B, left). However, a dispersion of assembled NR-hIAPP nanohelices enables red light corresponding to the maximum *g*-factor to be transmitted and easily observed (Fig. 4B, right), which was also verified by the optical rotatory dispersion (ORD) spectrum (Fig. 4D and fig. S34). Furthermore, polarized optical microscopy in the 650- to 750-nm range enabled direct, high-contrast visualization of NR-hIAPP assemblies (Fig. 4C), which provided high-*g* assemblies a previously unused advantage in biological studies over CD and ORD spectroscopies.

The intensity of transmitted polarized light rotated by NR-hIAPP assemblies (Fig. 4E and fig. S35) could be used to evaluate the conditions needed for peptides to form amyloid fibers. Thus, the nanohelix formation was tested for different concentrations of hIAPPs from 1.0 to 5.0 μM. The critical concentration for amyloid fiber formation was 3.0 μM. The maximum *g*-factor of NR-hIAPP assemblies was observed when the hIAPP concentration was 4.0 μM.

To explore efficient drug discovery protocols for screening potential amyloid-fiber inhibitors, we tested epigallocatechin gallate (EGCG) and hIAPP-derived, all-D–amino acid D-NFGAIL peptide fragments (Fig. 4F and fig. S36) (*45*). On the basis of the intensity of the transmitted red color, we observed that EGCG exhibited strong inhibition when the molar ratio of EGCG to hIAPPs was >5, whereas D-NFGAIL was less effective even with higher D-NFGAIL–to–hIAPP molar ratios.

This method can be used to overcome the limitations of traditional absorption and fluorescence methods when using complex biological media such as serum, homogenized tissues, and actual organs, which is critical for drug discovery. When benzothiazole dye thioflavin T (ThT) fluorescence probes were used to monitor the dissociation of amyloid fibers with EGCG (*45*) in fetal bovine serum (FBS) and pancreatic tissue, the ThT fluorescence signals were strongly obscured by the fluorescent backgrounds originating from the biological matrix (fig. S37, D, E, J, and K). By comparison, the dissociation process was clearly observed by the plasmonic CD spectrum and polarization rotation imaging platform (fig. S37, A to C and F to I), which indicates that high–*g*-factor nanoassemblies can be successfully applied in biological environments.

Extended interparticle registry in the helical assemblies of plasmonic particles resulted in nanostructures with high *g*-factors. LC-like optical effects originated from the lower scattering and smaller electrical fields in HE (as compared with LE) states. The optical asymmetry of self-assembled nanostructures is thousands of times as great as that of individual plasmonic units, which provides guidance for the design of chiroplasmonic nanocomposites (*46*) for optoelectronics and biomedical needs. Because supramolecular interactions involving hydrophobic forces are typical for nearly all (bio)organic assemblies, their synergistic assemblies with NPs and NRs into fibrous chiroplasmonic superstructures could be expected for a wide range of biomolecules.

REFERENCES AND NOTES

1. J. T. Collins *et al*., *Adv. Opt. Mater.* **5**, 1700182 (2017).
2. F. P. Milton, J. Govan, M. V. Mukhina, Y. K. Gun'ko, *Nanoscale Horizons* **1**, 14–26 (2016).
3. W. Ma *et al*., *Chem. Rev.* **117**, 8041–8093 (2017).
4. S. M. Morrow, A. J. Bissette, S. P. Fletcher, *Nat. Nanotechnol.* **12**, 410–419 (2017).
5. M. Hentschel, M. Schäferling, X. Duan, H. Giessen, N. Liu, *Sci. Adv.* **3**, e1602735 (2017).
6. A. G. Mark, J. G. Gibbs, T. C. Lee, P. Fischer, *Nat. Mater.* **12**, 802–807 (2013).
7. M. R. Craig, P. Jonkheijm, S. C. J. Meskers, A. P. H. J. Schenning, E. W. Meijer, *Adv. Mater.* **15**, 1435–1438 (2003).
8. H. Goto, *Macromolecules* **40**, 1377–1385 (2007).
9. M. Schulz *et al*., *Nat. Commun.* **9**, 2413 (2018).
10. P. Nordlander, C. Oubre, E. Prodan, K. Li, M. I. Stockman, *Nano Lett.* **4**, 899–903 (2004).
11. J. Yeom *et al*., *Science* **359**, 309–314 (2018).
12. G. González-Rubio *et al*., *Science* **368**, 1472–1477 (2020).
13. H. E. Lee *et al*., *Nature* **556**, 360–365 (2018).
14. E. Chiellini, G. Galli, *Macromolecules* **18**, 1652–1658 (1985).
15. Q. Xue, T. Kimura, T. Fukuda, S. Shimada, H. Matsuda, *Liq. Cryst.* **31**, 137–143 (2004).
16. A. D. Merg *et al*., *J. Am. Chem. Soc.* **138**, 13655–13663 (2016).
17. J. Cheng *et al*., *ACS Nano* **11**, 3806–3818 (2017).
18. J. Bergueiro *et al*., *Nanoscale Horizons* **5**, 495–500 (2020).
19. A. Kuzyk, R. Jungmann, G. P. Acuna, N. Liu, *ACS Photonics* **5**, 1151–1163 (2018).
20. Y. Tang, A. E. Cohen, *Phys. Rev. Lett.* **104**, 163901 (2010).
21. C. S. Ho, A. Garcia-Etxarri, Y. Zhao, J. Dionne, *ACS Photonics* **4**, 197–203 (2017).
22. A. Lee *et al*., *J. Am. Chem. Soc.* **133**, 7563–7570 (2011).
23. K. Yao, Y. Liu, *Nanoscale* **10**, 8779–8786 (2018).
24. J. Kumar *et al*., *Proc. Natl. Acad. Sci. U.S.A.* **115**, 3225–3230 (2018).
25. W. Chen *et al*., *Nano Lett.* **9**, 2153–2159 (2009).
26. A. Kuzyk *et al*., *Nature* **483**, 311–314 (2012).
27. J. J. W. Wiltzius *et al*., *Protein Sci.* **17**, 1467–1474 (2008).
28. S. Bedrood *et al*., *J. Biol. Chem.* **287**, 5235–5241 (2012).
29. J. Lu *et al*., *ACS Nano* **11**, 3463–3475 (2017).
30. J. Yan *et al*., *Chem. Mater.* **32**, 476–488 (2020).
31. Q. Zhang *et al*., *Science* **365**, 1475–1478 (2019).
32. G. Cheng, D. Xu, Z. Lu, K. Liu, *ACS Nano* **13**, 1479–1489 (2019).
33. X. Lan *et al*., *J. Am. Chem. Soc.* **140**, 11763–11770 (2018).
34. H. Liu, X. Shen, Z.-G. Wang, A. Kuzyk, B. Ding, *Nanoscale* **6**, 9331–9338 (2014).
35. A. V. Kajava, U. Aebi, A. C. Steven, *J. Mol. Biol.* **348**, 247–252 (2005).
36. S. Linse *et al*., *Proc. Natl. Acad. Sci. U.S.A.* **104**, 8691–8696 (2007).
37. A. K. Srivastava *et al*., *Protein Sci.* **28**, 1567–1581 (2019).
38. S. K. Mudedla, N. A. Murugan, H. Agren, *J. Phys. Chem. B* **122**, 9654–9664 (2018).
39. G. Liu *et al*., *J. Am. Chem. Soc.* **132**, 18223–18232 (2010).
40. S. A. Kotler, P. Walsh, J. R. Brender, A. Ramamoorthy, *Chem. Soc. Rev.* **43**, 6692–6700 (2014).
41. S. M. Butterfield, H. A. Lashuel, *Angew. Chem. Int. Ed.* **49**, 5628–5654 (2010).
42. E. Prodan, C. Radloff, N. J. Halas, P. Nordlander, *Science* **302**, 419–422 (2003).
43. A. De Simone *et al*., *J. Pharm. Biomed. Anal.* **178**, 112899 (2020).
44. J. Seo *et al*., *Nat. Chem.* **9**, 39–44 (2017).
45. M. F. M. Engel *et al*., *J. Am. Chem. Soc.* **134**, 14781–14788 (2012).
46. Y. Kim *et al*., *Nat. Mater.* **15**, 461–468 (2016).

ACKNOWLEDGMENTS

We thank T. Lu, L. Wang, and F. Li for hIAPP preparation; Y.-X. Chang for self-assembly; H.-L. Wang, F.-L. Zhang, and W. Choi for the support of FDTD simulation; and L. Wang for cryo-TEM tomography reconstruction and their helpful discussions. We thank M. S. Lee for CD measurement and very helpful discussions. A.F.d.M. is grateful to CNPq for a Fellowship of Research Productivity (2020). The authors acknowledge the access to the high-performance computing

(HPC) resources of the SDumont supercomputer (National Laboratory for Scientific Computing, LNCC/MCTI, Brazil, https://sdumont.lncc.br). **Funding:** K.L. gratefully acknowledges the financial support from the National Natural Science Foundation of China (21534004, 21674042, and 21911530179), the JLU Science and Technology Innovative Research Team (2017TD-06), and the Open Project of State Key Laboratory of Supramolecular Structure and Materials (sklssm201736). K.L. also thanks the Jilin Province International Collaboration Base of Science and Technology (YDZJ202102CXJD004). K.L., T.S., and Z.H. acknowledge financial support from the Interdisciplinary Innovation Project of the First Hospital of JLU (JDYYJCHX001 and JDYYJCHX2020002). The authors thank the Brazilian funding agencies CAPES (process 001), CNPq, and FAPESP (processes 2012/15147-4, 2013/07296-2, and 17/12063-8) for financial support. This work was supported by the NSF project "Energy- and Cost-Efficient Manufacturing Employing Nanoparticles" (NSF 1463474) and a Vannevar Bush DoD Fellowship to N.A.K. entitled "Engineered Chiral Ceramics" (ONR N000141812876); partially supported by Office of Naval Research Multidisciplinary University Research Initiative Award ONR N00014-18-1-2497 (N.A.K. and J.L.); and NSF 1566460 "Nanospiked Particles for Photocatalysis" is also acknowledged (N.A.K. and N.S.R.). N.A.K. is also grateful to the Defense Advanced Research Projects Agency (DARPA) for the HR00111720067 project entitled "Electromagnetic Processes and Normal Modes in Bacterial Biofilms," the Newton Award ONRHQ00342010033 entitled "Pathways to Complexity with 'Imperfect' Nanoparticles," and for discretionary funds from the University of Michigan for the supplementary funding for this work. **Author contributions:** J.L., K.L., and N.A.K. conceived the work and planned the experiments. J.L., Y.X., and N.-N.Z. assembled products for optical measurements and structure characterization. J.L. and N.S.R. performed cryo-TEM tomography reconstruction. J.L. conducted the drug screening experiment in buffer. A.F.d.M., K.B., and W.R.G. carried out MD simulations. Y.X., S.L., T.S., and Z.H. conducted drug screening experiments in serum and porcine pancreas. J.L. and N.A.K. carried out the electromagnetic computer simulations. N.A.K., J.L., A.F.d.M., and K.L. wrote the manuscript and compiled figures with discussion of results and feedback on the manuscript from all authors. **Competing interests:** The authors declare no competing interests. **Data and materials availability:** All data are available in the main text or the supplementary materials. Correspondence and requests for materials should be addressed to A.F.d.M., N.A.K., and K.L.

SUPPLEMENTARY MATERIALS

science.sciencemag.org/content/371/6536/1368/suppl/DC1
Materials and Methods
Figs. S1 to S37
Tables S1 to S4
References (*47*–*85*)
Movies S1 to S3

22 July 2020; accepted 9 February 2021
Published online 25 February 2021
10.1126/science.abd8576

CORONAVIRUS

SARS-CoV-2 M^{pro} inhibitors with antiviral activity in a transgenic mouse model

Jingxin Qiao[1]*, Yue-Shan Li[1]*, Rui Zeng[1]*, Feng-Liang Liu[2,3]*, Rong-Hua Luo[2,3]*, Chong Huang[1]*, Yi-Fei Wang[4]*, Jie Zhang[1], Baoxue Quan[1], Chenjian Shen[1], Xin Mao[1], Xinlei Liu[1], Weining Sun[1], Wei Yang[1], Xincheng Ni[1], Kai Wang[1], Ling Xu[2,3], Zi-Lei Duan[2,3], Qing-Cui Zou[3], Hai-Lin Zhang[3,5], Wang Qu[3], Yang-Hao-Peng Long[3], Ming-Hua Li[3], Rui-Cheng Yang[1], Xiaolong Liu[1], Jing You[1], Yangli Zhou[1], Rui Yao[1], Wen-Pei Li[1], Jing-Ming Liu[1], Pei Chen[4], Yang Liu[1], Gui-Feng Lin[1], Xin Yang[1], Jun Zou[1], Linli Li[4], Yiguo Hu[1], Guang-Wen Lu[1], Wei-Min Li[1], Yu-Quan Wei[1], Yong-Tang Zheng[2,3]†, Jian Lei[1,6]†, Shengyong Yang[1]†

The COVID-19 pandemic caused by severe acute respiratory syndrome coronavirus 2 (SARS-CoV-2) continually poses serious threats to global public health. The main protease (M^{pro}) of SARS-CoV-2 plays a central role in viral replication. We designed and synthesized 32 new bicycloproline-containing M^{pro} inhibitors derived from either boceprevir or telaprevir, both of which are approved antivirals. All compounds inhibited SARS-CoV-2 M^{pro} activity in vitro, with 50% inhibitory concentration values ranging from 7.6 to 748.5 nM. The cocrystal structure of M^{pro} in complex with MI-23, one of the most potent compounds, revealed its interaction mode. Two compounds (MI-09 and MI-30) showed excellent antiviral activity in cell-based assays. In a transgenic mouse model of SARS-CoV-2 infection, oral or intraperitoneal treatment with MI-09 or MI-30 significantly reduced lung viral loads and lung lesions. Both also displayed good pharmacokinetic properties and safety in rats.

The COVID-19 pandemic is caused by severe acute respiratory syndrome coronavirus 2 (SARS-CoV-2) (*1*–*3*). Despite intensive countermeasures implemented around the world, morbidity and mortality remain high with many countries facing a new wave of infections (*4*, *5*). Because limited antiviral agents are available to combat SARS-CoV-2 infection, the development of specific antiviral drugs against SARS-CoV-2 is urgently needed.

SARS-CoV-2 is an enveloped positive-sense single-stranded RNA virus belonging to the genus *Betacoronavirus* (*1*–*3*, *6*). This virus contains a ~30-kb RNA genome encoding two large overlapping polyprotein precursors (pp1a and pp1ab), four structural proteins (spike, envelope, membrane, and nucleocapsid), and several accessory proteins (*1*, *2*, *6*). The cleavage of the two polyproteins (pp1a/pp1ab) into individual nonstructural proteins is essential for viral genome replication. This cleaving process is performed by two viral proteases: main protease (M^{pro}, also named 3CL protease) and papain-like protease (*7*). These viral proteases are thus important antiviral targets (*8*, *9*). Notably, M^{pro} exclusively cleaves polypeptides after a glutamine (Gln) residue, and no known human protease displays the same cleavage specificity as M^{pro} (*9*, *10*). This may allow the development of drugs that are specific to M^{pro} to reduce potential side effects.

Despite some SARS-CoV-2 M^{pro} inhibitors being reported (*11*–*21*) and a dipeptidyl inhibitor by Pfizer entering phase I clinical trials (*14*, *15*, *22*), previous literature on inhibitors of SARS-CoV-2 M^{pro} (*11*–*22*) has not included infection data in an animal model. Here, we describe the design of 32 new SARS-CoV-2 M^{pro} inhibitors, two of which show effective antiviral activity in mice.

The design of SARS-CoV-2 M^{pro} inhibitors was based on the reported crystal structures of SARS-CoV-2 M^{pro} (*11*–*13*) and our cocrystal structures of SARS-CoV-2 M^{pro} in complex

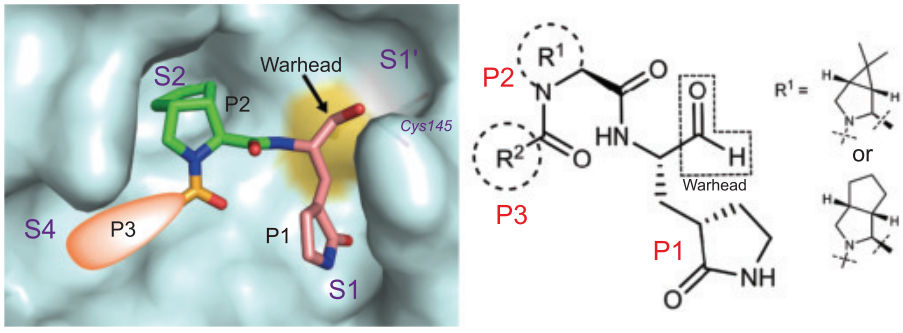

Fig. 1. Schematic diagram of the design of novel SARS-CoV-2 M^{pro} inhibitors.

[1]State Key Laboratory of Biotherapy, West China Hospital, Sichuan University, Chengdu, Sichuan 610041, China. [2]Key Laboratory of Animal Models and Human Disease Mechanisms of the Chinese Academy of Sciences, Kunming Institute of Zoology, Chinese Academy of Sciences, Kunming, Yunnan 650223, China. [3]Kunming National High-level Biosafety Research Center for Non-human Primates, Center for Biosafety Mega-Science, Kunming Institute of Zoology, Chinese Academy of Sciences, Kunming, Yunnan 650107, China. [4]Key Laboratory of Drug Targeting and Drug Delivery Systems, Ministry of Education, West China School of Pharmacy, Sichuan University, Chengdu, Sichuan 610041, China. [5]State Key Laboratory of Genetic Resources and Evolution, Kunming Institute of Zoology, Chinese Academy of Sciences, Kunming, Yunnan 650223, China. [6]National Clinical Research Center for Geriatrics, West China Hospital, Sichuan University, Chengdu, Sichuan 610041, China.
*These authors contributed equally to this work.
†Corresponding author. Email: yangsy@scu.edu.cn (S.Y.); leijian@scu.edu.cn (J.L.); zhengyt@mail.kiz.ac.cn (Y.-T.Z.)

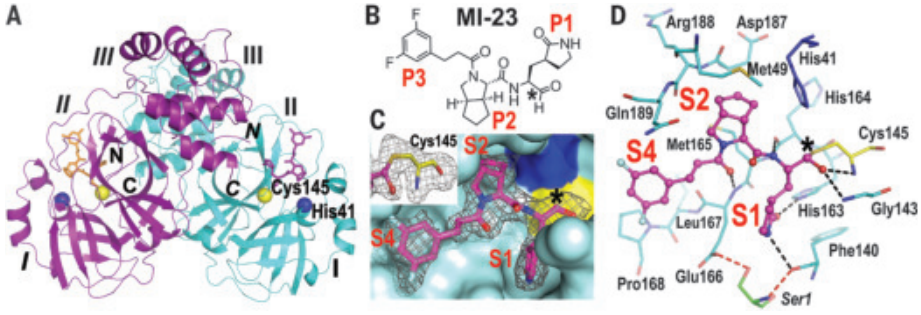

Fig. 2. Overall structure of SARS-CoV-2 M^{pro}–MI-23 complex. (**A**) Cartoon view of the M^{pro} dimer (molecule A, cyan; molecule B, purple). Three domains (I, II, and III) of each monomer are marked. The catalytic dyad Cys^{145}-His^{41} is located in the cleft between domains I and II. MI-23 in both molecules is shown in purple or orange. The N and C termini of each M^{pro} are labeled. Labels for molecule B are in italics. (**B**) The chemical structure of MI-23. (**C**) The MI-23 binding pocket of M^{pro}. $F_o - F_c$ density map (gray mesh, σ = 2.5) is shown for MI-23 (purple). Cys^{145} and His^{41} are shown in yellow and blue, respectively. The covalent bond is formed by Cys^{145} and the warhead aldehyde. $F_o - F_c$ density map (σ = 2.5) is shown in gray. (**D**) Interactions between M^{pro} and MI-23; the hydrogen bonds between them are shown as black dashed lines. Ser^{1} from molecule B interacts with Glu^{166} and Phe^{140} in molecule A (red dashed lines) to support S1 pocket formation. The warhead carbon is marked with a black asterisk in (B), (C), and (D). Images in (A), (C), and (D) were prepared using PyMOL (https://pymol.org).

with the approved antivirals against hepatitis C virus infection, boceprevir (PDB entry 7COM) and telaprevir (PDB entry 7C7P) (fig. S1). The active site of M^{pro} is composed of four sites (S1′, S1, S2, and S4), which often accommodate four fragments (P1′, P1, P2, and P3, respectively) of peptidomimetic inhibitors (*8*, *10*). In our design of new inhibitors (Fig. 1), we fixed P1 as an optimal fragment, used P2 that was derived from either boceprevir or telaprevir, and allowed P3 to change. First, an aldehyde was used as the warhead in P1 to form a covalent bond with the catalytic site Cys^{145}, which is essential for the antiviral activity (*13*). Relative to other bulky warheads, the small and highly electrophilic aldehyde has been reported to be more potent (*7*, *10*, *20*, *22*). However, the clinical safety of the generated aldehydes remains to be determined because of possible off-target effects due to the high electrophilicity of aldehyde (*23*). Second, we chose a five-membered ring (γ-lactam) derivative of glutamine to occupy the S1 site of M^{pro}, which not only mimics the native P1 glutamine of the substrates but also increases the activity of inhibitors (*24*, *25*). Third, we used a bicycloproline moiety, either (1*R*,2*S*,5*S*)-6,6-dimethyl-3-aza-bicyclo[3.1.0] hexane-2-formamide (P2 of boceprevir) or (1*S*,3a*R*,6a*S*)-octahydrocyclopenta[c]pyrrole-1-formamide (P2 of telaprevir), as a P2 fragment. This was inspired by our cocrystal structures of SARS-CoV-2 M^{pro} in complex with boceprevir and telaprevir (fig. S1), in which the two bicycloproline moieties suitably occupy the S2 pocket of M^{pro}. In particular, the rigid and hydrophobic bicycloproline is expected to increase drug exposure in vivo (*26*). Finally, by analyzing the characteristics of the S4 site of M^{pro}, we decided to use hydrophobic subgroups of medium size for P3 to enhance the potency and pharmacokinetic (PK) properties of the resulting inhibitors. We thus designed and synthesized 32 compounds with various P3 fragments (MI-01 to MI-32; fig. S2). Among these compounds, MI-01 to MI-14 contain P2 of boceprevir, whereas MI-15 to MI-32 include

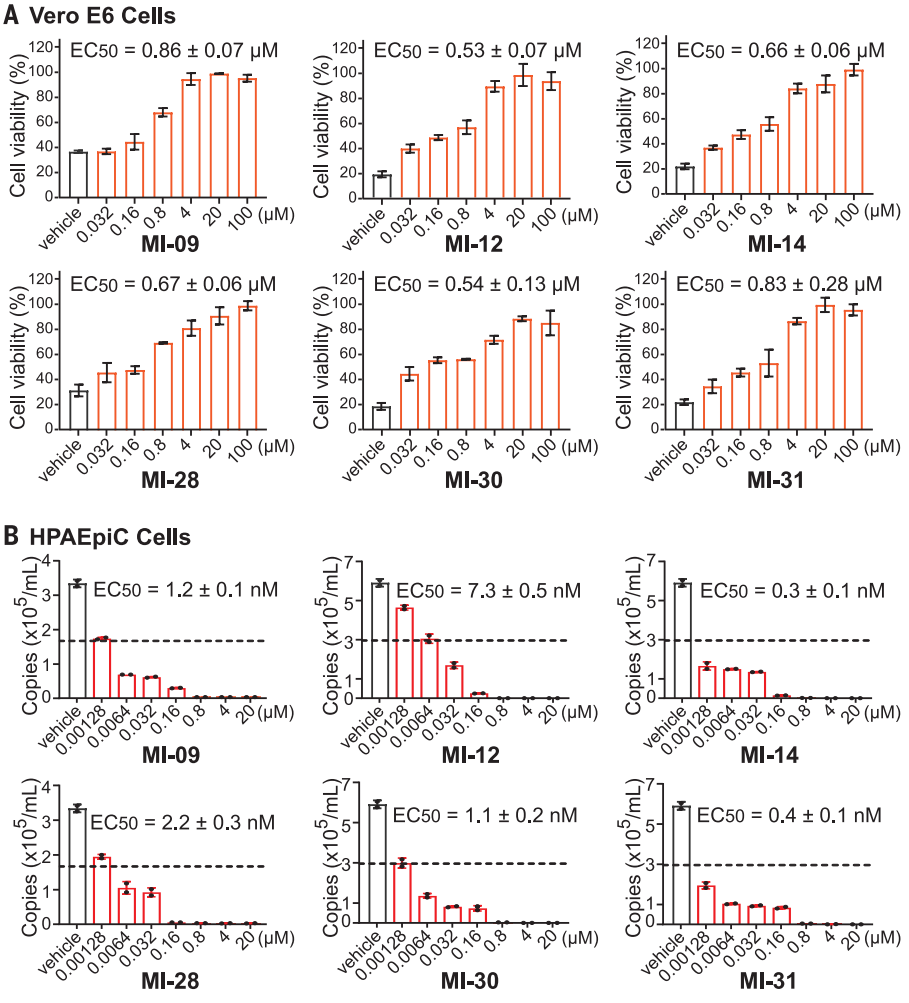

Fig. 3. Antiviral activity of six compounds against SARS-CoV-2 in cell-based assays. (**A**) Vero E6 cells were infected with SARS-CoV-2 at a multiplicity of infection (MOI) of 0.1 and treated with different concentrations of test compounds (MI-09, MI-12, MI-14, MI-28, MI-30, and MI-31). At 3 dpi, the cytopathic effect caused by SARS-CoV-2 infection was quantitatively analyzed using CCK8 according to the manufacturer's protocol. Data are means ± SD; *n* = 3 biological replicates. (**B**) HPAEpiC cells were infected with SARS-CoV-2 at an MOI of 0.01 and treated with different concentrations of test compounds (MI-09, MI-12, MI-14, MI-28, MI-30, and MI-31). At 2 dpi, viral RNA copies (per ml) were quantified from cell culture supernatants by RT-qPCR. Data are means ± SD; *n* = 2 biological replicates.

A

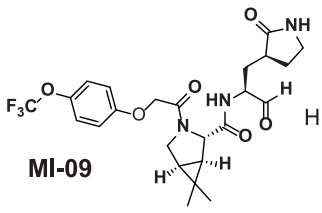

M^{pro} IC_{50}	15.2 ± 0.4 nM
HPAEpiC EC_{50}	1.2 ± 0.1 nM
i.p. F	78.0 ± 4.1%
p.o. F	11.2 ± 6.4%

B

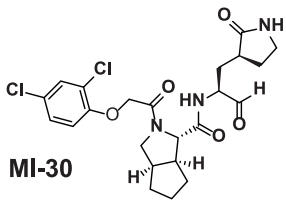

M^{pro} IC_{50}	17.2 ± 0.6 nM
HPAEpiC EC_{50}	1.1 ± 0.2 nM
i.p. F	76.2 ± 20.9%
p.o. F	14.6 ± 1.0%

C

	MI-09		MI-30
Virus dose		2×10^6 $TCID_{50}$	
Administration	i.p.	p.o.	i.p.
Dose	50 mg/kg, qd	50 mg/kg, bid	50 mg/kg, qd
Virus dose		5×10^6 $TCID_{50}$	
Administration	i.p.	p.o.	i.p.
Dose	100 mg/kg, qd	100 mg/kg, bid	100 mg/kg, qd

D

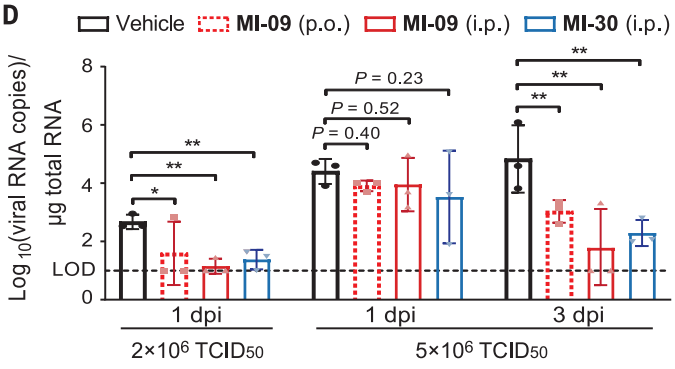

E

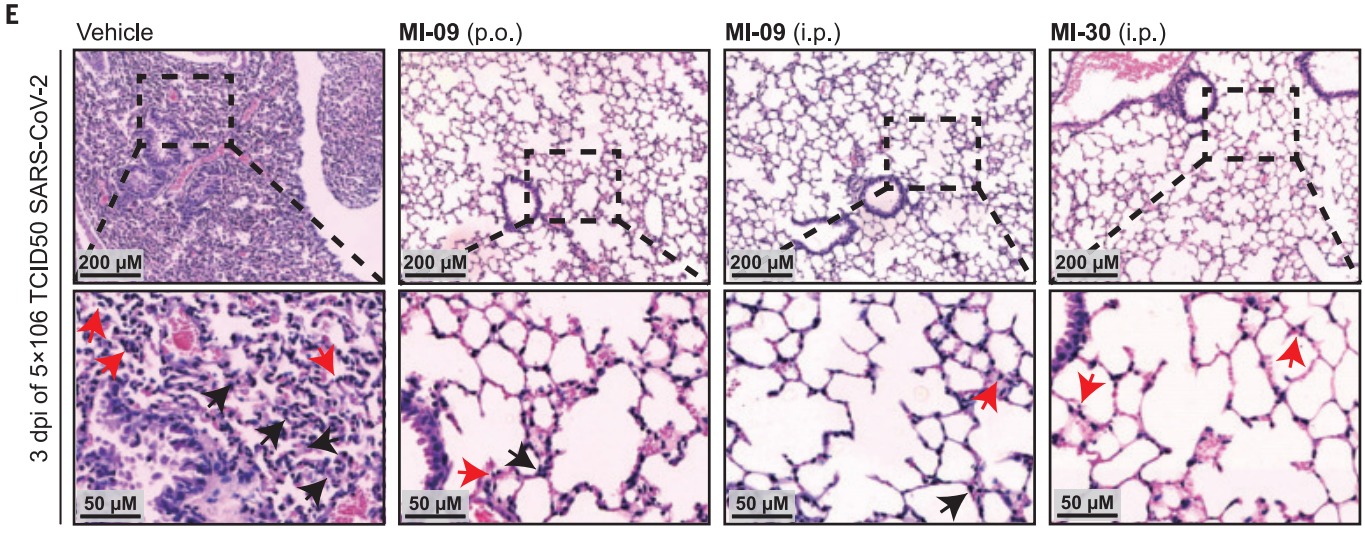

F

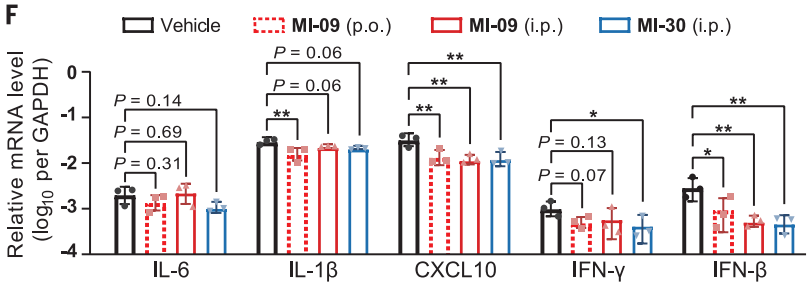

G

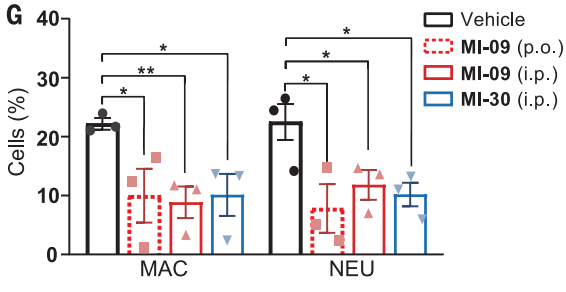

H

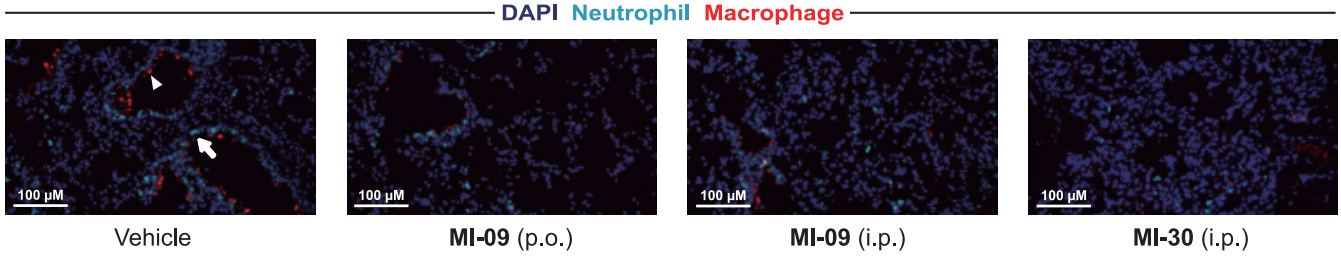

Fig. 4. MI-09 and MI-30 reduce lung viral loads and lung lesions in a SARS-CoV-2 infection transgenic mouse model. (**A** and **B**) Chemical structures and summary of in vitro activity data and bioavailability of MI-09 and MI-30. (**C**) Overview of in vivo study design. (**D**) Viral loads in the lungs of SARS-CoV-2–infected hACE2 transgenic mice. Mice infected with the indicated dose of SARS-CoV-2 were treated with MI-09, MI-30, or vehicle solution, and then were killed at 1 or 3 dpi. Five lung lobes of each mouse were collected to determine viral loads. Data (means ± SD) represent the median of five lung lobes of individual mice. The horizontal dotted line shows the viral load limit of detection (LOD) of 1.0 $\log_{10}$ RNA copies. Data below the LOD are shown at the LOD. $^{*}P < 0.05$, $^{**}P < 0.01$ (two-tailed unpaired Student's *t* test). (**E**) Representative images of lung histopathological changes from SARS-CoV-2–infected hACE2 mice (5×10^6 $TCID_{50}$) at 3 dpi. Magnified views of the boxed regions for each image are shown below. Black arrows indicate alveolar septal thickening; red arrows point to inflammatory cell infiltration. See fig. S4 for whole-lung tissue scan images of SARS-CoV-2–infected hACE2 mice at 3 dpi. (**F**) Representative chemokine and cytokine assessment of the lung tissues ($n = 3$) of the indicated groups, as detected in lung tissue homogenate at 3 dpi. Data are means ± SD. $^{*}P < 0.05$, $^{**}P < 0.01$ versus the vehicle group (one-way analysis of variance). (**G** and **H**) Infiltration analysis for neutrophils and macrophages in the lungs of SARS-CoV-2–infected hACE2 mice (5×10^6 $TCID_{50}$) at 3 dpi. (G) Percentages of macrophages and neutrophils in the lungs. $^{*}P < 0.05$, $^{**}P < 0.01$ (unpaired Student's *t* test). (H) Representative images of fluorescence staining. White triangle and arrow indicate macrophage and neutrophil, respectively.

P2 of telaprevir. [See supplementary materials for chemical structures (fig. S2), synthetic routes, and characterization of these compounds by nuclear magnetic resonance and electrospray ionization mass spectrometry.]

The 32 compounds' biochemical activities against SARS-CoV-2 M^{pro} were determined by a fluorescence resonance energy transfer (FRET) assay. For this, recombinant SARS-CoV-2 M^{pro} protein was prepared. The turnover number (k_{cat})/Michaelis constant (K_m) value of the recombinant protein was determined as 50,656 ± 4221 M^{-1} s^{-1}, similar to a previous result (*11*). In the FRET assay, all 32 compounds (MI-01 to MI-32) showed potent inhibitory activities on SARS-CoV-2 M^{pro}, with 50% inhibitory concentration (IC_{50}) values ranging from 7.6 to 748.5 nM (table S1). Of these, 24 compounds displayed two-digit nanomolar IC_{50} values, and three exhibited single-digit values (MI-21, 7.6 nM; MI-23, 7.6 nM; MI-28, 9.2 nM). The positive controls GC376 and 11b, two of the most potent SARS-CoV-2 M^{pro} inhibitors reported (*13*, *17*), exhibited IC_{50} values of 37.4 nM and 27.4 nM in the same assay, respectively. Next, a differential scanning fluorimetry (DSF) assay was performed to validate the direct binding between our compounds and SARS-CoV-2 M^{pro}. All the compounds displayed large thermal shifts ranging from 12.5° to 21.7°C (table S1), indicating their tight binding to SARS-CoV-2 M^{pro}. It is noteworthy that the two different bicycloproline moieties (P2) did not affect the inhibitory activities and binding abilities (e.g., MI-03 versus MI-21, MI-12 versus MI-28, and MI-14 versus MI-30; table S1 and fig. S2).

To illustrate the detailed binding mode of our compounds with SARS-CoV-2 M^{pro}, we determined the 2.0-Å structure of M^{pro} in complex with one of the most active compounds, MI-23 (IC_{50} = 7.6 nM) (Fig. 2, A to D). The crystal structure of the M^{pro}–MI-23 complex belongs to space group *C*2 (table S2) with one molecule per asymmetric unit. The biological dimer of M^{pro} is formed by an M^{pro} monomer and its symmetry-mate across the crystallographic two-fold axis (Fig. 2A). MI-23 binds to the active site of M^{pro} as expected (Fig. 2, C and D). The carbon of the warhead aldehyde interacts with the sulfur atom of catalytic residue Cys^{145} to form a 1.8-Å covalent bond (Fig. 2C). The oxygen of the aldehyde forms two hydrogen bonds with the main-chain amides of Cys^{145} and Gly^{143} (forming the "oxyanion hole") (Fig. 2D). The P1 γ-lactam ring of MI-23 inserts deeply into the S1 pocket. The oxygen and nitrogen of lactam form two hydrogen bonds with the side chain of His^{163} (2.8 Å) and the main chain of Phe^{140} (3.3 Å), respectively. The main-chain amide of P1 makes a 2.9-Å hydrogen bond with the backbone O of His^{164}. Because of the conformational restraints inherent in the structure of proline (*27*), the rigid P2 bicycloproline of MI-23 adopts the trans-exo conformation with restricted N–Cα bond rotation (the φ torsion angle is ~ −61.8°). This causes the bicycloproline group to point to the hydrophobic S2 pocket, where it forms hydrophobic interactions with Cγ of Met^{165}, Cβ and Cγ of Gln^{189} and His^{41}, Cε of Met^{49}, and the backbone C and Cα of Asp^{187} and Arg^{188}. The backbone oxygen of P3 interacts with the backbone amide of Glu^{166} with a 2.9-Å hydrogen bond. The 1-ethyl-3,5-difluorobenzene moiety of P3 shows an extended conformation and occupies the S4 site. This moiety forms hydrophobic interactions with Cγ of Gln^{189} and the backbone C and Cα of Leu^{167} and Pro^{168} (Fig. 2D). The benzene ring of P3 also forms a very weak hydrophobic interaction with Gly^{251} from an adjacent translational symmetry protomer as a result of crystal packing. Overall, the binding pattern of the representative compound MI-23 with M^{pro} is consistent with our design concept.

We then selected 20 compounds with IC_{50} < 50 nM in the enzyme inhibition assay to examine their cytotoxicity and cellular antiviral activity. First, the cytotoxicity of these compounds was evaluated using the Cell Counting Kit-8 (CCK8) assay (Beyotime Biotechnology), and no compounds showed cytotoxicity [half cytotoxic concentration (CC_{50}] > 500 μM] in the cell lines tested, including Vero E6, HPAEpiC, LO2, BEAS-2B, A549, and Huh7 cells (tables S3 and S4).

Next, the compounds' cellular antiviral activity was examined by a cell protection assay. In this assay, the viability of SARS-CoV-2–infected Vero E6 cells with or without treatment with the compounds was assessed using CCK8. All the compounds dose-dependently protected cells from death with 50% effective concentration (EC_{50}) values ranging from 0.53 to 30.49 μM (table S4). Of note, six compounds, including MI-09 (0.86 μM), MI-12 (0.53 μM), MI-14 (0.66 μM), MI-28 (0.67 μM), MI-30 (0.54 μM), and MI-31 (0.83 μM), exhibited nanomolar or low micromolar EC_{50} values (Fig. 3A). We noticed that some compounds (e.g., MI-22 and MI-25) with high potency in the enzymatic assay showed marginal activity in the cell protection assay, perhaps due to relatively low lipophilic groups in P3 and the resulting poor cell membrane permeability (*28*). Quantitative reverse transcription polymerase chain reaction (RT-qPCR) revealed that all six compounds inhibited SARS-CoV-2 virus replication in HPAEpiC cells with low-nanomolar EC_{50} values (0.3 to 7.3 nM) (Fig. 3B). In the same CCK8 and RT-qPCR assays, the positive control GC376 showed EC_{50} values of 1.46 μM and 153.1 nM, respectively, and the corresponding values for 11b were 0.89 μM and 23.7 nM. To further corroborate the antiviral potency of these compounds, we conducted RT-qPCR in another cell line, Huh7. The six compounds showed antiviral EC_{50} values of 31.0 to 96.7 nM, whereas GC376 and 11b displayed EC_{50} values of 174.9 nM and 74.5 nM, respectively (fig. S5).

To identify which of the six compounds is suitable for in vivo antiviral studies, we conducted PK experiments in Sprague-Dawley rats. Two compounds, MI-09 and MI-30, showed relatively good PK properties with oral bioavailability of 11.2% and 14.6%, respectively (table S5). Because a compound with oral bioavailability of >10% has potential for development as an oral drug (*29*), MI-09 and MI-30 were selected for further in vivo antiviral study. The key PK parameters of MI-09 and MI-30 are summarized in Fig. 4, A and B. When administered intravenously (i.v.) (10 mg/kg), intraperitoneally (i.p.) (20 mg/kg), and orally

(p.o.) (20 mg/kg), MI-09 showed area under the curve (AUC) values of 7429 hours·ng ml^{-1}, 11,581 hours·ng ml^{-1}, and 1665 hours·ng ml^{-1}, respectively, whereas MI-30 displayed AUC values of 9768 hours·ng ml^{-1}, 14,878 hours·ng ml^{-1}, and 2843 hours·ng ml^{-1}, respectively. After i.p. administration, MI-09 or MI-30 displayed a half-life ($T_{1/2}$) of 4.53 hours, a bioavailability of 78.0%, and a clearance rate (CL) of 22.67 ml min^{-1} kg^{-1}. The corresponding values for MI-30 were $T_{1/2}$ = 3.88 hours, bioavailability = 76.2%, and CL = 17.10 ml min^{-1} kg^{-1}. On the basis of the EC_{50}/EC_{90} values from HPAEpiC cells, a single i.p. dose of 20 mg kg^{-1} day^{-1} MI-09 or MI-30 maintained the plasma levels at EC_{50} (1.2 nM for MI-09, 1.1 nM for MI-30) and EC_{90} (47.9 nM for MI-09, 58.8 nM for MI-30) for ~24 hours and 6 hours (fig. S3, A and B), respectively. Also, a single p.o. dose of 20 mg kg^{-1} day^{-1} MI-09 or MI-30 sustained the plasma levels at EC_{50} and EC_{90} for ~10 hours and 6 hours (fig. S3, C and D), respectively. Moreover, according to the EC_{50}/EC_{90} values from Vero E6 cells, with a single i.p. dose of 20 mg kg^{-1} day^{-1} MI-09 or MI-30, the durations of drug plasma levels above EC_{50} (0.86 μM for MI-09, 0.54 μM for MI-30) and EC_{90} (3.62 μM for MI-09, 2.12 μM for MI-30) were ~3 hours and 2 hours, respectively. A single p.o. dose of 20 mg kg^{-1} day^{-1} MI-09 or MI-30 caused the drug plasma concentrations to reach EC_{50} but not EC_{90} in Vero E6 cells.

MI-09 and MI-30 were then evaluated for their toxicity in rats. In an acute toxicity experiment, no rats died after i.v. (40 mg/kg), i.p. (250 mg/kg), or p.o. (500 mg/kg) treatment with either MI-09 or MI-30 (table S6). In a repeated dose toxicity study, treatment with MI-09 or MI-30 by i.v. at 6 and 18 mg kg^{-1} day^{-1}, i.p. at 100 and 200 mg kg^{-1} day^{-1}, or p.o. at 100 and 200 mg/kg twice daily for 7 consecutive days did not result in noticeable toxicity in the animals (table S6).

Further, we investigated the in vivo antiviral activity of our compounds in a human angiotensin-converting enzyme 2 (hACE2) transgenic mouse model, which is susceptible to SARS-CoV-2 (*30*). In our pilot study, hACE2 transgenic mice were intranasally inoculated with SARS-CoV-2 [2×10^6 $TCID_{50}$ (50% tissue culture infectious dose) virus per mouse] and were then treated with vehicle (control), MI-09 [50 mg/kg p.o. twice daily (bid) or 50 mg/kg i.p. once daily (qd)] or MI-30 (50 mg/kg i.p. qd) starting at 1 hour prior to virus inoculation (Fig. 4C) and continuing until 5 days post-infection (5 dpi). During the 6-day period, no abnormal behaviors or body weight loss were observed in any animals tested. At 1 dpi, the mean viral RNA loads in the lung tissues of the three treatment groups were significantly ($P < 0.05$, Student's t test) lower than that of the control group (Fig. 4D). At 3 and 5 dpi, the viral RNA loads in the lung tissues of treatment groups were almost undetectable, and those of the control group were also very low [below the limit of detection (LOD)], which might be due to the mild degree of infection.

We thus increased the virus challenge dose of SARS-CoV-2 to 5×10^6 $TCID_{50}$, which mimics a moderate infection. The mice were treated as described above, except that the doses increased to 100 mg/kg for both i.p. and p.o. administration of MI-09 and MI-30 (Fig. 4C). The higher dose of virus challenge led to a higher level of viral loads in the lungs of infected mice, as expected. The mean viral RNA loads in the lung tissues of the three treatment groups were slightly lower than those of the control group at 1 dpi and significantly lower ($P < 0.05$, Student's t test) at 3 dpi (Fig. 4D). At 5 dpi, the viral loads in the lung tissues were undetectable in the treatment groups and were low (near or below LOD) in the control group.

Histopathological analysis was performed for the lungs of mice infected with SARS-CoV-2 at 5×10^6 $TCID_{50}$. At 3 dpi, the vehicle-treated mice showed moderate alveolar septal thickening and inflammatory cell infiltration, whereas all compound-treated animals exhibited slight alveolar septal thickening and mild inflammatory cell infiltration (Fig. 4E). To investigate whether the compounds ameliorate lung damage by affecting host immune response, we studied the expression of inflammatory cytokines and chemokines as well as immune cell infiltration in the lungs. MI-09 or MI-30 reduced the expression levels of IFN-β and CXCL10 (Fig. 4F). Also, fewer neutrophils and macrophages occurred in the lungs of compound-treated mice than in control mice (Fig. 4, G and H), suggesting inhibition of immune cell infiltration. Together, our results show that i.p. or p.o. administration of MI-09 or MI-30 could efficiently inhibit SARS-CoV-2 replication and ameliorate SARS-CoV-2–induced lung lesions in vivo, and they represent an important step toward the development of orally available anti–SARS-CoV-2 drugs.

REFERENCES AND NOTES

1. P. Zhou *et al.*, *Nature* **579**, 270–273 (2020).
2. F. Wu *et al.*, *Nature* **579**, 265–269 (2020).
3. Coronaviridae Study Group of the International Committee on Taxonomy of Viruses, *Nat. Microbiol.* **5**, 536–544 (2020).
4. P. Smith, *BMJ* **370**, m3350 (2020).
5. M.-K. Looi, *BMJ* **371**, m4113 (2020).
6. Y. Chen, Q. Liu, D. Guo, *J. Med. Virol.* **92**, 418–423 (2020).
7. R. Hilgenfeld, *FEBS J.* **281**, 4085–4096 (2014).
8. K. Anand, J. Ziebuhr, P. Wadhwani, J. R. Mesters, R. Hilgenfeld, *Science* **300**, 1763–1767 (2003).
9. L. Zhang *et al.*, *J. Med. Chem.* **63**, 4562–4578 (2020).
10. T. Pillaiyar, M. Manickam, V. Namasivayam, Y. Hayashi, S.-H. Jung, *J. Med. Chem.* **59**, 6595–6628 (2016).
11. Z. Jin *et al.*, *Nature* **582**, 289–293 (2020).
12. L. Zhang *et al.*, *Science* **368**, 409–412 (2020).
13. W. Dai *et al.*, *Science* **368**, 1331–1335 (2020).
14. R. L. Hoffman *et al.*, *J. Med. Chem.* **63**, 12725–12747 (2020).
15. B. Boras *et al.*, bioRxiv 293498 [preprint]. 13 September 2020.
16. M. Westberg *et al.*, bioRxiv 275891 [preprint]. 16 September 2020.
17. C. Ma *et al.*, *Cell Res.* **30**, 678–692 (2020).
18. M. D. Sacco *et al.*, *Sci. Adv.* **6**, eabe0751 (2020).
19. W. Zhu *et al.*, *ACS Pharmacol. Transl. Sci.* **3**, 1008–1016 (2020).
20. K. S. Yang *et al.*, *ChemMedChem* **15**, 1–8 (2020).
21. A. D. Rathnayake *et al.*, *Sci. Transl. Med.* **12**, eabc5332 (2020).
22. R. Cannalire, C. Cerchia, A. R. Beccari, F. S. Di Leva, V. Summa, *J. Med. Chem.* acs.jmedchem.0c01140 (2020).
23. C. Gampe, V. A. Verma, *J. Med. Chem.* **63**, 14357–14381 (2020).
24. P. S. Dragovich *et al.*, *J. Med. Chem.* **42**, 1213–1224 (1999).
25. R. P. Jain *et al.*, *J. Med. Chem.* **47**, 6113–6116 (2004).
26. Y. Yip *et al.*, *Bioorg. Med. Chem. Lett.* **14**, 251–256 (2004).
27. H. K. Ganguly, G. Basu, *Biophys. Rev.* **12**, 25–39 (2020).
28. P. Bazzini, C. G. Wermuth, in *The Practice of Medicinal Chemistry*, C. G. Wermuth, D. Aldous, P. Raboisson, D. Rognan, Eds. (Academic Press, ed. 4, 2015), pp. 319–357.
29. Y. C. Martin, *J. Med. Chem.* **48**, 3164–3170 (2005).
30. S.-H. Sun *et al.*, *Cell Host Microbe* **28**, 124–133.e4 (2020).

ACKNOWLEDGMENTS

We thank S. Huang (Department of Biochemistry and Molecular Biology, Louisiana State University Health Sciences Center) for careful proofreading; H.-Y. Zheng, X.-Y. He, and W.-W. Huang (Key Laboratory of Animal Models and Human Disease Mechanisms of the Chinese Academy of Sciences, Kunming Institute of Zoology) for their assistance in animal experiments; and the staff of Shanghai Synchrotron Radiation Facility beamline BL19U1 and J. Hakanpää of PETRA III beamline P11 (Hamburg, Germany). **Funding:** Supported by the fast-track research fund on COVID-19 of Sichuan Province (2020YFS0006, 2020YFS0010), the fast-track grants of SARS-CoV-2 research from West China Hospital, Sichuan University (HX-2019-nCoV-053, HX-2019-nCoV-039), the National Natural Science Foundation of China (81930125 and 00402354A1028), 1.3.5 project for disciplines of excellence, West China Hospital, Sichuan University, the Fundamental Research Funds for the Central Universities (20822041D4060), and the National Key R&D Program of China (2020YFC0842000 to Y.-T.Z.). **Author contributions:** S.Y., J.L., and Y.-T.Z. conceived and supervised the research and designed the experiments; S.Y., Y.-F.W., Y.-S.L., and J.L. performed the drug design; Y.-S.L., C.H., J.Zh., B.Q., C.S., X.M., Xin.L., R.-C.Y., Xiao. L., J.Y., and S.Y. performed chemical syntheses, separation, purification, and structural characterizations; J.L., R.Z., and J.Q. performed gene expression and protein purification, crystallization, and diffraction data collection with the assistance of K.W. and X.N.; J.L., R.Z., and S.Y. determined and analyzed the crystal structures; J.Q., Y.Z., R.Y., W.-P.L., J.-M.L., P.C., Y.L., and G.-F.L. performed enzymatic inhibition assays, DSF assays, and cellular cytotoxicity assays; R.-H.L. and F.-L.L. performed cellular antiviral assays and in vivo antiviral studies with the assistance of L.X., Z.-L.D., Q.-C.Z., H.-L.Z., W.Q., Y.-H.-P.L., and M.-H.L.; W.S., W.Y., and J.Q. performed in vivo toxicity studies; L.L., Y.H., G.-W.L., W.-M.L., and Y.-Q.W. analyzed and discussed the data with the assistance of X.Y. and J.Z.; and S.Y., J.L., and Y.-T.Z. wrote the manuscript with the assistance of J.Q., Y.-F.W., Y.-S.L., and L.L. **Competing interests:** Sichuan University has applied for PCT and Chinese patents covering MI-09 and MI-30 as well as related compounds with a bicycloproline structure in P2 position. **Data and materials availability:** The coordinates and structure factors of SARS-CoV-2 M^{pro} in complex with MI-23, boceprevir, and telaprevir have been deposited into PDB with accession numbers 7D3I, 7COM, and 7C7P, respectively.

SUPPLEMENTARY MATERIALS

science.sciencemag.org/content/371/6536/1374/suppl/DC1
Figs. S1 to S5
Tables S1 to S7
Materials and Methods
Supplementary Text
References (*31*–*41*)
MDAR Reproducibility Checklist

8 October 2020; accepted 12 February 2021
Published online 18 February 2021
10.1126/science.abf1611

CORONAVIRUS

Intranasal fusion inhibitory lipopeptide prevents direct-contact SARS-CoV-2 transmission in ferrets

Rory D. de Vries[1]*, Katharina S. Schmitz[1]*, Francesca T. Bovier[2,3,4]*, Camilla Predella[2,5], Jonathan Khao[6], Danny Noack[1], Bart L. Haagmans[1], Sander Herfst[1], Kyle N. Stearns[2,3,7], Jennifer Drew-Bear[2,3], Sudipta Biswas[8], Barry Rockx[1], Gaël McGill[6,9], N. Valerio Dorrello[2], Samuel H. Gellman[10], Christopher A. Alabi[8]†, Rik L. de Swart[1]†, Anne Moscona[2,3,7,11]†, Matteo Porotto[2,3,4]†

Containment of the COVID-19 pandemic requires reducing viral transmission. Severe acute respiratory syndrome coronavirus 2 (SARS-CoV-2) infection is initiated by membrane fusion between the viral and host cell membranes, which is mediated by the viral spike protein. We have designed lipopeptide fusion inhibitors that block this critical first step of infection and, on the basis of in vitro efficacy and in vivo biodistribution, selected a dimeric form for evaluation in an animal model. Daily intranasal administration to ferrets completely prevented SARS-CoV-2 direct-contact transmission during 24-hour cohousing with infected animals, under stringent conditions that resulted in infection of 100% of untreated animals. These lipopeptides are highly stable and thus may readily translate into safe and effective intranasal prophylaxis to reduce transmission of SARS-CoV-2.

Infection by severe acute respiratory syndrome coronavirus 2 (SARS-CoV-2) requires membrane fusion between the viral envelope and the host cell, at either the cell surface or the endosomal membrane. The fusion process is mediated by the viral transmembrane spike glycoprotein (S). Upon viral attachment or uptake, host factors trigger large-scale conformational rearrangements in S, including a refolding step that leads directly to membrane fusion and viral entry (*1*–*3*). Peptides corresponding to the highly conserved heptad repeat (HR) (Fig. 1A) domain at the C terminus of the S protein (HRC peptides) (Fig. 1B) can prevent this refolding and inhibit fusion, thereby preventing infection (*4*–*8*). The HRC peptides form six-helix bundle-like assemblies with the extended intermediate form of the S protein trimer, disrupting the structural rearrangement of S that drives membrane fusion (*4*) (see also movie S1).

Our approach in designing SARS-CoV-2 S-specific fusion inhibitors builds on our previous work that demonstrated that lipid conjugation of HRC-derived inhibitory peptides markedly increases antiviral potency and in vivo half-life (*9*, *10*). These peptides successfully inhibit human parainfluenza virus type 3 (HPIV-3), measles virus, influenza virus, and Nipah virus infection (*9*, *11*–*13*). Furthermore, the combination of dimerization and lipopeptide integration into cell membranes protects the respiratory tract and prevents systemic lipopeptide dissemination (*14*). Lipid-conjugated peptides administered intranasally to animals reached high concentrations both in the upper and lower respiratory tract, and the lipid could be designed to modulate the extent of transit from the lung to the blood and organs (*9*, *14*). We propose a SARS-CoV-2–specific lipopeptide as a candidate antiviral for preexposure and early postexposure prophylaxis for SARS-CoV-2 transmission in humans.

We recently described a monomeric SARS-CoV-2 HRC-lipopeptide fusion inhibitor (*4*) against SARS-CoV-2 with in vitro and ex vivo efficacy superior to previously described HRC-derived fusion inhibitory peptides (*6*, *7*). To further improve antiviral potency, we compared monomeric and dimeric HRC-peptide derivatives (Fig. 1C). Figure 1D shows antiviral potency in a quantitative cell–cell fusion assay of four monomeric and two dimeric SARS-CoV-2 S-derived 36–amino acid HRC peptides (Fig. 1B; see also figs. S1A and S3 for structure and characterization), with or without appended cholesterol. Dimerization increased the peptide potency for both nonlipidated peptides and their lipidated counterparts (Fig. 1D). A dimeric cholesterol-conjugated lipopeptide based on the HPIV-3 F protein HRC domain, used as a negative control, did not inhibit fusion at any concentration tested (black line in Fig. 1D; see fig. S1, B and C, for additional negative controls). Among the monomeric lipopeptides, the peptide bearing 24 molecules of polyethylene glycol (PEG_{24}) was most potent. The dimeric cholesterol-conjugated peptide ($[SARS_{HRC}\text{-}PEG_4]_2$-chol; red line in Fig. 1D) was the most potent lipopeptide against SARS-CoV-2 among our panel. This peptide also robustly inhibited fusion mediated by the S proteins of several emerging SARS-CoV-2 variants [including D614G, the variant bearing the Asp^{614}→Gly mutation (*15*)], the recent variants of concern B.1.1.7 and B.1.351 (*16*, *17*), and the S protein of SARS-CoV and Middle East respiratory syndrome coronavirus (MERS-CoV) (Fig. 1E). Proposed anchoring of the dimeric lipopeptide in the host cell membrane and interactions with the viral S protein are shown in fig. S2 and movie S1. Collectively, these data suggest that the $[SARS_{HRC}\text{-}PEG_4]_2$-chol lipopeptide is equipped to combat an evolving pandemic.

For other enveloped respiratory viruses, we previously showed that both ex vivo and in vivo dimeric lipopeptides (administered intranasally) displayed increased retention in the respiratory tract compared with monomeric compounds (*14*). In this study, we compared local and systemic biodistribution of our most potent monomeric and dimeric lipopeptides ($SARS_{HRC}\text{-}PEG_{24}$-chol and $[SARS_{HRC}\text{-}PEG_4]_2$-chol) at 1, 8, and 24 hours after intranasal inoculation or subcutaneous injection in humanized K18 hACE2 mice (Fig. 2 and fig. S4). The two lipopeptides reached a similar lung concentration at 1 hour after intranasal administration (~1 to 2 μM). At 8 and 24 hours, the dimeric $[SARS_{HRC}\text{-}PEG_4]_2$-chol lipopeptide remained at high concentrations in the lung with minimal entry into the blood, but the monomeric peptide entered the circulation and the lung concentration decreased (Fig. 2A). The dimeric $[SARS_{HRC}\text{-}PEG_4]_2$-chol lipopeptide was distributed throughout the lung after intranasal administration (Fig. 2B). A cellular toxicity (MTT) assay in primary human airway epithelial cells showed minimal toxicity even after 6 days at the highest concentrations tested (<20% at 100 μM) and no toxicity at its 90% maximal inhibitory concentration (IC_{90}) (~35 nM) (fig. S5). The longer respiratory tract persistence of $[SARS_{HRC}\text{-}PEG_4]_2$-chol, in concert with its in vitro efficacy, led us to advance this dimeric lipopeptide.

[1]Department of Viroscience, Erasmus MC, Rotterdam, Netherlands. [2]Department of Pediatrics, Columbia University Vagelos College of Physicians and Surgeons, New York, NY, USA. [3]Center for Host–Pathogen Interaction, Columbia University Vagelos College of Physicians and Surgeons, New York, NY, USA. [4]Department of Experimental Medicine, University of Campania "Luigi Vanvitelli," Caserta, Italy. [5]Department of Biomedical Engineering, Politecnico di Milano, Milan, Italy. [6]Digizyme Inc., Brookline, MA, USA. [7]Department of Physiology and Cellular Biophysics, Columbia University Vagelos College of Physicians and Surgeons, New York, NY, USA. [8]Robert Frederick Smith School of Chemical and Biomolecular Engineering, Cornell University, Ithaca, NY, USA. [9]Center for Molecular and Cellular Dynamics, Department of Biological Chemistry and Molecular Pharmacology, Harvard Medical School, Boston, MA, USA. [10]Department of Chemistry, University of Wisconsin–Madison, Madison, WI, USA. [11]Department of Microbiology and Immunology, Columbia University Vagelos College of Physicians and Surgeons, New York, NY, USA.
*These authors contributed equally to this work.
†Corresponding author. Email: caa238@cornell.edu (C.A.A.); r.deswart@erasmusmc.nl (R.L.d.S.); am939@cumc.columbia.edu (A.M.); mp3509@cumc.columbia.edu (M.P.)

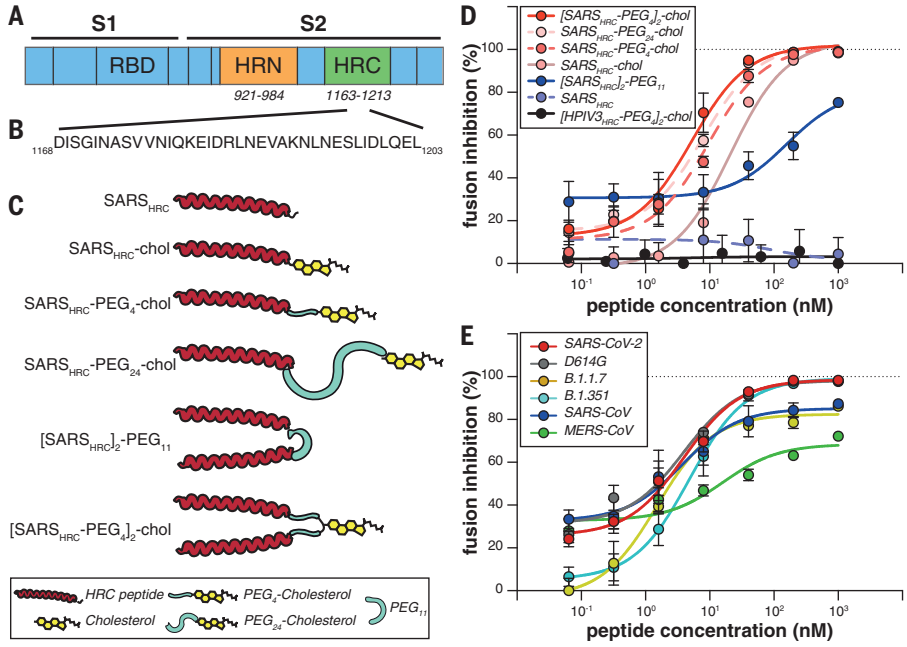

Fig. 1. Peptide-lipid conjugates that inhibit SARS-CoV-2 spike (S)–mediated fusion. (**A**) The functional domains of SARS-CoV-2 S protein, the receptor binding domain (RBD) and heptad repeats (HRN and HRC), are indicated. (**B**) Sequence of the peptides derived from the HRC domain of SARS-CoV-2 S. Single-letter abbreviations for the amino acid residues are as follows: A, Ala; C, Cys; D, Asp; E, Glu; F, Phe; G, Gly; H, His; I, Ile; K, Lys; L, Leu; M, Met; N, Asn; P, Pro; Q, Gln; R, Arg; S, Ser; T, Thr; V, Val; W, Trp; and Y, Tyr. (**C**) Monomeric and dimeric forms of lipid-tagged SARS-CoV-2 inhibitory peptides that were assessed in cell–cell fusion assays. (**D**) Cell–cell fusion assays with different inhibitory peptides. The percentage inhibition is shown for six different SARS-CoV-2–specific peptides and a control HPIV-3–specific peptide at increasing concentrations. Percent inhibition was calculated as the ratio of the relative luminescence units in the presence of a specific concentration of inhibitor (X) and the relative luminescence units in the absence of inhibitor, corrected for background luminescence. Percent inhibition = 100 × [1 − (luminescence at X − background)/(luminescence in absence of inhibitor − background)]. The difference between the results for $[SARS_{HRC}\text{-}PEG_4]_2$-chol and $SARS_{HRC}$-PEG_4-chol lipopeptides was statistically significant [two-way analysis of variance (ANOVA), $P < 0.0001$]. (**E**) Fusion inhibitory activity of $[SARS_{HRC}\text{-}PEG_4]_2$-chol peptide against emerging SARS-CoV-2 S variants, MERS-CoV-2 S, and SARS-CoV S. Data in (D) and (E) are means ± standard error of the mean (SEM) from three separate experiments, with the curve representing a four-parameter dose-response model.

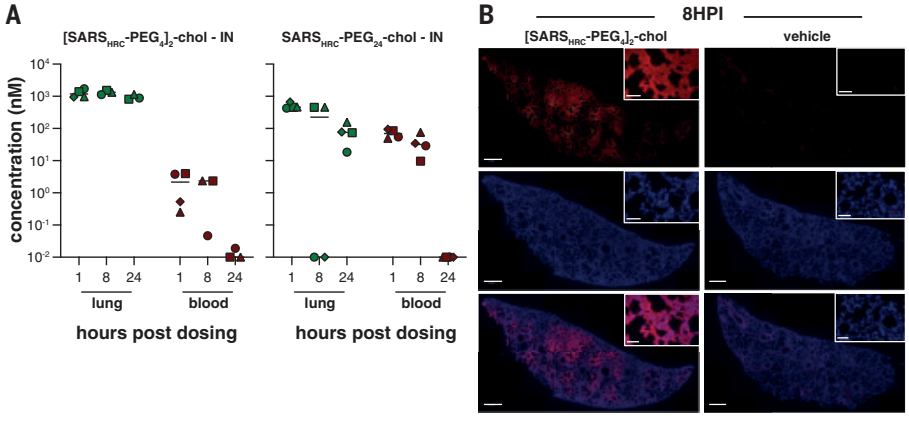

Fig. 2. Biodistribution of $[SARS_{HRC}\text{-}PEG_4]_2$-chol and $SARS_{HRC}$-PEG_{24} peptides after intranasal administration to mice. (**A**) The concentration of lipopeptides (*y* axis) was measured by ELISA in lung homogenates and plasma samples ($n = 4$ mice, with the exception of $[SARS_{HRC}\text{-}PEG_4]_2$-chol IN, for which $n = 3$ at 8 and 24 hours, and $n = 1$ for vehicle treatment). Median is indicated by horizontal bar. (**B**) Lung sections of $[SARS_{HRC}\text{-}PEG_4]_2$-chol-treated (or vehicle-treated) mice were stained with anti-SARS-HRC antibody (red) confirming broad distribution of $[SARS_{HRC}\text{-}PEG_4]_2$-chol in the lung (8 hours post inoculation, 8HPI). Scale bar, 500 μm in lung tile scan and 50 μm in magnification; representative images and a full tile scan are shown. Nuclei were counterstained with 4′,6-diamidino-2-phenylindole (blue).

The lead peptide, $[SARS_{HRC}\text{-}PEG_4]_2$-chol, was assessed for its ability to block entry of SARS-CoV-2 in VeroE6 cells or VeroE6 cells overexpressing transmembrane serine protease 2 (TMPRSS2), one of the host factors thought to facilitate viral entry at the cell membrane (*2*). Whereas viral fusion in VeroE6 cells predominantly occurs after endocytosis, the virus enters TMPRSS2-overexpressing cells by fusion at the cell surface, reflecting the entry route in airway cells (*18*). This difference is highlighted by chloroquine's effectiveness against SARS-CoV-2 infection in Vero cells but its failure in TMPRSS2-expressing Vero cells and the human lung (*19*). The $[SARS_{HRC}\text{-}PEG_4]_2$-chol peptide dissolved in an aqueous buffer containing 2% dimethyl sulfoxide (DMSO) inhibited virus entry after 8 hours with a half-maximal inhibitory concentration (IC_{50}) of ~300 nM in VeroE6 and ~5 nM in VeroE6-TMPRSS2 cells (Fig. 3A). To strengthen translational potential toward human use, the lipopeptide was reformulated in sucrose instead of DMSO, resulting in equivalent in vitro potency (Fig. 3B). A control dimeric fusion-inhibitory lipopeptide directed against HPIV-3 blocked infection by HPIV-3 but did not inhibit SARS-CoV-2 infection. The in vitro efficacy data are summarized in table S1.

Ferrets are an ideal model for assessing respiratory virus transmission, either by direct contact or by aerosol transmission (*20*, *21*). Mustelids are highly susceptible to infection with SARS-CoV-2, as also illustrated by frequent COVID-19 outbreaks at mink farms. Direct-contact transmission of SARS-CoV in ferrets was demonstrated in 2003 (*22*), and both direct-contact and airborne transmission of SARS-CoV-2 have been shown in ferrets (*20*, *23*). Direct-contact transmission in the ferret model is highly reproducible (100% transmission from donor to acceptor animals), but ferrets display limited clinical signs. After infection via direct inoculation or transmission, SARS-CoV-2 can readily be detected in and isolated from the throat and nose, and viral replication leads to seroconversion.

To assess the efficacy of $[SARS_{HRC}\text{-}PEG_4]_2$-chol in preventing SARS-CoV-2 transmission, naïve ferrets were dosed prophylactically with the lipopeptide before being cohoused with SARS-CoV-2–infected ferrets. In this setup, transmission via multiple routes can theoretically occur (aerosol, orofecal, and scratching or biting), and ferrets are continuously exposed to infectious virus during the period of cohousing, providing a stringent test for antiviral efficacy. The study design is shown in fig. S6. Three donor ferrets (gray in fig. S6) were inoculated intranasally with 5×10^5 50% tissue culture infective dose ($TCID_{50}$) SARS-CoV-2 on day 0. Twelve recipient ferrets

housed separately were treated by nose drops with a mock preparation or [$SARS_{HRC}$-PEG_4]$_2$-chol peptide (red and green, respectively, in fig. S6) 1 and 2 days post inoculation (dpi) of the donor animals. The [$SARS_{HRC}$-PEG_4]$_2$-chol peptides for intranasal administration were dissolved to a concentration of 6 mg/ml in an aqueous buffer containing 2% DMSO, and ferrets were administered a final dose of 2.7 mg/kg of body weight (450 µl, divided equally in both nostrils). Peptide stocks and working dilutions had similar IC_{50} values, confirming that peptide-treated ferrets were dosed daily with comparable amounts (fig. S7, A and B). Six hours after the second treatment on 2 dpi, one infected donor ferret [highly positive for SARS-CoV-2, as indicated by reverse transcription–quantitative polymerase chain reaction (RT-qPCR)] was cohoused with four naïve recipient ferrets (two mock-treated and two peptide-treated). After a 24-hour transmission period in three separate, negatively pressurized HEPA-filtered Animal Biosafety Level 3 (ABSL3)–isolator cages, cohousing was stopped and donor, mock-treated, and peptide-treated ferrets were rehoused as separate groups. Additional [$SARS_{HRC}$-PEG_4]$_2$-chol

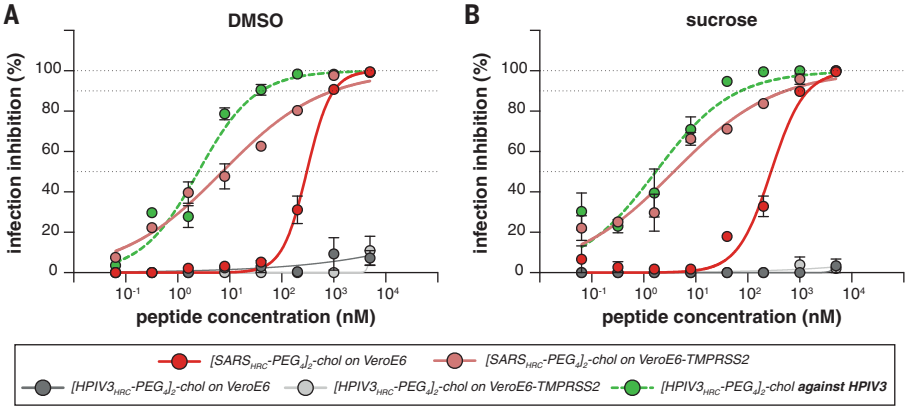

Fig. 3. Inhibition of infectious SARS-CoV-2 entry by [$SARS_{HRC}$-PEG_4]$_2$-chol and [HPIV-3_{HRC}-PEG_4]$_2$-chol peptides. (**A** and **B**) The percentage inhibition of infection is shown on VeroE6 and VeroE6-TMPRSS2 cells with increasing concentrations of [$SARS_{HRC}$-PEG_4]$_2$-chol (red lines) and [HPIV-3_{HRC}-PEG_4]$_2$-chol (gray lines). DMSO-formulated (A) and sucrose-formulated (B) stocks were tested side by side. Mean ± SEM of triplicates is shown; dotted lines show 50% and 90% inhibition. Additionally, the potency of [HPIV-3_{HRC}-PEG_4]$_2$-chol was confirmed by inhibition of infectious HPIV-3 entry (dotted green lines, performed on Vero cells).

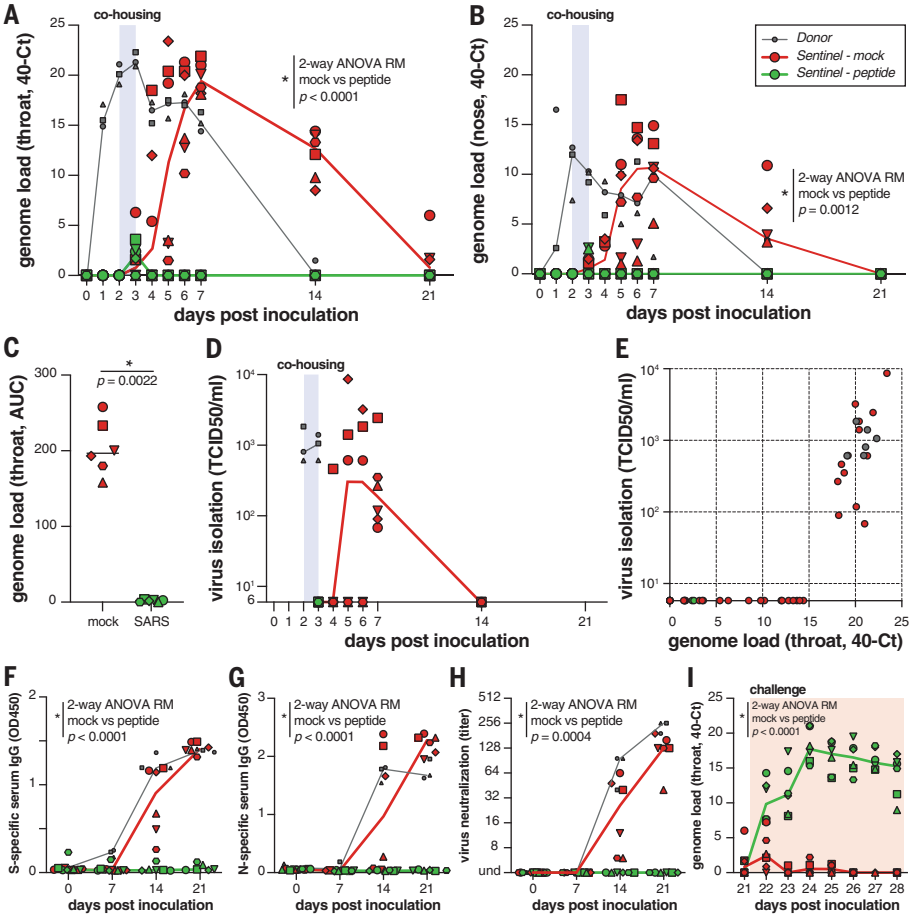

Fig. 4. [$SARS_{HRC}$-PEG_4]$_2$-chol prevents SARS-CoV-2 transmission in vivo. (**A** and **B**) Viral loads detected in throat (A) and nose (B) swabs by RT-qPCR. (**C**) Comparison of the AUC from genome loads reported in (B) for mock- and peptide-treated sentinels. (**D**) Viral loads detected in throat swabs by virus isolation on VeroE6. (**E**) Correlation between viral loads in the throat as detected via RT-qPCR and virus isolation. Presence of anti-S (**F**) or anti-N (**G**) antibodies was determined by IgG ELISA assay. Presence of neutralizing antibodies was determined in a virus neutralization assay (**H**). Virus neutralizing antibodies are displayed as the end-point serum dilution factor that blocks SARS-CoV-2 replication. Direct inoculation of peptide-treated or mock-treated animals with SARS-CoV-2 led to productive infection in only the previously peptide-treated animals (**I**), in the absence of S-specific, N-specific, and neutralizing antibodies. Donor animals shown in gray, mock-treated animals in red, peptide-treated animals in green. Symbols correspond to individual animals (defined in fig. S6). Line graphs in (A), (B), (D), and (F) to (I) connect the median of individual animals per time point. Mock- and peptide-treated groups were compared using two-way ANOVA repeated measures [(A), (B), and (F) to (I)] or Mann-Whitney test (C).

peptide treatments were given to recipient animals on 3 and 4 dpi.

The viral loads (detection of viral genomes using RT-qPCR) for directly inoculated donor animals (gray), mock-treated recipient animals (red), and lipopeptide-treated recipient animals (green) are shown in Fig. 4, A and B. All directly inoculated donor ferrets were productively infected, as shown by SARS-CoV-2 genome detection in throat and nose swabs, and efficiently and reproducibly transmitted the virus to all mock-treated acceptor ferrets (Fig. 4, A and B, red curves). Productive SARS-CoV-2 infection was not detected in the throat or nose of any of the peptide-treated recipient animals (Fig. 4, A and B, green curves). A slight rise in viral loads in samples collected at 3 dpi was detected (at the end of the cohousing), confirming that peptide-treated animals were exposed to SARS-CoV-2. In Fig. 4C, the area under the curve (AUC) shows the notable difference between the mock-treated and the peptide-treated animals. No infectious virus was isolated from lipopeptide-treated ferrets, whereas infectious virus was detected in all mock-treated ferrets (Fig. 4D). Virus isolation data correlated with genome detection (Fig. 4E).

Seroconversion occurred in donor ferrets and six of six mock-treated animals by 21 dpi but occurred in none of the peptide-treated recipient animals, as shown by S- and nucleocapsid (N)–specific immunoglobulin G (IgG) enzyme-linked immunosorbent assay (ELISA) and virus neutralization (Fig. 4, F to H). Successful challenge infection confirmed that in-host virus replication had been completely blocked by the $[SARS_{HRC}\text{-}PEG_4]_2$-chol treatment (Fig. 4I and fig. S8) and that none of the peptide-treated animals were protected, whereas the mock-treated animals (which had seroconverted) were all protected. Collectively, these data show that intranasal prophylactic administration of the $[SARS_{HRC}\text{-}PEG_4]_2$-chol peptide had protected six of six ferrets from transmission and productive infection.

In light of the persistence of the dimeric lipopeptide in the murine lung (Fig. 2 and fig. S4), we assessed the potential for a single administration of sucrose-formulated lipopeptide in a ferret transmission experiment 2 hours before cohousing to prevent or delay infection. In this experiment, we used a dimeric HPIV-3–specific lipopeptide as a mock control (fig. S9). Although sucrose formulation had resulted in promising results in vitro at small scale (Fig. 3B), formulation at larger scale resulted in incomplete dissolution. As a consequence, the sucrose-formulated $[SARS_{HRC}\text{-}PEG_4]_2$-chol lipopeptide was administered at a substantially lower concentration than in the experiment with the DMSO-formulated lipopeptide (fig. S7, C and D). Nevertheless, the SARS-CoV-2 lipopeptide provided a significant level of protection as compared with the HPIV-3 control group, and four of six SARS-CoV-2 lipopeptide-treated animals were protected against infection. This experiment suggests that single-administration preexposure prophylaxis is promising, although the optimal formulation and dosing regimen are an area of ongoing experimentation.

The intranasal $[SARS_{HRC}\text{-}PEG_4]_2$-chol peptide presented in this study is a successful prophylaxis that prevents SARS-CoV-2 transmission in a relevant animal model, providing complete protection during a 24-hour period of intense direct contact. Parallel approaches to prevent transmission that target the interaction between S and angiotensin-converting enzyme 2 have shown promise in vitro [e.g., the "miniprotein" approach (*24*)]. The lipopeptide described here acts on the S2 domain after shedding of S1 (fig. S2 and movie S1) and is complementary to strategies that target the functions of S1 or maintain S in its prefusion conformation, e.g., synthetic nanobodies (*25*). Fusion-inhibitory lipopeptides could be used for pre- and postexposure prophylaxis in combination with these strategies and in conjunction with treatments [e.g., ribonucleoside analogs (*26*)] that reduce replication in a treated infected individual. A combination of drugs that target different aspects of the viral life cycle is likely ideal for this rapidly evolving virus. Of note, the $[SARS_{HRC}\text{-}PEG_4]_2$-chol lipopeptide is equally active against several emerging SARS-CoV-2 variants, including D614G as well as the recent variants of concerns B.1.1.7 and B.1.351. The $[SARS_{HRC}\text{-}PEG_4]_2$-chol peptide has a long shelf life, does not require refrigeration, and can easily be administered, making it particularly suited to treating hard-to-reach populations. This is key in the context of COVID-19, which has affected every community, with the burden falling disproportionately on low-income and otherwise marginalized communities. This HRC lipopeptide fusion inhibitor is feasible for advancement to human use and should readily translate into a safe and effective nasal spray or inhalation-administered fusion inhibitor for SARS-CoV-2 prophylaxis, supporting containment of the ongoing COVID-19 pandemic.

REFERENCES AND NOTES

1. F. Li, *Annu. Rev. Virol.* **3**, 237–261 (2016).
2. M. Hoffmann *et al.*, *Cell* **181**, 271–280.e8 (2020).
3. Y. Wan, J. Shang, R. Graham, R. S. Baric, F. Li, *J. Virol.* **94**, e00127-20 (2020).
4. V. K. Outlaw *et al.*, *mBio* **11**, e01935-20 (2020).
5. S. Xia *et al.*, *Sci. Adv.* **5**, eaav4580 (2019).
6. S. Xia *et al.*, *Cell Res.* **30**, 343–355 (2020).
7. Y. Zhu, D. Yu, H. Yan, H. Chong, Y. He, *J. Virol.* **94**, e00635-20 (2020).
8. X. Wang *et al.*, *Int. J. Mol. Sci.* **21**, 3843 (2020).
9. M. Porotto *et al.*, *PLOS Pathog.* **6**, e1001168 (2010).
10. A. Pessi *et al.*, *PLOS ONE* **7**, e36833 (2012).
11. T. N. Figueira *et al.*, *ACS Nano* **12**, 9855–9865 (2018).
12. T. N. Figueira *et al.*, *Bioconjug. Chem.* **29**, 3362–3376 (2018).
13. C. Mathieu *et al.*, *Sci. Rep.* **7**, 43610 (2017).
14. T. N. Figueira *et al.*, *J. Virol.* **91**, e01554-16 (2016).
15. L. Zhang *et al.*, *Nat. Commun.* **11**, 6013 (2020).
16. A. Muik *et al.*, *Science* **371**, 1152–1153 (2021).
17. K. Wu *et al.*, bioRxiv 2021.01.25.427948 [Preprint]. 25 January 2021. https://doi.org/10.1101/2021.01.25.427948.
18. A. Z. Mykytyn *et al.*, *eLife* **10**, e64508 (2021).
19. M. Hoffmann *et al.*, *Nature* **585**, 588–590 (2020).
20. M. Richard *et al.*, *Nat. Commun.* **11**, 3496 (2020).
21. V. J. Munster *et al.*, *Science* **325**, 481–483 (2009).
22. B. E. Martina *et al.*, *Nature* **425**, 915 (2003).
23. Y. I. Kim *et al.*, *Cell Host Microbe* **27**, 704–709.e2 (2020).
24. L. Cao *et al.*, *Science* **370**, 426–431 (2020).
25. M. Schoof *et al.*, *Science* **370**, 1473–1479 (2020).
26. R. M. Cox, J. D. Wolf, R. K. Plemper, *Nat. Microbiol.* **6**, 11–18 (2021).

ACKNOWLEDGMENTS

We thank J. S. Orange, S. G. Kernie, M. Lamers, E. Verveer, A. Mykytyn, and M. Koopmans for their contributions to this study. **Funding:** This work was supported by funding from the National Institutes of Health (AI146980, AI121349, and NS091263 to M.P.; AI114736 to A.M.; and HHSN272201400008C to S.H.), the Sharon Golub Fund at Columbia University Irving Medical Center (CUIMC), the Children's Health Innovation Nucleation Fund of the Pediatrics Department at CUIMC, and a Harrington Discovery Institute COVID-19 Award to A.M. A.M. is the inaugural Sherie L. Morrison Professor of Immunology. **Author contributions:** Conceptualization: R.D.d.V., S.H.G., C.A.A., R.L.d.S., A.M., and M.P. Formal analysis: R.D.d.V., K.S.S., F.T.B., C.P., N.V.D., C.A.A., R.L.d.S., A.M., and M.P. Funding acquisition: B.L.H., R.L.d.S., A.M., and M.P. Investigation: R.D.d.V., K.S.S., F.T.B., C.P., J.K., D.N., K.N.S., S.H., J.D.-B., S.B., G.M., N.V.D., S.H.G., C.A.A., R.L.d.S., A.M., and M.P. Resources: B.L.H., B.R., N.V.D., C.A.A., R.L.d.S., A.M., and M.P. Supervision: R.L.d.S., N.V.D., C.A.A., A.M., and M.P. Visualization: R.D.d.V., K.S.S., F.T.B., J.K., G.M., N.V.D., S.H.G., C.A.A., A.M., and M.P. Writing – original draft: R.D.d.V., R.L.d.S., A.M., and M.P. Writing – final version: All coauthors provided feedback on the final draft. **Competing interests:** R.D.d.V., F.T.B., R.L.d.S., A.M., and M.P. are listed as inventors of $[SARS_{HRC}\text{-}PEG_4]_2$-chol on a provisional patent application covering findings reported in this manuscript. **Data and materials availability:** All data are available in the manuscript or the supplementary materials. Materials are available by MTA with the Trustees of Columbia University, NYC. Reagents are available from the corresponding authors under a material agreement with Columbia University.

SUPPLEMENTARY MATERIALS

science.sciencemag.org/content/371/6536/1379/suppl/DC1
Materials and Methods
Figs. S1 to S10
Table S1
References (*27*–*33*)
MDAR Reproducibility Checklist
Movie S1

29 October 2020; resubmitted 4 January 2021
Accepted 9 February 2021
Published online 17 February 2021
10.1126/science.abf4896

IMMUNOLOGY

The molecular assembly of the marsupial γμ T cell receptor defines a third T cell lineage

Kimberly A. Morrissey[1]*, Marcin Wegrecki[2]*, T. Praveena[2,3], Victoria L. Hansen[1], Lijing Bu[1], Komagal Kannan Sivaraman[2], Samuel Darko[4], Daniel C. Douek[4], Jamie Rossjohn[2,3,5]†‡, Robert D. Miller[1]†‡, Jérôme Le Nours[2,3]†‡

αβ and γδ T cell receptors (TCRs) are highly diverse antigen receptors that define two evolutionarily conserved T cell lineages. We describe a population of γμTCRs found exclusively in non-eutherian mammals that consist of a two-domain (Vγ-Cγ) γ-chain paired to a three-domain (Vμ-Vμj-Cμ) μ-chain. γμTCRs were characterized by restricted diversity in the Vγ and Vμj domains and a highly diverse unpaired Vμ domain. Crystal structures of two distinct γμTCRs revealed the structural basis of the association of the γμTCR heterodimer. The Vμ domain shared the characteristics of a single-domain antibody within which the hypervariable CDR3μ loop suggests a major antigen recognition determinant. We define here the molecular basis underpinning the assembly of a third TCR lineage, the γμTCR.

In jawed vertebrates, two main T cell lineages, αβ and γδ (*1*–*4*), are defined by the expression of αβ T cell receptor (TCR) and γδTCR heterodimers, respectively. Each chain contains two extracellular domains, a variable (V) and a constant (C) domain. More recently, TCRs predicted to have distinctly different architecture from αβTCRs and γδTCRs, such as TCRμ in marsupials and monotremes, have been described (*5*, *6*) (Fig. 1A). TCRμ has an atypical genomic organization predicted to encode a protein structure containing three extracellular domains (Vμ-Vμj-Cμ) (*5*). Because of the lack of any other candidate new TCR chain within the opossum genome and because of its ancestral relationship with TCRδ, we hypothesized that TCRμ would pair with TCRγ (*7*, *8*).

To establish what paired with the TCRμ chain, a single-cell transcriptome RNA-sequencing dataset was generated using the gray short-tailed opossum (*Monodelphis domestica*). Among peripheral blood mononuclear cells, 94% were αβ T cells, 6% were γδ T cells, and there were no γμ T cells (table S1). By contrast, among splenocytes, 57% were αβ T cells, 37% were γμ T cells, and 6% were γδ T cells (table S1). In splenocytes, functional TCRμ transcripts were only found in T cells containing functional TCRγ transcripts (tables S2 and S3). Phenotypic analysis of γμ T cell transcriptomes revealed that all were $CD4^-$, with the majority (75.5%) characterized as $CD8\alpha\alpha^+$ and the remainder mostly double-negative ($CD4^-CD8^-$) (table S1).

There are eight gene clusters encoding TCRμ in the opossum genome, of which six are complete and composed of the Vμ, Dμ, Jμ, Vμj, and Cμ gene segments (*7*). Vμj is a germline-encoded V gene. Among the splenic γμ T cells, only three clusters were used, with the majority being cluster 5 (57%) (fig. S1). The opossum TCRγ locus contains nine Vγ segments, seven Jγ segments, and one Cγ gene segment (*7*). Analysis of opossum γμ and γδ T cells revealed little overlap in the Vγ gene segments used by these T cell populations (Fig. 1, B to D). Similarly, there were differences in the Vγ-Jγ combinations between γμ and γδ T cells (fig. S2).

The complementarity-determining region 3 (CDR3γ) generated by Vγ2Jγ3 recombinants used in γμTCRs was markedly conserved (Fig. 1D). This is likely due to recurrent recombination events among γμ T cells driven in part by microhomology between the Vγ2 and Jγ3 gene segments (fig. S3). The Vγ2 and Jγ3 gene segments contained a short stretch of identical nucleotides at their 3′ and 5′ ends, respectively, which facilitates recombination (*9*). This may account for the limited junctional diversity in 45% of the Vγ2Jγ3 recombinants (fig. S3). Although 32% of the Vγ2Jγ3 recombinants did not use microhomology in recombination, they still encoded a restricted CDR3 length of seven residues (fig. S3). γμ T cells that did not use Vγ2 had CDR3μ loops of comparable length to those using Vγ2, although with greater sequence variation (Fig. 1, D and E, and table S4). Generally, the Vμ domain had a longer and more variable CDR3 than that of Vγ (Fig. 1 and table S4). Vμ was encoded by an exon generated by recombination of the Vμ, Dμ, and Jμ segments, which could include a variable number of Dμ segments. Indeed, 53% of CDR3μ loops were encoded by three D segments (fig. S5 and table S5). This, combined with an average of 11 P/N nucleotides, resulted in a CDR3μ loop with a mean length of 19 residues. The CDR3μ loop was longer than the CDR3δ in γδTCRs, as well as the unpaired single V domain CDR3 found in camelid heavy-chain-only (VHH), shark immunoglobulin (Ig) new antigen receptor (NAR) antibodies, and shark NAR-TCR (*10*) (table S4). Thus, CDR3μ loops are longer than typical TCR and single V domain CDR3 loops.

Recombinant expression and subsequent purification of two distinct γμTCRs, Spl_145 and Spl_157, revealed the exclusive formation of the γμTCR heterodimer (fig. S6). We then determined the crystal structures of both of these γμTCRs (Fig. 2, A and B, and table S6). Similar to the antigen (Ag)–binding fragments of antibodies (Fabs), αβTCRs, and γδTCRs (Fig. 2, C and D), the two γμTCR structures revealed that the Vμj-Cμ domains paired with the Vγ-Cγ domains, whereas the unpaired N-terminal Vμ domain was positioned translationally across the top of the Vμj and Vγ domains (Fig. 2, A and B). Thus, γμTCRs adopt an asymmetrical topology that is dissimilar to the symmetrical architectures of Fabs, αβTCRs, and γδTCRs.

Vμ and Vμj had greater sequence similarity to antibody V domains than to conventional TCR V domains (*5*). The Vμj and Vμ domains also harbored a V-set Ig-like β-sandwich fold (Fig. 2, E and G) and were more structurally similar to single-chain antibodies (nanobodies) and antibody Fab fragments heavy chain (VH) (Fig. 2, F and H) than to the variable Vδ domains of γδTCRs (fig. S7, A to C). The Cμ domain (Fig. 2I) exhibited the classical C-set Ig-like fold adopted by the constant domain of γδTCRs and αβTCRs (Fig. 2J) (*11*). The Cγ and Vγ domains adopted highly the similar overall architecture of the human Cγ and Vγ domains of γδTCRs (fig. S7, D to F).

Upon γμTCR heterodimer formation, the total buried surface area (BSA) at the Vμj-Cμ–Vγ-Cγ interface of the both γμTCRs was ~3500 $Å^2$ (figs. S8 and S9 and tables S7 and S8). The γμTCRs and γδTCRs shared highly similar Vμj-Cμ and Vγ-Cγ interdomain juxtapositions with the Vγ-Cγ and Vδ-Cδ of γδTCRs, respectively (fig. S9, M and N). At the Vμj-Vγ2 interface of the Spl_145 γμTCR, the highly conserved and short CDR3γ loop (Fig. 1D) contributed to ~35% of the BSA of the Vγ domain interface and made a series of contacts with the Vμj domain (Fig. 3A, i, v, and vi, and table S7). The CDR3γ loop also interacted closely with the conserved CDR3μj loop (Fig. 3A) and contributed to ~35% of the BSA of the Vμj domain. Moreover, the CDR3μj loop mediated additional contacts with the CDR1γ loop (Fig. 3A, iv) and Vγ framework (FW) residues (Fig. 3A, vii). Thus, the CDR1γ and CDR3γ loops

[1]Department of Biology, Center for Evolutionary and Theoretical Immunology, University of New Mexico, Albuquerque, NM, USA. [2]Infection and Immunity Program and Department of Biochemistry and Molecular Biology, Biomedicine Discovery Institute, Monash University, Clayton, Victoria, Australia. [3]Australian Research Council Centre of Excellence in Advanced Molecular Imaging, Monash University, Clayton, Victoria, Australia. [4]Human Immunology Section, Vaccine Research Center, National Institute of Allergy and Infectious Diseases, National Institutes of Health, Bethesda, MD, USA. [5]Institute of Infection and Immunity, Cardiff University School of Medicine, Heath Park, Cardiff, UK.

*These authors contributed equally to this work.

†These authors contributed equally to this work and are co-senior authors.

‡Corresponding author. Email: jamie.rossjohn@monash.edu (J.R.); rdmiller@unm.edu (R.D.M.); Jerome.lenours@monash.edu (J.L.N.)

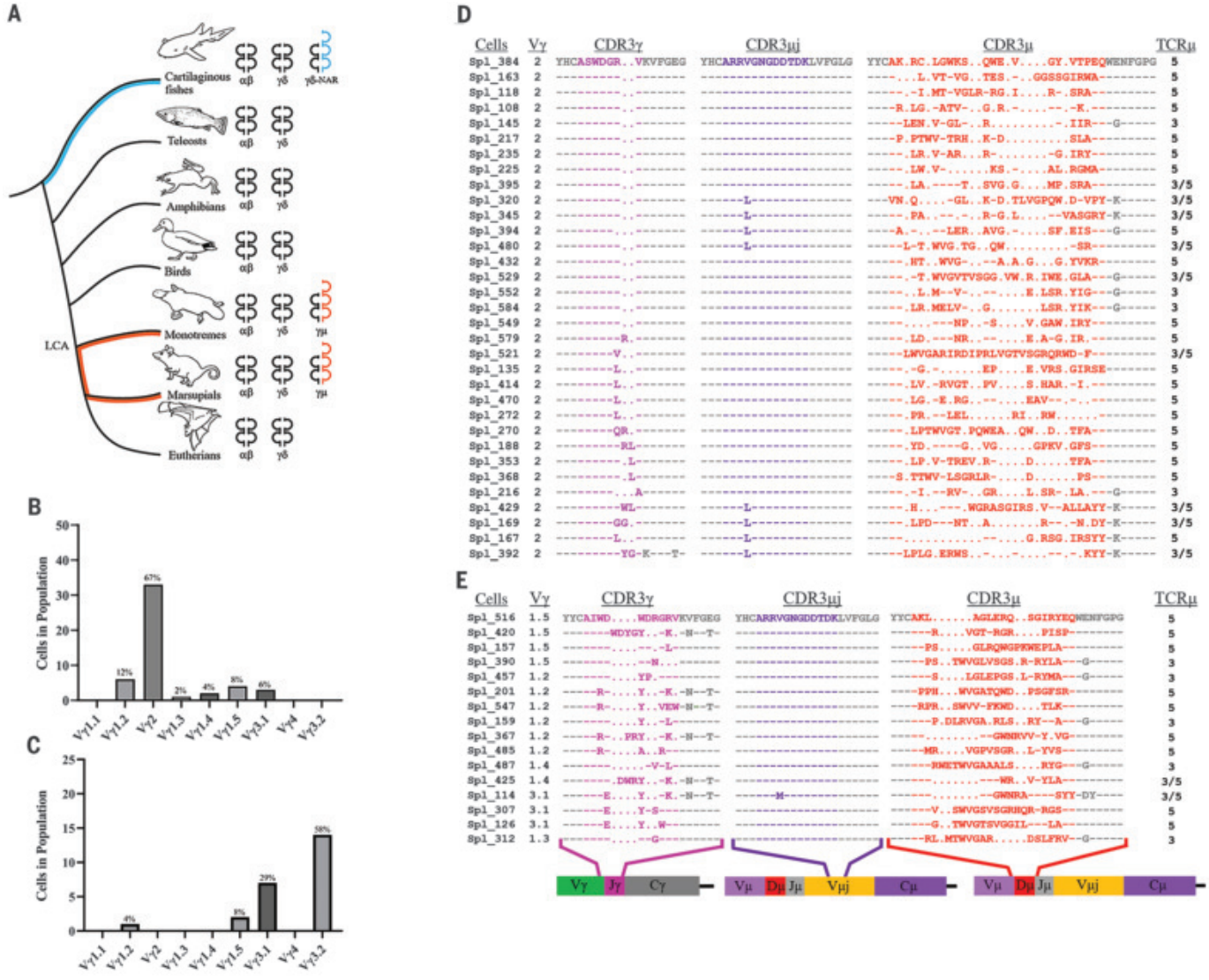

Fig. 1. γμTCR lineage and sequences. (**A**) Phylogenetic tree depicting the NAR-TCRδ in blue and the TCRμ lineage in orange. (**B** and **C**) Vγ usage within splenic γμ T cells (spleen only) (B) and γδ T cells (spleen and peripheral blood) (C). The Vγs on the *x*-axes are ordered as found in the germline genomic TCRγ locus (*7*). Percentages of each cell population are indicated above each bar. (**D**) Amino acid alignment of CDR3s from the 33 γμTCRs that were Vγ2^{+}: CDR3γ, magenta; CDR3μj, purple; and CDR3μ, red. (**E**) Amino acid alignment of CDR3 from all γμTCRs that are Vγ2^{-}: CDR3γ, magenta; CDR3μj, purple; and CDR3μ, red. The alignments in (D) and (E) include the proximal cysteine and terminal phenylalanines that define the border of the CDR3 region. Sequences flanking the CDR3 are depicted in gray. Dashes represent sequence identity and dots represent gaps in the alignment. The Vγ and TCRμ clusters used in each cell are indicated. Diagrams of regions of the transcripts presented in the alignments are shown at the bottom.

play a major structural role in mediating contacts with the Vμj domain. Because of their location within the γμTCR heterodimer, the Vμj domain CDR loops are unlikely to represent an Ag-recognition determinant.

Although the Spl_157 and Spl_145 γμTCRs differ by their Vγ gene segment usage, they share a highly similar overall VμjCμ-VγCγ architecture, molecular footprints (Fig. 3), and conserved molecular interactions (figs. S8 to S10 and tables S7 and S8). Although their CDR3γ loops differed in length and sequence, a germline-encoded tryptophan and a glycine residue mediated highly conserved interactions with a triad of CDR3μj residues (Arg/Asp/Asp) (Figs. 3A, v and 3B, iv and fig. S10). However, the CDR3γ of the Spl_145 γμTCR that used the Vγ2 gene (Fig. 1A) made more extensive interactions with the FWμj residues (Fig. 3A, vi) relative to the Spl_157 γμTCR (Fig. 3B, v), which used a much less frequent Vγ1.5 (Fig. 1A). The germline Jγ3 encodes the Arg103γ in clones using this gene segment and, given the preferential pairing of Vγ2-Jγ3 in γμ T cells, this may have contributed to the biased use of Vγ2 in γμTCRs.

Both γμTCR structures contained two molecules in the asymmetric unit, where the Vμ domain of each molecule adopted distinct conformations (Fig. 4, A and B). Here, the Vμ-Vμj connecting residues Leu^{134} and Glu^{137} (in Spl_145 γμTCR) and Leu^{136} and Glu^{139} (in Spl_157 γμTCR) acted as a mechanical hinge (Fig. 4, A and B) (*12*). In the Spl_145 γμTCR, the Vμ overall positions differed from each other by an ~56° angle rotation and ~7-Å translation along a screw axis (*12*) (Fig. 4A). In the Spl_157 γμTCR, this movement involved a rotation of ~20° around the defined hinge axis (*12*) (Fig. 4B).

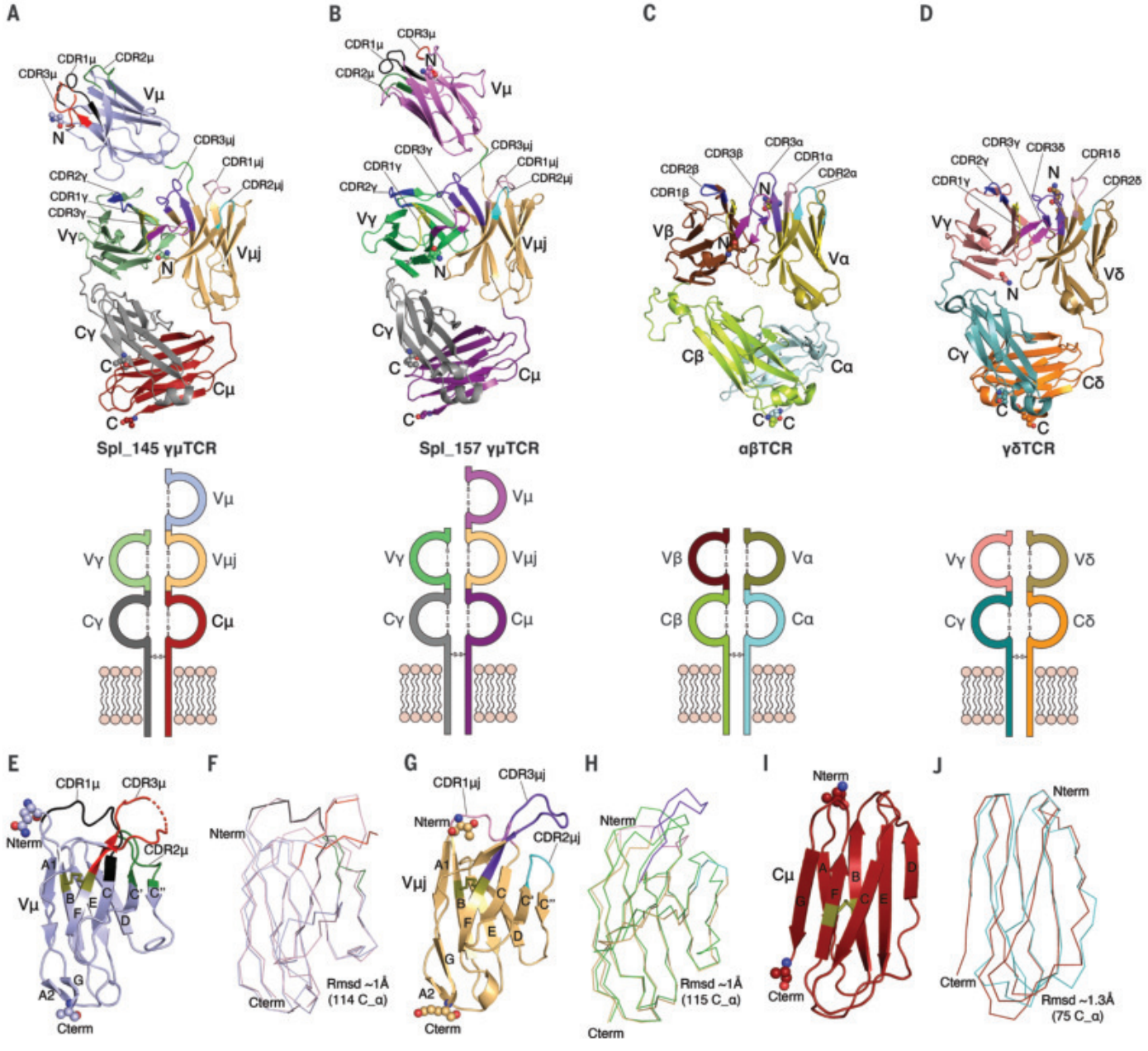

Fig. 2. Overview of γμTCR, αβTCR, and γδTCR crystal structures. Cartoon representation (top panels) and graphic version (bottom panels) of γμTCR, αβTCR, and γδTCR. (**A**) Spl_145 γμTCR: Vμ, light blue; Vμj, light orange; Cμ, brick red; Vγ, pale green; Cγ, gray; CDR3μ, red; and CDR3γ, magenta. (**B**) Spl_157 γμTCR: Vμ, violet; Vμj, light orange; Cμ, deep purple; Vγ, lime green; and Cγ, gray. (**C**) αβTCR (PDB code: 4WW1): Vα, olive; Cα, pale cyan; Vβ, brown; and Cβ, lemon-lime. (**D**) γδTCR (PDB code: 4LFH) (*11*): Vγ, salmon; Cγ, light teal; Vδ, sand; and Cδ, orange. The CDR loops are colored as follows: CDR1γ and CDR1β, yellow; CDR2γ and CDR2β, blue; CDR3γ and CDR3β, magenta; CDR1μj, CDR1δ, and CDR1α, light pink; CDR2μj, CDR2δ, and CDR2α, cyan; CDR3μj, CDR3δ, and CDR3α, purple; CDR1μ, black; CDR2μ, forest green; and CDR3μ, red. The hinge region connecting the Vμ and Vμj domains is shown in green. (**E**) Cartoon representation of the Vμ domain (Spl_145 γμTCR): Vμ, light blue; CDR1μ, black; CDR2μ, forest green; CDR3μ, red; and disulfide bond, olive green. (**F**) Superposition of the Cα backbone of the Spl_145 γμTCR Vμ domain (light blue) with VH of the monoclonal antibody (PDB code: 5GRJ). (**G**) Cartoon representation of the Vμj domain: Vμ, light orange; CDR1μj, light pink; CDR2μj, cyan; CDR3μj, purple; and disulfide bond, olive green. (**H**) Superposition of the Cα of the Vμj domain with a nanobody (PDB code: 6H6Y). (**I**) Cartoon representation of the Cμ domain: Cμ, brick red; disulfide bond, olive green. (**J**) Superposition of the Cα backbone of the Cμ domain with a human Cδ domain (PDB code: 4LFH).

Because the hinge region was conserved among all γμTCRs (fig. S11A), this Vμ domain flexibility may be generally applicable to all γμTCRs.

In canonical VH domains, residues at positions 42, 49, and 50 were occupied by hydrophobic residues that were involved in pairing with VL. However, as seen in the VHH folds of camelids (*13*, *14*), these corresponding three positions in the Vμ domain were occupied by polar residues (His44μ, Asn/Ser51μ, and Arg/Lys/Ser52μ), which increase the solubility of the monomeric Vμ domain (Fig. 4C). In the VH and VHH domains, the Ag-binding interface is formed by the CDR loops (*15*–*17*). In the γμTCRs, the corresponding CDR1μ and

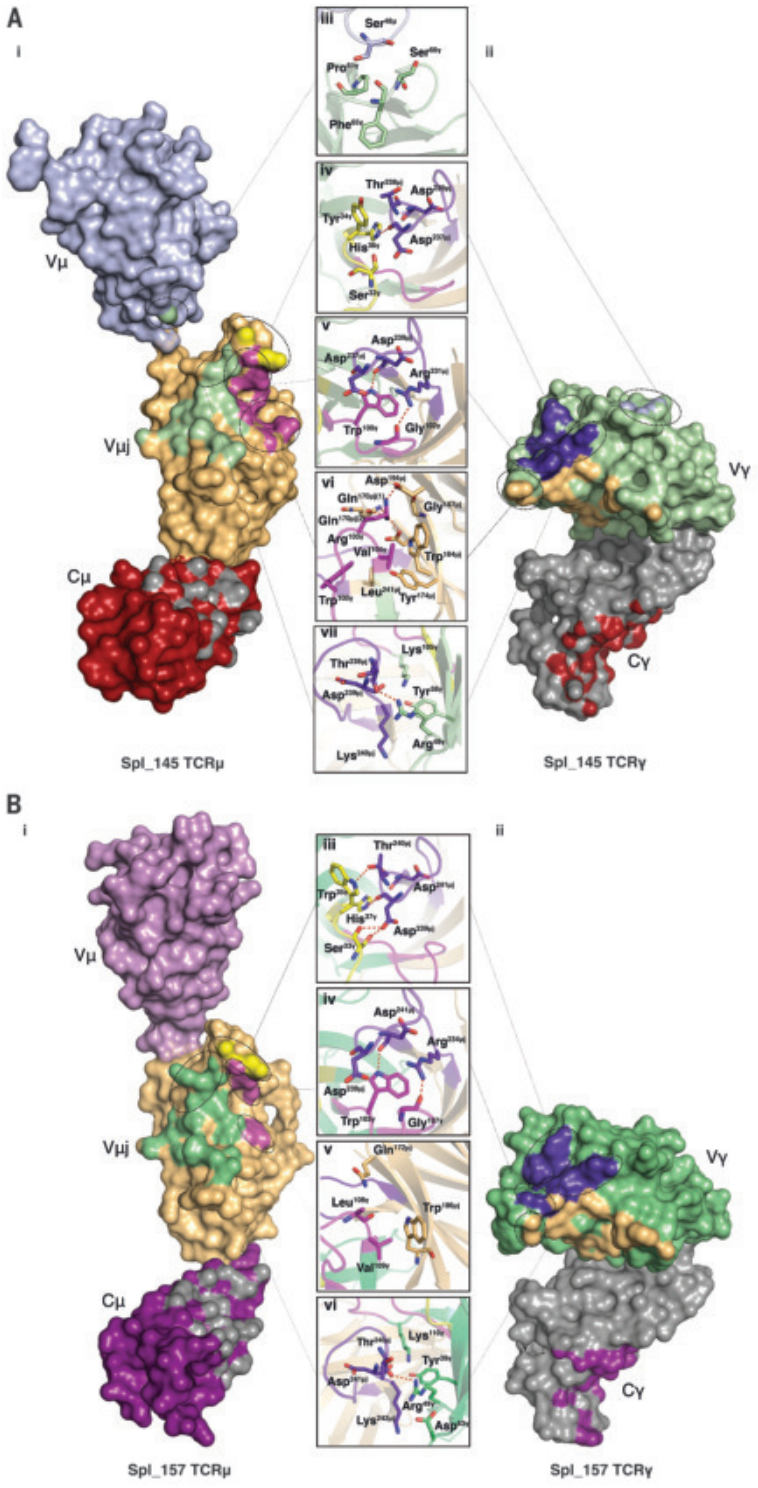

Fig. 3. γμTCR heterodimeric interactions. (**A**) Footprint of the Spl_145 TCRγ on the molecular surface of Spl_145 TCRμ: Vμ, light blue; Vμj, light orange; Cμ, brick red; CDR1γ, yellow; CDR3γ, magenta; Framework-Vγ (FWγ), pale green; and Framework-Cγ, gray (i). Footprint of the Spl_145 TCRμ on the molecular surface of Spl_145 TCRγ: Vγ, pale green; Cγ, gray; CDR3μj, purple; Framework-Vμj (FWμj), light orange; Framework-Vμ (FWμ), light blue; and Framework-Cμ, brick red (ii). Molecular interactions at the Spl_145 Vμ-Vμj/Vγ interface: FWμ (light blue) with FWγ (pale green) (iii); CDR3μj (purple) with CDR1γ (yellow) (iv); CDR3γ (magenta) with CDR3μj (purple) (v); CDR3γ (magenta) with FWμj residues (vi); and CDR3μj (purple) with FWγ residues (vii). For clarity, only the hydrogen bonds are shown as red dashed lines. (**B**) Footprint of the Spl_157 TCRγ on the molecular surface of Spl_157 TCRμ: Vμ, violet; Vμj, light orange; Cμ, deep purple; CDR1γ, yellow; CDR3γ, magenta; Framework-Vγ (FWγ), lime green; and Framework-Cγ, gray (i). Footprint of the Spl_157 TCRμ on the molecular surface of Spl_157 TCRγ: Vγ, lime green; Cγ, gray; CDR3μj, purple; Framework-Vμj (FWμj), light orange; and Framework-Cμ, brick red (ii). Molecular interactions at the Spl_157 Vμj/Vγ interface: CDR3μj (purple) with CDR1γ (yellow) (iii); CDR3γ (magenta) with CDR3μj (purple) (iv); CDR3γ (magenta) with FWμj residues (v); and CDR3μj (purple) with FWγ residues (vi). For clarity, only the hydrogen bonds are shown as red dashed lines.

CDR2μ loops showed reduced variability between different TCRμ gene clusters (Fig. 4C). This limited diversity was further reduced within all of the γμTCR transcripts detected in the spleen, where the CDR1μ and CDR2μ loops were highly conserved (Fig. 4D, fig. S11A and fig. S11B). An analogous reduction in the CDR1 and CDR2 loop diversity was previously observed in a specific subset of bovine antibodies (*18*). The length and composition of the CDR3μ loop varied among the γμTCRs, and no bias toward specific residues was seen (Fig. 1D and fig. S11). Moreover, the crystal structures of both γμTCRs indicated that the CDR3μ loop formed a large, flexible, and structurally diverse protrusion atop the Vμ domain (Fig. 4E).

γμ T cells are present in the spleen but absent in the blood, indicating that, like some γδ T cell subsets, these cells are tissue resident by nature. γμ T cells are also frequently CD8αα^{+}, although the significance of the CD8 homodimer on these cells remains unclear. The physiological role of γμ T cells is unknown, as is the nature of the ligand(s) for the γμTCRs. TCRs predicted to be similar in structure to the γμTCR have independently evolved twice in vertebrates: in cartilaginous fish (NAR-TCR)

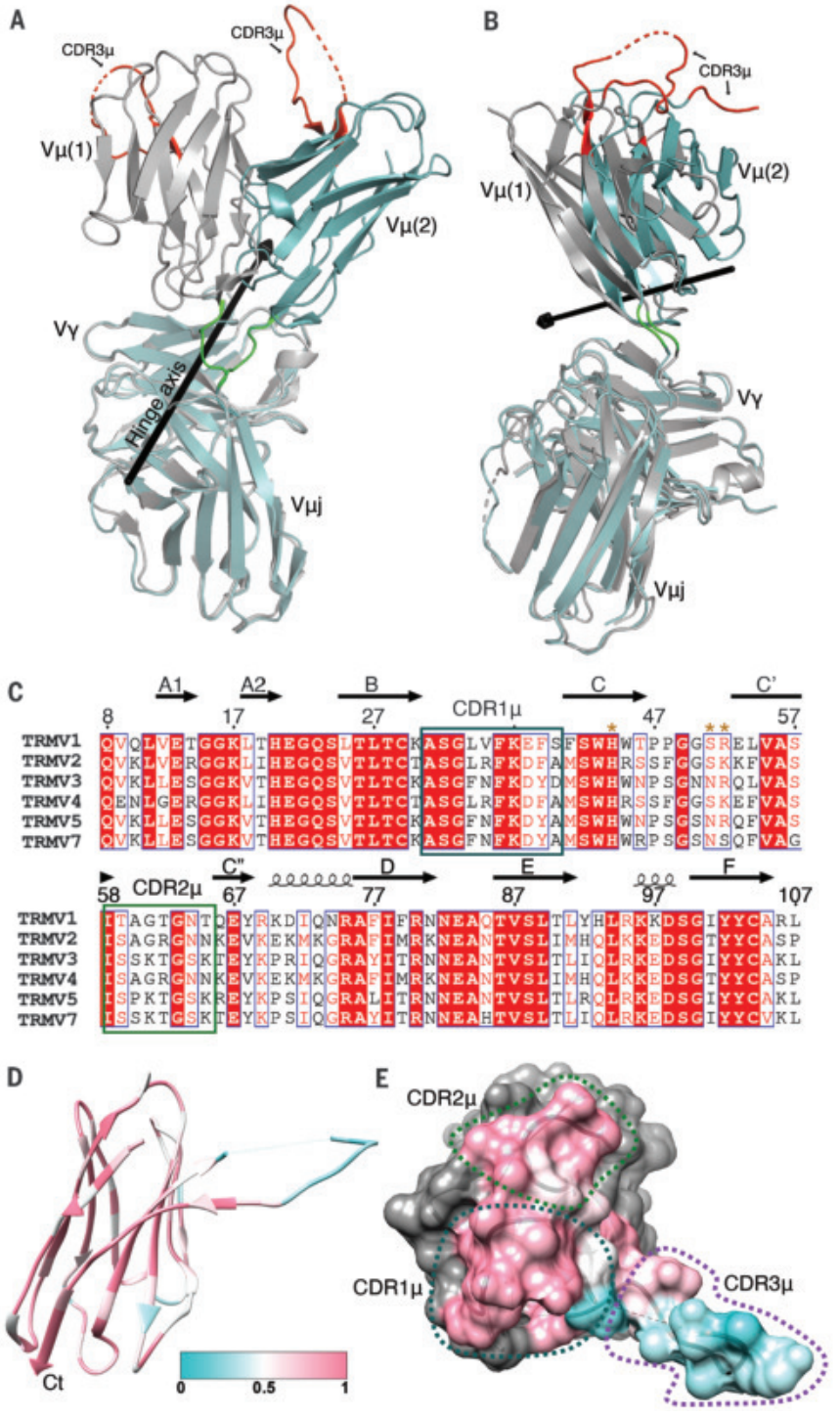

Fig. 4. Structure of the Vμ domain. (**A** and **B**) Superposition of the two molecules present in the asymmetric unit of the Spl_145 γμTCR (A) and Spl_157 γμTCR (B). In both γμTCRs, molecule 1 (chains A and B) and molecule 2 (chains C and D) are colored in gray and light teal, respectively. The Vμ and Vμj interdomain hinge axis was determined using the DynDom program (*12*) and is shown as a black arrow. The CDR3μ loop and the hinge region are colored red and green, respectively. Dashed red lines relate to a disordered region not visible in the electron density. For clarity, only the Vμ, Vμj, and Vγ domains are shown. (**C**) Sequence alignment of the translated germline Vμ segments in *M. domestica*. The positions of the CDR1μ and CDR2μ loops are shown in blue and green boxes, respectively. Polar FR residues 44/51/52 are marked with brown asterisks. Numbering is based on the TCRμ of the Spl_145 γμTCR structure. (**D**) Overview of the fold of the Vμ domain from Spl_145 γμTCR rendered by sequence variation from least (cyan) to most (pink) conserved residues. The conservation score was calculated from the alignment shown in (C). (**E**) Conservation of the surface formed by the CDR1μ, CDR2μ, and CDR3μ loops atop the Vμ domain of the Spl_145 γμTCR rendered from least (cyan) to most (pink) conserved residues. The conservation score was calculated using only the TCRμ chain detected in splenic cells (fig. S11A).

and in mammals (TCRμ). The NAR-TCR is a three-extracellular-domain TCRδ chain with an unpaired V related to the V of IgNAR light-chain-less antibodies (*19*). TCRμ likely evolved from a TCRδ that uses VH genes and is extant in the platypus and some nonmammalian vertebrates (*8*, *20*, *21*).

For αβTCRs and γδTCRs, the CDR loops of both chains form the Ag-recognition site (*22*). This paradigm does not operate for γμTCRs. Here, the structure and reduced diversity of the Vμj-Vγ domains of the γμTCR suggest that it plays an architectural role. By contrast, the diversity of the CDR3μ loop is indicative of a direct Ag-recognition determinant. Consistent with this, γμ T cells express the CD3 components involved in conventional T cell signaling (table S1). There is precedence for single, unpaired Ig domains directly binding Ag. Given the similarity of Vμ to camel VHH and shark IgNAR, it may also be a potential source of nanobodies (*23*, *24*). Here, we describe the basis underpinning the assembly of a third TCR lineage and highlight the importance of examining immune systems from diverse species (*25*).

REFERENCES AND NOTES

1. S. M. Hedrick, D. I. Cohen, E. A. Nielsen, M. M. Davis, *Nature* **308**, 149–153 (1984).
2. Y. Yanagi *et al.*, *Nature* **308**, 145–149 (1984).

3. Y. Chien *et al*., *Nature* **312**, 31–35 (1984).
4. M. B. Brenner *et al*., *Nature* **322**, 145–149 (1986).
5. Z. E. Parra *et al*., *Proc. Natl. Acad. Sci. U.S.A.* **104**, 9776–9781 (2007).
6. X. Wang, Z. E. Parra, R. D. Miller, *J. Immunol.* **187**, 5246–5254 (2011).
7. Z. E. Parra *et al*., *BMC Genomics* **9**, 111 (2008).
8. Z. E. Parra, M. Lillie, R. D. Miller, *Mol. Biol. Evol.* **29**, 3205–3214 (2012).
9. L. Liang *et al*., *J. Biol. Chem.* **280**, 31442–31449 (2005).
10. L. S. Mitchell, L. J. Colwell, *Proteins* **86**, 697–706 (2018).
11. A. P. Uldrich *et al*., *Nat. Immunol.* **14**, 1137–1145 (2013).
12. R. A. Lee, M. Razaz, S. Hayward, *Bioinformatics* **19**, 1290–1291 (2003).
13. A. Steels, L. Bertier, J. Gettemans, "Use, applications and mechanisms of intracellular actions of camelid VHHs," in Antibody engineering, T. Böldicke, Ed. (IntechOpen, 2018); pp. 205–229.
14. S. Spinelli *et al*., *Nat. Struct. Biol.* **3**, 752–757 (1996).
15. K. A. Henry, C. R. MacKenzie, *MAbs* **10**, 815–826 (2018).
16. V. K. Nguyen, R. Hamers, L. Wyns, S. Muyldermans, *EMBO J.* **19**, 921–930 (2000).
17. V. Kunik, B. Peters, Y. Ofran, *PLOS Comput. Biol.* **8**, e1002388 (2012).
18. T. C. Deiss *et al*., *Cell. Mol. Immunol.* **16**, 53–64 (2019).
19. M. F. Criscitiello, M. Saltis, M. F. Flajnik, *Proc. Natl. Acad. Sci. U.S.A.* **103**, 5036–5041 (2006).
20. Z. E. Parra, Y. Ohta, M. F. Criscitiello, M. F. Flajnik, R. D. Miller, *Eur. J. Immunol.* **40**, 2319–2329 (2010).
21. Z. E. Parra, K. Mitchell, R. A. Dalloul, R. D. Miller, *J. Immunol.* **188**, 3912–3919 (2012).
22. J. Rossjohn *et al*., *Annu. Rev. Immunol.* **33**, 169–200 (2015).
23. C. Hamers-Casterman *et al*., *Nature* **363**, 446–448 (1993).
24. A. S. Greenberg *et al*., *Nature* **374**, 168–173 (1995).
25. A. S. Flies; Wild Comparative Immunology Consortium, *Science* **369**, 37–38 (2020).

ACKNOWLEDGMENTS

We thank the staff at the National Synchrotron for assistance with data collection, the staff at the Monash Macromolecular crystallization facility for setting up the crystallization trials, L. Rashleigh for assisting in the production of the soluble γμTCRs, and G. Petukhova (Uniformed Services University of the Health Sciences) for generously assisting with *M. domestica* tissue collection. The crystallography research was undertaken on the MX1 and MX2 beamlines at the Australian Synchrotron, part of ANSTO. **Funding:** This work was supported by the ARC Centre of Excellence (CE140100011), the National Institutes of Health (award P30 GM110907), the National Science Foundation (award IOS-13531232), and by the Intramural Program of the National Institutes of Health. J.L.N. is supported by an ARC Future Fellowship (FT160100074). J.R. is supported by an Australian ARC Laureate Fellowship (FL160100049). K.A.M. is supported by a National Science Foundation Graduate Research Fellowship (DGE-1939267). **Author contributions:** K.A.M. and M.W. are joint first authors and contributed to data generation, data analysis, and writing the manuscript. T.P. and K.K.S. provided key reagents and samples. V.L.H., L.B., S.D., and D.C.D. provided reagents and analyses. J.R., R.D.M., and J.L.N. are co-senior authors. They conceived the study, analyzed the data, and cowrote the manuscript. **Competing interests:** The authors declare no competing interests. **Data and materials availability:** Atomic coordinates and structure factors of the Spl_145, Spl_157, and truncated Spl_118 γμTCRs have been deposited in the Protein Data Bank under numbers 7K0X, 7K0Z, and 7L15, respectively. The RNASeq data were deposited in the National Center for Biotechnology Information (NCBI) under BioSample accession SAMN15061401 through SAMN15061779.

SUPPLEMENTARY MATERIALS

science.sciencemag.org/content/371/6536/1383/suppl/DC1
Materials and Methods
Figs. S1 to S11
Tables S1 to S9
References (*26*–*39*)
MDAR Reproducibility Checklist

8 September 2020; accepted 4 February 2021
10.1126/science.abe7070

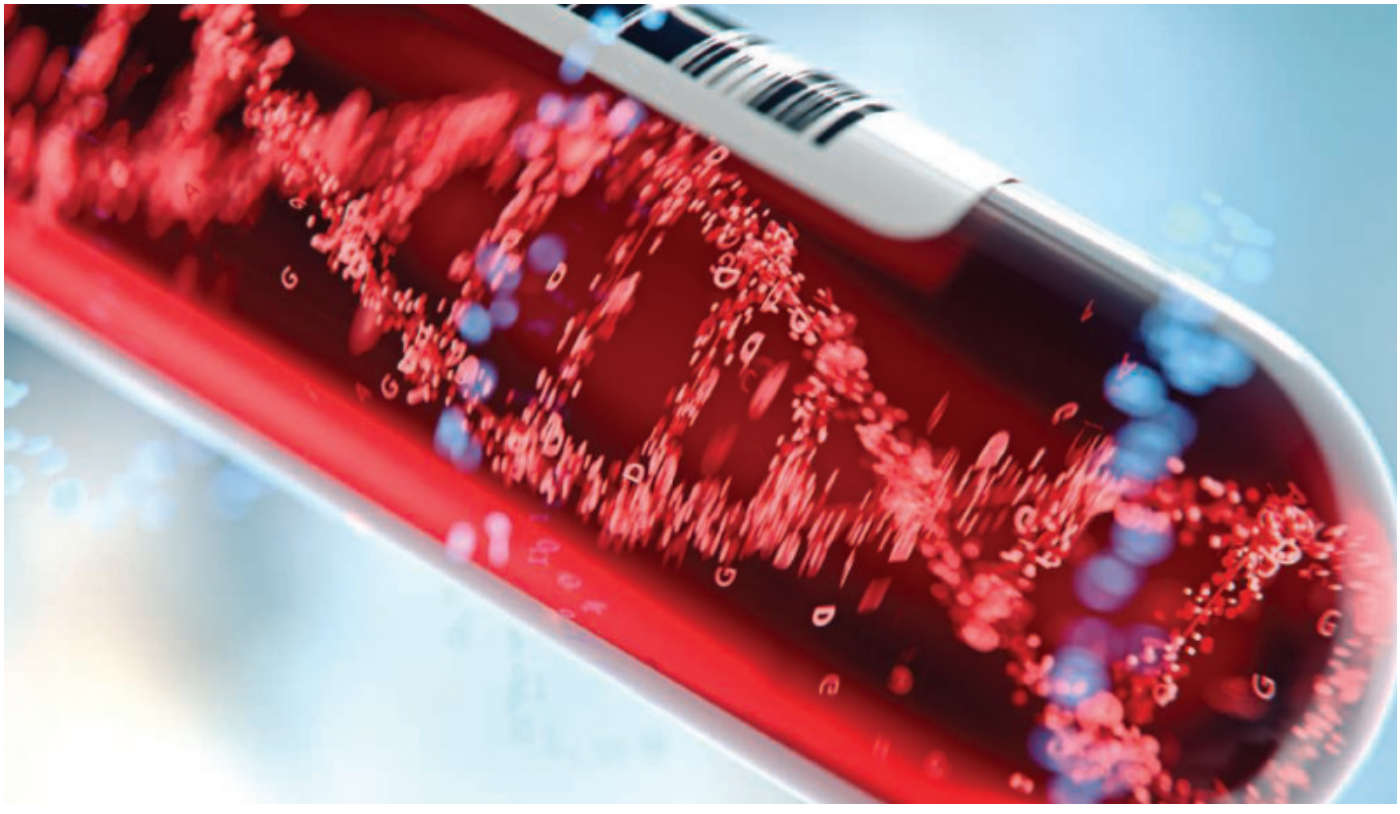

Better, faster, and earlier: Cancer screening has come of age, with many methods capable of testing multiple cancers in one sample.

Catching cancer extremely early

A variety of tests under development promise easier and more complete cancer-screening capabilities. With just a single blood sample, some diagnostics will search for signs of dozens of cancers. In addition to their biological capabilities, these screening methods benefit from advanced computation, including artificial intelligence. The question is, how well might these tests work?

By Mike May

No one doubts the value of diagnosing cancer at the earliest possible stage. Sometimes, though, the magnitude of the impact is underappreciated. Pharmacologist David Crosby, head of prevention and early detection research at **Cancer Research UK**, and his colleagues emphasized the early-detection effect on treatment results: "57% of people with lung cancer survive their disease for 5 years or more when diagnosed at stage I compared with only 3% of those diagnosed at stage IV" (*1*).

Existing cancer-screening tools help, but only when people get them. As an example, low-radiation computer tomography (CT) scans can reveal lung cancer, but as Sam Cykert, professor at the **University of North Carolina School of Medicine**, points out, "By far, the highest lung-cancer death rates in Americans are among black men, and they hardly ever get CT screening."

With a simple blood test, possibly part of a regular exam every few years, more people might get screened for colon and other cancers. "Today, the majority of cancers are found too late, when outcomes are often fatal, because most deadly cancers have no available screening tests," says Josh Ofman, chief medical officer and head of external affairs at **GRAIL**, a biotechnology company based in Menlo Park, California. "Current guideline-recommended screenings are critical, but in the United States they cover only five cancers and screen for a single cancer at a time."

Catching cancer as early as possible promises much better outcomes, but that depends on easy and accurate screening methods. How close is oncology to that goal?

Markers at miniscule levels

For blood cancers, cancerous cells are relatively easy to access and identify–as easy as looking under a microscope, at least for a seasoned pathologist. The same cannot be said for solid tumors, but the blood does carry signs of these cancers as well.

Tumors lose pieces of DNA, but they're hard to find in the blood. Of the cell-free DNA in the blood of someone with cancer, the circulating tumor DNA (ctDNA) might account for just 0.1%. Once extracted, that ctDNA can be analyzed–usually with next-generation sequencing (NGS)–for modifications, such as single-nucleotide variants, insertion-deletion mutations, and copy-number variations. Those changes in ctDNA carry information

cont.>

Upcoming features

■ Microscopy—April 23 ■ Genetics—September 24

about the kind of cancer that created it. That's what most advanced cancer-screening tests look for in blood samples.

For example, **Singlera Genomics** developed the PanSeer assay, which looks for tumor-specific patterns of methylation in ctDNA with NGS. Geneticist Li Jin and his colleagues at **Fudan University** in Shanghai applied PanSeer to blood samples of 605 asymptomatic people, which included 191 patients diagnosed with cancer within 4 years of sample collection. The scientists reported: "PanSeer detects cancer in 95% … of asymptomatic individuals who were later diagnosed…. These results demonstrate that cancer can be noninvasively detected up to four years before current standard of care" (*2*).

That's the kind of early detection that oncologists would like to see on a regular basis. Many companies hope to make that a reality.

Colon-cancer challenges

Cykert noted that people without insurance can't easily get a colonoscopy. Maybe a blood-based test for colon cancer could be easier to obtain and less expensive. That's what **Guardant Health** hopes to provide.

An electrical engineer and one of Guardant Health's co-founders and president, AmirAli Talasaz, says that they've tested blood samples from more than 150,000 patients and "looked at tumor DNA shed from solid tumors." From this work, Guardant Health has recently introduced a test for early-stage colorectal cancer.

"The front end of our chemistry is homebrewed technology," Talasaz says. "We take a tube of blood and isolate the plasma and circulating free DNA, and then–in one assay–we find the sequence and methylation signature." This analysis utilizes tagging methylated DNA with barcodes and then applying NGS. As Talasaz says, "The beauty of our technology is our assay." He adds that the homebrewed technology "increases accuracy of NGS by orders of magnitude."

This is a yes or no test. Either a patient's sample is positive for ctDNA or it's not. Talasaz says that the company's data indicate that this test specificity is 91%.

Multiplexing screens

Tests for specific kinds of cancer certainly have a place in oncology. These blood tests follow the tradition of prostate-specific antigen (PSA) tests for prostate cancer and mammograms for breast cancer. Some companies, though, want to test for many cancers in one assay.

Isaac Kinde, vice president, technology assessment and co-founder at **Thrive**, an Exact Sciences company based in Cambridge, Massachusetts, says its blood test analyzes mutations in about 2,000 base pairs of ctDNA to screen for multiple cancers. Kinde calls these among "the most commonly mutated regions within cancer." The company's test, CancerSEEK, also looks for several cancer-related proteins.

As Kinde explains, "A prototype version of our test was used in real-time to detect cancers [in 10,000 women not previously known to have cancer] and then led to interventions earlier than what could have been done before." He adds, "The sensitivity for various cancer types will vary due to biology." That is, some solid cancers shed more ctDNA than others, or less will reach the blood, which will impact the sensitivity of any ctDNA-based test.

Bending the curve

Other multicancer screening tools are also in development. One of them is GRAIL's Galleri test. "In clinical studies, an earlier version of Galleri showed the ability to detect more than 50 types of cancers–over 45 of which lack recommended screening today–with a low false-positive rate of less than 1%," Ofman says. "When a cancer signal is detected, the Galleri test also pinpoints where the cancer signal originated in the body with high accuracy, all from a single blood draw."

GRAIL's technology uses artificial intelligence (AI) and machine learning (ML) to analyze data from cell-free DNA in a patient's blood. Ofman says that the analysis "examines these patterns of DNA methylation to identify signatures that distinguish cancer from noncancer and help to distinguish different cancer types from each other."

By detecting so many cancers at an early stage, Ofman believes "we can bend the cancer mortality curve." There's some evidence that this might be possible.

For example, GRAIL's PATHFINDER study is evaluating the use of its technology in clinical practices. At the study sites, oncologists used GRAIL technology to detect signals in the blood for more than 50 cancers. Intermountain Healthcare's precision medicine program, **Intermountain Precision Genomics**, in Utah, served as one test site in that study. As Lincoln Nadauld, oncologist and chief of precision health and academics at Intermountain explains: "When a positive signal was detected, we worked those patients up, and we found cancers in patients who were previously asymptomatic. We wouldn't have found those cancers otherwise."

Increasing computation

The enormous amount of data collected in cancer screening and the need to analyze it quickly create significant challenges. To address these issues, some companies collaborate with computation experts.

In China, **Ningbo Konfoong Bioinformation Tech (KFBio)**, a digital pathology company, set up a collaboration with **Intel**, a technology company based in Santa Clara, California, to screen for cervical cancer. Instead of using blood samples, KFBio uses slides of liquid-based cytology specimens obtained from Pap smears into images. Intel is helping with the image analysis. These slides are scanned at 40,000 by 40,000 pixels, and the resulting 1.6 gigapixels include lots of information, says Prashant Shah–global head of artificial intelligence for health and life sciences at Intel, and an advisor on AI for the U.S. National Institutes of Health.

The objective is to analyze the slides as quickly and accurately as possible. Using Intel's technology and expertise, the company increased the speed of analysis 8.4 times. In addition to being speedy, the AI-based model must run on various computers. Running the model that analyzes the slides takes hundreds of thousands of gigabytes of computer memory. cont.>

Featured participants

American Cancer Society
www.cancer.org

Cancer Research UK
www.cancerresearchuk.org

Fudan University
www.fudan.edu.cn/en

GRAIL
grail.com

Guardant Health
guardanthealth.com

Intel
www.intel.com

Intermountain Precision Genomics
intermountainhealthcare.org

Ningbo Konfoong Bioinformation Tech (KFBio)
en.kfbio.cn

Perelman School of Medicine, University of Pennsylvania (UPenn)
www.med.upenn.edu

Singlera Genomics
singleraoncology.com

Thrive
thrivedetect.com

University of North Carolina School of Medicine
www.med.unc.edu

U.S. National Cancer Institute (NCI)
www.cancer.gov

"Using our Xeon-based servers and optimizing neural-network algorithms using OpenVINO, we created a solution that can run efficiently on small- and large-footprint hardware," Shah says. That's necessary for the screening tool to be used around the world.

When data from patients is being used, issues beyond screening must be considered. Intel is also working with the **Perelman School of Medicine at the University of Pennsylvania (UPenn)** to train an AI-based model on brain tumors. Doing that with high accuracy requires masses of data pooled across institutions, but security and privacy concerns reduces the number of clinics and hospitals that will participate. That's because traditional ML models collect data in one centralized location for the computing, but there's a better way to do it. "Federated learning splits up part of the training so it happens on each owner's data, shares the learning, or the model, to a central location, and combines all the models in a single aggregate view," explains Jason Martin, principal engineer in the Security Solutions Lab and manager of the Secure Intelligence Team at Intel Labs. "Then, the global trained model goes back out to the sites, and it's done in an ongoing cycle." So, the clinic or hospital that collected the data never needs to let anyone else see it.

Martin notes that his research with UPenn reaches "99% of the accuracy of a traditional approach." It also makes it possible to use far more data to train the model. With a traditional approach, UPenn can provide data from around 500 patients with brain tumors; by taking the federated approach, 29 institutions are set up to provide data from more than 1,000 patients each. Ultimately, this AI-driven model could look at a patient's brain data, scan it for areas of concern, and quickly direct a pathologist to any cells that need expert attention.

Added approaches

No matter how much screening improves, it's not the only tool that can be used against cancer. Changes in behavior must also be encouraged.

According to the **U.S. National Cancer Institute (NCI)**, "Smoking, poor nutrition, and physical inactivity are just some of the human behaviors that have been linked to the development of many common cancers." Although NCI notes that smoking causes 30% or more of the cancer deaths in the United States, it also reports that "cigarette smoking prevalence among adults has declined steadily since 1992," and that "initiation of the use of cigarettes among children and adolescents aged 12–17 started falling more rapidly in 2010" (*4*).

Even though the general population is decreasing cancer-causing behaviors, that cannot prevent all cancer. So despite the most advanced prevention programs, screening remains crucial–but participation could be improved. As the American Cancer Society puts it, "Research on barriers related to cancer screening shows that multiple factors–public policy, organizational systems and practice settings, clinicians, and the patients themselves–influence cancer screening and that a diverse set of interventions targeted at each of these can improve cancer screening rates" (*5*).

Steps ahead

Nadauld sees cancer screening as a standard part of future health care. He says, "I foresee patients coming in for their well-patient visit, and while they're getting their cholesterol checked, for example, they will also get a blood test to see if they have one of dozens of different kinds of cancer."

To him and many of his colleagues, the promise of screening tests in development is amazing. Nadauld says, "As a medical oncologist, I have longed for this kind of test."

Undoubtedly, sophisticated cancer screening offers many benefits, but follow-up matters as well. "Even people who get screened for cancer today can fall through the cracks on the path to treatment," Cykert explains. "That takes a system–running the tests, training people to explain the tests and the treatment options, and getting patients treated."

Overall, combating cancer effectively depends on the integration of many factors. From expanding efforts on prevention to developing more accurate and available screening and treatment, it takes the entire health care system to reduce the incidence of cancer and improve the outcomes. And no matter how lifestyles improve, and no matter how much environmental exposure to carcinogens is reduced, cancer screening will maintain a fundamental role in health care. The promise of making these tests much more effective will impact people in every age group worldwide.

References

1. D. Crosby *et al.*, *Lancet Oncol.* **21**, 1397–1399 (2020).
2. X. Chen *et al.*, *Nat. Comm.* **11**, 3475. (2020).
3. A. M. Lennon *et al.*, *Science* **369**, eabb9601 (2020).
4. National Cancer Institute, "Cancer Trends Progress Report" (2020), https://progressreport.cancer.gov.
5. American Cancer Society, "Cancer Prevention & Early Detection: Facts & Figures 2019-2020" (2020), https://www.cancer.org/content/dam/cancer-org/research/cancer-facts-and-statistics/cancer-prevention-and-early-detection-facts-and-figures/cancer-prevention-and-early-detection-facts-and-figures-2019-2020.pdf.

Mike May is a freelance writer and editor based in Florida.

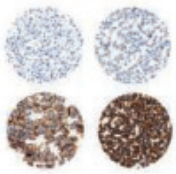

Breast Cancer Cell-Line Array

AMS Biotechnology announces a HER2 control cell-line array that is proven as an effective slide quality control for human epidermal growth factor receptor 2 (HER2) expression in breast-cancer tissue samples. This FFPE cell-pellet microarray delivers a full dynamic range of HER2, estrogen receptor (ER), and progesterone receptor (PR) expression, validated by the Ventana system, to give immunohistochemical (IHC) data in strong concordance with the routinely processed tissue sample sections. Using cell-line controls significantly lowers the costs of IHC examinations, fluorescence in situ hybridization, and NGS applications while enabling high levels of standardization and reliability. The new HER2 cell-line microarray is perfect for cancer research establishments and laboratories that require results while not compromising on consistency or quality.

AMS Biotechnology
For info: 617-945-5033
www.amsbio.com/ffpe-cancer-cell-line-controls

Leukapheresis Products

Lonza has expanded its renowned human primary cell offerings with the launch of fully customizable, high-quality cryopreserved Leukopaks. The frozen Leukopaks enable long-distance shipping of leukapheresis products without the concern of reduced cell viability encountered with fresh Leukopaks. Being suitable for long-term storage in research labs, the cryopreserved Leukopaks will also allow immediate access to viable cells for greater convenience and workflow flexibility. They come in a range of sizes, including packs of 2.5, 5, and 9.5 billion cells, which can be subdivided into separate smaller bags for greater convenience. Specific donor characteristics like age, gender, and human leukocyte antigen (HLA) type are also available, with a wide range of recallable donors and several product-testing options, using a unique costing structure that allows customers to pay only for the customization they need. A Leukopak is an enriched, leukapheresis-derived product containing high concentrations of peripheral blood mononuclear cells, such as T cells, B cells, and monocytes. Such cells are critical for immunotherapy research and for optimizing cell-therapy process development before progressing to full clinical manufacture.

Lonza
For info: 800-638-8174
bioscience.lonza.com

Single-Cell Analysis Reagent

Immudex ApS announces the launch of dCODE Dextramer (RiO) reagents. These DNA-barcoded MHC Dextramer reagents are designed to be compatible with the BD Rhapsody system and used for multiplexing, allowing the identification of many different T-cell specificities in the same sample. dCODE Dextramer reagents are used to determine T-cell antigen-specificity at single-cell resolution, providing simultaneous information on gene expression and surface-marker expression. By creating personalized dCODE Dextramer libraries, it is possible to profile T cells and get a new understanding of T-cell immunity. dCODE Dextramer reagents consist of a dextran polymer backbone carrying multiple major histocompatibility complex (MHC)-peptide complexes, a corresponding unique DNA barcode oligo, and R-phycoerythrin for sorting of dCODE Dextramer positive cells before loading the sample into the BD Rhapsody system. The unique DNA barcode oligo comprises BD Rhapsody-compatible PCR handle sequences for PCR amplification, a unique molecular identifier (UMI) sequence, and a DNA barcode sequence that specifies the MHC-peptide specificity.

Immudex
For info: +45-(0)-29-13-42-24
www.immudex.com

Nucleic-Acid Quantification

Tecan has launched the Frida Reader for the Fluent Automation Workstation, offering researchers the ability to quantify nucleic acids without sample loss. This unique solution performs UV absorbance-based quantification and purity assessment in a hanging drop, avoiding the consumption of rare and precious samples following nucleic acid purification (NAP). Efficient NAP is crucial prior to applications such as NGS or PCR/quantitative PCR, but laboratories working with low-volume, high-value samples cannot always afford to lose a portion of their samples for quantification and purity assessment. The Frida Reader eliminates this issue by allowing assessment of sample quality and quantity without any sample loss, aspirating the sample back into the pipette tip after performing hanging-drop absorbance measurements. It uses four separate wavelengths—230 nm, 260 nm, 280 nm, and 320 nm—to allow real-time nucleic acid quantification in the 5 ng/µL–1,000 ng/µL range, as well as quality control measurements to identify protein contamination.

Tecan
For info: +41-(0)-44-922-89-22
www.tecan.com/fridareader

T-Cell Transduction

Whether you're working with difficult-to-transduce cells like primary T cells or just want to ensure high transduction efficiency, System Bioscience's TransDux reagents are ready to deliver. Our newer TransDux MAX Lentiviral Transduction Reagent can increase transduction efficiencies by up to eightfold compared to polybrene, while our original TransDux formulation is still available for researchers who are not yet ready to make the change. TransDux MAX comes in an easy-to-use, two-component format (TransDux and MAX Enhancer) that is good for 100 transduction reactions. Simply mix both reagents into conditioned media from target cells, and infect with your lentivirus of choice for a higher level of transduction efficiency. TransDux MAX is broadly compatible and does not interfere with downstream gene expression or functional assays.

System Biosciences
For info: 888-266-5066
systembio.com

Electronically submit your new product description or product literature information! Go to www.sciencemag.org/about/new-products-section for more information.

Newly offered instrumentation, apparatus, and laboratory materials of interest to researchers in all disciplines in academic, industrial, and governmental organizations are featured in this space. Emphasis is given to purpose, chief characteristics, and availability of products and materials. Endorsement by *Science* or AAAS of any products or materials mentioned is not implied. Additional information may be obtained from the manufacturer or supplier.

Zhengzhou University is one of the key universities of the national "211 Project", and of "World 1st University Project", as well as of universities co-sponsored by the Henan Provincial Government and the Ministry of Education. It was born in 10th, July 2000 when the former ZZU, Zhengzhou University of Technology (ZUT) and Henan Medical University (HMU) merged into one, and now developed into a comprehensive university with 12 major disciplines, namely liberal arts, science, engineering and medicine, etc. It has over 50,000 full-time undergraduates, more than 23,000 full-time postgraduates and nearly 2,500 international students. Meanwhile, there are 30 first-level disciplines authorized to confer doctorate degrees, 3 professional doctorate programs, 28 postdoctoral research stations; 3 "first-class" disciplines and 6 national key (being cultivated) disciplines. ZZU is home to 12 national scientific and research platforms including state key laboratories, engineering research centers, engineering laboratories, etc. Among a total of 5800 faculty members, there are 16 academicians of Chinese Academy of Science and Chinese Academy of Engineering, 2 members of Chinese Academy of Social Sciences and 4 overseas academicians as well as 78 elected into national talent programs (projects). They have formed a strong team with academicians and academic masters as the head, distinguished scholars as academic leaders, and outstanding PhDs as core talents.

Rooted in the broad and profound culture of the Central Plains of China and nurtured by blended diversified cultures and disciplines, ZZU people have developed the virtues of tolerance, lenience and can-do spirit and pursued ZZU's mission and spirit of seeking truth and being responsible, thus forming typical school ethos-- Perseverance, Trust-worthiness, Benevolence, Tolerance, Modesty, Prudence, and Critical Thinking and Diligence. Standing at this new starting line, ZZU decided where to go and laid out a three-step strategy to make it to the list of world-class comprehensive & research-oriented universities by the middle of this century. To achieve high-quality development, the university has made efforts to strengthen itself though talents. With the idea of "top-notch talents breakthrough, team integration, talent cultivation and structural optimization", ZZU implemented Distinguished Professor Program to attract more academic masters, and Innovation Talent Cultivation Program to create an ideal environment for the growth of innovative talents.

ZZU, your stage to make a difference!

RECRUITING POSITION

Distinguished Professor, Top Talent

A competitive remuneration package and scientific research services referring to the standards of world-class universities will be provided for the right candidates.

HOW TO APPLY

Please send full curriculum vitae (please note the position and discipline you are applying for) to **rcb@zzu.edu.cn**.

MEDICINE

Medicine, referred to as the earliest established discipline in Zhengzhou University, is also a first-class discipline in Zhengzhou University's key construction.

Over the past 92 years since Zhengzhou University was founded, numbers of distinguished experts and scholars have been devoted to teaching and clinical research, including Prof. Dong Minsheng, an otolaryngology expert; Prof. Shen Qiong, founder of esophageal cytology; Prof. Su Shouzhi, human parasitology specialist; and Prof. Zhang Xiaofang, inventor of the grid method for locating intraocular foreign bodies, and so on.

The college of medicine currently has 14 medical schools or departments and 11 affiliated hospitals, forming a modern medical discipline system such as basic medicine, clinical medicine, preventive medicine, pharmacy, nursing, stomatology, a complete training system for undergraduates, masters and doctors, and a fully functional medical research system.

The college of medicine has 5 national and 46 provincial scientific research platforms, including the State Key Laboratory of Esophageal Cancer Prevention and Control jointly established by the province and the ministry, and established a national tele-medicine center. Five affiliated hospitals were selected for the National Capacity Improvement Project of Refractory Disease Diagnosis and Treatment, and two National Regional Medical Centers and five sub-Centers of Clinical Research Center were built to play a leading role in the region and serve the "Healthy China" strategy.

The College seeks outstanding scholars with strong commitment to excellence in teaching and research. Candidates in any area of medicine will be considered, with particular emphasis on candidates who will complement or extend the college's strengths. Preference will be given to those with teaching and research experiences and Ph.D. in medicine or a related field. Duties include undergraduate or graduate teaching and research.

Tel: +86-371-66658832 Email: ams@zzu.edu.cn

北京大学
120th ANNIVERSARY OF PEKING UNIVERSITY
1898–2018

THE COLLEGE OF ENVIRONMENTAL SCIENCES AND ENGINEERING

is devoted to cutting-edge fundamental research and clean technologies for a sustainable future

To improve the environment in the midst of rapid development is a major challenge facing China. As one of China's earliest programs dedicated to environmental research and talent cultivation, the College of Environmental Sciences and Engineering (CESE) of Peking University (PKU) takes it as its mission to tackle Chinese and global environmental challenges. CESE has built a whole-process research system, integrating science, engineering and public policies. In line with the pursuit of **Excellence** and **Relevance**, CESE endeavors to establish a world-class environmental discipline and research platform, cultivate high-level talents with global vision, and become a top environment policy think tank. According to the latest ESI data, PKU Environmental Sciences program ranks in the top 0.2% in the world. In the latest U.S. News & World Report and Quacquarelli Symonds discipline lists, environmental sciences at PKU ranks 44th and 26th globally.

CESE has 67 faculty members with national and international reputations, including one academician of the Chinese Academy of Sciences and two academicians of the Chinese Academy of Engineering. CESE also boasts two Creative Research Groups of the National Natural Science Foundation, one State Key Laboratory, one Ministry of Education Key Laboratory and one International Joint Laboratory. The faculty members have held over 40 positions as associated editors or members of editorial boards for international journals, 26 positions in international academic associations/societies and won many international awards. Currently, CESE consists of the Department of Environmental Sciences, the Department of Environmental Engineering and the Department of Environmental Management. There are six research fields, including: Atmospheric Pollution and Climate Change, Environment and Human Health, Water Treatment and Microbial-Technology, Water Pollution Control and Integrated Watershed Management, Environmental and Resources Economics, Environmental Planning, Management and Sustainable Development. In recent years, CESE has successfully developed the environmental-media (atmosphere and hydrosphere)-based whole-process research system and the international-treaty –compliance-oriented global environmental governance studies. Building on solid basic research, CESE aims to promote policy implementation and technology application.

The development of new knowledge on atmospheric chemistry and physics is the key to the mitigation of China's severe air pollution. To meet this pressing need, CESE took the lead by proposing the 'Air Pollution Complex model' as well as the concept of 'Environmental Civilization' . Moreover, PKU discovered new mechanisms for the maintenance of the atmospheric oxidation capacity with global importance. The relevant findings were published in prestigious journals like *Science*, *Nature Geoscience* and *PNAS*. A comprehensive air pollution control technology system has been established, which integrates field observation, numerical simulation and pollution control strategy development so as to discover the formation mechanisms of air pollution complex and achieve the technological innovation of regional air pollution control. Using the newly developed system, CESE has conducted a series of major observational research campaigns over the Pearl River Delta (PRIDE-PRD) and promoted the establishment of a regional monitoring network and an early warning system for air pollution control. Approved and adopted by the government, the monitoring network results have become instrumental to decision making in both PRD and Hong Kong. It is the first one of its kind in China and helps PRD to be the first polluted region in China for compliance of $PM_{2.5}$ air quality standard. The air pollution in megacities and surrounding regions is of global importance. One typical case is the North China Plain, which is the largest territory covering many different provincial areas including Beijing. The coordinated provincial air pollution control thus has become a key strategic option. Based on a good understanding of the formation mechanism of air pollution, CESE developed strategies and methodologies for regional coordinated air pollution control, which successfully ensured the air quality during the 2008 Beijing Olympic Games in six provinces and cities. The theories and control technology system of complex air pollution developed by CESE also guaranteed the air quality for the Guangzhou Asian Games and the Shanghai World Expo, promoting the implementation of National Air Pollution Prevention and Control Action Plan. At present, CESE is organizing the country's best experts to explore the formation mechanism and source identification of the heavy air pollution around Beijing.

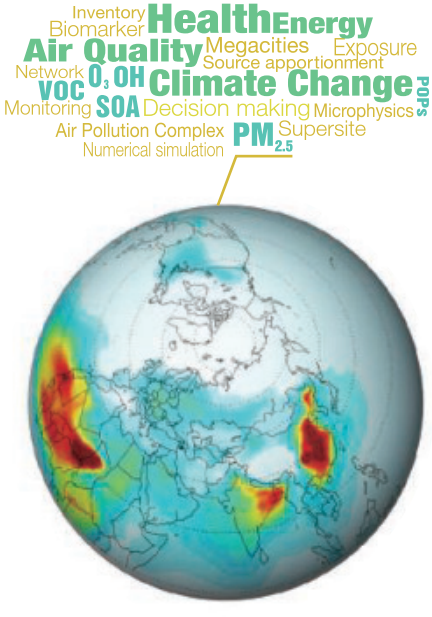

The focus of China's Clean Water Action Plan is on its major basins. CESE was the first to propose the concept of "All Materials Flux (AMF)" and has conducted the world' s largest AMF monitoring in the Yangtze and the Yellow River. Such research has successfully identified the lateral transport of soil carbon and land−atmosphere CO_2 flux induced by water erosion in China. The relevant findings were published in *PNAS*. CESE has developed a series of water pollutants removal techniques and integrated watershed simulation-optimization models, especially for nitrogen pollution, the most urgent problem in China. Several breakthroughs on the nitrogen water pollution control and treatment have been achieved in the past several years, including advanced nitrogen removal technology for municipal sewage, efficient nitrogen removal techniques for industrial wastewater, ecological treatment of sewage in rural area, and the control of non-point (distributed) sources of regional nitrogen contamination. The heterotrophic nitrification and aerobic denitrification microorganisms have been successfully isolated and cultured to solve the key problems of advanced nitrogen removal in municipal wastewater treatment plants. To facilitate the degradation of highly toxic organic pollutants from industrial wastewater, the macroporous functional carriers, which could enhance the microbial tolerance to toxic substances and high ammonia nitrogen, have been fabricated. The proposed biological-ecological multi-medium techniques greatly improve the abundance of denitrification functional bacteria and have been successfully used to treat the sewage in rural areas. The developed techniques have provided core technical support for the improvement of major basins in China, such as the South-North Water Diversion Project, the National Rural Safe Drinking Water Initiative, the Xiangjiang River heavy metal pollution treatment, the sediment treatment of the Yellow River and the Lake Dianchi eutrophication control.

CESE is concerned about public health risks due to environmental exposure. In view of the increasingly severe urban and regional environmental pollution in China, CESE takes full advantage of the many established disciplines of social, natural, and medical sciences at PKU, and promotes research in the field of environment and health by leading key research projects in collaboration with other disciplines, so as to establish the linkage between environmental exposure, internal exposure and health effect markers. Because of the palpable improvement of the air quality in Beijing during 2008 Olympic Games, CESE designed a "quasi-control" experiment by monitoring the biomarkers of inflammation, oxidative stress, immunity and vascular damage in order to find out the effect and mechanism of atmospheric pollution on human health. The results show that the oxidative effects among children, the cardiovascular system indicators among the elderly and cardiovascular function effects in healthy people are associated with atmospheric pollutants, especially the chemical composition of PM_{10} and $PM_{2.5}$. Based on the measurements of multiple organic pollutants in the placenta as an indicator of the fetus's in utero exposure in a case-control study, pollutants such as PAHs were found to be the risk factor with a significant dose-response relationship. Such studies have been published in *JAMA*, *Lancet* and *PNAS*.

It is PKU's tradition to work out China's global environmental strategies. Directly involved in treaty negotiation, signing and compliance, CESE served as the technical team leader in the development of China's Plan for the Montreal Protocol and the relevant Industry-Wide Solution and Control System, setting a benchmark for developing countries. CESE also took the lead in developing China's National Implementation Plan of the Stockholm Convention, which has been adopted by the State Council and contributed greatly to the all-out ban on the production, importation and consumption of controlled POPs. A number of international awards were bestowed on CESE, such as the Gold Award from SEPA, UNEP/WMO Vienna Convention Award, Best-of-the Best Awards from US EPA, Twentieth Anniversary Ozone Protection Award from UNEP, Special Commendation Award and Technical Leadership Award from the secretariat of the Montreal Protocol.

CESE has been proactive in promoting international cooperation by designing major research programs and promoting joint research. As the site of the International Program Office, CESE has facilitated the implementation of the Monsoon Asia Integrated Research on Sustainability (MAIRS), one of the core projects under the framework of Future Earth. In addition, CESE has mobilized dozens of world-renowned research institutes to participate in such major research programs as CAREBEIJING, PRIDE-PRD and AMF, and taken the lead in drafting the report on the Impacts of Megacities on Air Pollution and Climate for the WMO and IGAC.

CESE at PKU aims to cultivate high-level interdisciplinary talents in environmental discipline and to train pro-active leaders with a solid academic foundation, a strong sense of social responsibility, and global vision. The guideline for talent cultivation incorporates healthy personality, diversity, environmental concern, self-actualization, responsibility, independent thinking, innovation and team work. Graduates from CESE have made great contributions to sustainable development in and outside China. Many of them hold important positions in UN organizations, NGOs, the Chinese government, and the world's first-class universities and institutes.

CESE cordially welcomes job applicants and visiting scholars with expertise in related areas such as environmental science, engineering, health and management. Feel free to contact us:

Website: http://cese.pku.edu.cn
Email: huiliu@pku.edu.cn
Tel: +86-10-62754126
Fax: +86-10-62751480
Address: Environmental Building, Peking University, No.5 Yiheyuan Road, Beijing, China. 100871

By **Erika Moore**

The more mentors, the merrier

"Unfortunately, I don't have the bandwidth for a mentorship relationship right now." "I'm not sure I can help." "Why are we meeting again?" Those are just a few of the responses I've received in my quest to develop a broad range of mentors. Early in my grad school training, such reactions left me feeling dejected, battling impostor syndrome, and struggling to maintain the confidence to respond or email again. Since then, however, I've learned that they are an inherent part of crafting a mentor network—and that the pain is worth it.

Since the beginning of my scientific training, fellow students and well-meaning career counselors encouraged me to seek multiple mentors to help me find my way. But, as a self-conscious Black woman in a predominantly white field and institution, I felt intimidated. I was filled with self-doubt, embarrassed by how much I didn't know. How could I ask people to help me if I didn't even know what I needed help with?

But during my second year of grad school, I was desperate. I felt I had no idea what I was doing, and I needed guidance from people who were wiser and more experienced. So I flailed about, attempting to develop a mentoring network. I adopted a "nothing ventured, nothing gained" mentality and embraced the awkwardness of reaching out.

"I needed guidance from people who were wiser and more experienced."

Some of the responses were negative and discouraging—but not all were dead ends. One contact led to an internship in industry, the career direction I envisioned at the time. When that experience left me thinking academia might be a better fit, another path of contacts led me to my current assistant professor position. One email at a time, one informational interview after another, I became comfortable, confident, and strategic in building my network of mentors. Here's what I have learned.

CAST A WIDE NET. Sending cold contacts was scary, so I focused on the thrill of emailing people who had some of the coolest jobs I'd ever heard of. If I was inspired by someone's work, I emailed. If I loved the way they ran their lab, I emailed. If I was interested in learning more about their company, I emailed. Though a few people failed to respond, many did, leading to dozens of informational interviews that helped me home in on my ideal job.

GET TO THE POINT. As a grad student, I met someone at a conference who I hoped would be a future mentor—and followed up with a five-paragraph email. Their reply was simple: "I cannot respond to this. Too long." Another time, a mentor told me, "If I can't respond in six words, I'm not going to." Over the years, I learned to clearly include the what, the ask, and the when—for example, a 30-minute meeting to talk about X, offering three or four specific times. A clear, concise email encourages a quick, positive response.

CONSIDER THE CONTEXT. In graduate school, I asked a senior faculty member to serve as my departmental adviser. They flat out said no with no explanation, and I was left confused. Was it me? Had I come on too strong in my desperate desire to be mentored? Had I offended them somehow? A few months later, they moved institutions. I realized the move must have already been in the works when I asked, and their response didn't reflect negatively on me; they were just anticipating their own changing circumstances and knew that agreeing to be my adviser would have set me up for failure. When evaluating responses or advice, remember that everyone has their own affairs, perspective, and concerns.

COME PREPARED. My one strength was preparation. I came to every conversation with at least 10 questions, arranged in categories including shared experiences, career goals, and advice. Coming prepared helped me respect other people's time and utilize these meetings wisely. ■

Erika Moore is an assistant professor at the University of Florida in Gainesville. Send your career story to SciCareerEditor@aaas.org.

ILLUSTRATION: ROBERT NEUBECKER

GRC Frontiers of Science

Gordon Research Conferences

CONFERENCES

Alcohol-Induced End Organ Diseases

OCTOBER 24 – 29, 2021 • FOUR POINTS SHERATON / HOLIDAY INN EXPRESS • VENTURA, CA, US
CHAIRS: Gyongyi Szabo and Bernd Schnabl
VICE CHAIRS: Elizabeth J. Kovacs and Gavin E. Arteel

Alcohol-Induced End Organ Diseases GRS
OCTOBER 23 – 24, 2021
CHAIRS: Kyle L. Poulsen and Holly Hulsebus

Biotherapeutics and Vaccines Development

NOVEMBER 14 – 19, 2021 • VENTURA BEACH MARRIOTT • VENTURA, CA, US
CHAIRS: Michael J. Tarlov and Linda O. Narhi
VICE CHAIRS: Peter Tessier and Jessica R. Molek

Biotherapeutics and Vaccines Development GRS
NOVEMBER 13 – 14, 2021
CHAIRS: John S. Schardt and Maria-Monica Castellanos

Cannabinoid Function in the CNS

NOVEMBER 7 – 12, 2021 • FOUR POINTS SHERATON / HOLIDAY INN EXPRESS • VENTURA, CA, US
CHAIRS: Matthew N. Hill and Sachin Patel
VICE CHAIRS: Miriam Melis and Mario van der. Stelt

Cannabinoid Function in the CNS GRS
NOVEMBER 6 – 7, 2021
CHAIRS: Anissa Bara and Simon Chamberland

Carbon Capture, Utilization and Storage

OCTOBER 24 – 29, 2021 • JORDAN HOTEL AT SUNDAY RIVER • NEWRY, ME, US
CHAIR: Roger D. Aines
VICE CHAIR: Andre Bardow

Carbon Capture, Utilization and Storage GRS
OCTOBER 23 – 24, 2021
CHAIRS: Humera Ansari and Tony Feric

Cardiac Arrhythmia Mechanisms

OCTOBER 17 – 22, 2021 • FOUR POINTS SHERATON / HOLIDAY INN EXPRESS • VENTURA, CA, US
CHAIRS: David J. Christini and Ursula Ravens
VICE CHAIRS: Crystal M. Ripplinger and Edward J. Vigmond

Cardiac Arrhythmia Mechanisms GRS
October 16 – 17, 2021
CHAIRS: Enaam Chleilat and Jaclyn A. Brennan

Cell Biology of Metals

OCTOBER 17 – 22, 2021 • MOUNT SNOW • WEST DOVER, VT, US
CHAIRS: Caryn E. Outten and Mitchell Knutson
VICE CHAIRS: Angela Wilks and Kerry Kornfeld

Cell Biology of Metals GRS
OCTOBER 16 – 17, 2021
CHAIRS: Cassandra E. Nelson and Liu Liu

Central Nervous System Injury and Repair

OCTOBER 17 – 22, 2021 • JORDAN HOTEL AT SUNDAY RIVER • NEWRY, ME, US
CHAIRS: Yimin Zou and Simone Di Giovanni
VICE CHAIRS: Elizabeth J. Bradbury and Yishi Jin

Central Nervous System Injury and Repair GRS
OCTOBER 16 – 17, 2021
CHAIRS: Jaclyn T. Eisdorfer and Angela R. Filous

Chronobiology

OCTOBER 10 – 15, 2021 • MOUNT SNOW • WEST DOVER, VT, US
CHAIR: Samer Hattar
VICE CHAIR: Charlotte Helfrich-Forster

Chronobiology GRS
OCTOBER 9 – 10, 2021
CHAIRS: Anna-Marie Finger and Josh Mouland

Computer Aided Drug Design

NOVEMBER 7 – 12, 2021 • MOUNT SNOW • WEST DOVER, VT, US
CHAIR: Georgia B. McGaughey
VICE CHAIR: Matthias Rarey

Computer Aided Drug Design GRS
NOVEMBER 6 – 7, 2021
CHAIRS: Eva Nittinger and Sarah Kochanek

Lung Development, Injury and Repair

NOVEMBER 7– 12, 2021 • WATERVILLE VALLEY • WATERVILLE VALLEY, NH, US
CHAIRS: Anne-Karina Perl and Daniel Tschumperlin
VICE CHAIRS: Rory E. Morty and Xin Sun

Lung Development, Injury and Repair GRS
NOVEMBER 6 – 7, 2021
CHAIRS: Semil P. Choksi and Chimwemwe Mwase

Mammalian DNA Repair

OCTOBER 31 – NOVEMBER 5, 2021 • FOUR POINTS SHERATON / HOLIDAY INN EXPRESS • VENTURA, CA, US
CHAIR: Lee Zou
VICE CHAIR: Patricia L. Opresko

Mammalian DNA Repair GRS
OCTOBER 30 – 31, 2021
CHAIRS: Ragini Bhargava and Ahmed Diab

Medicinal Chemistry

OCTOBER 24 – 29, 2021 • MOUNT SNOW • WEST DOVER, VT, US
CHAIR: Janeta Popovici-Muller
VICE CHAIR: Cynthia A. Parrish

Medicinal Chemistry GRS
OCTOBER 23 – 24, 2021
CHAIR: Thomas R. Simpson

Phagocytes

OCTOBER 24 – 29, 2021 • WATERVILLE VALLEY • WATERVILLE VALLEY, NH, US
CHAIR: Michelle R. Lennartz
VICE CHAIR: Sergio D. Catz

Phagocytes GRS
OCTOBER 23 – 24, 2021
CHAIRS: Catherine M. Buckley and Fernando Montano Rendon

Physical Science of Cancer

NOVEMBER 14 – 19, 2021 • FOUR POINTS SHERATON / HOLIDAY INN EXPRESS • VENTURA, CA, US
CHAIRS: Josef Käs and Sharon Gerecht
VICE CHAIRS: David J. Odde and Jennifer M. Munson

Physical Science of Cancer GRS
NOVEMBER 13 – 14, 2021
CHAIRS: Sara Nizzero and Alexander J. McGhee

Stochastic Physics in Biology

OCTOBER 10 – 15, 2021 • FOUR POINTS SHERATON / HOLIDAY INN EXPRESS • VENTURA, CA, US
CHAIR: Yuhai Tu
VICE CHAIR: Jie Xiao

Stochastic Physics in Biology GRS
OCTOBER 9 – 10, 2021
CHAIRS: Corey Weistuch and Oleksandra Romanyshyn

Stress Proteins in Growth, Development and Disease

NOVEMBER 7– 12, 2021 • JORDAN HOTEL AT SUNDAY RIVER • NEWRY, ME, US
CHAIR: Brian C. Freeman
VICE CHAIR: Harm H. Kampinga

Stress Proteins in Growth, Development and Disease GRS
NOVEMBER 6 – 7, 2021
CHAIRS: Stephanie N. Gates and Jessica Kho

Three Dimensional Electron Microscopy

OCTOBER 31 – NOVEMBER 5, 2021 • JORDAN HOTEL AT SUNDAY RIVER • NEWRY, ME, US
CHAIR: Sharon G. Wolf
VICE CHAIR: Daniela Nicastro

Three Dimensional Electron Microscopy GRS
OCTOBER 30 – 31, 2021
CHAIRS: Cameron Varano and Colin M. Palmer

Join your GRC colleagues for safe, in person conferences featuring cutting edge presentations, stimulating discussion and informal networking opportunities at our remote locations in New England and California.

Advance the Frontiers of Science: October-November

Apply now at: www.grc.org

Custom Protein Expression

Work Smart - Not “Heart!”

“Let ProMab handle the protein expression so you can focus on the science!”

ProMab Biotechnologies protein expression platform has supported the CRO industry for over 15 years. Providing staple laboratory practices such as custom gene synthesis and vector design, addition of protein/peptide tags, and capacity for large scale protein production, take advantage of ProMab’s experience to enhance your scientific research.

ProMab’s Advantages

Multiple Expression Systems: Mammalian, Insect, Bacterial, Yeast

- Customizable protein/peptide synthesis
- Large scale production and purification
- Stable cell line development
- Quick turnaround time
- Dedicated technical support
- Downstream to antibody production

Additional services available.

All products are for research only

Discover more | www.promab.com

ProMab Biotechnologies, Inc.
2600 Hilltop Dr, Building B, Richmond, CA 94806
1.866.339.0871 | info@promab.com